Development of biomass-derived surface-modified carbon and polymer-based adsorbents for adsorptive elimination of organic and inorganic pollutants from aqueous setups

A Thesis

Submitted in Partial Fulfillment of the

Requirements for the Degree of

DOCTOR OF PHILOSOPHY

by

CHANDI CHARAN PATRA

(176106016)

Department of Biosciences and Bioengineering,

Indian Institute of Technology Guwahati,

Guwahati 781039, Assam, India

JULY 2022

THIS THESIS IS

DEDICATED TO MY

FAMILY & FRIENDS

INDIAN INSTITUTE OF TECHNOLOGY GUWAHATI

DEPARTMENT OF BIOSCIENCES AND BIOENGINEERING

GUWAHATI 781039

STATEMENT

I do hereby declare that the research findings of this thesis is the result of research work carried out by me in the Department of Biosciences and Bioengineering, Indian Institute of Technology Guwahati, Guwahati, Assam, India, under the supervision of **Dr. Selvaraju Narayanasamy**.

As per the general norms of reporting research findings, due acknowledgements have been made, wherever the research findings of other researchers have been cited in this thesis.

Chandi Patra.

Date: 22/07/2022

Chandi Patra

INDIAN INSTITUTE OF TECHNOLOGY GUWAHATI

DEPARTMENT OF BIOSCIENCES AND BIOENGINEERING

GUWAHATI 781039

CERTIFICATE

It is certified that the work described in this thesis entitled "**Development of biomass-derived surface-modified carbon and polymer-based adsorbents for adsorptive elimination of organic and inorganic pollutants from aqueous setups**" by **Mr. Chandi Patra** for the award of degree of **Doctor of Philosophy** is an authentic record of the results obtained from the research work carried out under my supervision in the Department of Biosciences and Bioengineering, Indian Institute of Technology Guwahati, Guwahati, Assam, India, and this work has not been submitted elsewhere for the award of any other degree.

Chandi Patra.

Chandi Patra
(Candidate)
Roll No: 176106016

CERTIFIED

Dr. Selvaraju Narayanasamy
(Thesis Supervisor)

Date: 22/07/2022

ACKNOWLEDGEMENTS

As I end another fascinating chapter of my career, I would like to express my gratitude towards the people who have helped me construct it into a successful one. Undertaking doctoral research provided me with a truly life-changing experience, and it would not be possible to do without the support and guidance that I received from numerous people. It gives me immense pleasure to heartfully acknowledge everyone who has guided, contributed and supported me in carrying out my doctoral research entitled "**Development of biomass-derived surface-modified carbon and polymer-based adsorbents for adsorptive elimination of organic and inorganic pollutants from aqueous setups**" at the Indian Institute of Technology Guwahati, Guwahati, Assam, India.

I owe my deepest gratitude to my supervisor **Dr. Selvaraju Narayanasamy**, Associate Professor, Department of Biosciences and Bioengineering, Indian Institute of Technology Guwahati, for guidance, advice, and tremendous support throughout my research venture. He was actively involved in acquiring and providing all the guidance to carry out my research. More importantly, he engaged with me in scientific to plan out the experiments and share his knowledge. His go get attitude, and scientific curiosity motivated me to work harder. I am genuinely grateful for his time and efforts to ensure that my research was carried out with good quality.

I am also very grateful to my doctorl committee members: **Prof. A. B. Kunnumakkara**, **Dr. R. Prasanna Venkatesh** and **Dr. Souptick Chanda** for their valuable suggestions and feedbacks over the course of my research. I would also like to thank **Prof. Ranjan Tamuli** for his valuable time in evaluating my First Annual Progress Seminar. I acknowledge the past and present Heads of the Department of Biosciences and Bioengineering, **Prof. Kannan Pakshirajan**, **Prof. Latha Rangan** and **Prof. Rakhi Chaturvedi**, for providing all the necessary departmental facilities during the tenure.

I am also grateful to the staff of **Departmental Central Instrumentation Facility** (DCIF, Department of Biosciences and Bioengineering) and the **Central Instrument Facility** (CIF, Indian Institute of Technology Guwahati), for all their technical and non-technical support, without which it would not be possible to carry out my research. I am also thankful to the office staff members of BSBE and CIF for all their support.

I would like to acknowledge the **Ministry of Human Resource Development** (MHRD, Government of India) for providing me with the fellowship during my PhD tenure.

I sincerely thank all the past and present lab members of the Biochemical and Bioenvironmental Engineering Lab for being very supportive and creating a healthy environment. Special regards to my senior fellows **Dr. Abhishek Ajmani** and **Dr. Shravan Kumar**, for helping me out in developing the lab during my early days. I extend my gratitude to my lab fellow **Dr. Tasrin Shahnaz** for helping me set up the lab, co-ordinate in several projects, and dedicating her valuable time to carry out powdered X-ray diffraction of my samples. I would also extend my gratitude to my close friend and lab member, **Mr. Ajit Kumar**, for helping me practically and emotionally on several occasions. I genuinely appreciate his constant help and involvement in solving many issues for my experiments. I am also grateful to all my lab juniors **Mr. Vishnu Priyan V.**, **Mr. C. Ragavan** and **Mr. Harish Kumar,** for their unrelenting help and support at times needed. Their constant presence and support eased many hurdles in my research venture.

I would also like to extend my deepest gratitude to all the previous M.Tech students **Mr. Rajmohan Medisetti**, **Mr. Vivek Sharma**, **Mr. Fazil SMM**, **Mr. Rishabh Gupta**, **Mr. Nitesh Kumar**, **Ms. Anjali J.** and the current M.Tech students, **Mr. Nirvesh** and **Mr. Bedadeep**. Their support and help have been integral in coming up with many new ideas and solving several problems to overcome various hurdles I faced during my research. Special regards to **Mr. Bedadeep** to convey his helping hands during his B.Tech project.

My next thanks go to my alma mater, IIT Guwahati, which gave me an opportunity of embarking on this fine endeavour of learning with ample facilities and an equally beautiful natural bounty of the Noth-East.

I am very fortunate to have great friends, batchmates, and peers who helped me overcome several hurdles during my research tenure. Special and wholehearted thanks to **Mr. Bipra Chatterjee**, **Mr. Pratik Nag**, **Mr. Chandra Bhanu Gupt** and **Mr. Shashikumar C.** For their unconditional love and support throughout my research work. I am also thankful to all my friends, **Mr. Deepak Patwa**, **Mr. Vidyaganesh R.**, **Mr. Suraj Panda**, **Mr. Allampalli Satya Sai Pawan**, **Mr. Mahesh Das** and **Mr. Manoj Kumar** for all the technical and non-technical help during my research journey. Finally, many thanks to my closest friend **Mr. Wazbir Hussian Barlaskar** for being with me during the most toughest and challenging phase of my life.

My deepest and endless gratitude to my family (Maa, Baba and Bhai), my grandparents and my family elders for their constant support, unconditional love, encouragement, patience and blessings. Their faith and unconditional sacrifices for me always motivated me and pushed me to achieve the best in life.

Finally, I want to express my heartfelt thanks to my brother **Kush Patra** and my Mtech guide, **Dr. Santosh Jha**. I lost them during my course of PhD. They always believed in me, and I hope to be blessed with their blessings for the rest of my life.

Chandi Patra

CONTENTS

ABSTRACT

The present era of industrialization and anthropogenic exploitation has depleted the natural resources and polluted the related ecosystems and habitats. Various biotic and abiotic methods have been exploited over the years, yet we are far from any prominent solution. Adsorption is one such competent method due to its ease of operation, effectivity in dilute systems, economic scalability and non-formation of any toxic by-products. Although adsorption is versatile and easy to adopt in practical forms, the adsorbent materials used are costly and cannot be easily regenerated and recycled, resulting in their large-scale production; thus limiting its acceptance as an ideal wastewater remediation process. There is an urge to mitigate the problems related to bio-remediation/adsorption of industrial wastes via designing cheap, reusable, environment friendly and above all, highly efficient adsorbents.

Biomass-derived carbonaceous adsorbents are preferred for wastewater treatment and remediation due to their extended surface area, porous structure, high adsorptive capacity and a high degree of surface reactivity. However, such carbonaceous adsorbents have their own limitations, making them less susceptible and dispersive in an aqueous medium, and thus, this affects their uptake capabilities and thus limit their applicability in water remediation. Thus, to enhance its efficiency in water remediation, the carbonaceous adsorbents have been surface modified/functionalized using various agents, viz. chelating agents like Ethylenediaminetetraacetic acid (EDTA), surfactant like Cetyltrimethylammonium bromide (CTAB), and polymer-like polypyrrole. Each surface modification serves a specific purpose to the carbonaceous adsorbents for their efficient and effective action for a varying grade of pollutants.

Simultaneously, biopolymers like chitosan are also extensively exploited in water remediation. However, chitosan has been deemed ineffective in wastewater remediation due to low porosity and specific surface area in flaked and powdered forms. One such modification is the development of porous fabricated chitosan via gelation method using $CaBr_2.xH_2O$/methanol solution.

Current work proposes the design of the adsorbents as mentioned above, their characterization and their other related studies to understand its efficiency against pollutants like heavy metals, azo anionic dyes and emerging pharmaceutical contaminants like antibiotics.

ABBREVIATIONS

AAC	Acid activated carbon (biomass derived)
AAC-CTAB	CTAB complexed acid activated carbon
AES	Atomic Emission Spectrometer
AMX	Amoxicillin
APS	Ammonium persulfate
APS	Ammonium persulfate
A_T	Temkin isotherm constant
B	Temkin adsorption heat constant
BB	Bromophenol Blue
BET	Brunauer-Emmett-Teller
$CaBr_2.xH_2O$	Calcium Bromide
$CaBr_2 \cdot xH_2O$	Calcium Bromide
C_e	Concentration of adsorbate at equilibrium
$C_{e,x}$	Equilibrium concentration of component ‘x’ from multi-component system of x+y
$C_{e,xy}$	Equilibrium concentration of all the components in the multicomponent mixture
Ch	Chitosan
CH_3OH	Methanol
C_i	Initial concentration of adsorbate
CIP	Ciprofloxacin
Co^{+2}	Cobalt ions
CO_3^{-2}	Carbonate ions
CR	Congo Red
Cr(VI)	Hexavalent Chromium
$Cr_2O_7^{-2}$	Dichromate ions
CrO_4^{-2}	Chromate ions
CTAB	Cetyltrimethylammonium bromide
CTAB	Cetyltrimethylammonium bromide

Cu^{+2}	Copper ions
DB	Direct Blue 6
DPC	1,5-diphenylcarbazide
EDS	Energy-dispersive X-ray spectroscopy
EDTA	Ethylenediaminetetra acetic acid
Fe^{+3}	Ferric ions
FT-IR	Fourier transforms infrared spectroscopy
g	Gram
g	Redlich-Peterson constants
h	Hours
H_2SO_4	Sulphuric acid
H_3PO_4	Phosphoric acid
HCl	Hydrochloride acid
HCl	Hydrochloric acid
$HCrO_4^-$	Hydrogen chromate ions
J	Joules
K	Kelvin
K_1	Pseudo-First order rate constant
K_2	Pseudo-Second order rate constant
$K_2Cr_2O_7$	Potassium dichromate
$K_{CL,xy}$	Competitive Langmuir constant
K_{DR}	Mean free energy of adsorption
K_F	Freundlich adsorption constant
K_{FK}	Frumkin constant
K_{id}	Intra-Particle Diffusion rate constant
kJ	Kilojoules
K_L	Langmuir constant
K_s	Sips adsorption constant
L	Litre
m	Sips model exponent
m	Meter
MCh	Fabricated Chitosan

mg	Milligram
mL	Mililitre
mol	Mole
M_{total}	Amount of adsorbate ions sent to the packed bed column
N	Normal (concentration)
NaClO	Sodium Hypochlorite
$NaHCO_3$	Sodium bicarbonate
NaOH	Sodium Hydroxide
Ni^{+2}	Nickel ions
nm	Nanometer
NO_3^{-2}	Nitrate ions
NPP	Raw (non-treated) *Pongamia pinnata* shells
OVAT	One-variable-at-a-time
Pa	Pascal
Pb^{+2}	Lead ions
PC	Biomass derived powdered carbon
pH_{IEP}	Iso-electric point
PO_4^{-3}	Phosphate ions
PPP	Phosphoric acid-treated *Pongamia pinnata* shells
PPy	Polypyrrole
PPy-PC	Polypyrrole complexed biomass derived powdered carbon
PPy+.	Polaron state of pyrrole
PPy++	Bipolaron state of pyrrole
PSV	Acid-activated *Sterculia villosa* Roxb. shells
PSV-C	Chelated-activated *Sterculia villosa* Roxb. shells
Q_{Binary}	Maximum adsorption capacity of the adsorbate in binary adsorptive systems
$Q_{CL,x}$	Maximum adsorption capacity for component ‘x’
Q_{DR}	Dubinin-Radushkevich maximum adsorption capacity
Q_e	Adsorption capacity of adsorbent at equilibrium
$Q_{e,xy}$	Adsorption capacity for ‘x’ from multi-component system of x+y
$Q_{e(eqm.)}$	Equilibrium adsorption capacity of a packed bed column

Q_L	Langmuir maximum adsorption capacity
Q_{RP}	Redlich-Peterson maximum adsorption capacity
Q_s	Sips maximum adsorption capacity
Q_{Single}	Maximum adsorption capacity of the adsorbate in single adsorptive systems
Q_t	Adsorption capacity at a specific time 't'
$Q_{Tertiary}$	Maximum adsorption capacity of the adsorbate in tertiary adsorptive systems
Q_{total}	Maximum column capacity
R	Universal gas constant (8.314 J/mol/K)
$R\text{-}SO_3^-$	Sulphonate (anion)
$R\text{-}SO_3H$	Sulphonate (neutral)
rpm	Rotations per minute
RSV	Raw (non-treated) *Sterculia villosa* Roxb. shells
SEM	Scanning electron microscopy
SMX	Sulfamethoxazole
SO_4^{-2}	Sulphate ions
SPP	Sulphuric acid-activated *Pongamia pinnata* shells
T	Temperature
USEPA	United States Environmental Protection Agency
UV	Ultraviolet
V_{eff}	Effective volume of packed bed column effluent
Vis	Visible
W	Total dry weight of the adsorbent used in packed bed column
WHO	World Health Organisation
Y	Percentage removal of adsorbate in packed bed column
Zn^{+2}	Zinc ions
α_{FK}	Interaction parameter for sorbate-sorbent interaction
$\Delta G°$	Gibb's free energy
$\Delta H°$	Change in enthalpy
$\Delta S°$	Change in entropy
ε	Polyani potential

θ	Fractional coverage of sorption sites
ρ	Density of investigated solution

LIST OF TABLES

CHAPTER 1

CHAPTER 2

CHAPTER 3

CHAPTER 4

CHAPTER 5

CHAPTER 6

APPENDIX

LIST OF FIGURES

Figure no. **Page no.**

CHAPTER 1

CHAPTER 2

CHAPTER 3

CHAPTER 4

CHAPTER 5

CHAPTER 6

CHAPTER 1

General introduction and theoritical background

1.1. General introduction

During the last hundred years, industrialisation has grown at a fast rate. It has thus increased the demand for exploitation of the Earth's natural resources at a careless rate, which has exacerbated the world's problem of environmental pollution (Briffa et al., 2020). Water is a primary resource for life on Earth, and access to clean water is critical for humans and the ecosystem. Nonetheless, during the last decades, water quality has been negatively influenced by a continuously increasing population, rapid industrialisation, increasing urbanisation, and careless utilisation of natural resources. Organic matter, nutrients, pharmaceutical and personal care products, poly- and perfluoroalkyl substances, biocides, heavy metals, dyes, radionuclides, plastics, nanoparticles and pathogens are the pollutants of primary concern (Zamora-Ledezma et al., 2021).

Most industrial wastes and effluents, partially treated or sometimes even untreated, are dumped directly into the soil, various water bodies, and aqueous streams. Various sources govern the gradual accumulation of such wastes into the water bodies.

1. Many industries, not having a proper waste management system, drain the waste in the freshwater, which goes into canals, rivers, and later into the sea. The toxic chemicals may change the colour of water, increase the number of minerals, called eutrophication, change the temperature of the water, and pose a severe hazard to water organisms.
2. The sewage and wastewater produced in each household are treated chemically and released into the sea along with fresh water. The sewage water carries pathogens, a typical water pollutant, other harmful bacteria, and chemicals that can cause serious health problems and diseases.
3. Mining is crushing the rock and extracting coal and other minerals from the underground. When extracted in the raw form, these elements contain harmful chemicals and can increase the number of toxic elements when mixed up with water, which may result in health problems. Mining activities emit a large amount of metal waste and sulfides from the rocks, which is harmful to the water.
4. In some countries, the garbage produced by households in paper, plastic, food, aluminium, rubber, and glass is collected and dumped into the sea. These items take two weeks to 200 years to decompose.
5. Farmers use chemical fertilisers and pesticides to protect crops from insects and bacteria. They are helpful for the plant's growth. However, when these chemicals are mixed up with water, they produce harmful pollutants for plants and animals. Also, when it rains, the chemicals mix up with rainwater and flow down into rivers and canals, which pose severe

damage to aquatic animals. When such things enter the sea, they cause water pollution and harm animals in the sea.

6. As the population has grown exponentially, so has the demand for housing, food, and cloth. As more cities and towns are developed, they have increased use of fertilisers to produce more food, soil erosion due to deforestation, rise in construction activities, inadequate sewer collection and treatment, landfills as more garbage is produced, increase in chemicals from industries to produce more materials.

This has led to a gradual accumulation of such toxic pollutants from trace to un-controlled levels; into the aqueous streams, which thus affects various ecological life forms via bio-accumulation and entering the food chain system.

Both biotic and abiotic processes have reported remediation of pollutants from wastewater. Biotic methods involve the biological decomposition of azo dyes using microorganisms (either individually or in specific consortia like fungi, yeasts and bacteria) associated with the advanced oxidation process (AOP). Both intracellular and extracellular enzymes (involved in the metabolic processes) like peroxidases, azo reductases, laccases, etc., participate in the dye degradation process directly or indirectly (Fatima et al., 2017). Biotic methods are eco-friendly and relatively cheap, but enzymes' inability to completely degrade or reduce certain types of azo dyes and the requirement of long retention time for activation of enzymes and degradation process renders them less preferable (Singh et al., 2015; Waghmode et al., 2019). Abiotic processes involve conventional methods like hydrolysis, photolysis, oxidation and reduction reactions, chemical and electrocoagulation, flocculation strategies, etc. (Kumar et al., 2019; Sher et al., 2020). However, these conventional methods have shortcomings like sludge production, associated high costs, the complexity of process and handling, time taking, and subsequent disposal issues (Saleem et al., 2019).

Adsorption can be concluded as one of the most competent methods due to its ease of operation, effectivity in dilute systems, economic scalability and non-formation of toxic by-products (Nodehi et al., 2020; Li et al., 2020). It is the mass transfer phenomenon in which a solid base (an adsorbent) can specifically adsorb adsorbate species from the aqueous systems onto its surface. It involves interphase accumulation of concentrated or dilutes sorbate species at the surface or interphase of the adsorbent (Ravi and Pandey, 2019; Gupt et al., 2020).

1.2. Heavy Metals and their properties

Heavy metals are defined as metallic elements with a relatively high density compared to water, at least five times greater than water. There has been an ongoing discussion regarding the definition of the term ‘heavy metals’. They are defined as heavy metals either due to their high atomic weight or their high density. Nowadays, the word ‘heavy metal’ has been used to describe metallic chemical elements and metalloids, which are toxic to the environment and humans. Some metalloids and lighter metals such as selenium, arsenic and aluminium are toxic. They have been termed heavy metals, while some are typically not toxic, such as gold (Tchounwou et al., 2012).

Metals cannot be broken down and are nonbiodegradable. Organisms may detoxify metal ions by hiding the active element within a protein or depositing them in intracellular granules in an insoluble form to be excreted in the organism’s faeces or for long-term storage. When the heavy metals are swallowed or inhaled into our bodies, they bioaccumulate in our system. Thus they are classified as dangerous. This bioaccumulation causes biological and physiological complications. Some heavy metals are necessary for life and are called essential elements required for various biochemical and physiological functions. They have been widely used in agriculture, industry, medicine and other sectors, to the effect that they have been dispersed into the environment, including our atmosphere, waters and soils (Duffus, 2001).

1.2.1. Sources of heavy metals

These heavy metals have been found naturally on the Earth's crust since the Earth's formation. The astounding increase of heavy metals has resulted in an imminent surge of metallic substances in both the terrestrial and aquatic environments (Pathania, 2016). Heavy metal pollution has emerged due to anthropogenic activity, which is the prime cause of pollution, primarily due to mining the metal, smelting, foundries, and other industries that are metal-based, leaching of metals from different sources such as landfills, waste dumps, excretion, livestock and chicken manure, runoffs, automobiles and roadworks. Heavy metal use in the agricultural field has been the secondary source of heavy metal pollution, such as pesticides, insecticides, fertilisers, and more (**Table 1.1.**). Natural causes can also increase heavy metal pollution such as volcanic activity, metal corrosion, metal evaporation from soil and water and sediment re-suspension, soil erosion, geological weathering (Walker et al., 2015; Tchounwou et al., 2012; Herawati et al., 2000; He et al., 2015

Table 1.1. *A list of heavy metals and their anthropogenic sources with their respective permissible limits*

Heavy Metal	Anthropogenic/Industrial Sources	Permissible limits
Vanadium (V)	Phosphorous fertilizers, batteries, high-pressure lamps, and oil-fired power plants (Tulcan et al., 2021)	0.020 mg/L in drinking water (Binkley and Simpson, 2003)
Chromium (Cr)	Plastic, pigment, wood preservative, electroplating, leather tanning, cement, mining, dyeing and fertilizer (Ramos et al., 2016)	0.05 mg/L in wastewater (Kinuthia et al., 2020) 0.1 mg/L in drinking water (US EPA, 2015)
Manganese (Mn)	Steel production, steel alloys, batteries, glass, fireworks, fertilizer, stock food additive, and organic synthesis catalysts (Rudi et al., 2020)	0.05 mg/L in drinking water (Manganese; US EPA, 2013)
Nickel (Ni)	Metal plating, mining, fertilizers, tanneries, batteries, paper, pesticides, electronics, petrochemical, textile (Nidheesh and Singh, 2017)	0.1 mg/L in drinking water (Gautam et al., 2016) 0.02 mg/L in wastewater (Aneyo et al., 2016)
Copper (Cu)	Mining, refining ores, fertilizer industries, tanneries, batteries, paper industries (Nidheesh and Singh, 2017)	0.010 mg/L in drinking water (Binkley and Simpson, 2003)
Zinc (Zn)	Pharmaceuticals, galvanizing, paints, pigments, insecticides, cosmetics	0.075 mg/L in drinking water (Binkley and Simpson, 2003)
Arsenic (As)	Mining, smelting of arsenic bearing minerals, pesticides (Kumar et al., 2016)	0.05 mg/L in drinking water (Gautam et al., 2016)
Cadmium (Cd)	Metal plating, mining activities, paint manufacture industries (Schmidt et al., 2016)	0.005 mg/L in drinking water 0.003 mg/L in wastewater (Kinuthia et al., 2020)
Mercury (Hg)	Coal-fired power stations, Waste incinerators, Mining for mercury, gold and other metals.	0.002 mg/L in drinking water 0.001 mg/L in wastewater (Kinuthia et al., 2020)

Lead (Pb)	Metal plating, mining activities, paint manufacturing industries (Schmidt et al., 2016)	0.015 mg/L in drinking water 0.01 mg/L in wastewater (Kinuthia et al., 2020)

Pollutants may enter the ecosystem in various ways and enter into the hydrosphere, lithosphere and atmosphere. Apart from also entering through natural ways, as previously said, anthropogenic activity is a significant cause of pollutants entering the ecosystem through volcanic activity and weathering of rocks. They can be an unintended release in shipwrecks, oil spills, mining and fires; in the intended application of biocides such as vector controls; and waste disposals such as industrial effluents and sewage disposal. The movement of heavy metals or any other pollutants depends on temperature, movements and direction of surface waters, circulation of air masses, and wind speed. Apart from these, other factors influence the distribution and movement of the pollutants, such as partition coefficient, polarity, vapour pressure, and molecular stability.

1.2.2. Transport of heavy metals into aqueous bodies

Urbanisation and industrialisation are the two primary culprits of water contamination. The runoffs transport the metals from villages, towns, cities and industries, which accumulate in the sediments of water bodies. Even if traces are transported to water bodies, they might still be toxic to human beings and other ecosystems. The toxicity of heavy metals depends on many factors, such as which metal is present, the nature of the metal, the biological role of the metal, the organism exposed, and the period of the organism's life when it is exposed. If one organism is affected, this will affect the food chain. Since humans are usually the last of the food chain, this will affect us more as we would have accumulated more heavy metals as the concentration increases along the food chain. Both industrial and domestic wastes usually are expelled into the sewage system.

Heavy metals are found in high concentrations of raw sewage, and they do not degrade easily in sewage treatment. They finally get concentrated in the sludge produced and then is dumped directly into the water bodies. Several controls have been set up due to the problems caused by sewage elimination into the rivers and seas without being treated. Stringent regulations have been placed, and better technology has been developed to decrease the amounts of pollutants thrown in the waters.

Sewage treatment is divided into three stages, primary, secondary and tertiary. The primary stage involves the sedimentation of the solid waste found in the wastewater, which occurs after filtering the larger contaminants. The water is then directed through various tanks and filters that will separate the contaminants from the water, forming a sludge fed into a digester that is further processed. The sludge at this stage contains approximately half the suspended solids present in water. Secondary treatment involves oxidation, which helps to purify the wastewaters and can be done in three ways: biofiltration, aeration or oxidation ponds. The tertiary treatment is the last step and consists of removing phosphates and nitrates from the water supply. This process usually uses activated carbon and sand to help in removing the contaminants. These are the basic steps used in sewage treatments depending on what the sewage contains and its processing. Many controls have been set up to counter the problems caused by sewage elimination into the rivers and seas. Stringent regulations have been placed, and better technology has been developed to decrease the amounts of pollutants thrown in the waters (Primary, Secondary, and Tertiary Wastewater Treatment: How Do They Work?; Di Bonito, 2008).

Pollutants can exist in diverse states: in surface waters, in solution or suspension form. They can be transported over an extensive distance by water, where particulate materials can descend to the bottom. Liquid droplets can either descend to the sediment or rise to the surface. Distance travelled in rivers depends on the currants, stability and physical state of the pollutant. When transported into the sea and oceans, wind and currents transport the pollutant further. The difference in density of the seawater plays another factor in transportation to a higher concentration of salt. The persistent pollutants such as heavy metals can then enter the food chain through marine life such as fish, affecting predators such as bigger fish, birds and mammals, including humans, which migrate and transport the pollutant to different ecosystems (Walker et al., 2016).

1.2.3. Toxic effects of heavy metals

Cellular organelles and cell components have been reported to be affected by heavy metals, such as the mitochondria, nuclei, lysosomes, cell membrane and enzymes. It has emerged that metal ions interact with DNA and nuclear proteins, thus causing DNA damage, leading to cell cycle modulation, apoptosis or carcinogenesis.

Heavy metals have been reported to interact with nuclear proteins and DNA, which cause site-specific damage. Two types of damages may be caused viz. “direct” or “indirect” damage. In “direct” damage, conformational changes occur to the biomolecules due to the metal. On the other hand, the heavy metal causes “indirect” damage, resulting from the production of reactive oxygen and nitrogen species, which comprise the hydroxyl and superoxide radicals, hydrogen peroxide, nitric oxide, and other endogenous oxidants. Metal toxicity causes the formation of free radicals, which causes DNA damage, alteration of sulphydryl homeostasis, and lipid peroxidation. Alterations have also been noted in metal-mediated calcium homeostasis due to membrane damage, which causes various calcium-dependent systems to be activated, including endonucleases. The free radical formation has been chiefly investigated for iron, copper, nickel, chromium and cadmium. The last three metals are recognised for their carcinogenic properties. Iron, copper, vanadium, chromium and cobalt follow the Fenton reaction of the superoxide and the hydroxyl radical (Eq. 1.1 and 1.2). Fenton reactions are primarily linked to mitochondria, microsomes and peroxisomes.

$$Me^{+}{}_{(n+1)} + O_2^{\bullet-} \longrightarrow Me^{+}{}_{(n)} + O_2 \qquad (1.1)$$

$$2O_2^{\bullet-} + 2H^{+} \longrightarrow H_2O_2 + O_2 \qquad (1.2)$$

$$\text{(Fenton reaction) } Me^{+}{}_{(n)} + H_2O_2 \rightarrow Me^{+}{}_{(n+1)} + OH^{\bullet} + OH^{-} \qquad (1.3)$$

Metal-mediated free radicals cause the mutagenicity of DNA base alterations revealing the link between carcinogenesis and oxidative damage. The free radicals formed cause a variety of DNA base modifications where most of which are pro-mutagenic, thus showing the vital link between the oxidative damage caused by the metals and their carcinogenicity. The metals cadmium, nickel, and arsenic inhibit the DNA repair mechanisms. Oxidative effects in DNA include (i) base modification which is seen by chromium and nickel; (ii) crosslinking, which is seen by nickel, copper and oxidant, iron and oxidant; (iii) strand scission, which is seen by nickel, cadmium, chromium, and oxidant; and (iv) depurination which is seen by copper, chromium and nickel (Tchounwou et al., 2012). A detailed list of toxic implications of heavy metals on humans and aquatic life has been listed in **Table 1.2.**

Table 1.2. *Toxic effects of heavy metals on humans and on aquatic ecosystems*

Heavy Metal	**Toxic effects (on humans)**	**Toxic effects (on aquatic ecosystem)**
Vanadium (V)	Headaches, rashes, impairment to the nervous system, liver and kidney haemorrhage, tremors, paralyses and behavioural changes, cardiac disease, inflammation of the gastrointestinal organs, blackening of teeth and tongue (Briffa et al., 2020)	Heavy metals can enter fish through three routes: the gills, the body surface, and the digestive tract. Fish development is hampered by toxic food loaded with heavy metals. One of
Chromium (Cr)	Gastrointestinal ulceration, nausea and vomiting, fever, diarrhoea, vertigo, toxic nephritis, liver damage, Kidney circulation, Lung Cancer, dermatitis (Briffa et al., 2020; Nabarlatz et al., 2012)	

the most obvious signs of metal toxicity in fish is growth inhibition. As a result, HMs concentrations in tissues cause various metabolic, physiological, and histological changes in fish and other freshwater species by altering various enzymes and metabolites. If water pH falls, HMs may be mobilized and discharged into the water column, endangering marine organisms such as crustaceans and insects. These toxic sediments kill the benthic organisms and reduce food availability for the gigantic organism. The bioaccumulation of heavy metals in freshwater fish has important ecological, environmental, and social implications. When metals are present in high concentrations in the environment, species accumulate higher amounts, causing biomagnification of metals in the trophic web, which harms the aquatic ecology since it relies on them in various ways, either directly or indirectly (Bonsignore et al., 2018; Mehmood et al., 2019; Dane and Şişman, 2020; Zaynab et al., 2022).

Manganese (Mn)	Hypotension, Manganism (Dullness, Behavioural changes, Lethargy, Weakness), Mimicry of Parkinson's' Disease (Tremors, Akathisia, Dystonia, Anxiety, Movement discoordination, Lack of facial expression) (Briffa et al., 2020)
Nickel (Ni)	Serious lung and kidney problems, gastrointestinal distress, pulmonary fibrosis, respiratory cancer and skin dermatitis (Cortés-Arriagada and Toro-Labbé, 2016)
Copper (Cu)	Hepatocellular degeneration, Necrosis, Cytotoxic to erythrocytes leading to haemolysis, Vomiting, cramps, convulsions, or even death (Khezami and Capart, 2005)
Zinc (Zn)	Nausea and vomiting, Pancreatic complications, Epigastric pain, Impaired immune function, Neutropenia, Stomach cramps, skin irritations, vomiting, nausea, phytotoxic and anaemia (Briffa et al., 2020; Paulino et al., 2006)
Arsenic (As)	Heart problems, Brain damage, Deoxyribonucleic acid (DNA) damage, Carcinogenic, dermatological, cardio renal and gastrointestinal effects (Briffa et al., 2020; Naseem and Tahir, 2001)
Cadmium (Cd)	Central nervous system complications, Immune system deficiencies, DNA impairment, Cancer, Detrimental effects on kidney, lungs, liver, heart and bones of human being (Briffa et al., 2020; Benes et al., 2000)
Mercury (Hg)	Genotoxic, Damages DNA and chromosomes, Impairment of pulmonary and kidney function, chest pain and dyspnoea (Briffa et al., 2020; Xi et al., 2015)
Lead (Pb)	Anemia, insomnia, headache, dizziness, irritability, weakness of muscles, hallucination and renal damages (Rangabhashiyam and Selvaraju, 2015)

1.2.4. About Chromium

Chromium is one such heavy metal which is a redox-active heavy metal; exists in both hexavalent, i.e. Cr(VI) and trivalent, i.e. Cr(III) oxidation forms in aqueous solutions (Bhaumik et al., 2016). Depending upon the pH of the aqueous medium, the Cr(VI) molecules can be in different forms, such as chromate (CrO_4^{2-}), hydro chromate ($HCrO_4^{-}$) or dichromate ($Cr_2O_7^{2-}$). Due to its negative charge, the Cr(VI) molecules are poorly absorbed and are easily repelled by weak negatively charged soil particles. Thus, these Cr(VI) particles are dispensed easily to the aqueous bodies. Alternately, Cr(III) occurs in cationic forms viz. $Cr(OH)_2^{+}$, $Cr(OH)^{2+}$ or Cr^{3+}, depending upon the pH of the water bodies. Thus, they are quickly taken up or adsorbed by the soil particles (negatively charged) and thus less dispersive than Cr(VI) molecules in the environment (Deng and Bai, 2004). Humans and animals are more exposed to Cr(VI) from drinking water than by any other means (Costa, 2003; Bendjeffal et al., 2018). As per the World Health Organization (WHO), the maximum tolerant concentration for total chromium in drinking water is 0.05 mg/L. The Office of Environmental Health Hazard Assessment (OEHHA) has developed the Public Health Goal (PHG) of 2.5×10^{-3} mg/L for total chromium (Rakhunde et al., 2012). Chrome plating, leather tanning, paint, wood treatment industries etc., are some of the major industries responsible for Cr(VI) pollution (Gupta et al., 2011).

1.3. Dyes

Dyes are synthetic aromatic compounds that are highly employed as colouring agents and are sometimes used to develop colour or change the colour of substances. The dyes are widely used in the various industrial sectors for different purposes, which include colouring of fibre and cloth colouring, biological and biochemical stains, foods and cosmetics, colour photography, electronics and lasers, solar cells, display panels, pigments in modern paints, printer inks, and leather products. Mainly, dyes are constituted of an abundant class of organic compounds with covalently attached unsaturated or saturated functional groups, including chromophore and auxochrome groups. These unsaturated groups (N=N, C=C or C≡C) are accountable for absorbing light in the visible zone, approximately (350–750 nm), where they only show colour. The chromophore group is called an electron acceptor, which is also responsible for the dye's colour, while the auxochrome group (–SH, –OH, or NH_2) represents the electron donor that is liable for dyeing capacity as well as enhancing the colour of the dye. Dyes must be soluble in the solvent or naturally occurring and synthetic. Not all coloured compounds can be considered dyes (Gupta et al., 2018).

Textile, pigments, paints and dye industries have been extensively using and producing synthetic dyes as their demand has seen a logarithmic rise over the past decade (Liu et al., 2011). To fulfil such rising industrial demands, about 1.6 million tons of dyes are being manufactured annually, 10–15% of which are being discarded in the form of unprocessed wastewater effluent into the aquatic systems (Alorabi et al., 2020). Among the diverse categories of synthetic dye species, anionic azo dyes hold approximately 70% of annual global dye production (Pattanaik et al., 2020; Sathishkumar et al., 2019). Textile industries (54%) account for half of the existing dye effluents seen in the worldwide environment, followed by the dyeing industries (21%), paper and pulp industries (10%), tannery and paint industries (8%), and the dye manufacturing industries (7%) (De Gisi et al., 2016). **Table 1.3.** presents various types of dyes with their sources and applications (Samsami et al., 2020; Benkhaya et al., 2020).

Table 1.3. *Class of dyes and their applications*

Dye Class	Example	Applications
Acid	C.I. Acid Red 249 dye, Acid Orange IV, Acid Blue 349, C.I. Acid Blue 7, Acid Blue 83, C.I. Acid Blue 25 (AB25), Acid Red 337, Acid Yellow 36, Acid Blue 147, C.I. Acid Blue 25 (anthraquinone), Acid Violet 17, Acid Orange 7, Acid Black-234 etc.	Cosmetics, food, leather, nylon, paper printing ink, silk, wool
Basic	Basic Red 9 monohydrochloride, Basic Blue 11, Basic Brown 1 (Bismarck Brown Y), Basic Blue 3, Basic Blue 24, Basic Blue 6, Basic Blue 22, Basic Violet 2 etc.	Inks, medicine, modified nylon, paper polyester
Direct	Direct Red 28, Direct Blue 38, Direct Red 2, Direct Blue 86, Direct Blue 71, Direct Orange 26, Direct Blue 6 etc.	Cotton, leather, nylon, rayon, silk, paper
Reactive	Reactive Red 3, Reactive Red 120, Reactive Red 147, Reactive Red 17, Reactive Red 6, Reactive Red 239, Reactive Blue 19 etc.	Cellulosic, cotton, nylon, silk, wool
Azo	Congo Red, Direct Blue 86, Direct Blue 71, Direct Red 28, Direct Black 38, Direct Red 2, Direct Orange 26, Direct Black 22, Acid Red 2, Disperse Yellow 7, Acid Orange 20, Methyl Red, Trypan Blue etc.	Acetate, cellulose, cotton, rayon, polyester
Disperse	Disperse Red 9, Disperse Violet 26, Disperse Red 60, Disperse Brown 1, Disperse Blue 56, Disperse Red 60, Disperse Blue 79, Disperse Orange 3 etc.	Acetate, acrylic fibres, cellulose, nylon, polyamide, polyester, cotton, plastic
Sulphur	Sulphur brilliant green (CI 53570), Sulphur blue dye (CI 53235), Sulphur black (CI 53185), Leuco sulphur black 1 (CI 53185), Phthalic anhydride etc.	Cotton, leather, paper, polyamide fibres, rayon, silk
Vat	Vat Blue (synthetic indigo), Vat Black 25, Indigo Carmine, Vat Green 1, Vat Yellow 1, Vat acid Blue 74, Vat Orange 15 etc.	Cotton, cellulosic fibres, polyester-cotton, rayon, wool

Physico-chemical approaches are currently being applied for the treatment of wastewater by industries. These are effective but environmentally destructive as these utilize a considerable amount of toxic chemicals and salts, which then end up in the environment and impart a negative impact on the environment, as well as generating a considerable amount of sludge as a secondary pollutant (Pandey et al., 2017; Zhang et al., 2004).

1.3.1. Sources of dyes and their spread

Industries are the key players in the economy of many nations. However, they are also significant polluters worldwide due to their potentially toxic wastewater, which contains a variety of organic and inorganic pollutants and which thus causes severe environmental pollution and toxicity in living beings upon exposure (Bharagava et al., 2018; Saxena and Bharagava, 2017). Industries use large quantities of synthetic chemicals (mainly dye) for various purposes, including dyeing and finishing agents. Several synthetic dyes are used heavily in different industries and include azo, triphenylmethane, anthraquinone, phthalein, nitro, methane, and quinoline dyes (Kabra et al., 2011a; Kabra et al., 2011b; Khan et al., 2013; Saxena et al., 2017).

Table 1.4. *Characteristics of dye based industrial wastewater*

Industrial Wastewaters	Dyes	Wastewater Characteristics
Textile wastewater	Azo or anthraquinone	Major pollutants in textile wastewater COD, BOD, solids, phenols, sulfur, and the intense color caused by different dyes and several toxic heavy metals like Cd, Cr, Cu, Fe, Pb, Mn, Ni and minerals like K, P.
Tannery wastewater	Acid dyes, mordant dyes, direct dyes, basic dyes, and pre-metal, methyl orange	Tannery wastewater contains high BOD, COD, TDS, TSS, phenols, chlorophenols, tannins, azo dyes, toxic metals such as Cr, Cd, Pb.

Paper industry wastewater	Vat dyes, basic dyes, sulfur dyes and cationic direct dyes	Paper industry wastewater contains dark brown color, very high level of BOD, COD, TDS due to presence of lignin and its derivatives from the raw cellulosic materials, chlorinated compounds, suspended solids (mainly fibers), fatty acids, tannins, resin acids, sulfur and sulfur compounds, etc.
Pharmaceutical wastewater	Synthetic dyes brilliant blue, allura red, tartrazine and erythrosine	Pharmaceutical wastewater contains intense color, conductivity, salinity, turbidity and contains very high chloride, COD, BOD, TSS, TDS, nitrates, phosphates, sulfates, alkalinity, and several toxic metals like Cd, Co, Fe, Mn, Ni, Pb, and Zn.

As a result, these highly toxic dyes are discharged along with different industrial wastewaters into the natural ecosystem, including rivers, ponds, lakes, and soil, and thus create severe environmental pollution. Textile industries consume a large volume of potable water for different dye applications and, therefore, discharge a considerable quantity of dye-containing wastewater into the environment, creating severe environmental pollution and health threats to living beings. Therefore, it is essential to adequately treat the wastewater to protect the environment and public health.

1.3.2. Toxic effects of dyes

Textile industries are the primary source of environmental pollution. Over 10,000 tons of different synthetic dyes are generated every year worldwide from different industrial units (Chen et al., 2004). Several synthetic dyes are employed in different industries, such as textile, food, cosmetic, paper, printing, colour photography, leather, and pharmaceutical industries, for various dyeing, scouring, bleaching, and finishing applications. However, textile industries consume the highest amount of total dyes (Saratale et al., 2013). Dyes are also applied for colouring purposes such as colouring fibres and cloth; biological and biochemical stains; colour photography; pigments in modern paints, printer inks, leather, nylon, polyester, polystyrene, cotton, rayon, flax, cellulosic, and polyamide and lubricants in the automotive and industrial cutting industries, and thus, they end up in the wastewaters. Dye effluents are highly coloured contain various toxic chemicals such as chlorine, formaldehyde, solvent, organic and inorganic compounds, aromatic amines, xenobiotic, pigments, alkali salts, and toxic heavy metals (lead, chromium, and mercury) (Bharagava and Mishra, 2018; Chowdhary et al., 2017; Mishra and Bharagava, 2016; Yadav et al., 2017).

Several industries discharge the solid wastes into water bodies such as ponds, lakes, rivers, streams, etc. They have harmful effects on water and soil ecology and lead to water and soil pollution and ecotoxicity in the environment (Kagalkar et al., 2010). Dye effluent is highly carcinogenic and mutagenic because of the presence of recalcitrant organic and inorganic pollutants, and if not adequately treated, it gets discharged into natural ecosystems and causes severe environmental contamination and health hazards (Mani and Bharagava, 2016). Dye effluents affect water or soil's chemical and biological properties and thus create environmental pollution (Parshetti et al., 2007). This has a negative effect on fishes and damages the phytoplankton and zooplankton species, thus ultimately affecting the aquatic ecosystem (Hashimoto et al., 2013). Dye effluents are also responsible for disturbed biogeochemical (nutrient) cycling, which occurs in soil niches, and thus create soil pollution.

It has been reported that approximately 15% of the total azo dye effluent discharged every year comes from textile industries (Chen and Chang, 2007; Stolz, 2001). Dye effluent contains the highest amount of recalcitrant colouring pollutants, suspended solids, or other toxic metals, which cause a negative impact on water chemistry such as colour, BOD and COD levels. Dyes have chromophoric groups that can strongly absorb sunlight, thus adversely affecting the photosynthesis of phytoplankton or algae species (Kagalkar et al., 2010). Azo dyes are generally soluble in water and hence highly assimilate, even through skin touch and inhalation, which causes cancer, splenic sarcomas, hepatocarcinoma, allergic reactions, nuclear anomalies in experimental animals and chromosomal aberrations in mammalian cells. Dye effluents have specific toxic chemicals that cause mutagenic, carcinogenic, and teratogenic effects in several organisms (Mani and Bharagava, 2016; Novotný et al., 2006; Parshetti et al., 2007).

Immediate release of unprocessed and non-treated dye waste effluents into the water bodies has affected the aquatic ecosystem and its living beings like intrinsic toxicity, severe mutagenic and carcinogenic effects, skin sensitisation and irritation, blockage of sunlight into the aquatic flora resulting and other devastating implications. United States Environmental Protection Agency (USEPA) has also documented such synthetic dye species as potentially health hazardous and detrimental for living beings and the ecosystem (Sonwani et al., 2020). The presence of aromatic rings with azoic linkages provides these synthetic dyes with thermal stability and optical and physicochemical stability, allowing them to become persistent and their prolonged existence in the ecosystem poses severe damaging effects (Qurrat-ul-Ain et al., 2020).

1.3.3. About Congo red, Direct blue 6 and Bromophenol blue

Direct blue 6, chemically known as tetrasodium;5-amino-3-[[4-[4-[(8-amino-1-hydroxy-3,6-disulfonatonaphthalen-2-yl)diazenyl]phenyl]phenyl]diazenyl]-4-hydroxynaphthalene-2,7-disulfonate (PubChem1) and Congo red, chemically known as disodium;4-amino-3-[[4-[4-[(1-amino-4-sulfonatonaphthalen-2-yl)diazenyl]phenyl]phenyl]diazenyl]naphthalene-1-sulfonate) (PubChem2) are anionic azo dyes with applications in the various dye, leather, textile, paint, cosmetics, carpet, pulp and paper industries, pigment, pharmaceutical industries etc. (Tang et al., 2015). Such anionic azo dyes possess one chromophore (azo group, i.e. -N=N- group), along with a hydroxyl (OH−) and a sulphonic (SO_3^-) group (Konicki et al., 2017). Bromophenol blue is another non-biodegradable synthetic hazardous dye with wide applications as a colour marker in labs, an acid-base indicator, agarose gel electrophoresis, and applications in drugs, cosmetics, etc. textile and printing ink industries.

Bromophenol blue is chemically known as 2,6-dibromo-4-[3-(3,5-dibromo-4-hydroxyphenyl)-1,1-dioxo-2,1λ6-benzoxathiol-3-yl]phenol (PubChem3). It is highly water-soluble and has been reported as a potential contaminant for soil and freshwater flora and fauna (Ameen et al., 2017).

1.4. Antibiotics

Antibiotics, as the term represents anti-: inhibit; -biotics: living microbial beings, represent drugs that inhibit microbial growth, especially bacteria. Antibiotics can be classified into two basic categories based on their type of action, i.e., Bacteriostatic (which inhibits the growth and reproduction of bacteria) and Bactericidal (which causes bacterial cell death). The classification of antibiotics based on their structural unit and some common examples (Mangla et al., 2022) are presented in **Table 1.5.**

Table 1.5. *Classification of antibiotics with their examples*

Class of antibiotics	Structural unit	Examples
Penicillin	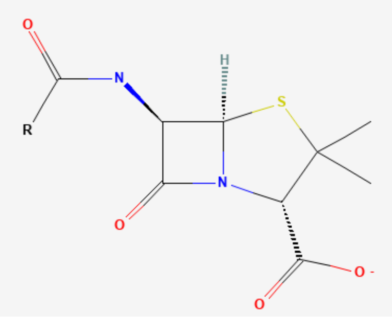	Penicillin, Amoxicillin, Ampicillin
Tetracyclines	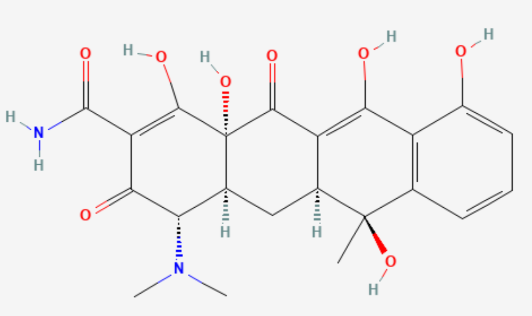	Doxycycline, Tetracycline, Oxytertacycline
Cephalosporins	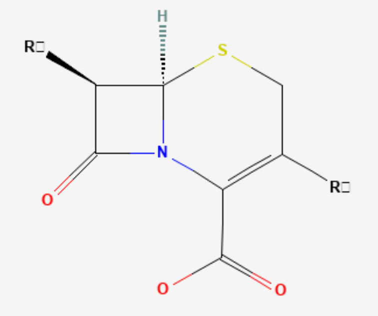	Cefuroxime (Ceftin), Ceftriaxone (Rocephin), Cefalexin

Quinolones	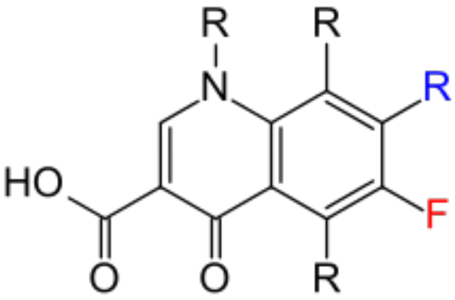	Ciprofloxacin, Levofloxacin, Norfloxacin
Lincomycin	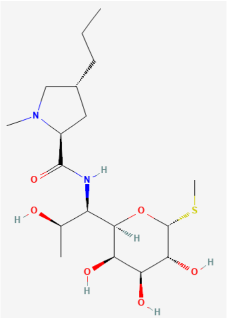	Clindamycin, Lincomycin
Macrolides	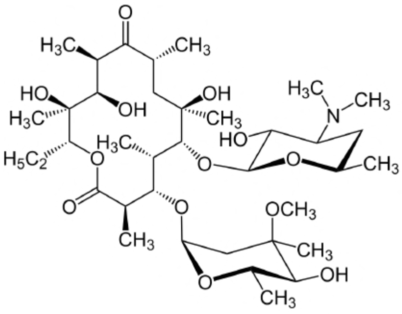	Azithromycin, Clarithromycin, Roxithromycin
Sulfonamides	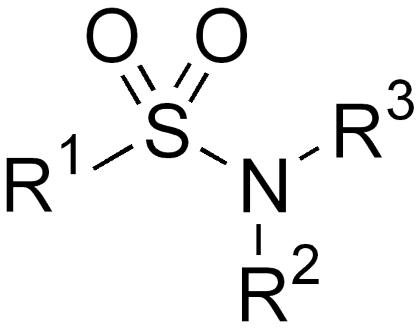	Sulfamethoxazole, Sulfasalazine, Sulfadiazine
Glycopeptides	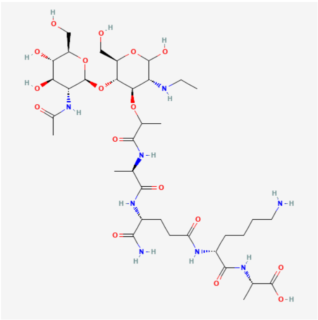	Dalbavancin, Oritavancin, Vancomycin

Aminoglycosides	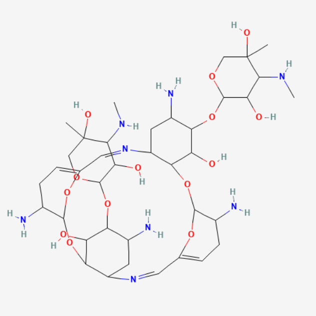	Gentamycin, Tobramycin, Neomycin
Carbapenems	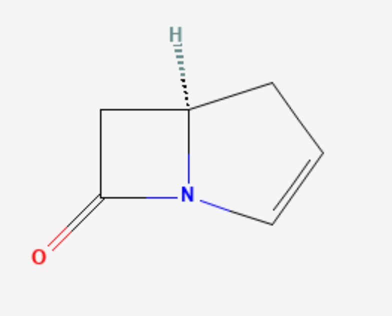	Imipenem, Meropenem, Etrapenem
Others		Trimethoprim,

Antibiotics come from a variety of sources and cause resistance in bacteria. However, significant contributors are domestic and pharmaceutical untreated effluents that flow directly to the sewage system. Due to the low biodegradability of some antibiotics, the presence of antibiotics and related genes are being detected worldwide in water samples, which can profoundly impact the health of all humans and animals. Antibiotics in aqueous media also affect non-target pathogens and alter the structure of algae (Malakootian et al., 2018).

1.4.1. Sources of antibiotics, its spread and toxicity effects

The rise in population and the hike in associated living standards have led to elevated demands and dependency on agriculture and animal production sectors. Approximately two-thirds of the globally produced antibiotics are used in agricultural and animal sectors, primarily as growth promoters or to treat or prevent diseases (Van et al. 2020). Consuming such products has eventually reduced humans' immunity, plaguing them with life-threatening disorders. This has led them to depend more on antibiotics and drugs for their well-being and immunity. Conclusively, the augmentation of antibiotics use among humans and the commercial sectors have led to a steady hike in the global use of antibiotics (Jubeen et al., 2019). The global antibiotic consumption was 63.2 billion kgs in 2010, and it is estimated to reach up to 105.3 billion kgs by 2030 (Harrabi et al., 2018).

Globally, two-thirds of antibiotics produced are used on animals (Van et al. 2020) and over the past decade, antibiotics have been increasingly used in agriculture and animal production, mainly to prevent and treat diseases and used as growth promoters. Antibiotic consumption in livestock reached 63,151 tons in 2010 and is predicted to increase by another 67% by 2030 (Boeckel et al., 2015). Due to intensive farming, antibiotic use has seen rapid growth in aquaculture, the fastest-growing food sector worldwide. In aquaculture systems, antibiotics are commonly applied with feed or directly to the aqueous systems and may later be released into the environment through run-off water or sedimentation of faeces and uneaten feed metabolites, which are then consumed by nearby fishes or invertebrates. Antibiotics are also frequently detected in agricultural lands' waterways, which points to large-scale use of the same in the agricultural sectors (Piña et al., 2020). Also, the pharmaceutical industries contribute significantly to the total antibiotic concentration added to the influent of the sewage treatment plant and the domestic effluents (Harrabi et al., 2018). Consequently, antibiotic residues have been detected in terrestrial, freshwater, and marine environments near pharmaceutical, agriculture and aquaculture facilities across the globe (Henriksson et al., 2018).

Since the dumping of antibiotics is poorly regulated on a local and global scale (Kraemer et al., 2019), it has led to the long term persistence of antibiotics in the environment. This has induced antibacterial-resistant genes among various pathogenic bacterial species that may enter the food chains and thus pose severe health issues to humans and other biological forms like heart disorders, damage to the nervous system, and improper blood flow in the bloodstream. Environmental risk assessment of the persistent antibiotics in the environment is challenging because of its source, low molecular weight (<1000 Da) and its movement patterns within the environment (Kraemer et al., 2019; Najafpoor et al., 2019). Over the years, antibiotic pollutants have gained the reputation of emerging contaminants as they are an imminent threat to various ecosystems and associated living beings in the near future.

1.4.2. About Sulfamethoxazole

Over the years, antibiotic pollutants have gained the reputation of emerging contaminants as they are an imminent threat to various ecosystems and associated living beings in the near future. One such emerging pharmaceutical contaminant is Sulfamethoxazole; 4-amino-*N*-(5-methyl-1,2-oxazol-3-yl)benzenesulfonamide (PubChem4). It is a broad spectrum sulfonamide bacteriostatic antibiotic, most commonly used with trimethoprim. European Union directive (93/67/EEC) has categorised it as a ‘toxic compound’ while the Environmentally Classified Pharmaceuticals, 2009 has classified it as a ‘highly toxic compound’(Prasannamedha and Kumar, 2020). Since wastewater treatment plants cannot fully eradicate Sulfamethoxazole from the aquatic environments, it is thereby categorised as a persistent pollutant (Carvalho and Santos, 2016). It has a half-life of 51.7 days in aquatic ecosystems. Given its persistent nature, such prolonged presence in the ecosystem could lead to its biomagnification or bioaccumulation, thus affecting the living beings (Prasannamedha and Kumar, 2020).

1.5. Conventional treatment techniques and their demerits

Both biotic and abiotic processes have reported remediation of pollutants from wastewater. Biotic methods involve the biological decomposition of azo dyes using microorganisms (either individually or in specific consortia like fungi, yeasts and bacteria) associated with the advanced oxidation process (AOP). Both intracellular and extracellular enzymes (involved in the metabolic processes) like peroxidases, azo reductases, laccases, etc., participate in the dye degradation process directly or indirectly (Fatima et al., 2017). Biotic methods are eco-friendly and relatively cheap, but enzymes' inability to completely degrade or reduce certain types of azo dyes and the requirement of long retention time for activation of enzymes and degradation process renders them less preferable (Singh et al., 2015; Waghmode et al., 2019).

Abiotic processes involve a multitude of conventional methods like chemical precipitation, coagulation/flocculation, ion exchange etc. (Crini and Lichtfouse, 2019; Yenkie et al., 2019). However, these conventional methods have shortcomings like sludge production, associated high costs, the complexity of process and handling, time taking, and subsequent disposal issues (Saleem et al., 2019). **Table 1.6.** lists the multitude of conventional techniques for wastewater treatment and their disadvantages.

Table 1.6. *Conventional techniques for wastetwater treatment and their disadvantages*

Technique	About/Features	Disadvantages
Screening (Mackenzie, 2020)	• Removes rags, paper, grit, plastics, and metals • Varying screen sizes available: coarse, fine and micro	Requires regular cleaning and maintenance
Coagulation/flocculation (Elmaleh and Jabbouri, 1991; Ødegaard, 1995)	• Forms flocs of suspended and colloidal particles by adding chemicals/ polymers • Mean residence time and recirculation ratio influences floc formation efficiency	• Cost of flocculants • Mixing and time
Filtration (granular) (Mackenzie et al., 2020)	Suspended/colloidal impurities are separated via passage through a porous medium	Head loss and effluent turbidity limits

Activated sludge (Ahmetović et al., 2015)	• Aerobic slurry consisting of microorganisms is added to the wastewater in a complete-mix suspended growth reactor • Solid retention time (SRT), that is, the average time sludge remains in the system, determines the overall performance	• Maintenance of microbial activity • Poor decolorization • Sludge bulking and foaming
Constructed wetlands (Zhang et al., 2017)	Engineered systems designed to use natural functions of vegetation, soil, and organisms to treat wastewater	• Species selection and maintenance are important to ensure long-term functionality
Advanced oxidation process (Deng and Zhao, 2015)	• Utilizes oxidation/ photo-Fenton reactions to degrade pollutants into smaller constituent molecules • Agents used include ozone, peroxide, UV light, Fenton's reagents	• High energy input for ozone and UV • Lack of scalable systems
Membrane filtration (Crini and Lichtfouse, 2019)	• Pressure based filtration using semi-permeable membranes • Membrane pore size varies depending on the particle/ molecular size of contaminant	• Clogging and fouling • High investment and membrane replacement costs
Incineration (Crini and Lichtfouse, 2019)	Destruction by combustion	High running costs Formation of dioxins and others pollutants (metals, etc.)

Such demerits have limited their application as a viable option for wastewater treatment and thus open up the scope to develop a viable method countering the disadvantages of the above mentioned conventional methods.

1.6. Significance of adsorption: adsorbents and their modifications

Current work emphasises ‘adsorption’ as a viable technique to eliminate pollutant species from aqueous setups. Adsorption is a mass transfer process where the ‘adsorbate’ molecules from one phase (either liquid or gas) are deposited onto the solid ‘adsorbent’ surface (**Figure 1.1.**). It involves interphase accumulation of concentrated or diluted sorbate species at the surface or interphase of the adsorbent (Dąbrowski, 2001).

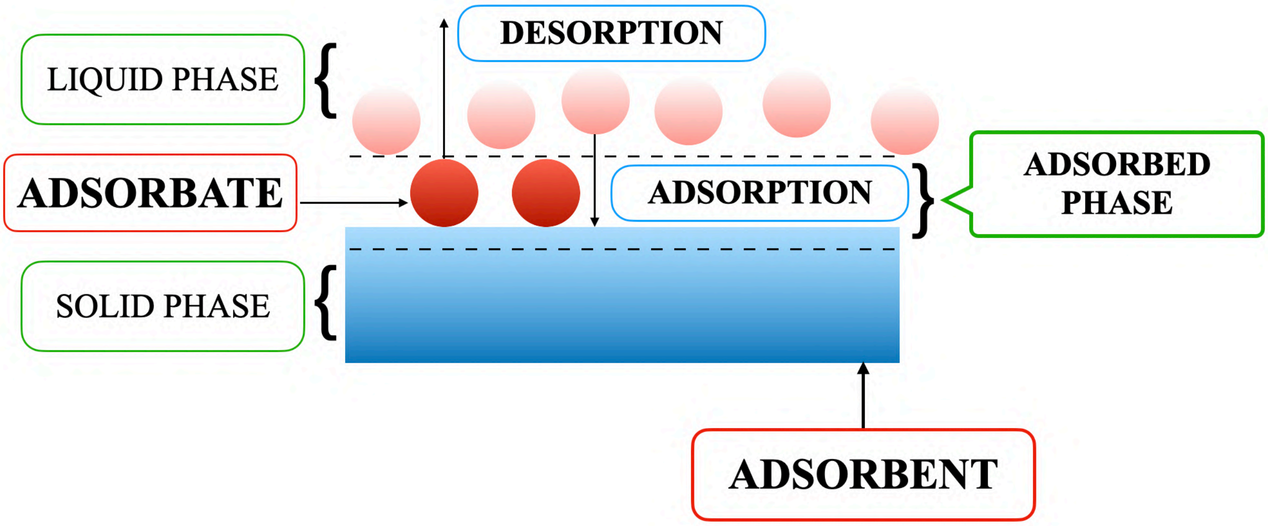

Figure 1.1. *Schematic representation of the adsorption phenomenon*

Adsorption holds various advantages over other conventional methods like the ease of operation as heavy machinery has no involvement, effectivity in dilute systems, economic scalability, and non-formation of toxic by-products (Nodehi et al., 2020; Li et al., 2020). Although adsorption is versatile and easy to adopt in usable forms, the adsorbent materials used are costly and cannot be easily regenerated and recycled, resulting in their large-scale production; thus limiting its acceptance as an ideal wastewater remediation process (Gupta et al., 2011).

Numerous reports have reported low-cost adsorbents such as bentonite, fly ash, peat, etc., to eliminate pollutants from aqueous setups. However, they have been deemed incompetent for their inefficiency in adsorbing an array of pollutants and are generally required in large amounts (Srinivasan and Viraraghavan, 2010).

1.6.1. Biomass-based Carbonaceous adsorbents

Owing to the demerits described above, many studies have opted for biomass-derived carbonaceous adsorbents like activated carbon as a viable alternative for adsorbents due to their porous morphology and surface functional groups that promote efficient uptake of pollutants (Tonucci et al., 2015).

Biomass-derived carbonaceous adsorbents are preferred for wastewater treatment and remediation due to their extended surface area, porous morphology, and high surface functional groups (Patra et al., 2019; Hassan et al., 2020). For economic scalability, cheap carbonaceous precursors such as lignocellulosic materials are mostly preferred over other precursors (Jawad et al., 2019). However, the choice of carbonaceous materials as potential adsorbents for water treatment has been limited due to several factors, as mentioned below:

- A single surface functional group is targeting a single pollutant at a time.
- The presence of hydrophobic regions limits the adsorbent's wettability in aqueous setups.
- Lack of Nitrogen-containing functional groups for targeting organic pollutants (antibiotics).

The quest to enhance the surface quality of carbonaceous adsorbents has resulted in many reports suggesting its surface modification or complexation with various reagents like surfactants, chelating agents, functional ligands etc.

A. Chelating agents: Chelating agents are organic or inorganic compounds capable of binding metal ions to form a complex ring-like structure called 'chelates'. Chelating agents possess "ligand" binding atoms that form covalent or co-ordinate linkages. Depending on the number of such linkages, a chelating agent may be a mono- or multi- dentate chelate or ligand (Flora and Pachauri, 2010; Chelating Agents, 2012). Ethylenediaminetetraacetic acid (EDTA) is one such example of a chelating agent, which is a hexadentate ligand. It can form four or six bonds with a metal ion, and it forms chelates with both transition-metal ions and main-group ions.

For the current thesis work, prepared carbonaceous adsorbent was complexed with EDTA for targeting hexavalent chromium (Cr(VI)) species from aqueous setups.

B. Surfactants: Surfactants are surface-active agents that create self-assembled molecular clusters called micelles in a solution (water or oil phase) and adsorb to the interface between a solution and a different phase (gases/solids). They are amphiphilic molecules with a hydrophilic polar head and hydrophobic non-polar tail.

They can be classified into ionic surfactants and nonionic surfactants. Ionic surfactants are subclassified into anionic surfactants, cationic surfactants and amphoteric surfactants (Nakama, 2017). Common hydrophilic groups of ionic surfactants are carboxylate ($–COO^–$), sulfate ($–OSO_3^–$), sulfonate ($SO_3^–$), carboxybetaine ($–NR_2CH_2COO^–$), sulfobetaine ($–N(CH_3)_2C_3H_6SO_3^–$), and quaternary ammonium ($–R_4N^+$). They are soluble in both organic solvent and water (Assadi et al., 2012).

Cetyltrimethylammonium bromide (CTAB) is a positively charged quaternary ammonium surfactant with a 16-carbon long alkyl chain and an ammonium head with three methyl groups attached. CTAB was complexed over prepared carbonaceous adsorbent for the current research to enhance its wettability and reduce its surface tension. This was done to enhance the surface availability of the prepared carbonaceous adsorbent towards the targeted dye pollutants.

C. **Polymers:** Several studies have reported that adsorbents rich with Nitrogen-containing functional groups offer positively charged surfaces for efficient adsorption of anionic adsorbate species like antibiotic pollutants. For this, various sources of nitrogen-containing functional groups like pyrrole molecules and other quaternary ammonium compounds have been used to treat prepared carbonaceous adsorbents (Saleh et al., 2017; Han et al., 2020; Kundu et al., 2018). Polypyrrole is a preferred polymer for the adsorptive elimination of organic pollutants due to its high nitrogen content and non-localised π-electron conjugated system (Li et al., 2012; Feng et al., 2022). It is a conductive heterocyclic polymer that can be easily polymerised over the adsorbent's surface. Pyrrole is environmentally stable due to its minimal bioavailability in the aqueous setups (Hong et al., 2016). Such properties make polypyrrole ideal for complexing with the prepared adsorbents for the current thesis work.

1.6.2. Chitosan based adsorbents

Biological materials like chitosan and its derivatives have also achieved much focus over the past decade as potential adsorbents. Chitosan is a natural polysaccharide synthesised via chitin deacetylation involving boiling chitin in the presence of alkaline reagents like potassium hydroxide. Deacetylation infers to the process of eliminating the acetyl groups from chitin and rendering them with reactive amino groups ($-NH_2$). These amino and hydroxyl groups render chitosan with adsorptive properties (Anitha et al., 2016; Rouhani Shirvan et al., 2019). However, low surface porosity and specific surface area limits its adsorptive capabilities and thus its application as a potential biological adsorbent.

For the current thesis work, commercially obtained chitosan was fabricated to porous chitosan by gelation using $CaBr_2 \cdot xH_2O/CH_3OH$ solution followed by vacuum drying.

1.7. Problem statement and related objectives

Present research involves the development of suitable adsorbents from biological precursors. Following their preparation, the adsorbents were studied to eliminate various pollutants. Accordingly, the adsorbents were subjected to various modifications to eliminate targeted pollutants effectively.

One of the most significant traits of an adsorbent is that it should be recyclable for multiple cycles. Thus, it is essential to understand the principle behind the regeneration process before recycling. Also, real-time wastewater may contain multiple pollutants and co-existing cationic and anionic salts with variable ionic strengths. Thus it is essential to understand the influence of such co-existing pollutants and ionic salts in the selective elimination of a pollutant by an adsorbent. It is also essential to understand the efficacy of the adsorbent in eliminating pollutants. This could be understood if the fate of the post adsorptive wastewater solution can be checked via phytotoxicity assay. Finally, it is also essential to understand the behaviour of the adsorbent in packed bed columns and its interaction with the continuous influx of pollutant solution under variable conditions. So based on the discussed problem statements, the current thesis work was detailed into the following objectives:

1. Synthesis of adsorbents from bio-based precursors and their characterisation.
2. Optimisation of various parameters affecting adsorption capabilities of the adsorbents in sequestering studied adsorbates; and related modeling of various isotherm and kinetics models and related thermodynamic studies.
3. Regeneration studies to evaluate the adsorbent's recyclability.
4. Synergistic and/or antagonistic removal behaviour in multicomponent systems; the influence of co-existing ions; the influence of variable ionic strengths and phytotoxicity assays for analysing adsorbent’s efficacy.
5. Continuous packed-bed column studies.

1.8. Thesis Outline and key highlights

Based on the above discussed objectives the thesis work has been divided in the following 7 chapters.

Chapter 1: General introduction and theoretical background

Highlights

- *General introduction of heavy metals, dyes and antibiotics*
- *Conventional treatment techniques and their demerits*
- *Importance of adsorption and adsorbents*

Chapter 2: Comparative assessment of raw and acid-activated preparations of novel *Pongamia pinnata* shells for adsorption of hexavalent chromium from simulated wastewater

Highlights

- *Synthesis of acid-activated carbon from shelled biomass*
- *Comparative analysis of powdered biomass and acid-activated carbon as adsorbents for eliminating hexavalent chromium (Cr(VI)) from aqueous setups*
- *Adsorptive elimination of hexavalent chromium (Cr(VI))*
- *Desorption-regeneration-readsorption for recyclability studies*

Chapter 3: Comparative assessment of raw *Sterculia villosa* Roxb. shells, derived acid-activated carbon and chelated acid-activated carbon for adsorptive elimination of hexavalent chromium from simulated aqueous setups

Highlights

- *Chelation of acid-activated carbon using Ethylenediaminetetraacetic acid (EDTA)*
- *Adsorptive elimination of hexavalent chromium (Cr(VI)) by chelated acid-activated carbon*
- *Desorption-regeneration-readsorption for recyclability studies*

Chapter 4: Cationic surfactant modification on biomass-derived acid-activated carbon for adsorptive elimination of anionic azo dyes

Highlights

- *Cationic surfactant (CTAB) modification of acid-activated carbon (prepared from lignocellulosic precursor)*
- *Adsorptive eliminating anionic azo dyes like Congo red (CR) and Direct blue 6 (DB) from aqueous systems*
- *Adsorption studies were done for single and binary adsorptive systems in order to understand the synergistic or antagonistic effect of one dye over the adsorption of other dye species with the help of Competitive Langmuir modelling studies*
- *Influence of co-existing cations and anions over the adsorption of dye species by the adsorbent*
- *Desorption-regeneration-readsorption for recyclability studies*
- *Phytotoxic assay to analyse the effectivity of adsorbent in eliminating dyes from aqueous systems were studied using Vigna mungo seeds.*

Chapter 5: Polypyrrole complexation on biomass-derived powdered carbon for adsorptive elimination of emerging pharmaceutical contaminant Sulfamethoxazole

Highlights

- *Complexation of polypyrrole over powdered carbon (prepared from lignocellulosic precursor) via in-situ oxidative polymerisation*
- *Adsorptive elimination of Sulfamethoxazole (SMX) residues from aqueous systems*
- *Influence of co-existing antibiotics and heavy metals and their co-adsorption*
- *Influence of variable ionic strengths of adsorbate's medium*
- *Desorption-regeneration-readsorption for recyclability studies*

- *Phytotoxic assay was done using Vigna mungo seeds to analyse the efficacy of the adsorbent in eliminating SMX species*
- *Performance and effectivity of the prepared adsorbent in packed bed column setup (Continous column studies)*

Chapter 6: Fabrication of Chitosan to porous Chitosan for adsorptive elimination of synthetic anionic dyes from single and multi-adsorptive systems

Highlights

- *Fabrication of chitosan by gelation with* $CaBr_2{\cdot}xH_2O/CH_3OH$ *solution followed by vacuum drying*
- *Adsorptive eliminating anionic azo dyes like Congo red (CR), Bromophenol Blue (BB) and Direct blue 6 (DB) from aqueous systems*
- *Adsorption elimination of CR, BB and DB from single and multi (binary and tertiary) adsorptive systems to understand the synergistic or antagonistic effect of one dye over the adsorption of other dye species with the help of competitive Langmuir isotherm model analysis.*
- *Impact of co-existing metal cations and anionic salts*
- *Phytotoxic assays via Vigna mungo (Black gram) seeds to evaluate the efficacy of the adsorbent in adsorbing the dye molecules from simulated aqueous setups*

Chapter 7: Overall conclusion and significance of thesis work

Highlights

- *Significance of thesis work in solving actual/real-time water problems*
- *Summary of thesis work*

NOTE: For accuracy, the experiments were carried out in triplicates and results were reported as mean ± standard deviation. The results showed the standard deviation limit to be within the ± 5% range, which can be attributed to the good statistical validity of the experimental data.

CHAPTER 2

Comparative assessment of *Pongamia pinnata* shells and derived acid-activated carbon for adsorptive removal of hexavalent chromium from simulated wastewater

The work embodied in this chapter is published in:

CHANDI PATRA, Tasrin Shahnaz, Senthilmurugan Subbiah, Selvaraju Narayanasamy; 2020, "Comparative assessment of raw and acid-activated preparations of novel Pongamia pinnata shells for adsorption of hexavalent chromium from simulated wastewater"; ***ENVIRONMENTAL SCIENCE AND POLLUTION RESEARCH,*** 27:14836-14851 **(SPRINGER, IF: 4.223)**

GaRAPHICAL ABSTRACT

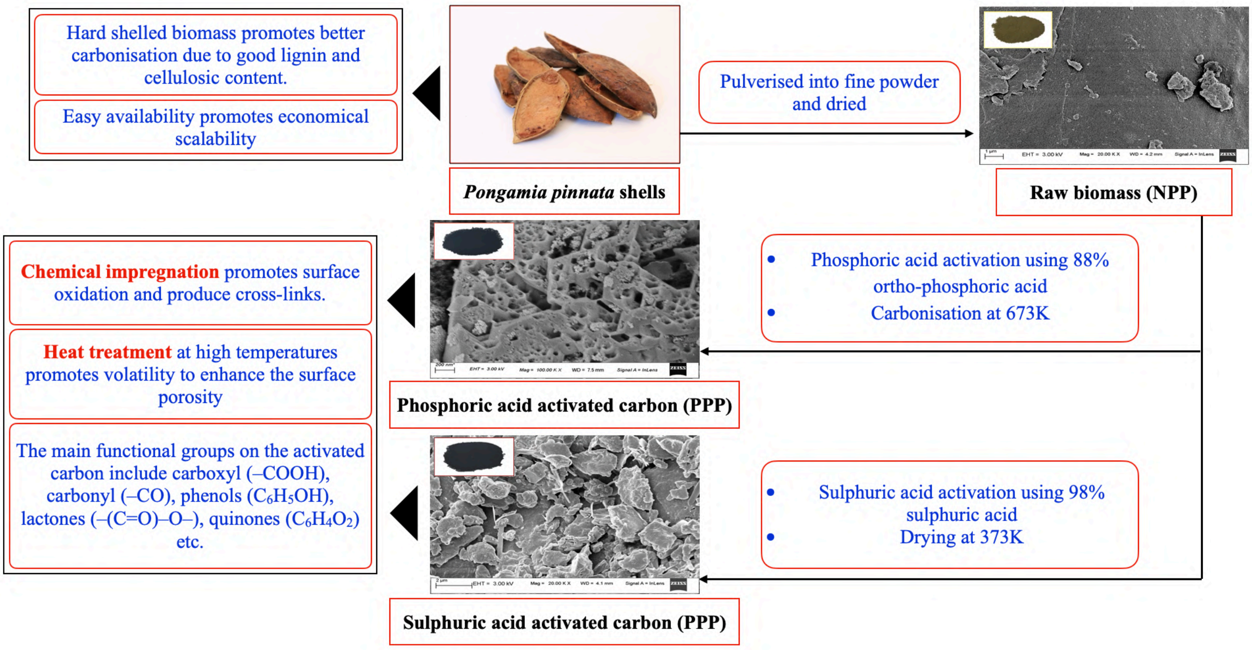

Hard shelled biomass promotes better carbonisation due to good lignin and cellulosic content.

Easy availability promotes economical scalability

***Pongamia pinnata* shells**

Pulverised into fine powder and dried

Raw biomass (NPP)

Chemical impregnation promotes surface oxidation and produce cross-links.

Heat treatment at high temperatures promotes volatility to enhance the surface porosity

The main functional groups on the activated carbon include carboxyl (–COOH), carbonyl (–CO), phenols (C_6H_5OH), lactones (–(C=O)–O–), quinones ($C_6H_4O_2$) etc.

- Phosphoric acid activation using 88% ortho-phosphoric acid
- Carbonisation at 673K

Phosphoric acid activated carbon (PPP)

- Sulphuric acid activation using 98% sulphuric acid
- Drying at 373K

Sulphuric acid activated carbon (PPP)

Abstract

The current study deals with the comparative assessment for efficient adsorption of Cr(VI) from simulated wastewater using raw (NPP), phosphoric acid-activated (PPP) and sulphuric acid-activated (SPP) *Pongamia pinnata* shells. Physico-chemical alterations of the adsorbent were characterised by scanning electron microscopy (SEM), Fourier transforms infrared spectroscopy (FT-IR), zeta-potential analysis, energy-dispersive X-ray spectroscopy (EDS) and total pore analysis using Brunauer-Emmett-Teller (BET). Parameters influencing the efficient adsorption of Cr(VI) species viz. initial pH of Cr(VI) solution, the dosage of adsorbent, adsorbent-Cr(VI) contact period, initial concentration of Cr(VI) ions and reaction temperature were optimised. Various two-parameter and three-parameter isotherm models, kinetic models and thermodynamic studies were performed using equilibrium data. Langmuir adsorption capacity for NPP (raw biomass), PPP (phosphoric acid-activated biomass) and SPP (sulphuric acid-activated biomass) was found to be 96.2, 152 and 192 mg/g, respectively. All the adsorbents gave the best fit for the pseudo-second-order model. Thermodynamic studies suggest spontaneous and endothermic interaction with an increased degree of randomness. Effect of co-existing cations and anions on Cr(VI) adsorption onto the adsorbents implied that minimal competition and the adsorption capacity of the adsorbents for Cr(VI) species remained unaffected. Regeneration studies suggest that activated adsorbents can be used up to three times with continuous desorption.

2.1. Materials and methods

The list of chemicals and their role in the current study are mentioned in **Table A.1.** (Appendix) in the supplementary information sheet.

2.1.1. Preparation of adsorbents

Pongamia pinnata fruits were collected locally from the IIT-Guwahati campus and dried at 353 K for 48 h in an oven. Once dried, the fruits were cracked open, and the seeds were separated from the shells. The shells were then pulverised to a fine powder (75–150 nm) and stored to be used as a raw adsorbent (NPP). A part of the pulverised adsorbent was used to produce acid-activated samples. Phosphoric acid activation of *Pongamia pinnata* shell biomass was done by mixing the biomass with 88% ortho-phosphoric acid in a 1:2.5 w/v (biomass/acid) proportion. The mixture was then dried at 373 K for 3–4 h, following which the dried sample was carbonised in a muffle furnace. The temperature was increased from normal room temperature (298-308 K) to 673 K and was maintained for 1.5 h. The carbonised/physically activated sample was then washed and soaked with 1% sodium bicarbonate for 24 h. Soaking helped in removing any acid present over the carbonised biomass. After soaking, the carbonised biomass was washed with distilled water repeatedly until the pH of the effluent water was neutral. Once pH≈7.0 was achieved, the sample was considered free from any residual acid. The carbonised biomass was dehydrated in an oven at 373 K for 12–24 h until the sample was a dry powder. The acid-activated sample was labelled PPP and stored for further experiments.

Sulphuric acid activation of the raw biomass was done by treating it with 98% sulphuric acid in the proportion 1:2 w/v (biomass/acid) and kept idle for a while. Once the sulphuric fume was released, the acid-treated biomass was kept in the oven for drying at 373 K for 36 h. The carbonised biomass was washed thoroughly and soaked overnight with 1% sodium bicarbonate. After soaking, the activated biomass was repeatedly washed with distilled water until the pH of the effluent was neutral. Finally, the sample was dehydrated in an oven at 373 K for 24–36 h and stored for further experiments and labelled SPP.

2.1.2. Batch adsorption experiments

The removal of hexavalent chromium by NPP, SPP, and PPP was examined by optimising variables in batch mode in a one-variable-at-a-time (OVAT) fashion. Different parameters like initial pH of Cr(VI) aqueous solution (2.0 to 10.0), dosage of adsorbent (0.4, 0.8, 1.2, 1.6, 2, 2.4, 2.8, 3.2, 3.6, 4 mg/mL), initial concentration of chromium (50, 100, 150, 200, 250 mg/L), variable time of reaction (10, 20, 30, 40, 60, 75, 90, 120, 180 min) and variable temperature (303, 313, 323 K) were optimised in batch experiments taking one variable at a time and keeping others constant. After the batch experiments were conducted for the desired period, the adsorbent was separated from the rest of the solution using a filter paper, and the filtrate was analysed for remnant chromium after adsorption. The concentration of chromate ion in the filtrate was measured using the standard calorimetric method after mixing it with acidified 1,5-diphenylcarbazide (DPC), which gives the filtrate a characteristic purple colour. The intensity of the developed purple colour depends upon the amount of Cr(VI) ions. The calorimetric study was done by a single beam UV-Visible spectrophotometer at 540 nm.

2.1.3. Effect of the co-existing cations and anions

Effect of coexisting cations and anions on Cr(VI) (in the form of $Cr_2O_7^{2-}$) adsorption onto NPP, PPP and SPP was investigated via batch adsorption experiment. Effect of co-existing cationic salts viz. ferric (Fe^{+3}), nickel (Ni^{+2}), zinc (Zn^{+2}) and copper (Cu^{+2}) and anionic salts viz. sulphate (SO_4^{-2}), nitrate (NO_3^{-2}), carbonate (CO_3^{-2}) and chloride (Cl^{-1}) was studied with 50 mg/L of Cr(VI) solution at pH 2.0.

2.1.4. Recyclability studies

The recyclability studies for NPP, PPP and SPP were carried out via repeated adsorption and desorption. For this study, the desorbing agents preferred were 0.1 N NaOH and 0.1 N HCl. After a single cycle of adsorption experiments, the adsorbent was continuously treated with 0.1 N NaOH and 0.1 N HCl for desorption. After the desorption process, the adsorbent was thoroughly rinsed with distilled water to wash away any residual NaOH or HCl clinging to the adsorbent. After washing, the adsorbents are dried and reused for consecutive adsorption processes. Adsorption-desorption experiments were conducted for two consecutive cycles for the recyclability analysis.

2.2. Results and discussion

2.2.1. Characterization of adsorbents

The adsorbents (normal and acid-activated) were characterised for various parameters. Characterisation of the samples defines the adsorbents' various physical/chemical/morphological aspects and their interaction with the sorbate molecules. The list of instruments used to characterise the prepared adsorbent has been detailed in **Table A.2.** (Appendix) with their make and model.

2.2.1.1. FT-IR analysis

FT-IR was conducted for evaluating the sorbate-sorbent interactions to determine the main surface functional groups of NPP, PPP and SPP involved in the adsorptive removal of Cr(VI) species. Spectral range for FT-IR analysis was taken from 500 to 4000 cm^{-1} for all the adsorbents (before and after Cr(VI) adsorption) as shown in **Figure 2.1. (A–C)**.

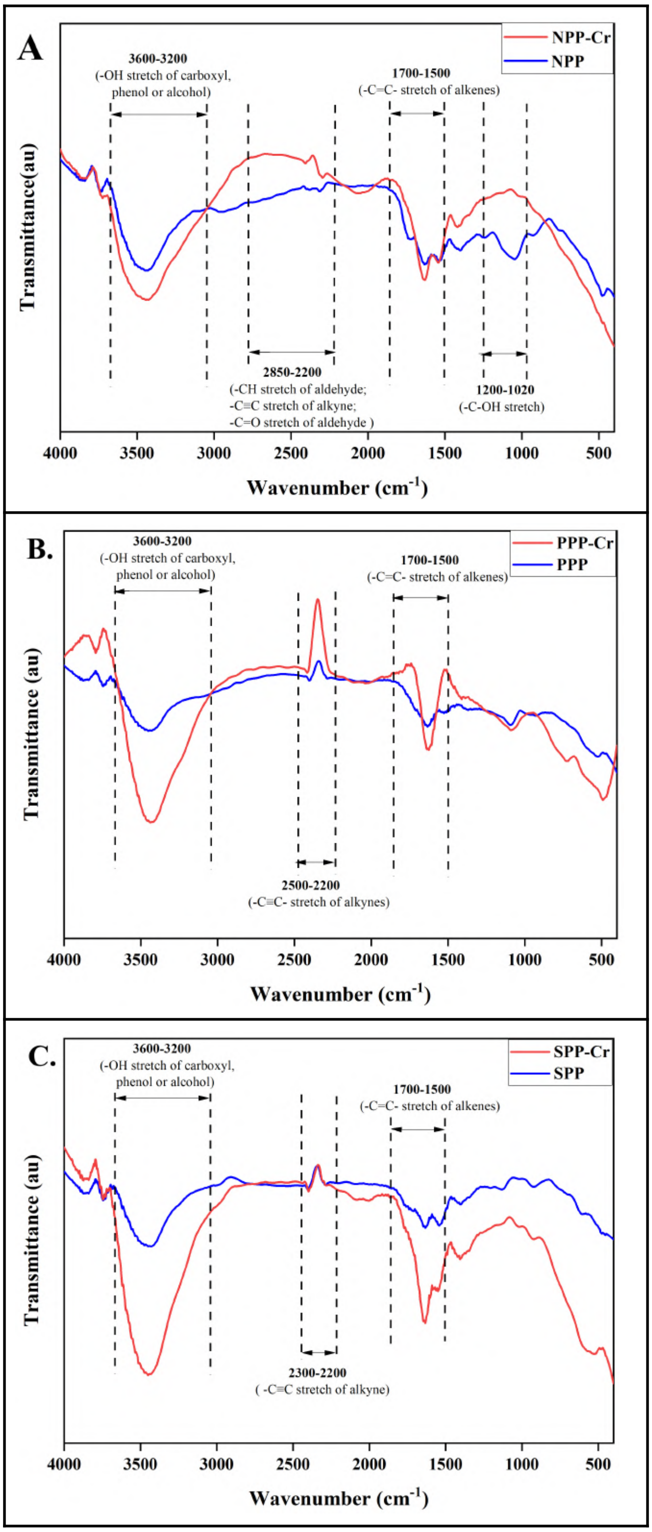

Figure 2.1. FT-IR analysis of (A): NPP; (B): PPP and (C): SPP before and after adsorption of Cr(VI)

A broad band observed between 3600 cm^{-1} and 3200 cm^{-1} was easily recognised for all the adsorbents depicting shifts due to hydroxyl groups (–OH stretch from carboxyls, phenols or alcohol groups). Peaks between 1700 cm^{-1} and 1500 cm^{-1} (due to weak C=C stretch of alkenes) were observed for all the adsorbents, before and after adsorption of Cr(VI) species. Presence of peaks between 2850 cm^{-1} and 2200 cm^{-1} (due to –CH stretch of aldehyde, C ≡ C stretch of alkynes or C=O stretch of aldehyde) was visible for NPP (with and without Cr(VI)). NPP also showed a significant peak at 1200 cm^{-1}–1020 cm^{-1} (due to –C–OH stretch) for Cr(VI)-adsorbed samples. Presence of peak at 2500 cm^{-1}–2200 cm^{-1} for PPP with Cr(VI) can be seen due to variable –C ≡ C– stretch. Corresponding peaks between 2300 cm^{-1} and 2200 cm^{-1} due to C≡C stretch of alkynes were also observed for SPP. Major changes in the intensities of band peaks before and after Cr(VI) adsorption revealed that the involvement of –OH, –CH, C=O, C–O–C, C=C and C≡C groups is involved inthe binding of Cr(VI) with all the adsorbents (NPP, PPP and SPP) (Sun et al., 2013; Sun et al., 2014; Enniya et al., 2018; Patra et al., 2019).

2.2.1.2. SEM analysis

SEM analysis was done for assessing the surface morphology and structure of the adsorbents. The SEM images of the non-treated adsorbents and the sorbate clad adsorbents are as shown in **Figure 2.2. (A–F)**.

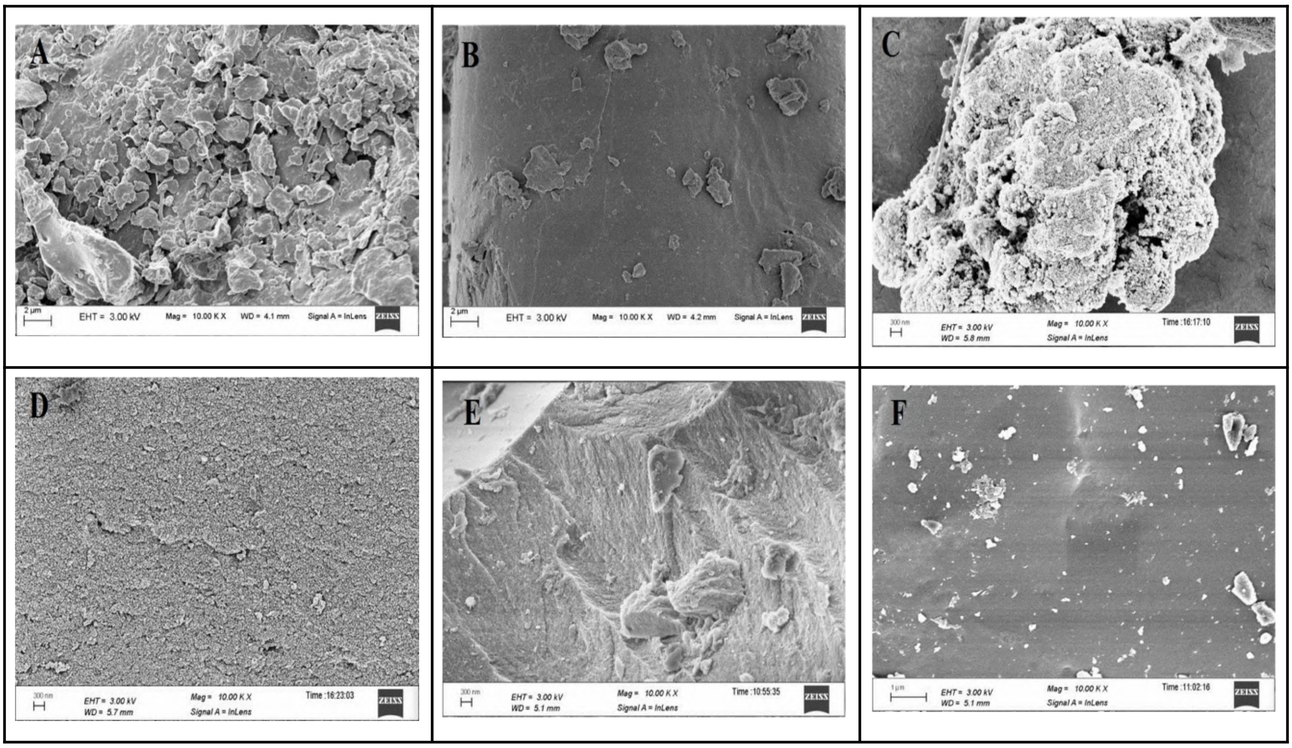

Figure 2.2. *SEM images of NPP* ***(A)****: before and* ***(B)****: after; PPP* ***(C)****: before and* ***(D)****: after; SPP* ***(E)****: before and* ***(F)****: after Cr(VI) adsorption*

The images for adsorbents without Cr(VI) showed the surface morphology as rough, with numerous visibly distinct uneven surface along with long ridges, exhibiting heterogeneous surface texture and providing a large surface area for Cr(VI) adsorption. External surfaces for PPP and SPP exhibit cavities, pores, macropores distinguished with long uneven hollow ridges. This enhanced porosity was primarily the reason for increased adsorption capacity. However, images of adsorbents with Cr(VI) showed smooth surfaces with less unevenness and ridges.

2.2.1.3. EDS analysis

Qualitative metal analysis of the adsorbents before and after Cr(VI) adsorption was done by EDS analysis. The EDS spectra for sorbent with and without Cr(VI) loaded are illustrated in **Figure 2.3. (A–F)**.

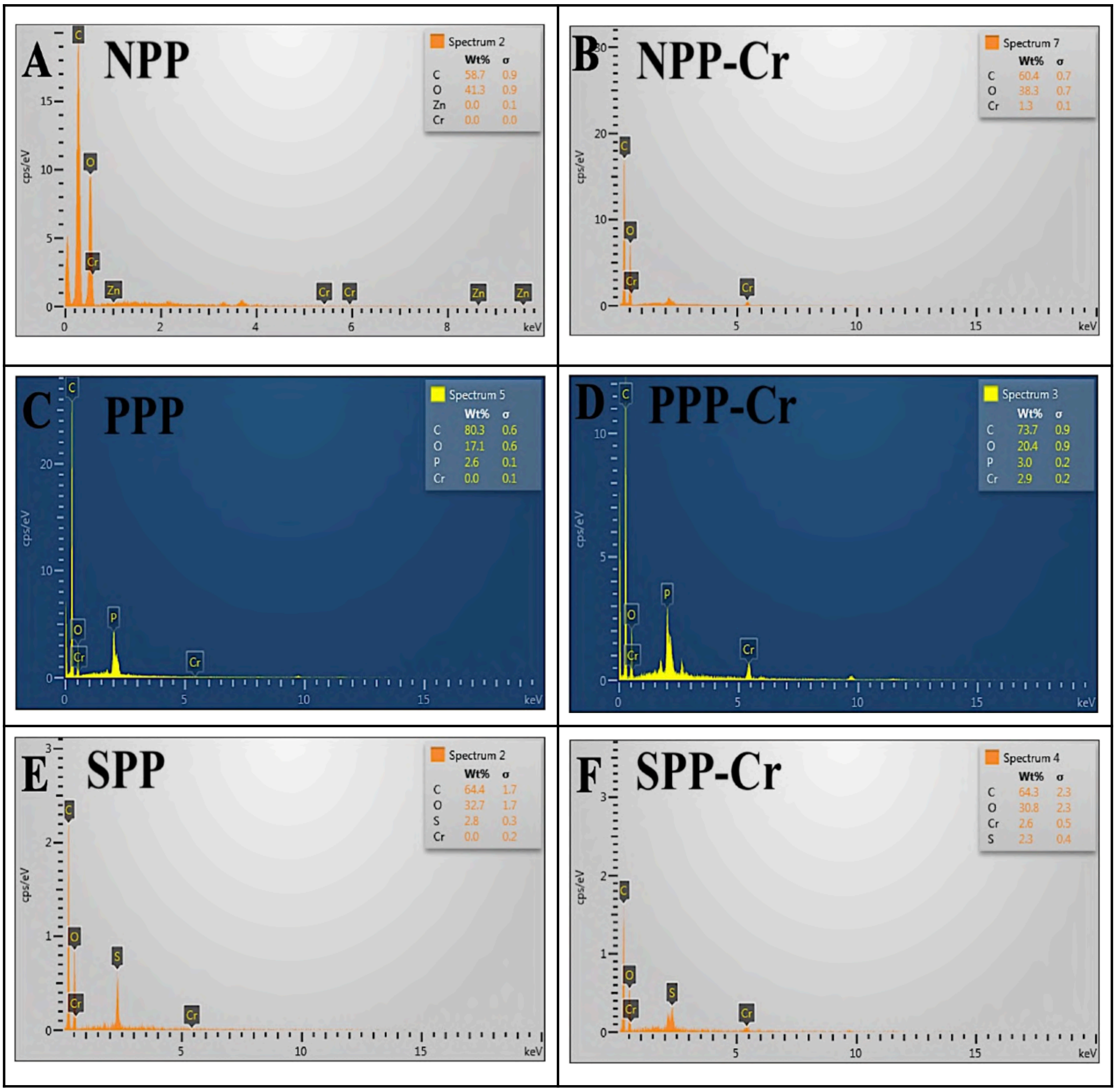

Spectrum 2	Wt%	σ
C	58.7	0.9
O	41.3	0.9
Zn	0.0	0.1
Cr	0.0	0.0

Spectrum 7	Wt%	σ
C	60.4	0.7
O	38.3	0.7
Cr	1.3	0.1

Spectrum 5	Wt%	σ
C	80.3	0.6
O	17.1	0.6
P	2.6	0.1
Cr	0.0	0.1

Spectrum 3	Wt%	σ
C	73.7	0.9
O	20.4	0.9
P	3.0	0.2
Cr	2.9	0.2

Spectrum 2	Wt%	σ
C	64.4	1.7
O	32.7	1.7
S	2.8	0.3
Cr	0.0	0.2

Spectrum 4	Wt%	σ
C	64.3	2.3
O	30.8	2.3
Cr	2.6	0.5
S	2.3	0.4

Figure 2.3*. EDS analysis of NPP (****A****): before and (****B****): after; PPP (C): before and (****D****): after; SPP (****E****): before and (****F****): after Cr(VI) adsorption*

Distinct peaks of chromium were visible for the sorbent samples with Cr(VI), which, however, were absent for samples without Cr(VI). Conclusively, SPP and PPP showed enhanced Cr(VI) percentage compared to NPP due to increased pore size and intensity caused by acid activation. Hence, EDS analysis directly confirmed Cr(VI) sorption over the adsorbents.

2.2.1.4. Total pore analysis/Brunauer-Emmett-Teller analysis

Total pore or Brunauer-Emmett-Teller analysis of all the adsorbents (NPP, SPP and PPP) was measured using BET pore analysis. Results verified that the raw biomass (NPP) has a specific surface area of 4.02 m^2/g. Sulphuric acid-activated adsorbents (SPP) showed an elevated specific sur- face area with 552.28 m^2/g, while phosphoric acid-activated adsorbents (PPP) showed the highest total surface area with 935.02 m^2/g as compared to SPP and NPP. **Table 2.1.** represents the pore diameter (nm), total pore volume (cm^3/g) and specific surface area (m^2/g) for all the adsorbents. BET analysis verified that acid activation followed by pyrolysis increased the specific surface area of PPP and SPP compared to NPP, and hence, there was an increase in the available sites for Cr(VI) adsorption.

Table 2.1. *Total pore analysis/Brunauer-Emmett-Teller (BET) analysis of NPP, PPP and SPP*

Porosity Parameters	NPP	PPP	SPP
Total pore volume (cm^3/g)	0.003	0.924	0.109
Pore diameter (nm)	3.18	3.96	2.44
Specific surface area (m^2/g)	4.02	935.02	552.28

2.2.1.5. Zeta potential studies

Zeta potential (mV) was measured within the pH range of 2.0-10.0. It is the potential difference between the liquid dispersion medium and the outer stable stationary layer of the fluid attached to the adsorbent (dispersed particle). Zeta potential can be used to quantify the electrical potential of the solid particle surface, which can be used to analyse the basicity or acidity of the stable adsorbent surfaces. All the adsorbents showed an erratic behaviour to variable initial pH values (**Figure 2.4.**). PPP shows a positive zeta potential value at pH 2.0, after which it shows gradual negative zeta-potential values from the pH range of 3.0 to 10.0. On the other hand, NPP shows positive potential values from pH 2.0 to 8.0, after which it dips to negative potential values. SPP shows negative zeta potential values within the pH range from 2.0 to 10.0. The iso-electric point (pH_{IEP}) value of the original carbon is 3.5. Oxidation via acid treatment results in a decrease of the pH_{IEP} values, likely to PPP (between pH 2.0 and 3.0) and SPP (pH < 2.0), which was detected due to the presence of lactone and carboxylic functional groups with lower dissociation pH values. Negative zeta potential also indicates that oxidation treatment with phosphoric and sulphuric introduced oxygen-containing functional groups on the surfaces of the adsorbents (Song et al., 2010).

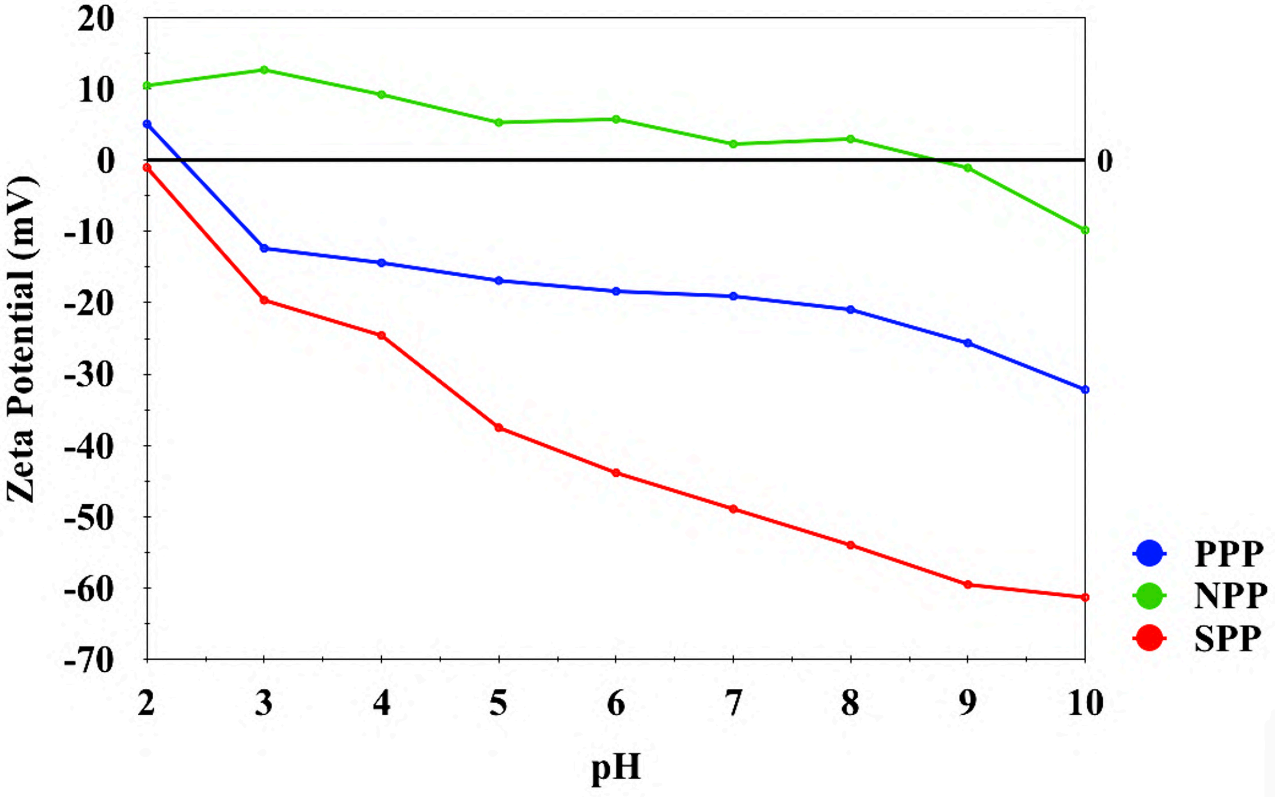

Figure 2.4. *Zeta potential analysis of NPP, PPP and SPP*

2.2.2. Physiochemical properties of the prepared carbon

Physiochemical activation of the biomass involved two steps in series: (i) chemical (acid) impregnation and (ii) heat treatment. Chemical impregnation involves impregnating the precursor with the chemical agents (H_2SO_4 and H_3PO_4 in the current study). Chemical impregnation promotes the formation of cross-links, leading to forming a rigid porous matrix. Acid activation of biomass prior to pyrolysis oxidises the porous carbon surface as it increases the acidic property, thus removing the mineral elements and improving the hydrophilic nature of the surface. The acid-treated oxidised carbon surface is more negatively charged than that of actual activated carbon due to the dissociation of surface acid groups, which increases the electrostatic adsorbate-adsorbent interaction. Acidic functional groups (i.e. oxygen functional groups containing proton donors) on carbon surfaces have been reported to remove heavy metals from water. The main functional groups on the activated carbon responsible for uptake of heavy metals include carboxyl (–COOH), carbonyl (–CO), phenols (C_6H_5OH), lactones (–(C=O)–O–), quinones ($C_6H_4O_2$) etc. (Bhatnagar et al., 2013; Toles et al., 1999; Xie et al., 2012). Heat treatment at high temperatures promotes volatility to these pore matrices and reduce the risk of volume contraction and hence enhance the surface porosity (Nakagawa et al., 2007; Gerçel and Gerçel, 2007; Karagöz et al., 2008).

2.2.3. Effects of various parameters

2.2.3.1. Effect of pH studies

The pH studies of the aqueous chromium solution played a vital aspect in controlling the sorbent efficiency for eliminating Cr(VI) from the simulated wastewater. Effect of variable initial pH ranging from 2.0 to 10.0 for sorbate concentration was studied, keeping the other parameters constant (**Figure 2.5.**). The trend shows that pH 2.0 was best suited for adsorption by all the adsorbents (NPP, PPP and SPP). At low pH, the adsorbents tend to be positively charged; thus, the anionic hydrogen chromate ($HCrO_4^-$) ions (due to chromium speciation in aqueous solution) show more electro-static pull towards the positively charged adsorbents. However, at higher pH values, the adsorbent surface tends to be negatively charged, and hence the attractive pull tends to reduce. The adsorption efficiency for NPP, PPP and SPP turns out to be 88.67%, 96% and 95.67%, respectively, at pH = 2.0.

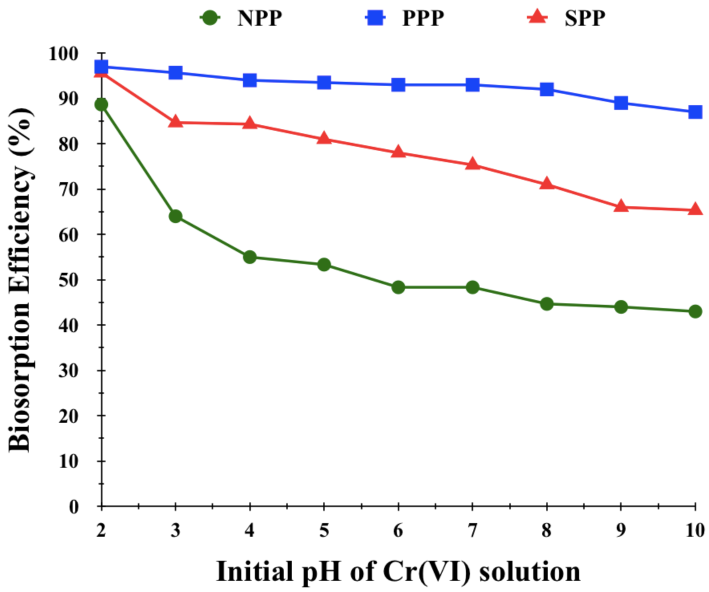

Figure 2.5. *Effect of initial pH of Cr(VI) solution over its adsorption efficiency by NPP, PPP and SPP*

2.2.3.2. Effect of adsorbent dosage

Effect of optimised adsorbent dosage too played a crucial role in sorption of the sorbate over the sorbent. The adsorbents' removal of Cr(VI) was studied by taking variable dosages of the adsorbents. Variable dosages ranging from 0.4 to 4 mg/mL (0.4, 0.8, 1.2, 1.6, 2, 2.4, 2.8, 3.2, 3.6, 4 mg/mL) were taken and checked for optimal dosage for maximal sorption of Cr(VI) at 303 K and pH=2.0. A total of 3.6 mg/mL of NPP gave 98% efficiency compared to 3.2 mg/L of PPP and 2 mg/L of SPP, giving 99.67% and 97.67% efficiency, respectively, after 3 h of incubation at 120 rpm. After reaching the maximal adsorption efficiency and minimal adsorption capacity, further dosages halted to equilibrium as shown in **Figure 2.6**. The possible reason for such behaviour would be the limited availability of the Cr(VI) molecules for filling up the adsorption sites, with the increase in dosage of adsorbents, which caused a reduction in adsorption capacity (mg/g) with increase in dosage of adsorbent.

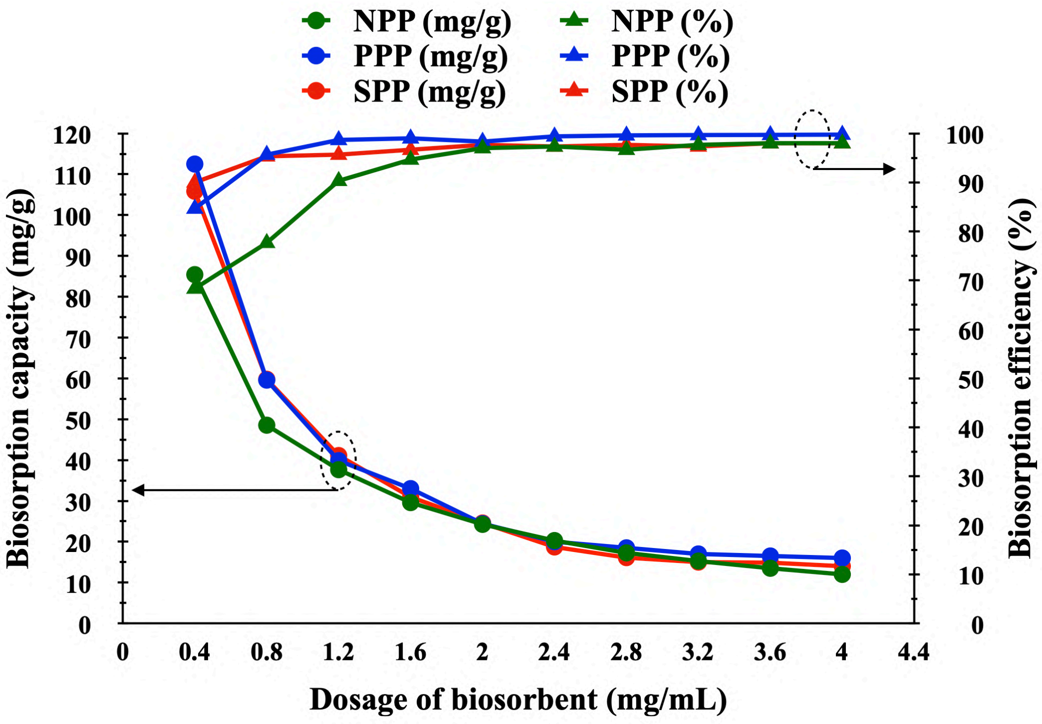

Figure 2.6. *Effect of variable dosage of the adsorbents vis. NPP, PPP and SPP on the adsorption of Cr(VI)*

2.2.3.3. Effect of initial adsorbate concentration and contact time

This study was conducted to know the maximum adsorption capacity of the adsorbents with limited adsorbent dosage over time. For the study, five different concentrations of Cr(VI) viz. 50, 100, 150, 200 and 250 mg/L were taken. For all the concentrations, the adsorption capacity showed a logarithmic rise for the first 10–15 min, after which the rise slowed down and sublimed to equilibrium (data not shown). The possible reason for such behaviour was that all the sorbate molecules initially tend to interact with the adsorption sites. However, when the sites were limited, the sorbate molecules had to compete, thus responsible for depreciation in the capacity. Finally, when almost all the sites were filled, the sorption process achieved equilibrium where sorption rates equalised with the rate of desorption. However, with the increase in concentration, the removal efficiency of the sorbate molecules reduced from 49.34% to 27.75% for NPP, 92 %to 56% for PPP and 65.33% to 47.63% for SPP, though all the adsorbents showed an increase in adsorption capacity (mg/g). **Figure 2.7.** shows the variation of adsorption efficiency (%) and adsorption capacity (mg/g) by NPP, PPP and SPP, with the variable initial concentration of Cr(VI).

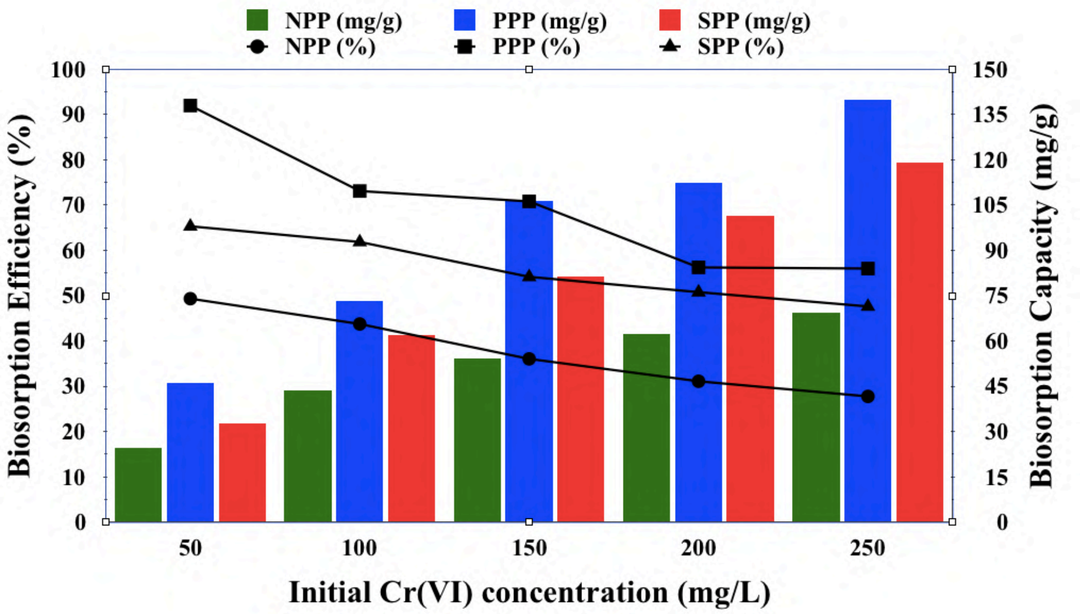

Figure 2.7. Effect of variable initial Cr(VI) concentration on adsorption capacity and efficiency by NPP, PPP and SPP

2.2.4. Effect of temperature and thermodynamic study of adsorption

Temperature played a crucial role in regulating the adsorption efficiency of the adsorbents. This study was done for three different temperatures viz. 303 K, 313 K and 323 K for variable concentrations, 50 to 250 mg/L. With the increase in temperature, the sorption efficiency of PPP and SPP increased; however, NPP showed the opposite behaviour. The adsorption capacity reduced with the increase in temperature and the increase with the initial concentration of Cr(VI) solution. The possible reason for such behaviour may be due to the activation of PPP and SPP surface due to acid activation and pyrolysis. Activation must have led to temperature-dependent sites, which enhanced the adsorption capacity with the increase in temperature.

The experimental data for temperature was used to calculate the thermodynamic parameters (ΔG°, ΔH°, and ΔS°) for the sorption of Cr(VI) by NPP, PPP and SPP and the data obtained is represented in **Table 2.2.** Negative values for change in Gibb's free energy (ΔG°) for the interaction of Cr(VI) with NPP, PPP and SPP revealed that the interaction was spontaneous and thermodynamically favourable and feasible. Change in enthalpy (ΔH°), for the interaction of Cr(VI) with NPP, PPP and SPP showed positive values; thus, change in enthalpy for such interaction was endothermic. Positive values for the change in entropy (ΔS°) indicated an increase in the degree of randomness of Cr(VI) adsorption by NPP, PPP and SPP.

Table 2.2. *Thermodynamics parameters (ΔG°, ΔH° and ΔS°) for adsorption of Cr(VI) by NPP, PPP and SPP*

C_i (mg/L)	T(K)	NPP			PPP			SPP		
		ΔG° (kJ/mol)	**ΔH° (kJ/mol)**	**ΔS° (J/molK)**	**ΔG° (kJ/mol)**	**ΔH° (kJ/mol)**	**ΔS° (J/molK)**	**ΔG° (kJ/mol)**	**ΔH° (kJ/mol)**	**ΔS° (J/molK)**
50	303	-17.3	28.3	151.2	-23.6	75.5	326.5	-19.0	104.3	409.5
	313	-18.9			-25.4			-24.6		
	323	-19.1			-28.2			-25.4		
100	303	-16.8	10.5	88.9	-19.9	12.6	108.1	-18.6	63.9	272.0
	313	-16.2			-21.0			-20.4		
	323	-17.4			-20.7			-22.6		
150	303	-16.0	10.6	86.4	-19.6	12.8	106.6	-17.8	52.2	231.7
	313	-15.2			-19.8			-20.2		
	323	-16.6			-20.4			-21.0		
200	303	-15.4	4.3	62.3	-18.0	19.8	124.0	-17.5	43.6	201.9
	313	-13.2			-17.8			-19.3		
	323	-15.7			-19.3			-20.2		
250	303	-15.0	3.6	57.0	-18.0	12.1	99.1	-17.2	30.4	157.5
	313	-14.1			-18.1			-18.8		
	323	-14.0			-18.8			-19.0		

2.2.5. Adsorption isotherms

Equilibrated experimental data retrieved from the batch experiments were fitted with various two-parameter and three-parameter isotherm models for the chemico-physical analysis of the sorbent-sorbate interactions. Two-parameter isotherm models studied were Langmuir, Freundlich, Dubinin-Radushkevich, Frumkin and Temkin isotherm models. Three-parameter isotherms included Redlich-Peterson and Sips, isotherm models. These isotherms have been detailed in **Table A.3.** (Appendix). The corresponding values of the constants/exponents of the isotherms and the coefficients of determination (R2) are presented in **Table S.2.1.** (Supplementary data). Langmuir isotherm model fitted best for Cr(VI) adsorption by NPP, PPP and SPP, thus indicating monolayer formation between Cr(VI) and the adsorbents. The coefficient of determination (R^2) values for NPP, PPP and SPP for the Langmuir isotherm model is 0.99, 0.98 and 0.99, respectively. Simultaneously, the coefficient of determination (R2) for the Freundlich isotherm model is 0.97, 0.95 and 0.98 for NPP, PPP and SPP, which are comparatively less than Langmuir isotherm. Langmuir maximum adsorption capacity was found to be 96.2 mg/g for NPP, 152 mg/g for PPP and 192 mg/g for SPP for Cr(VI) adsorption. Conclusively, the adsorption capacity of the adsorbent increases with activation, as demonstrated by SPP and PPP. Values of Freundlich isotherm model constants K_f and n favour the capacity and intensity of adsorption of Cr(VI) by the adsorbents. Dubinin-Radushkevich isotherm shows the least fit for the adsorption process since it has the least coefficient of determination values (R^2) compared to Langmuir and Freundlich isotherm models, thus suggesting its least applicability with the adsorption phenomenon. Values for Frumkin isotherm constant, α, are greater than zero, thus suggesting an attraction between sorbate molecules. Temkin constant (B) values, related to the heat of sorption (J/mol), were 113 J/mol for NPP, 96.4 J/mol for PPP, and 60.7 J/mol for PPP SPP. Reduced values for bt of the activated samples revealed that more coverage of sorbate molecules occurred over the activated adsorbents (PPP and SPP) than normal adsorbents (NPP), which resulted in reduced heat of sorption for PPP and SPP than NPP. Redlich-Peterson and Sips isotherm models showed a high coefficient of determination values, i.e. $R^2 > 0.99$. This ascertains the good fitting of these models with the adsorption process of Cr(VI) with the adsorbents. Values for g (Redlich-Peterson exponent) and ms (Sips exponent), for NPP (g = 0.99; ms = 1.14), PPP (g=0.75; m =0.69) and SPP (g=0.76; m =1.04) are near to unity suggesting Cr(VI) interaction with adsorbents to follow Langmuir isotherm model and also indicate the surface of adsorbents to be homogenous. **Figure 2.8.** shows the non-linear isotherm plot analysis for NPP, PPP and SPP.

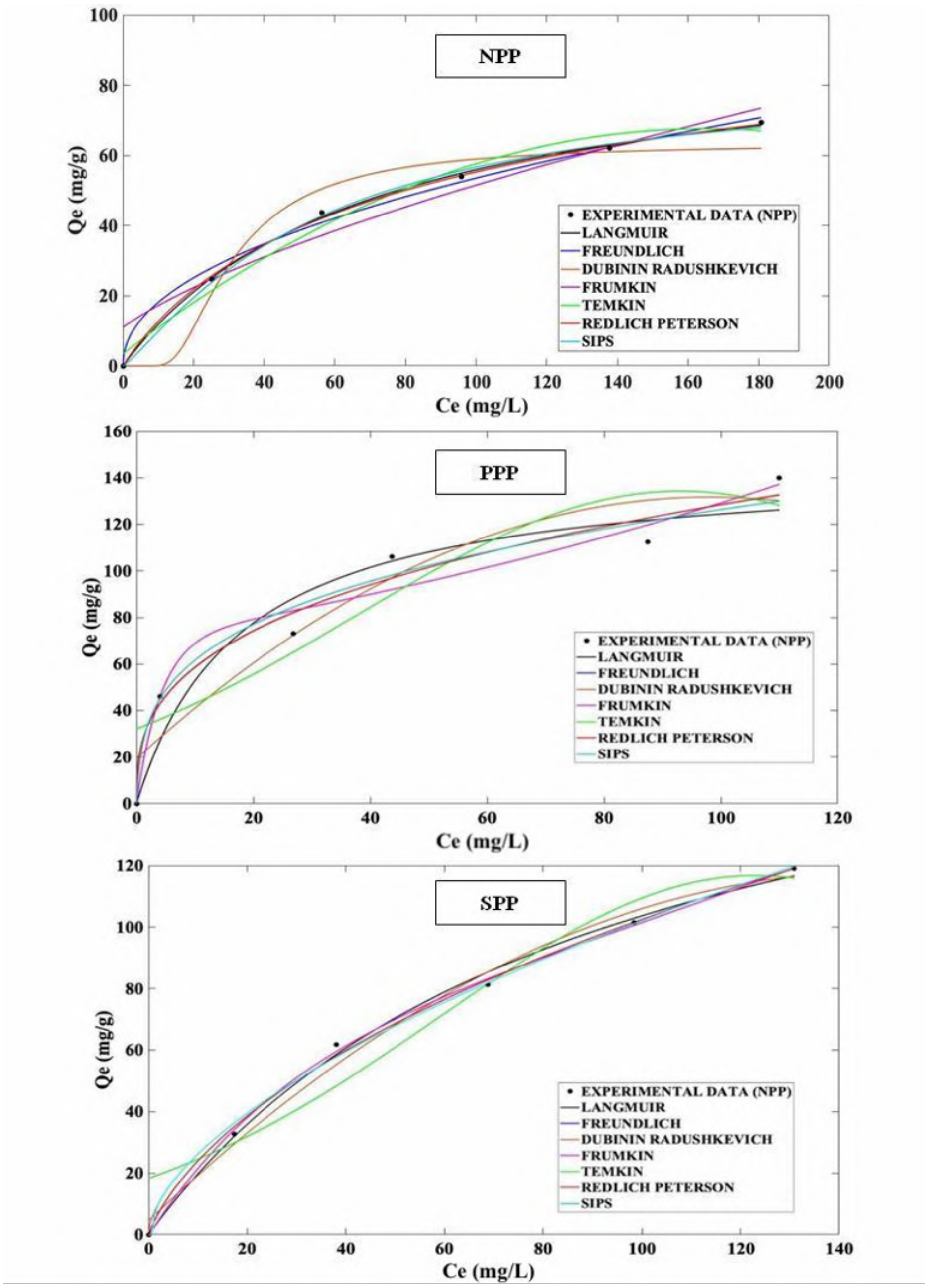

Figure 2.8. *Non-linear fitting of isotherm models for the adsorption of Cr(VI) by NPP, PPP and SPP*

2.2.6. Kinetic parameters

In order to evaluate the mechanisms involved and the rate-limiting steps in the interaction between Cr(VI) and the adsorbents, various parameters like the pseudo-first-order, pseudo-second-order and intra-particle diffusion were studied. These kinetic models have been detailed in **Table A.4.** (Appendix). The parameters were studied, and their coefficients of determination (R^2) values, along with the constants, are detailed in **Table S.2.2.** (Supplementary data). For pseudo-first-order reaction, the R^2 values of the adsorbents were low, and thus, the suitability of the pseudo-first-order model for the uptake of Cr(VI) by NPP, SPP and PPP is less. R^2 values for the pseudo-second-order kinetics were very high, i.e. $R^2 > 0.99$; thus, this model fitted best for Cr(VI) removal by the adsorbents (NPP, SPP and PPP). This model confirmed that the rate-limiting step for adsorption of Cr(VI) by NPP, PPP and SPP was governed by chemisorption. Simultaneously, the R^2 values of intra-particle diffusion are the lowest, and hence, it fits the least with the experimental data; thus, attributing intra-particle diffusion was not only the rate-determining step. **Figure 2.9.** shows the non-linear kinetic plot analysis for NPP, PPP and SPP for Cr(VI) adsorption.

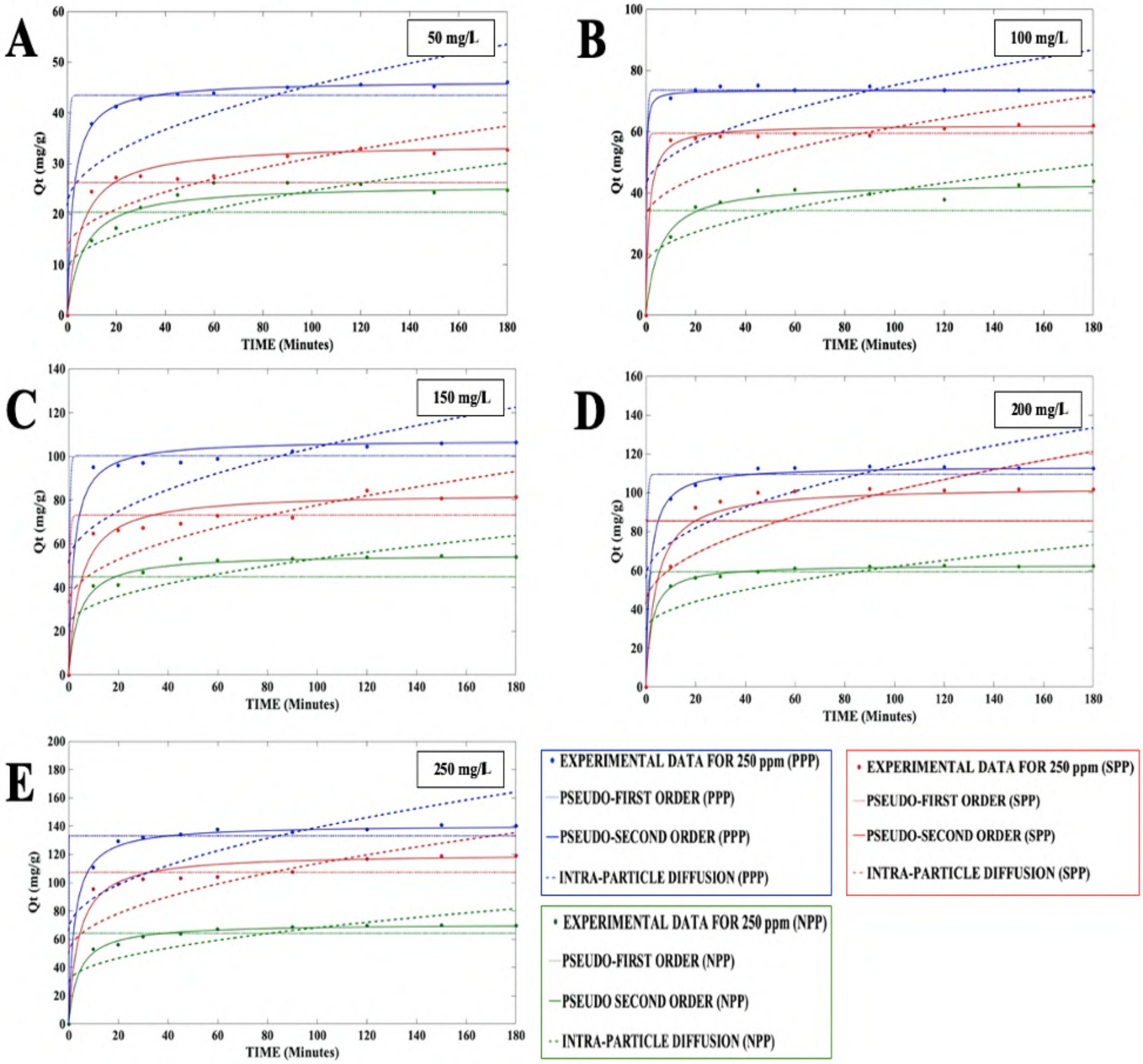

Figure 2.9. *Non-linear fitting of kinetic models for the adsorption by NPP, PPP and SPP at initial Cr(VI) concentration of; (A): 50 mg/l, (B): 100 mg/l, (C): 150 mg/l, (D): 200 mg/l and (E): 250 mg/l*

2.2.7. Effect of co-existing cations and anions

Batch experiments were carried out to analyse the individual effects of co-existing cations and anions at an initial Cr(VI) concentration of 50 mg/L and pH 2.0, using NPP, PPP and SPP. **Figure 2.10.** shows that the co-existence of cations (Fe^{3+}, Ni^{2+}, Zn^{2+}, Cu^{2+}) and anions (SO_4^{2-}, NO_3^{2-}, CO_4^{2-} and Cl^-) have a nominal effect on the adsorption of Cr(VI) species. At an initial Cr(VI) concentration of 50 mg/L, the adsorption capacity of NPP, PPP and SPP showed a slightly reduced adsorption capacity as compared to the adsorption capacity in the absence of cations. The possible reason for such affect is due to presence of metal cations in the form of M^{+2} and its hydration forms as M(OH)+ and $M(OH)_2$ at pH 2.0. According to Tobin et al., 1984, the adsorption of metal ions depends on their ionic radius; the greater the ionic radius, the smaller the radius of metal hydrates and thus greater the ion exchange on the adsorbent surface. Since Fe^{3+}, Ni^{2+}, Zn^{2+} and Cu^{2+} have ionic radius closer to Cr(VI), the co-existence of such cations would compete with Cr(VI) species for adsorption, and thus, there was a slight reduction in Cr(VI) adsorption. Like cations, the co-existence of anions showed a similar trend with nominal reduction in adsorption capacity by all the adsorbents. The possible reason for such behaviour may be the negatively charged anions competing with the anionic forms of Cr(VI) at pH 2.0 for the active sites on the adsorbent's surface (Dong et al., 2018).

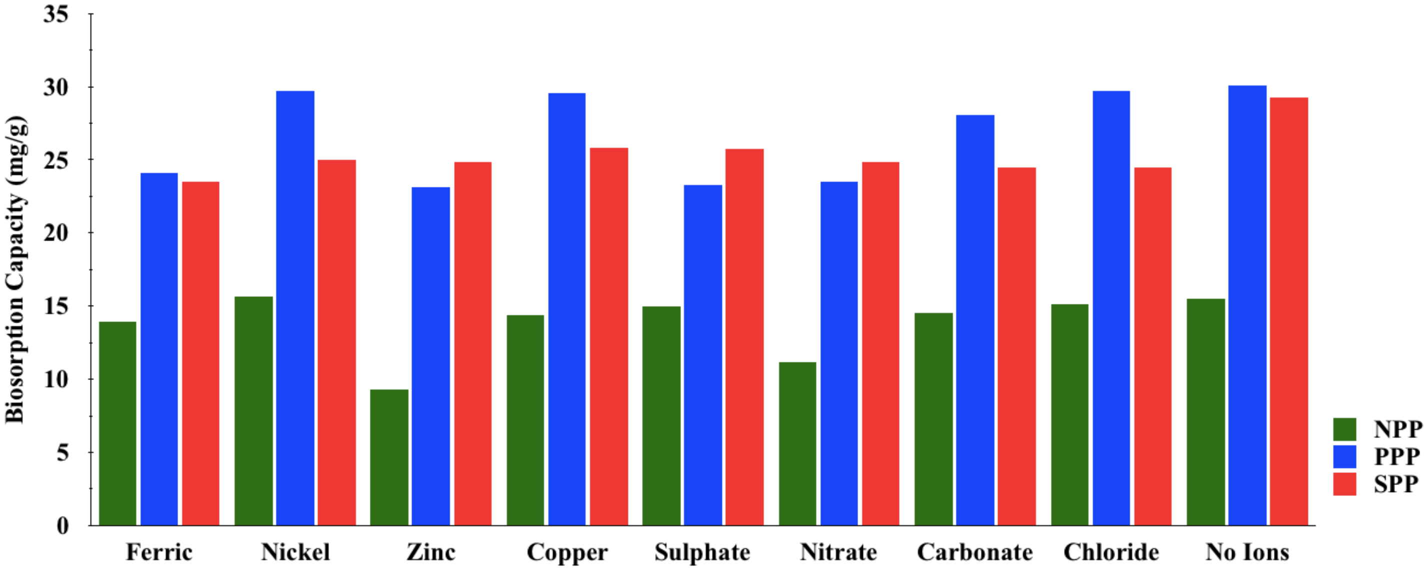

Figure 2.10. Effect of co-existing cations and anions on the adsorption of Cr(VI) by NPP, PPP and SPP

2.2.8. Reusability/regenerative studies

After a single use for the removal of Cr(VI), the adsorption capacity of the adsorbents was studied to know the extent to which the adsorbents can be recycled for the removal of Cr(VI). This helps in selecting a suitable adsorbent, which can be retrieved and recycled a good number of times. The adsorbents were treated with 0.1 N HCl and 0.1 N NaOH for regenerative studies. After a single regeneration cycle, the adsorption efficiency for desorbed NPP reduced from 74.17% to 36.25%. The second regeneration gave an efficiency of 35.08%. For PPP, the efficiency fell from 96.67% to 81.5% for the first generation recycle and 72.86% for the second regeneration. Finally, for SPP, the efficiency fell from 95.83% to 84.17% for the first generation recycling and 73.27% for the second regeneration. Based on the decline in efficiency, further regeneration seemed pointless. This depreciation in adsorption capacity during consecutive cycles was due to some structural or morphological modifications on the surface of the pores of the adsorbent and the blockage of certain functional groups or the inter-pores of the adsorbents the Cr(VI) from the previous run.

2.3. Significant findings

Pongamia pinnata shells in raw form (NPP) and activated forms (PPP and SPP) were studied for the removal of Cr(VI) from simulated wastewater. The present study proves that both raw and activated forms of *Pongamia pinnata* shells are potent adsorbents for removing Cr(VI) from an aqueous solution. Initial pH, dosage of adsorbents, initial concentration of Cr(VI) and temperature were effectively optimised for efficient removal of Cr(VI) by respective sorbents. Determination of coefficient (R2) values verified NPP, PPP and SPP to follow Langmuir isotherm. Adsorption isotherms verified the formation of a monolayer of Cr(VI) species over the adsorbents as per Langmuir and electro-static force of attraction between the sorbate and sorbent molecules as per Frumkin isotherm model. Values of g (Redlich-Peterson) and m (Sips) suggest fitting of Langmuir isotherm model by NPP, PPP and SPP. Among all the studied kinetic parameters, pseudo-second-order fitted the best for all the adsorbents. The interaction of NPP, PPP and SPP with the simulated wastewater was spontaneous and thermodynamically stable. All the adsorbents showed endothermic sorbate-adsorbent interaction with an increased degree of randomness of adsorption.

SUPPLEMENTARY DATA FOR CHAPTER 2

Table S.2.1. *Adsorption isotherm model parameters, constants and coefficient of determination (R^2) for removal of Cr(VI) by NPP, PPP and SPP*

ISOTHERMS		**Isotherm constants**	**NPP**	**PPP**	**SPP**
Two-parameter models	**Langmuir**	**Q_L (mg/g)**	96.2	152	192
		K_L (L/mg)	0.01	0.06	0.01
		R^2	0.99	0.98	0.99
	Freundlich	**K_F (mg/g) (mg/L)$^{-1/n}$**	4.95	28.5	5.77
		n	1.93	3.09	1.60
		R^2	0.97	0.95	0.98
	Dubinin-Radushkevich	**K_{DR} (mol^2/J^2)**	1×10^{-4}	3×10^{-6}	6×10^{-5}
		E_{DR}	0.07	0.43	0.09
		R^2	0.93	0.73	0.89
	Frumkin	**K_{FK}**	5.8×10^{-5}	2.7×10^{-6}	6×10^{-6}
		α	6.48	7.37	7.37
		R^2	0.99	0.97	0.98
	Temkin	**A_T (L/g)**	0.12	1.14	0.11
		B (J/mol)	113	96.4	60.7
		R^2	0.99	0.89	0.98
Three-parameter models	**Redlich-Peterson**	**Q_{RP} (mg/g)**	91.0	143.6	153.8
		K_{RP}	0.02	1.21	0.05
		g	0.99	0.75	0.76
		R^2	0.99	0.99	0.99
	Sips	**Q_S (mg/g)**	85.5	175.2	183.7
		K_S	0.01	0.40	0.01
		m	1.14	0.69	1.04
		R^2	0.99	0.99	0.99

Table S.2.2. *Kinetic model parameters and constants for adsorption and coefficient of determination (R^2) for the removal of Cr(VI) using NPP, PPP and SPP*

C_i (mg/L)	**$Q_{e\ Exp.}$ (mg/g)**	**Pseudo-first order**			**Pseudo-second order**			**Intra-particle diffusion**		
		K_1 (1/min)	**Q_e (mg/g)**	**R^2**	**K_2 (g/mg min)**	**Q_e (mg/g)**	**R^2**	**K_{id} (mg/g min$^{0.5}$)**	**C (mg/g)**	**R^2**
					NPP					
50	24.7	0.03	26.2	0.24	7×10^{-3}	25.8	0.99	1.60	8.67	0.69
100	44.8	0.04	43.8	0.69	4×10^{-3}	43.3	0.99	2.47	16.11	0.64
150	55.0	0.05	54.4	0.78	5×10^{-3}	55.2	0.99	3.1	22.09	0.63
200	62.2	0.05	62.5	0.80	8×10^{-3}	62.9	0.99	3.26	29.36	0.53
250	69.9	0.06	69.7	0.86	4×10^{-3}	70.9	0.99	3.92	28.93	0.62
					PPP					
50	46.8	0.04	46	0.65	8×10^{-3}	46.3	0.99	2.38	21.6	0.52
100	73.1	0.02	75	0.09	4×10^{-3}	73.5	0.99	3.38	41.3	0.38
150	107	0.05	106	0.80	3×10^{-3}	108	0.99	5.32	51.0	0.50
200	113	0.05	113	0.56	9×10^{-3}	114	0.99	5.77	56.1	0.49
250	140	0.05	141	0.80	3×10^{-3}	141	0.99	7.33	65.7	0.53
					SPP					
50	33.7	0.05	32	0.90	3×10^{-3}	33.9	0.99	1.84	12.7	0.65
100	61.9	0.04	62.2	0.73	8×10^{-3}	62.1	0.99	3.0	31.4	0.46
150	81.3	0.04	84.4	0.69	2×10^{-3}	83.3	0.99	4.51	32.6	0.63
200	103	0.07	102	0.80	4×10^{-3}	103	0.99	5.88	42.3	0.59
250	120	0.06	119	0.85	1×10^{-3}	120	0.99	6.40	49.5	0.60

CHAPTER 3

Comparative assessment of raw *Sterculia villosa* Roxb. shells, derived acid-activated carbon and chelated acid-activated carbon for adsorptive elimination of hexavalent chromium from simulated aqueous setups

The work embodied in this chapter is published in:

CHANDI PATRA, Raj Mohan Naidu Medisetti, Kannan Pakshirajan, Selvaraju Narayanasamy; 2019, "Assessment of raw, acid-modified and chelated biomass for sequestration of hexavalent chromium aqueous solution using *Sterculia villosa Roxb.* Shells"; ***ENVIRONMENTAL SCIENCE AND POLLUTION RESEARCH,*** 26, 23625-23637 **(SPRINGER, IF: 4.223)**

GRAPHICAL ABSTRACT

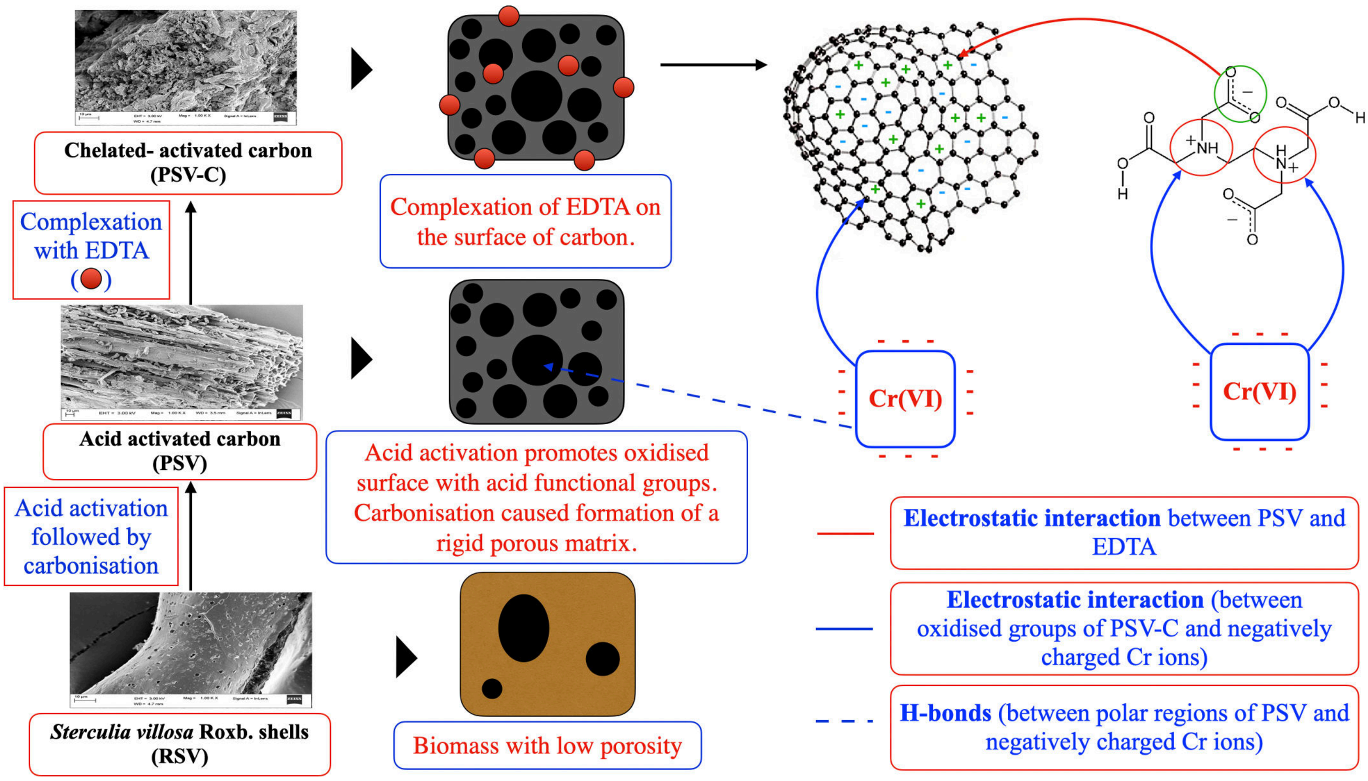

Abstract

This study reveals the efficient adsorption of Cr(VI) species from simulated wastewater using raw (RSV), acid-activated (PSV) and Ethylenediaminetetra acetic acid (EDTA) chelated-activated (PSV-C) *Sterculia villosa* Roxb. shells. Batch optimization experiments were carried out for determining the optimal pH, dosage of adsorbent, initial Cr(VI) concentration and incubation temperature. Physico-chemical alterations in the adsorbents prior and following adsorption of Cr(VI) species were characterized. Equilibrated experimental data at different temperatures was evaluated as a function of time for understanding the isotherm, kinetics and thermodynamics of the adsorption process. Sorption rates for all the adsorbents (RSV, PSV and PSV-C) alternately fitted to the Langmuir isotherm model and Langmuir maximum adsorption capacity for RSV, PSV and PSV-C were found to be 57.78, 163.51 and 188.68 mg/g, respectively. Cr(VI) sorption by these adsorbents followed pseudo-second-order kinetics. Thermodynamic studies suggest endothermic interaction and increased degree of randomness between the adsorbents and Cr(VI) species. Regeneration of the adsorbents following sorption–desorption revealed that it could be reused and recycled several times for Cr(VI) removal from wastewater.

3.1. Materials and methods

The list of chemicals and their role in the current study are mentioned in **Table A.1.** (Appendix) in the supplementary information sheet.

3.1.1. Preparation of adsorbents

Sterculia villosa Roxb. shells were collected locally from the IIT-Guwahati campus and were washed with detergent for dirt and soil removal, followed by drying in an oven at 353 K for 48 h. The shells were then pulverized to fine powder (75–150 nm) and stored for further use (RSV). Acid activation of the pulverized sample was carried out by blending it with 88% ortho-phosphoric acid. The prepared acidified mixture was oven-dried at 473 K for 4–5 h, following which it was carbonized in a muffle furnace at 673 K for 1.5 h. The carbonized sample, thus prepared, was then washed with 1–2% sodium bicarbonate for 24 h followed by further washing with distilled water repeatedly until the pH of the effluent water was the same as that of distilled water. Once desired pH was achieved, the sample was free from any residual acid, following which it was dehydrated in an oven at 373 K for 12–24 h. The acid-activated sample was labelled PSV and stored for further experiments. For chelation, phosphoric acid-activated (PSV) samples were treated with 1 M EDTA in the ratio of 3:10 (adsorbent in gm: EDTA in ml) under stirring conditions for 48 h at room temperature. The treated-activated samples were repeatedly centrifuged at 5000 rpm and washed with distilled water until supernatant turned into a clear solution. The final products were oven-dried and stored and were termed PSV-C.

3.1.2. Batch adsorption experiments

Adsorption experiments in batch mode were performed to study the influences of different physico-chemical parameters, viz. pH of initial solution (2–10), initial Cr(VI) concentration (50–250 mg/l), temperature (303–333K) and dosage of adsorbents (0.2–2 mg/ml). All the sorption experiments were carried out in a thermo-stated shaking incubator (ORBITEK-LE), with a total volume of 25 ml of Cr(VI) solution stirred at fixed rpm for a period of 4 h. Following incubation, the spent adsorbents were collected by filtration, and the concentration of remaining Cr(VI) species in solution was determined by UV-visible spectrophotometry at $\lambda_{max.}$=540 nm with diphenyl carbazide as a complexing agent in an acidic medium (Saranya et al., 2018).

3.1.3. Desorption and recyclability experiments

Desorption attributes to reverse adsorption, which relates to removing adsorbate from the adsorbent's surface using an effective desorption medium. The recyclability of RSV, PSV and PSV-C were evaluated by continuous adsorption-desorption studies. Desorbing agent (0.1 N NaOH) was used for washing the adsorbent's surface after every adsorption step to remove any residual Cr(VI) species left from the previous adsorption run. After desorption, the treated adsorbents were oven-dried and re-used for the next adsorption cycle. All the spent adsorbents were evaluated for desorption studies for up to six cycles.

3.2. Results and discussion

3.2.1. Characterization of the adsorbents

The prepared adsorbents were characterized for pore analysis, surface-elemental analysis, surface morphology and surface functional group analysis. The list of instruments used in the present study with their make and model has been detailed in **Table A.2.** (Appendix).

3.2.1.1. BET pore analysis

The specific surface area of the adsorbents was measured using BET pore analysis. Results thus obtained showed that the raw biomass (RSV) has a specific surface area of 0.442 m^2/g. Activated adsorbent (PSV) showed an elevated specific surface area with 971.97 m^2/g. Chelated samples (PSV-C) also showed an increment in the specific surface area with 788.46 m^2/g compared with RSV. **Table 3.1.** represents the total pore volume (cm^3/g), pore diameter (nm) and specific surface area (m^2/g) for RSV, PSV and PSV-C. BET analysis verified that acid activation followed by pyrolysis increased the specific surface area of the adsorbent (m^2/g) as shown by PSV; there was an increase in the available sites for Cr(VI) adsorption.

Table 3.1. *BET pore analysis of RSV, PSV and PSV-C*

Porosity parameters	**RSV**	**PSV**	**PSV-C**
Total pore volume (cm^3/g)	0.008	0.321	0.387
Pore diameter (nm)	3.307	3.867	3.218
Specific surface area (m^2/g)	0.442	971.971	788.463

3.2.1.2. SEM analysis

SEM analysis signifies the morphological changes of *Sterculia villosa* Roxb. shells subjected to acid activation and pyrolysis followed by chelation. As illustrated in **Figure 3.1. (A, B and C)** RSV shows a rough, dense surface with very low pore density. The acid-activated adsorbent, PSV, presents an enhanced porosity and heterogeneity with increased and distinct visible macro-pores and micro-pores of variable sizes and shapes. The SEM images of activated and chelated adsorbent, i.e. PSV-C revealed a complete heterogeneous surface with increased cavities and intense deep ridges and pores. Conclusively, surface heterogeneity and unevenness increase with acid-activation and it further increases with chelation, which is evident with increased adsorption capacity.

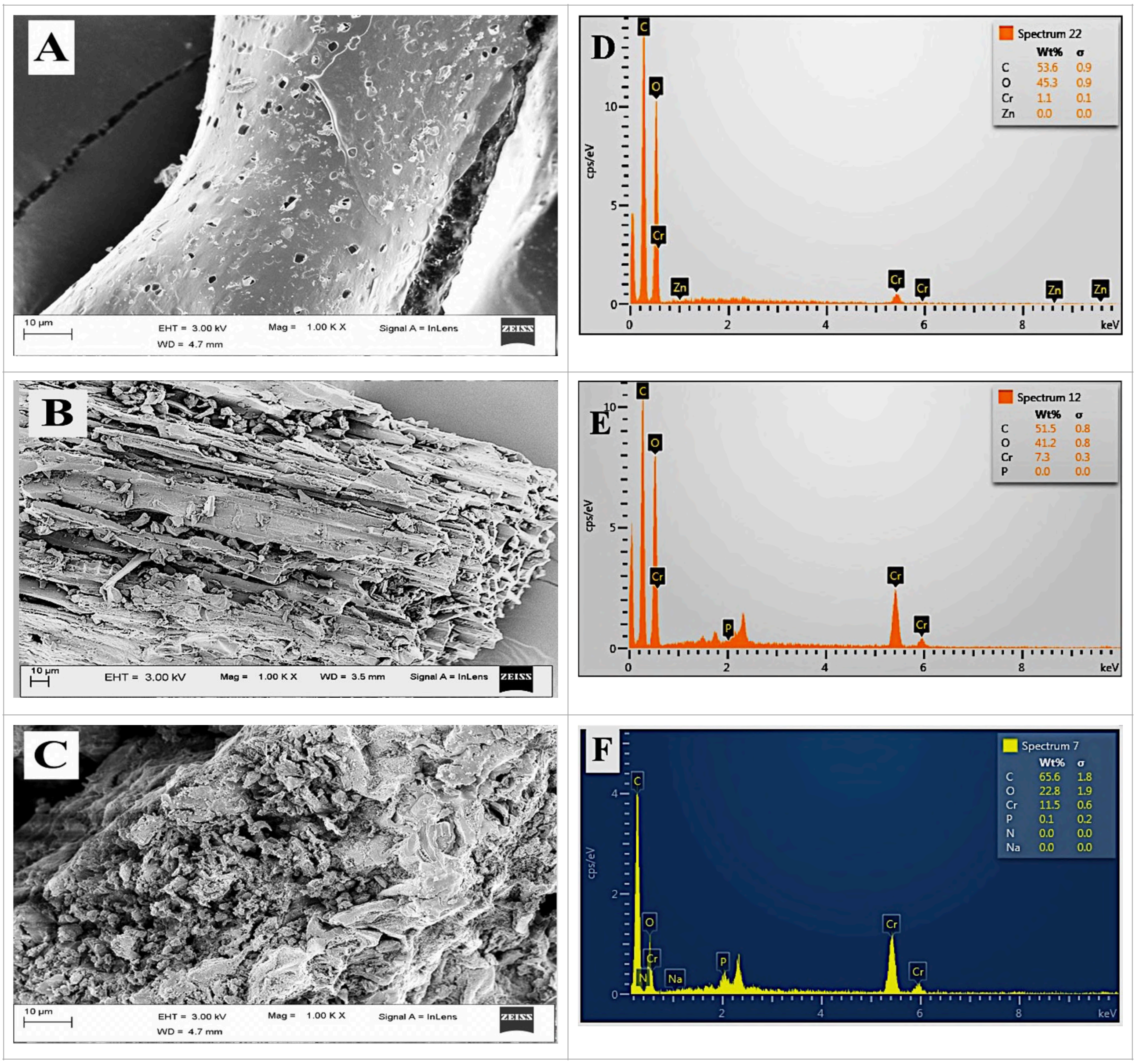

Figure 3.1. *Scanning electron microscopy (SEM) images of **(A)**: RSV; **(B)**: PSV; **(C)**: PSV-C. Energy-dispersive X-ray spectroscopy (EDX) analysis of Cr(VI)-adsorbed **(D)**: RSV; **(E)**: PSV; **(F)**: PSV-C*

3.2.1.3. EDS analysis

Qualitative elemental analysis of the adsorbents after Cr(VI) adsorption was done by EDS analysis, spectra of which is illustrated in **Figure 3.1. (D, E and F)**. Distinct chromium peak heights followed the order: RSV < PSV < PSV-C. This result is likely because Cr(VI) adsorption increases with the increase in specific surface area, as revealed by BET pore analysis in the case of PSV. Chelation with EDTA further showed peak elevation for Cr(VI) uptake as shown by PSV-C. Conclusively, EDS analysis directly confirmed Cr(VI) adsorption over the adsorbent's surface.

3.2.1.4. FT-IR analysis

FT-IR analysis was conducted to determine the surface functional groups of the adsorbents (RSV, PSV and PSV-C) involved in the sequestration of Cr(VI) species from simulated aqueous solutions. Spectral range for FT-IR analysis was taken from 500 to 4000 cm^{-1} for all the adsorbents prior and after Cr(VI) adsorption and is depicted in **Figure 3.2.** A broad band observed in the range 3600–3000 cm^{-1} is easily identified for all the adsorbents (after adsorption) depicting shifts due to hydroxyl groups (–OH) stretch. Peaks can also be reported at 2324 cm^{-1} for RSV–Cr (RSV with Cr after adsorption), 2330 cm^{-1} for PSV–Cr and 2359 cm^{-1} for PSV–C–Cr which corresponds to –CN stretch. Peaks between 1500 cm^{-1} and 1700 cm^{-1} for all the adsorbents following adsorption (RSV–Cr, PSV–Cr, PSV–C–Cr) corresponds to strong C=O (amide) stretch. RSV–Cr shows a major peak between 800 cm^{-1} and 1200 cm^{-1} due to strong C–X (alkyl halide) stretches. PSV–C and PSV–C–Cr showed major peaks in the range 1050 cm^{-1} –1150 cm^{-1} (strong C–OH stretch), 1300 cm^{-1} – 1450 cm cm^{-1} (strong NO_2 stretch), and 800 cm^{-1} –950 cm^{-1} (strong C–X stretch). Presence of NO_2 stretch for chelated adsorbent (PSV–C and PSV–C–Cr) could be possibly due to presence of chelating agent (EDTA). Major variations in intensities of the peaks before and after Cr(VI) adsorption revealed the involvement of the responsible functional groups in the adsorption phenomena. Overall large numbers of peaks were available for PSV–C/PSV–C–Cr which are attributed to the acid-treatment and chelation of the sorbent's surface that resulted in high adsorption capacity of the adsorbents.

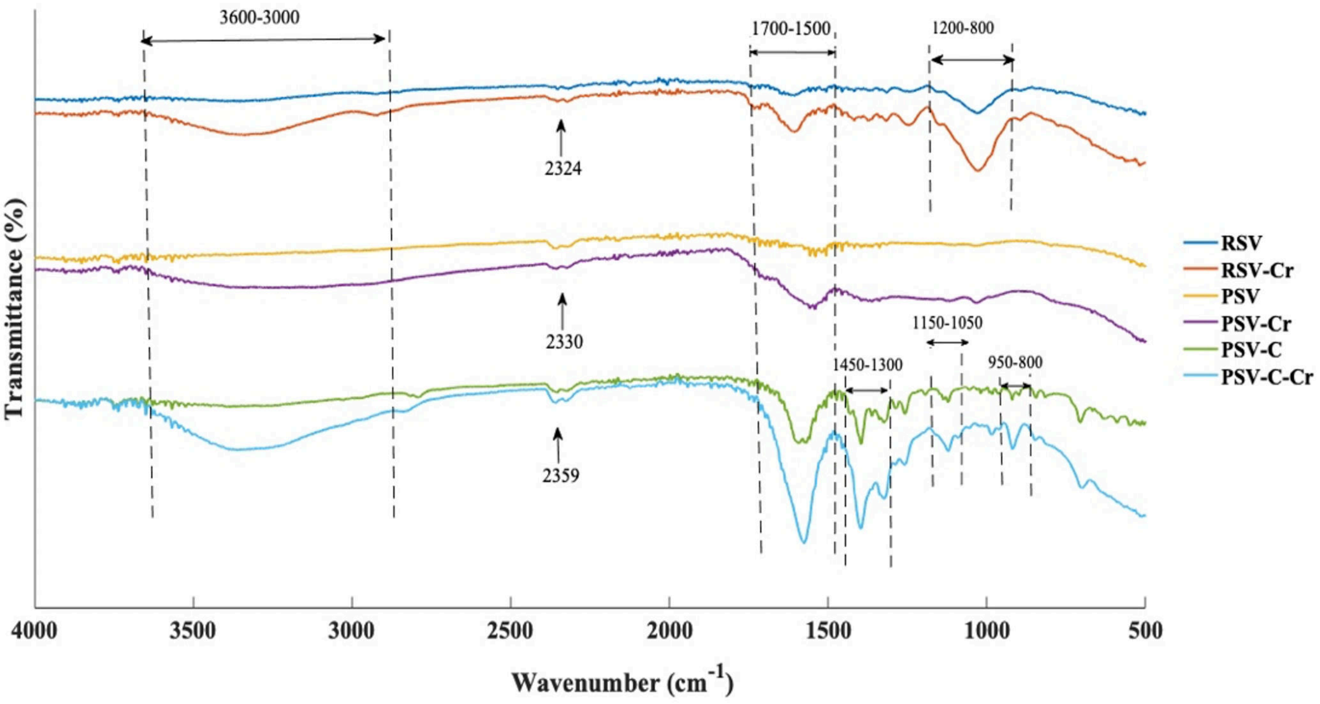

Figure 3.2. *FTIR spectrum showing peaks due to different functional groups on the adsorbents before and after loading units of Cr(VI)*

3.2.2. Effects of various parameters

3.2.2.1. Influence of initial pH of Cr(VI) solution

Initial pH of Cr(VI) aqueous solution is one of the most significant parameter in adsorption due to protonation/de-protonation of the adsorbent's active sites, speciation of the Cr(VI) ions and interactions of the adsorbent with the adsorbate. pH ranging from 2 to 10 was chosen to determine optimum pH for the adsorption of Cr(VI) species by the adsorbents, considering 50 ppm of initial Cr(VI) solution. All the adsorbents showed an efficient adsorption capacity (%) at an initial pH 2.0, as shown in **Figure 3.3. (A)**. At this acidic pH, Cr(VI) predominantly occurs as anionic forms, viz. hydrogen chromate ($HCrO_4^{-2}$), chromate (CrO_4^{-2}) or dichromate ($Cr_2O_7^{-2}$) ions. These anionic Cr(VI) forms show affinity towards the protonated adsorbent surface, thus causing attractive electrostatic pull and favouring the adsorption phenomenon. As the pH increases from 2 to 10, a decline in the adsorption capacity is observed, probably due to a reduction in protonation of the adsorbent surface. Based on the assessment of removal efficiency (%) of Cr(VI) species, pH 2.0 is considered as the optimum pH for all the adsorption phenomena.

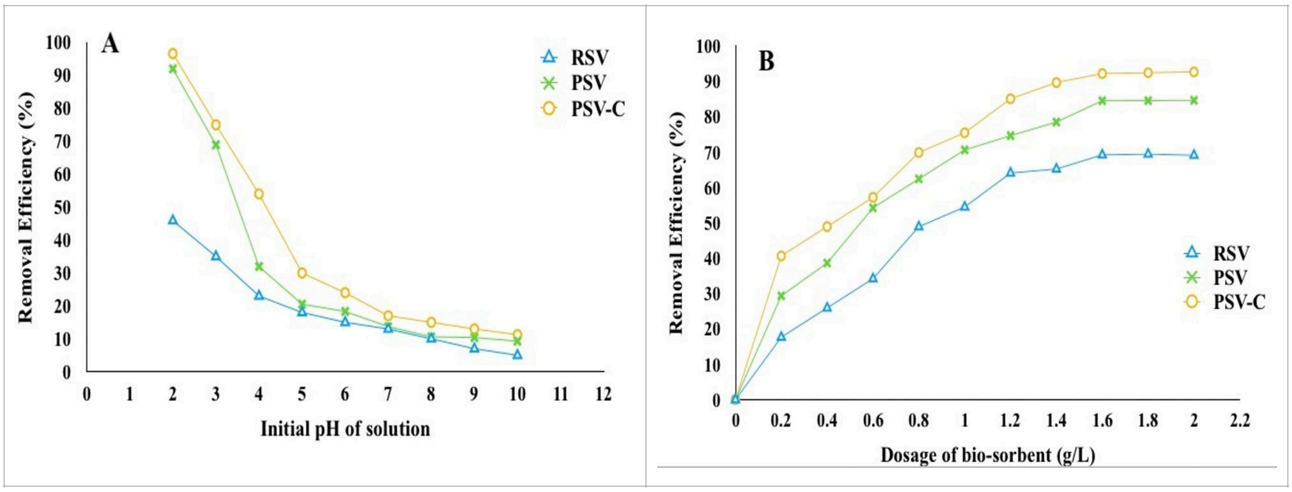

Figure 3.3. *Effect of **(A)**: initial pH of solution, and **(B)**: adsorbents dosage on Cr(VI) removal efficiency*

3.2.2.2. Influence of adsorbent's dosage

Effect of adsorbent's dosage on the sequestration of Cr(VI) species from simulated aqueous solutions was carried out at different adsorbent dosages in the range 0.2–2 mg/ml (with 25 ml of Cr(VI) solution), initial pH 2 and an initial Cr(VI) concentration of 50 mg/l; incubated for 240 min. The effect of adsorbent dosage on Cr(VI) adsorption capacity (mg/g) and efficiency (%) at equilibrium is illustrated in **Figure 3.3. (B)**. The removal efficiency of Cr(VI) species increased with an increase in the adsorbent dosage. Maximum Cr(VI) adsorption efficiency was observed at 2 mg/ml for all the adsorbents viz. RSV (69.12%), PSV (84.65%) and PSV–C (92.70%), which is due to the availability of more vacant binding sites with an increase in the dosage of adsorbents. Further increase in dosage did not help in a further rise in adsorption efficiency since all the Cr(VI) species were adsorbed.

3.2.2.3. Influence of initial Cr(VI) concentration and contact time

Effects of different Cr(VI) initial concentration on the sorption capacity of the adsorbents was studied by considering Cr(VI) concentration in the range 50–250 mg/L, at an optimal adsorbent dosage of 2 mg/ml, initial pH 2 and for an incubation period of 240 min. **Figure. 3.4.** shows the variation of adsorption capacity (mg/g) and percentage removal (%) of Cr(VI) by RSV, PSV and PSV-C at different Cr(VI) initial concentrations. These results verified that Cr(VI) adsorption increases with an increase in the Cr(VI) initial concentration for the first 10–15 min, and it gradually attained equilibrium due to saturation of adsorptive sites. Further increase in the initial Cr(VI) concentration did not show any effect. As the initial concentration was increased the equilibrium adsorption capacity also increased from 25.19 mg/g (50 mg/L) to 47.22 mg/g (250 mg/L) for RSV, 45.83 mg/g (50 mg/L) to 114.38 mg/g (250 mg/L) for PSV and 48.34 mg/g (50 mg/L) to 171.86 mg/g (250 mg/L) for PSV-C.

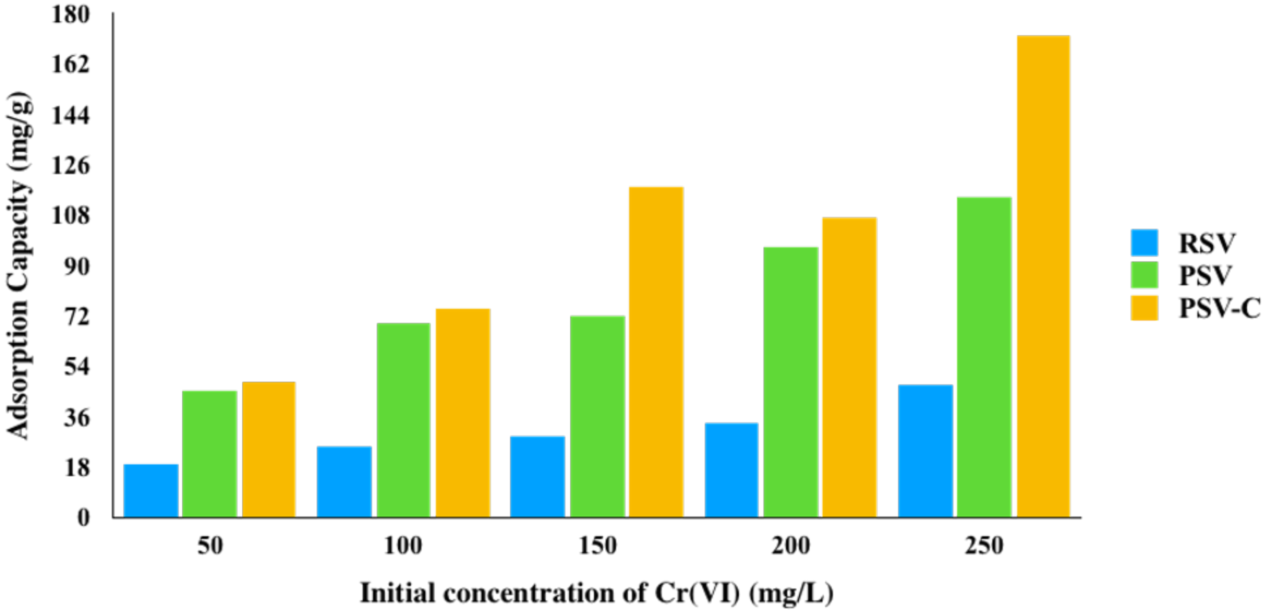

Figure 3.4. *Effect of initial Cr(VI) concentration on Cr(VI) adsorption capacity by RSV, PSV and PSV-C*

3.2.3. Influence of temperature and thermodynamic study of adsorption

Influence of temperature on the adsorption of Cr(VI) by RSV, PSV and PSV-C were examined by varying the temperatures from 303 to 333 K for different initial concentrations of Cr(VI) in the range 50–250 mg/L.

Table 3.2. presents the estimated values of the thermodynamic parameters, i.e. $\Delta G°$, $\Delta H°$ and $\Delta S°$ for different temperature and Cr(VI) concentrations. Negative values of $\Delta G°$ for Cr(VI) adsorption by RSV, PSV and PSV-C confirmed spontaneous and thermodynamic favourability. Positive values of $\Delta H°$ and $\Delta S°$ verified the endothermic nature of adsorption and rise in the degree of disorderness by the adsorbents, respectively.

Table 3.2. *Estimated thermodynamics parameters (ΔG°, ΔH° and ΔS°) for adsorption of Cr(VI) species by RSV, PSV and PSV-C*

C_i (mg/L)	T(K)	RSV			PSV			PSV-C		
		ΔG° (kJ/mol)	**ΔH° (kJ/mol)**	**ΔS° (J/molK)**	**ΔG° (kJ/mol)**	**ΔH° (kJ/mol)**	**ΔS° (J/molK)**	**ΔG° (kJ/mol)**	**ΔH° (kJ/mol)**	**ΔS° (J/molK)**
50	303	−16.19	38.56	180.8	−24.92	65.76	300.65	−21.84	44.96	224.73
	313	−17.79			−27.32			−26.58		
	323	−18.14			−30.98			−27.15		
	333	−19.94			−30.22			−26.48		
100	303	−14.66	17.06	105.50	−19.39	48.00	221.72	−22.13	13.68	114.79
	313	−15.87			−20.63			−20.30		
	323	−15.88			−21.68			−21.23		
	333	−16.35			−23.86			−23.27		
150	303	−13.67	21.84	118.12	−18.71	21.38	131.73	−19.84	15.98	116.46
	313	−15.07			−19.10			−18.55		
	323	−15.03			−19.55			−19.24		
	333	−15.96			−20.72			−20.56		
200	303	−13.35	22.62	120.47	−17.15	21.80	128.86	−19.22	3.35	72.60
	313	−15.18			−18.15			−17.69		
	323	−15.79			−18.45			−18.17		
	333	−15.37			−19.23			−19.06		
250	303	−12.76	23.33	119.20	−16.36	20.38	121.55	−17.75	8.44	85.96
	313	−13.77			−17.40			−17.63		
	323	−13.82			−17.40			−17.19		
	333	−15.09			−18.40			−18.42		

3.2.4. Isotherm studies

Various isotherms models, viz. Langmuir, Freundlich, Dubinin-Radushkevich, Frumkin and Redlich-Peterson were used to describe the equilibrium data obtained between the adsorbate species and adsorbent molecules. These isotherms have been detailed in **Table A.3.** (Appendix). **Table 3.3.** presents the different isotherm parameters estimated in this study along with the coefficient of determination (R^2) values.

Table 3.3. *Estimated adsorption isotherm model parameters, constants and coefficient of determination (R^2) for adsorption of Cr(VI) species by RSV, PSV and PSV-C at different temperatures (K)*

Isotherm Models		303 K			313 K			323 K			333 K		
		RSV	**PSV**	**PSV-C**	**RSV**	**PSV**	**PSV-C**	**RSV**	**PSV**	**PSV-C**	**RSV**	**PSV**	**PSV-C**
Langmuir	Q_L	40.49	106.38	188.68	53.53	144.42	120.68	56.81	135.85	130.56	57.78	163.51	139.52
	K_L	0.02	0.12	0.06	0.04	0.05	0.07	0.03	0.10	0.08	0.01	0.09	0.23
	R^2	0.99	0.99	0.99	0.99	0.99	0.99	0.99	0.99	0.99	0.99	0.99	0.99
Freundlich	K_f	6.62	39.86	25.93	11.63	19.80	24.62	8.95	29.36	46.68	3.25	31.32	49.29
	n	3.23	5.26	2.33	3.72	2.51	3.15	3.08	5.24	5.05	1.67	2.80	6.25
	R^2	0.99	0.95	0.89	0.99	0.95	0.98	0.99	0.90	0.99	0.99	0.93	0.96
D-R	Q_{DR}	31.50	89.65	142.18	43.61	109.16	97.80	44.63	113.97	114.84	60.72	127.64	118.60
	K_{DR}	81.02	0.81	7.12	43.81	12.86	8.03	61.42	5.80	18.52	126.87	37.75	0.45
	E_{DR}	0.08	0.79	0.27	0.11	0.20	0.25	0.09	0.29	0.16	0.06	0.12	1.06
	R^2	0.84	0.78	0.96	0.85	0.93	0.91	0.89	0.95	0.90	0.91	0.92	0.89
Frumkin	K_{FK}	13.64	1.04	0.04	16.71	1.34	2.63	13.96	1.03	4.01	3.07	0.12	0.05
	α_{FK}	6.65	6.84	8.23	5.37	6.20	5.83	5.71	6.35	5.27	7.51	7.64	8.47
	R^2	0.99	0.96	0.95	1.00	0.97	0.98	1.00	0.96	0.99	0.99	0.95	0.90
R-P	K_{RP}	3.08	33.77	12.07	3.93	7.56	12.22	2.34	12.99	16.62	1.06	20.03	36.88
	Q_{RP}	0.29	0.59	0.06	0.17	0.06	0.17	0.08	0.10	0.18	0.01	0.20	0.30
	g	0.77	0.88	1.00	0.85	0.96	0.90	0.88	1.00	0.93	0.97	0.90	0.98
	R^2	0.99	0.99	0.99	0.99	0.99	0.99	0.99	0.99	0.99	0.99	0.99	0.99

The Langmuir isotherm model gave the best fit for the Cr(VI) species adsorption onto the adsorbents; RSV, PSV and PSV-C at all temperatures from 303 to 333 K. Thus, a monolayer formation between Cr(VI) species and the adsorbents can be concluded. The theoretical maximum adsorption capacity (Q_L) as determined by the Langmuir model for RSV and PSV were 57.78 mg/g and 163.51 mg/g, respectively, at 333 K and 188.68 mg/g for PSV-C at 303 K. Hence, it can be further concluded that acid activation of the raw adsorbent caused an increment in monolayer adsorption capacity. Monolayer adsorption capacity further increased with chelation of the acid-activated sorbent. The possible reason for the decline in adsorption capacity of PSV-C with the temperature rise is due to the splitting of EDTA molecules from the adsorbent surface at higher temperatures. Separation factor values for all the adsorbents were between 0 and 1 (for all temperatures), thus indicating a favourable monolayer adsorption process as suggested by the Langmuir isotherm model. High adsorption capacities and low separation factor values suggest RSV, PSV and PSV-C as potent adsorbents for Cr(VI) species removal from aqueous solution. Coefficient of determination (R^2) values for Freundlich and Dubinin-Radushkevich isotherm models indicates that the fitness due to these models was poor compared with that of the Langmuir adsorption isotherm. However, values for the Freundlich isotherm model (n) were greater than 1, thus confirming favourable adsorption phenomenon by all the adsorbents at all temperatures. Frumkin isotherm model showed a better fit than Freundlich and Dubinin-Radushkevich isotherm model for all temperatures. Interaction parameters (α_{FK}) values were found positive, and thus it can be concluded that some attractive forces exist between the adsorbate species. Redlich-Peterson isotherm model showed relatively higher R^2 values, indicating that it is pretty accurate in predicting the Cr(VI) sorption phenomenon onto the adsorbents. Values for g (Redlich-Peterson exponent) are almost near to one for all the temperatures, suggesting that interaction between Cr(VI) with RSV, PSV and PSV-C follows Langmuir isotherm model.

3.2.5. Kinetic parameters

In order to evaluate the Cr(VI) sorption mechanism involved and the rate-limiting step in the interaction between Cr(VI) species and the adsorbents, various kinetic models like pseudo-first-order, pseudo-second-order and intra-particle diffusion models were applied to the kinetics data. These kinetic models have been detailed in **Table A.4.** (Appendix). Parameters estimated from these kinetic models and their coefficient of determination values (R^2) are presented in **Table 3.4.** R^2 values due to the pseudo-first-order model are relatively low, and thus the relevance of pseudo-first-order with the adsorption of Cr(VI) species by RSV, PSV and PSV-C are minimal. Coefficient of determination (R^2) values for the pseudo-second-order kinetics were comparatively high, i.e. $R^2 > 0.99$, and hence pseudo-second-order kinetic model gave the best fit for Cr(VI) removal by the adsorbents (RSV, PSV and PSV-C). Experimental adsorption capacities ($q_{e\ exp.}$) were also similar to the theoretical adsorption capacities estimated by the pseudo–second–order model, as shown in **Table 3.4.** These results confirm that the rate-limiting step for adsorption of Cr(VI) species by RSV, PSV and PSV-C is governed by chemisorption. R^2 values due to the intra-particle diffusion model are the least, thus showing a very poor fitness of the model with the experimental data and, hence, it could be concluded that intra-particle diffusion is not the only rate-determining step.

Table 3.4. *Estimated kinetic parameters and constants and coefficient of determination (R^2) for the adsorption of Cr(VI) species using RSV, PSV and PSV-C*

C_i (mg/L)	$Q_{e\ Exp.}$ (mg/g)	Pseudo-first order			Pseudo-second order			Intra-particle diffusion		
		K_1 (1/min)	Q_e (mg/g)	R^2	K_2 (g/mg min)	Q_e (mg/g)	R^2	K_{id} (mg/g min$^{0.5}$)	C (mg/g)	R^2
RSV										
50	19.11	0.04	20.39	0.55	0.002	21.26	0.99	0.95	6.63	0.79
100	25.19	0.03	37.53	0.63	0.002	27.11	0.99	1.20	8.78	0.81
150	28.65	0.03	43.43	0.68	0.001	31.86	0.99	1.48	8.45	0.89
200	33.42	0.03	47.59	0.71	0.002	36.00	0.99	1.49	13.08	0.85
250	34.22	0.01	1.18	0.22	0.007	35.04	0.99	0.73	25.31	0.26
PSV										
50	44.96	0.02	19.15	0.72	0.001	47.50	0.99	1.06	29.40	0.97
100	69.13	0.02	28.55	0.95	0.001	73.02	0.99	2.44	36.35	0.89
150	94.75	0.01	13.65	0.70	0.002	95.90	0.99	2.04	67.94	0.47
200	96.38	0.02	39.59	0.97	0.001	99.27	0.99	2.76	57.02	0.91
250	101.38	0.01	9.53	0.56	0.003	103.93	0.99	2.36	72.53	0.50
PSV-C										
50	44.33	0.01	7.91	0.78	0.004	45.12	0.99	0.94	31.84	0.77
100	89.71	0.01	13.70	0.69	0.002	90.44	0.99	2.06	62.26	0.53
150	118.04	0.01	15.37	0.83	0.002	120.53	0.99	1.51	97.98	0.85
200	149.26	0.02	19.97	0.73	0.001	152.51	0.99	3.88	100.16	0.50
250	159.86	0.01	24.00	0.70	0.002	160.60	0.99	3.17	117.70	0.45

3.2.6. Regeneration and reusability studies

Regeneration and reusability potential of the adsorbents for Cr(VI) species removal by RSV, PSV and PSV-C were examined. **Figure 3.5.** shows the Cr(VI) adsorption efficiency following successive regeneration for 6 cycles. All the adsorbents were regenerated by desorption (washing) with 0.1 N NaOH solution. After every desorption cycle, the adsorbents were oven-dried and then again used for Cr(VI) adsorption studies. Cr(VI) removal efficiency by RSV gradually reduced in the order of 51.17%, 39.65%, 23.23%, 16.81%, 11.39% and 3.97%. After the sixth cycle, further regeneration and resorption was found to be irrelevant. Similarly, in case of PSV, the Cr(VI) adsorption efficiency was in the order of 72.65%, 43.93%, 38.20%, 32.47%, 26.74% and 11.07%. In case of PSV-C, Cr(VI) adsorption efficiency was in the order 84.54%, 68.82%, 58.38%, 37.95%, 22.13% and 12.88%. Successive desorption/regeneration and adsorption studies reveal that the adsorbents RSV, PSV and PSV-C can be efficiently reused up to certain cycles. This decline in the adsorption efficiency with successive cycles is probably due to structural modifications on the adsorbent's surface. Another probable reason could be that some Cr(VI) ions are still retained in the pores of the adsorbents that are not desorbed even after the washing step. From these results of regeneration and reusability studies with RSV, PSV and PSV-C, it can be concluded that the adsorbents can be well reused up to a certain number of sorption–desorption cycles, which is an important factor sustaining the long-term use of these adsorbents for Cr(VI) removal from wastewater.

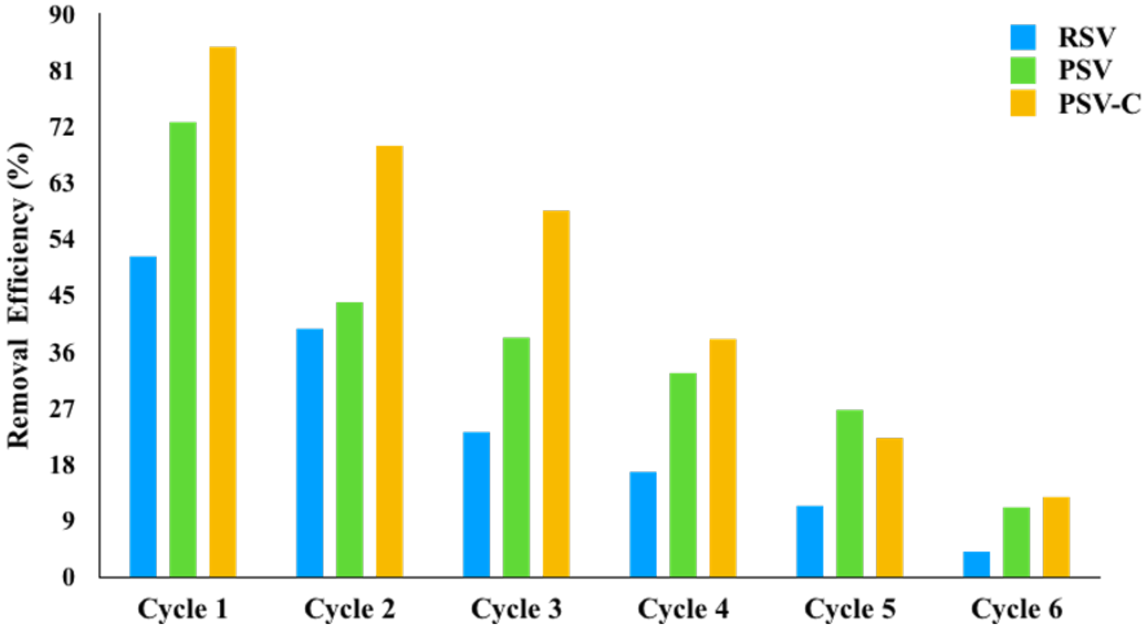

Figure 3.5. *Removal efficiency of Cr(VI) by the adsorbents at the end of six sorption–desorption cycles*

3.3. Significant findings

Sterculia villosa Roxb. shells were exploited in raw (RSV), and acid-activated (PSV) forms to increase its efficiency towards the removal of Cr(VI) species from aqueous solution. In order to further enhance the Cr(VI) sorption capacity of the acid-activated adsorbent, PSV was chelated using 1 M EDTA to form a chelated acid-activated adsorbent (PSV-C). The adsorption capacity for the raw adsorbent increased with acid activation, which further increased with chelation. The removal capacities and efficiencies of the adsorbents (RSV, PSV and PSV-C) were highly influenced by parameters, such as pH of the aqueous solution, adsorbent dosage, initial chromium concentration in aqueous solutions and incubation temperature. Cr(VI) sorption isotherm study revealed the Langmuir model as the best fit for all the adsorbents (RSV, PSV and PSV-C) at different temperatures, and the kinetics of Cr(VI) sorption followed the pseudo-second-order model for all the adsorbents. Thermodynamically, Cr (VI) adsorption by RSV, PSV and PSV-C was spontaneous and favourable. Interaction between the Cr(VI) species and the adsorbents was endothermic and showed an increase in the degree of randomness. Desorption and re-use of the adsorbents indicated its suitability for reusability up to some cycles following regeneration of the loaded adsorbent by desorption using NaOH.

CHAPTER 4

Cationic surfactant modification on biomass derived acid-activated carbon for adsorptive elimination of anionic azo dyes

The work embodied in this chapter is published in:

CHANDI PATRA, Rishabh Gupta, Das Bedadeep, Selvaraju Narayanasamy; 2020, "Surface treated acid-activated carbon for adsorption of anionic azo dyes from single and binary adsorptive systems: A detail insight"; ***ENVIRONMENTAL POLLUTION,*** *266, 115102* **(ELSEVIER, IF: 8.071)**

GRAPHICAL ABSTRACT

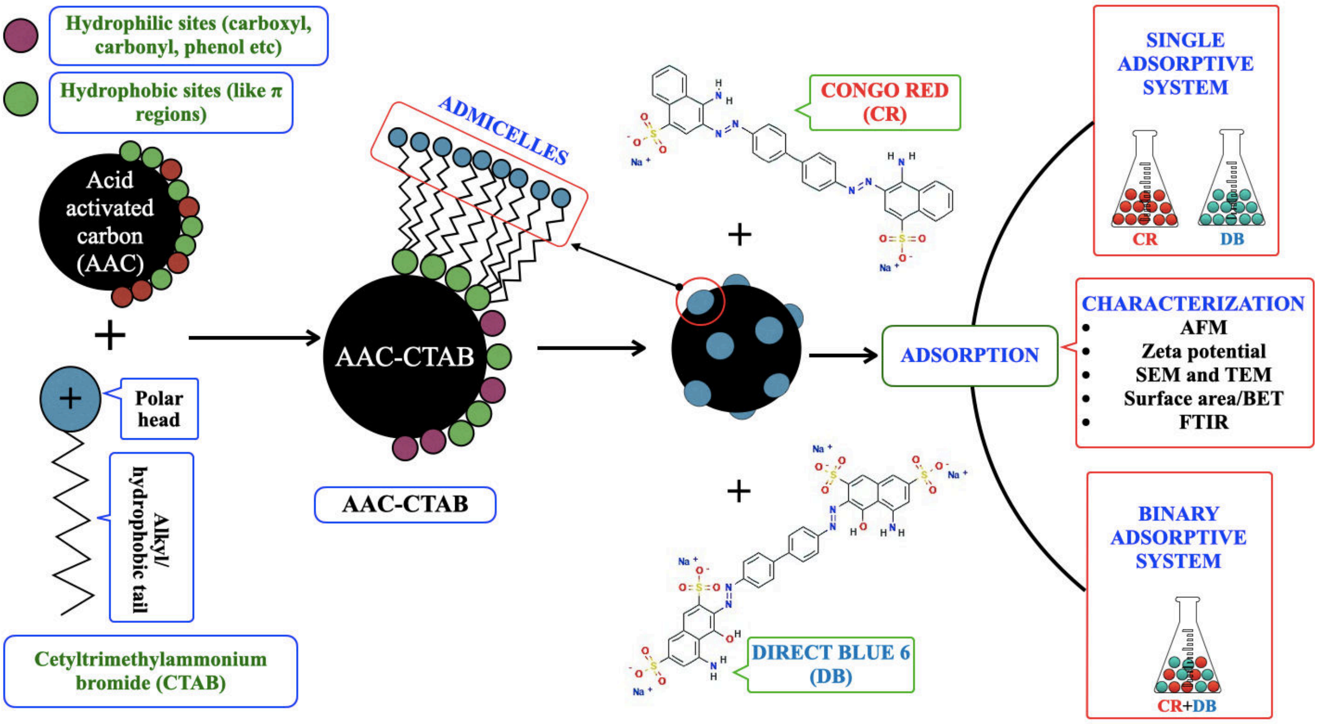

Abstract

The current study deals with the surface modification of acid-activated carbon (prepared from *Pongamia pinnata* shells) with Cetyltrimethylammonium bromide (CTAB) and its role as an adsorbent in eliminating anionic azo dyes viz. Congo red (CR) and Direct blue 6 (DB) from single and binary adsorptive systems. Binary adsorptive system involved the synergistic and antagonistic influence of one dye over the adsorption of other dye. Physico-chemical alterations due to surfactant modification and post adsorption were studied using atomic force microscopy (AFM), Zeta Potential, scanning electron microscopy (SEM), Energy-dispersive X-ray spectroscopy (EDS), surface area analysis and Fourier-transformed infrared spectroscopy (FT-IR). Process parameters influencing efficient adsorption of CR and DB species viz. initial pH of dye solution, adsorbent dosage, incubation temperature and initial concentration of dye species were optimized. Sorbate-sorbent interaction studies for a single adsorptive system revealed sorbate's monolayer formation over the adsorbent's surface and the involvement of chemisorption, as verified by the Langmuir isotherm model and pseudo-second-order model, respectively. Langmuir maximum adsorption capacity of the adsorbent was 555.56 mg/g for CR and 625.00 mg/g for DB. Meanwhile, the competitive Langmuir model verified that both CR and DB had an antagonistic/competitive effect over each other's adsorption for a binary adsorptive system. Thermodynamic analysis revealed the adsorptive process as exothermic, spontaneous and thermodynamically favourable with an elevated degree of dis-orderedness. Co-existing cations and anions has a nominal effect on the adsorption capacity of dyes. Recyclability studies verified a modest efficiency of 62.52% for CR and 50.47% for DB species after the 4th adsorption-desorption cycle, thus affirming its recyclability potential. Phytotoxic assay affirmed the effectivity of the adsorbent in adsorbing dye species from aqueous solutions using *Vigna mungo* seeds as the model.

4.1. Materials and methods

The list of chemicals and their role in the current study are mentioned in **Table A.1.** (Appendix).

4.1.1. Synthesis of adsorbent

Acid activated carbon (AAC) was prepared from *Pongamia pinnata* shells, and its detailed explanation has been reported in Chapter 2. Acid activation was done by treating the precursor with 88% ortho-phosphoric acid in 1:2.5 w/v (biomass/acid) proportion followed by high-temperature carbonisation at 673 K, resulting to form acid activated carbon (AAC). The choice of optimised CTAB concentration for surface modification of activated carbon was based on the critical micellar concentration (CMC) of CTAB for a fixed dosage of acid-activated carbon (1 gm), as shown in **Figure 4.1.**

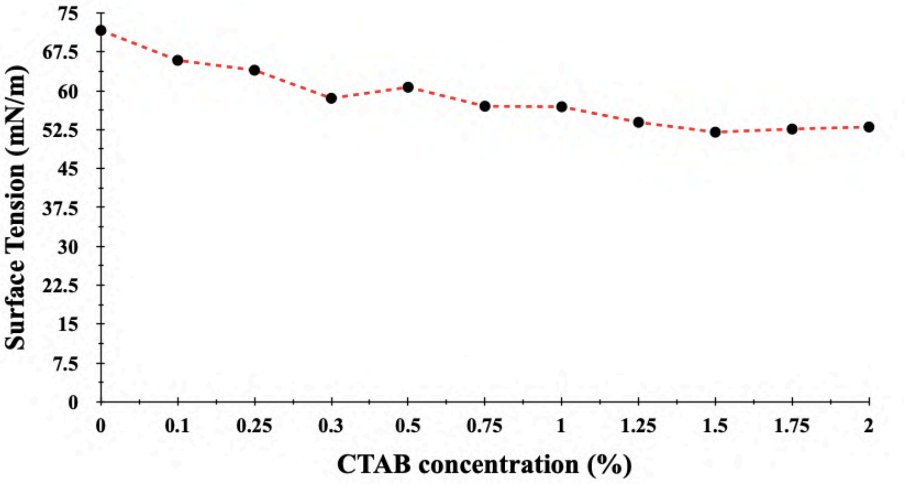

Figure 4.1. *Effect of variable CTAB concentrations over the surface tension of distilled water with acid activated carbon*

For CTAB modification, 1 gm of acid-activated carbon was selected as the required standard activated carbon dosage for CTAB modification, and it was added to a series of variable concentrations of 20 mL CTAB solution (0.25% to 1%); followed by mixing in a shaker incubator at 313 K in fixed rpm for 24 h. The choice of incubation temperature was based on Blin et al., 2002. The mixture was rinsed with distilled water to eliminate any remnant CTAB species. The final filtered mixture was oven-dried at 353 K and stored. Optimised CTAB concentration for activated carbon surface modification was based on Congo red (CR) and Direct blue 6 (DB) adsorption efficiencies by CTAB modified activated carbon with all selected CTAB concentrations as presented in **Figure 4.2 (A).**

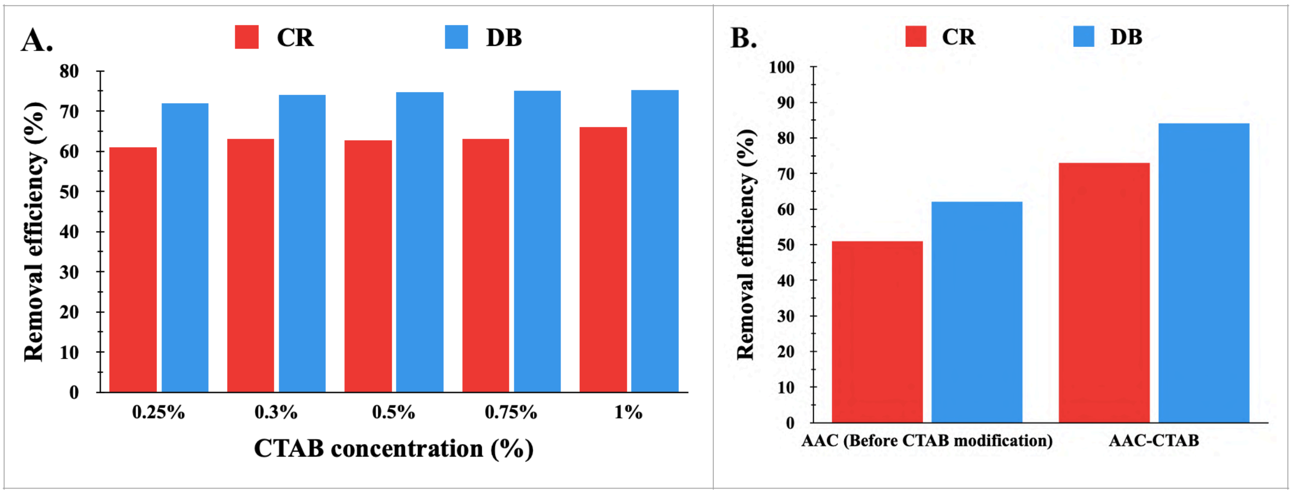

***Figure 4.2. (A)**: Removal efficiencies of CR and DB by acid activated carbon modified with variable CTAB concentrations; **(B)**: Comparative removal efficiencies of Congo red (CR) and Direct blue 6 (DB) using acid activated carbon before and after CTAB modification*

From the available data, 0.25% CTAB concentration was chosen as the optimised CTAB concentration for modifying 1 gm of activated carbon, and thus it was labelled AAC-CTAB. **Figure 4.2. (B)** depicts comparative removal efficiencies of anionic azo dyes (CR and DB) using acid activated carbon (AAC) before and after CTAB modification (AAC-CTAB).

It is evident that surfactant modification has enhanced dye adsorption efficiencies compared to untreated acid activated carbon. **Figure 4.3.** summarises the current work involving the preparation of CTAB modified AAC i.e. AAC-CTAB and its adsorptive interaction with Congo red (CR) and Direct blue 6 (DB).

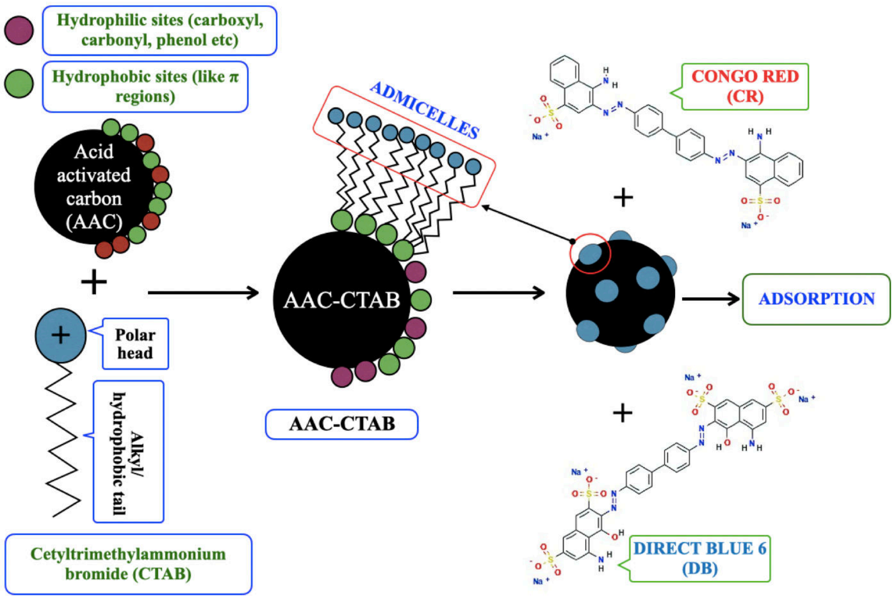

***Figure 4.3.** Schematic summary of the adsorbent (AAC-CTAB) preparation and targeted adsorbate dye species (CR and DB)*

4.1.2. Adsorption experiments and assessment

Various process parameters directly influence the adsorption of the adsorbate (anionic azo dyes species) by the adsorbent (AAC-CTAB). These include initial pH of dye (CR and DB) solution (2.0–10.0), initial dye concentration (50–250 mg/L), incubation temperature (293–323K) and variable dosages of AAC-CTAB (0.25–1.25 mg/mL). The choice of these parameters was based on several reported articles, as they influence the adsorption capabilities of the adsorbent. All the interaction experiments were incubated in a thermo-stated shaker (ORBITEK-LE), at a specific rotation speed of 150 rpm, for a duration of 12 h. The choice of agitation speed was based on the fact that it should be sufficient enough (neither too high nor too low) to ensure the availability of all the binding sites for effective adsorption. For the current study, 150 rpm was found sufficient (based on earlier studies for similar powdered absorbent) for ensuring proper adsorbate-adsorbent interaction, and thus all the experiments were carried out with the same agitation speed. The choice of contact time was initially based on periodic analysis of dye removal till the adsorption values were constant, especially for studies involving optimisation of pH of adsorbate and dosage of adsorbent. An incubation period of 12 h was considered for the rest of the studies.

4.1.3. Single and Binary adsorption system studies

Single adsorptive systems refer to aqueous systems having one dye with the adsorbent, while binary adsorptive systems refer to aqueous systems having both the dye species (CR and DB) at the same time with the adsorbent. All single and binary adsorptive systems were studied using batch experiments for equilibrium time. Experimental data obtained from single adsorption systems were used to study the sorbate-sorbent interactions using two-parameter and three-parameter isotherm models. Detailed theory of all the adsorption isotherms has been described in **Table A.3.** (Appendix).

It was also used to study the kinetics of sorbate-sorbent interactions using models like pseudo-first-order, pseudo-second-order and intra-particle diffusion. Detailed theory of all the kinetics models has been described in **Table A.4.** (Appendix). Thermodynamics involved in the sorbate-sorbent interactions were also studied at different temperatures.

For binary adsorption systems, which involved the co-existence of CR and DB in one system, were investigated with variable working concentrations of 50+50, 100+100, 150+150, 200+200 and 250+250 mg/L. Langmuir competitive isotherm models were applied to investigate the equilibrium data of binary adsorption systems and analyse the antagonistic/competitive effect of one dye over the adsorption of other dye (Manjunath et al., 2020). For binary studies, a common pH of 2.0 was maintained (based on optimised pH for the single adsorptive system), and a dosage of 1 mg/ml for AAC-CTAB was maintained for all the binary initial concentrations mixture.

4.1.4. Influence of co-existing ions

Realtime wastewater may contain several cationic or anionic salts, which may influence the uptake of dye pollutants by the adsorbent. Thus, in order to understand the influence of such co-existing cations and anions; batch adsorption experiments were carried out in the presence of cationic salts of ferric (Fe^{+3}), copper (Cu^{+2}), cobalt (Co^{+2}) and zinc (Zn^{+2}) and anionic salts of sulphate (SO_4^{-2}), chloride (Cl^{-1}), nitrate (NO_3^{-2}) and carbonate (CO_3^{-2}). The effect of co-existing ions was studied with 100 mg/L of CR and DB solutions, each mixed with 100 mg/L of cationic and anionic salt solutions individually at a 1:1 ratio. The pH of all the batch setups were kept equal to that of distilled water with fixed dosages of AAC-CTAB in each one of them. This was done to ensure uniformity for relative analysis of the mass transfer of the sorbate molecules over the adsorbent's surface under the influence of ionic salts.

4.1.5. Desorption and recyclability studies

Recyclability assessment of AAC-CTAB in removing CR and DB was done via repeated cycles of adsorption followed by desorption with 0.1N NaOH (desorbing agent). After a single cycle of adsorption experiment, the adsorbent was treated with 0.1 N NaOH for shedding out the pre-adsorbed CR and DB species, followed by continuous rinsing with distilled water to wash out the excessive NaOH. After rinsing, the adsorbents were dried and recycled for successive adsorption cycles. Adsorption-desorption and recycle experiments were carried out till the adsorption capability of AAC-CTAB was minimal.

4.1.6. Phytotoxicity assay

Vigna mungo (black gram) seeds were used for early growth assay as phytotoxic assessment of adsorptive removal of CR and DB in single and binary adsorptive systems. *Vigna mungo* seeds were selected due to their easy availability since it is a typical agricultural plant in North-East India. The phytotoxicity assessment assays were conducted as per prescribed guidelines mentioned in USEPA, 1996 (Naraginti and Yong, 2019; Prasad and Rao, 2013; Dutta et al., 2018) with some additional modifications. Initially, the seeds were washed with 1% Sodium Hypochlorite (NaClO) solution followed by rinsing with distilled water and then dried at room temperature. Once dried, the seeds were planted on cotton soaked dye solution without adsorption treatment (control sample plates), dye solution after adsorption treatment (test sample plates) and distilled water (blank plate). 50 mg/L of CR and DB at pH 2.0 were taken for single and binary adsorption systems, and a fixed dosage of AAC-CTAB was taken for all the sets of experiments. The seeds were allowed to germinate in the dark for four days at room temperature, after which the root length was measured and reported.

4.2. Results and discussion

4.2.1. Adsorbent characterization

The list of instruments used for characterisation in the present study with their make and model has been detailed in **Table A.2.** (Appendix).

4.2.1.1. Atomic force microscopy analysis

Atomic force microscopy captured the surface modifications caused by CTAB modifications over acid activated carbon, as shown in **Figure 4.4 (A, B).** In contrast to the surface of the original acid activated carbon (AAC), the surface of the CTAB modified acid activated carbon (AAC-CTAB) showed conical-shaped aggregates, as depicted in **Figure 4.4 (B).**

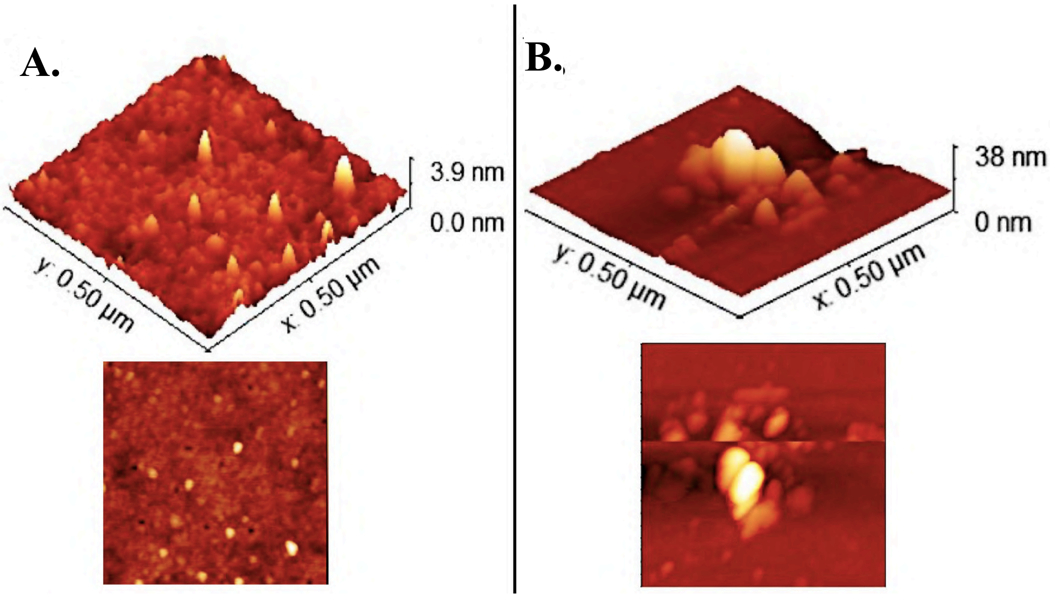

***Figure 4.4.** AFM image of **(A)** Acid activated carbon (AAC); and **(B)** AAC after CTAB surfactant modification (AAC-CTAB)*

The height of these conical aggregates elevated from 3.9 nm (AAC) to 38 nm on the CTAB-modified acid activated carbon surface. Activated carbon possess hydrophobic sites which exhibit favourable hydrophobic interactions with the hydrophobic alkyl tails of CTAB under the control of entropic and enthalpic favourability (Ntakirutimana et al., 2019). These interactions cause the

CTAB molecules to form a circular plane on the surface of the activated carbon, with the hydrophobic (alkyl) tails directing inwards and the hydrophilic (head) group directing outwards. However, with the increase in surfactant concentration, increased hydrophobic interactions among alkyl tails and electrostatic repulsions among cationic heads result in stacking of tails and upward tilting of polar heads, resulting in conical shaped micelle formation (Wang et al., 2018; Tang et al., 2017) as illustrated in **Figure 4.4 (A, B).**

4.2.1.2. Zeta potential of adsorbent

Zeta potential refers to the potential of the stable stationary layer of fluid on the adsorbent's surface relative to the potential of the fluid dispersion medium. Zeta potential (mV) of the adsorbent was measured within the initial pH range of 2.0-10.0 of the aqueous dispersion medium, maintaining the same pH range for the adsorbent's surface. The Zeta potential of activated carbon (AAC) and AAC-CTAB as the function of dispersed solution pH is represented in **Figure 4.5.** AAC showed a positive zeta potential value at pH 2.0. Beyond that, AAC showed negative zeta-potential values from pH 3.0 to 10.0. The acid treatment of the lignocellulosic precursor led to an oxidised surface due to oxygen-containing functional groups, which attributed to very low isoelectric point values (pH_{IEP} 2.0-3.0). Similarly, the AAC-CTAB surface too showed positive zeta potential values from pH 2.0-4.0, beyond which it showed negative zeta potential values from pH 4.5-10.0. However, the isoelectric point (pH_{IEP}) for AAC-CTAB was found at pH 4.05 (4.0-4.5).

Acid activated carbon (AAC) surface has weak acidic groups providing it with a negative charge, which further attracts excessive H^+ ions and creates positive potential as compared to the aqueous dispersion phase. This was the reason for positive zeta potential values at low pH for both AAC and AAC-CTAB. However, with elevated pH values, the number of OH- ions also increased, thus neutralising the positively charged stationary phase over the adsorbent's surface and thus tends to negative zeta potential values. As shown in **Figure 4.5.**, AAC-CTAB has positive zeta potential values from pH 2.0-4.0 as compared to AAC (2.0-3.0) and has higher pH_{IEP} values than AAC. This was due to surfactant modification of acid-activated carbon surface that provided it with positively charged nitrogen heads and thus pertaining it with an extra positive charge (White et al., 2007; de la Cruz et al., 2012).

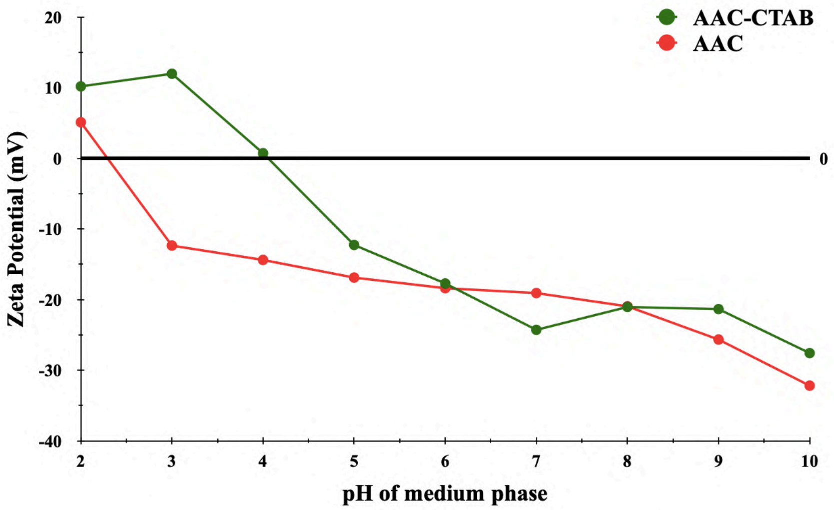

Figure 4.5. *Zeta potential of AAC and AAC-CTAB at different pH*

The influence of zeta potential values over AAC-CTAB's adsorption efficiencies has been represented in **Figure 4.6.** It was understood by combining the studies for the influence of initial pH of dye solution and zeta potential of AAC-CTAB at variable pH of dispersion phase. **Figure 4.6.** shows three distinctive regions with regards to the effect of zeta potential values over the adsorption efficiencies of AAC-CTAB. Such variations of adsorption efficiencies w.r.t. zeta potential can be concluded into the following as per Dai, 1994:

- In the first region, zeta potential values range from 0 mV to +12 mV (which lies in between pH 2.0 to 4.0), corresponding to which the adsorption efficiencies for both CR and DB is relatively high (between 70% to 85%). In this region, there are electrostatic attraction forces between the negatively charged anionic azo dye species (CR and DB) and the positively charged adsorbent (AAC-CTAB) corresponding to increased zeta potential values.
- In the second region, potential values range from 0 to -20 mV (pH range from 4.0 to 8.0); the corresponding adsorption efficiencies for both CR and DB remains almost unchanged. Here dispersion forces between the dye species and AAC-CTAB dominate, resulting in constant adsorption efficiencies.
- In the third and final region (where zeta potential values are less than -30 mV), the adsorption efficiencies are the least for both CR and DB. This was due to dominating repulsion forces between the adsorbate and the adsorbent resulting in lowered adsorption efficiencies.

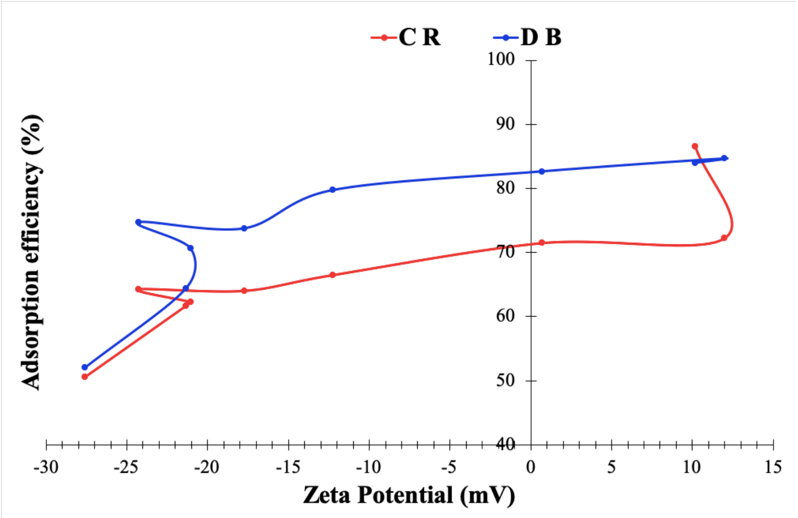

Figure 4.6. *Influence of zeta potential over the adsorption of Congo red (CR) and Direct blue 6 (DB) by AAC-CTAB*

4.2.1.3. Surface morphology and elemental analysis

Scanning electron microscopy (SEM) suggest major surface changes after surfactant (CTAB) modification of activated carbon followed by further changes due to adsorption of DB and CR. **Figure 4.7.** represents the SEM image for activated carbon (AAC) prior to CTAB modification. AAC surface exhibited deep cavities and non-uniform pores distinguished with long uneven hollow ridges. This enhanced porosity is why carbonaceous adsorbents are mostly preferred for adsorptive processes. AAC-CTAB surface shows irregular and dense morphology with high pore density and heterogeneity along with enhanced and distinct visible macro and micro-pores. However, post dye adsorption, there was a gradual reduction in the pore density along with ridges and cavities, as shown in **Figure 4.7.** (for AAC-CTAB/CR and AAC-CTAB/DB). It’s possibly due to the adsorptive filling of dye molecules into the pores and cavities of the AAC-CTAB surface, thus causing a gradual reduction in the surface irregularities. SEM images for AAC-CTAB surface prior and after dye adsorption goes vis-a-vis the surface area/BET data as represented in **Table 4.1.** High values of porosity and surface area of AAC-CTAB surface before adsorption compared to surface after adsorption support the trend of SEM images. This further verifies the morphological reduction of surface heterogeneity and unevenness due to the adsorption of dyes on the AAC-CTAB surface.

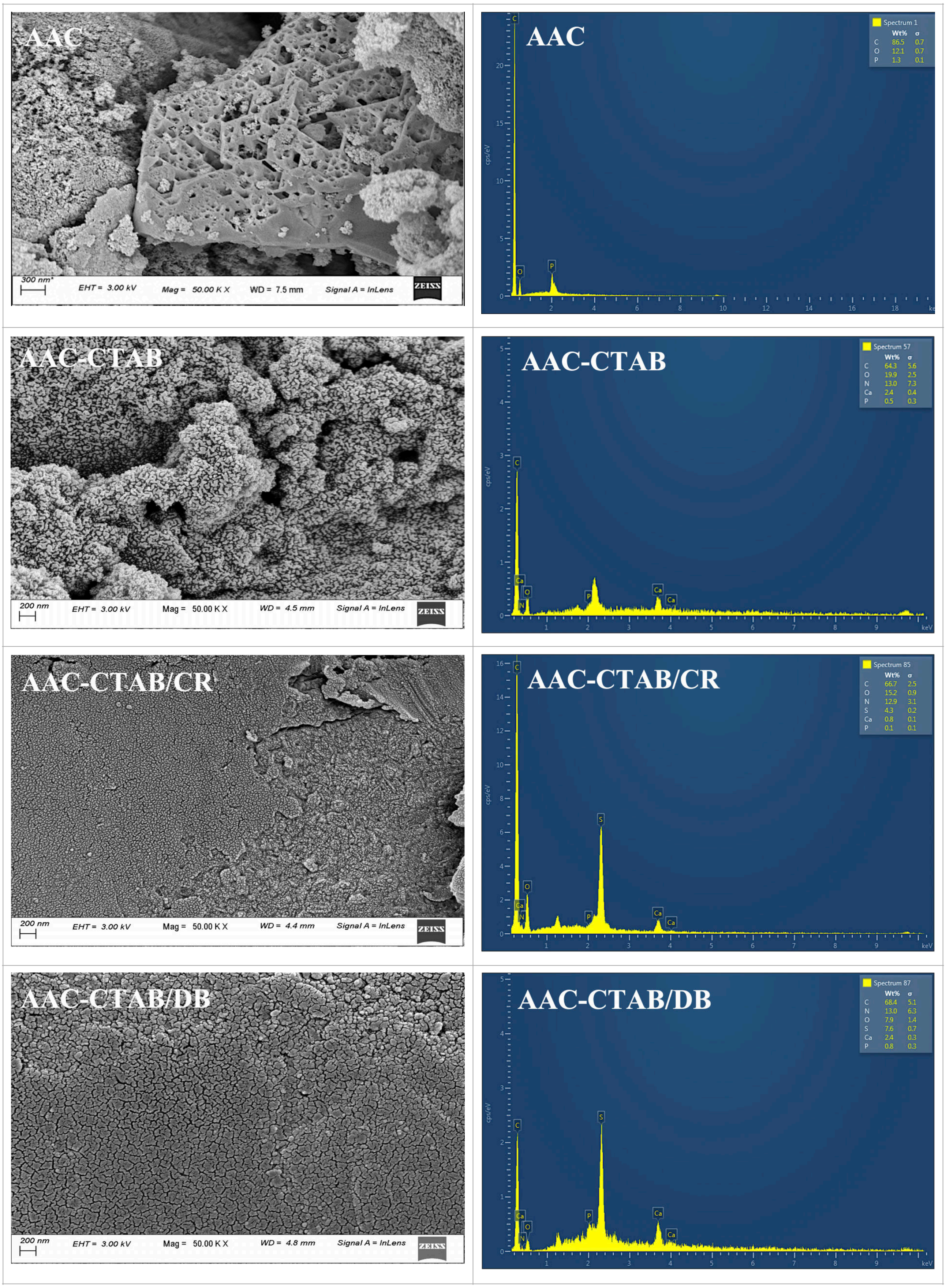

Figure 4.7. *SEM images and EDS spectra of AAC and AAC-CTAB surface before adsorption and after adsorption of CR and DB*

Energy-dispersive X-ray spectroscopy (EDS) of AAC as shown in **Figure 4.7.** (for AAC) verified the presence of phosphorous (P) peaks and thus affirmed phosphoric acid activation of lignocellulosic precursor to form acid activated carbon. Further, as shown in **Figure 4.7.** (for AAC-CTAB), presence of additional nitrogen peaks for AAC-CTAB spectrum verified the surface modification of acid-activated carbon with CTAB. The presence of sulphur peaks for AAC-CTAB after adsorption of CR and DB verified the adsorption of dyes on the adsorbent's surface, as shown in **Figure 4.7.** (for AAC-CTAB/CR and AAC-CTAB/DB). Conclusively, both SEM images and EDS spectrums verified CTAB modification of acid-activated carbon to form AAC-CTAB and also affirmed the adsorption of dyes over AAC-CTAB.

4.2.1.4. Surface area/BET analysis

The surface area analysis of the acid-activated carbon (AAC) before and after CTAB modification and before and after dye adsorption was studied using Brunauer-Emmett-Teller (BET)-total pore analysis, and the same has been reported in **Table 4.1.** The specific surface area (m^2/g) of the acid-activated carbon prepared from *Pongamia pinnata* shells (AAC) was 935.02 m^2/g, as reported in Patra et al., 2020. After CTAB modification (AAC-CTAB), the specific surface area gradually reduced to 580.822 m^2/g due to surface coating with CTAB molecules. Surface area/BET analysis verified high surface parameters like specific surface area (m^2/g), pore diameter (nm) and total pore volume (cm^3/g) for AAC-CTAB surface before adsorption, which gradually reduced after adsorption of CR and DB as reported in **Table 4.1.** However, BET parameters for AAC-CTAB adsorbed with CR are superior to AAC-CTAB adsorbed with DB, suggesting more sorption of DB as compared to CR molecules. It could be due to the high affinity of AAC-CTAB surface towards DB compared to CR in the single adsorptive systems. The same can be verified from Langmuir maximum adsorption capacity (mg/g) values (**Table S.4.1.** (Supplementary data)), where AAC-CTAB with CR have less value than AAC-CTAB with DB.

Table 4.1. *Surface area/BET analysis of AAC-CTAB before and after adsorption of CR and DB*

Porosity parameters	**Total pore volume (cm^3/g)**	**Average Pore Diameter (nm)**	**Specific Surface Area (m^2/g)**
AAC-CTAB	1.008	6.944	580.822
AAC-CTAB/CR	0.843	4.792	496.647
AAC-CTAB/DB	0.758	3.980	403.391

4.2.1.5. FT-IR analysis

Functional groups on the surface of AAC-CTAB active sites involved in adsorbing the studied dye molecules was studied using FT-IR. The spectral range for FT-IR analysis was conducted from 500 cm^{-1} to 4000 cm^{-1} as shown in **Figure 4.8.** AAC showed a major peak from 3600 cm^{-1} to 3200 cm^{-1} as compared to AAC-CTAB. This peak was due to strong and broad -OH (alcohol and carboxylic acid) stretching and medium N-H (amine and amide groups) stretching. -OH stretching due to alcohol and carboxylic acid groups verifies the presence of acidic functional groups developed due to surface oxidation of AAC during acid treatment. Another major peak from 1200 cm^{-1} to 1020 cm^{-1} for AAC was due to strong C-OH (alcohol) stretching. Multiple minor peaks from 2250 cm^{-1} to 1900 cm^{-1} for AAC-CTAB are due to variable C≡N (nitrile) stretching and C≡C (alkyne) stretching. A major peak between 1600 cm^{-1} to 1450 cm^{-1} for AAC-CTAB was due to medium C-H bending of methyl groups of alkane. This was likely due to methyl chain groups of the CTAB hydrophobic tails, thus affirming the CTAB modification of AAC surface. AAC-CTAB complexed with CR and DB showed peak changes in the range of 3500 cm^{-1} to 3350 cm^{-1} as compared to AAC-CTAB itself. These peak changes could be due to strong -OH (alcohol and carboxylic) and -NH (amine) stretches involved in binding CR and DB species. Similar peak changes were observed between 2400 cm^{-1} to 2275 cm^{-1} which could be due to variable -C≡C and strong -C≡N stretches for AAC-CTAB adsorbed with CR and DB. Minor peak changes were observed for AAC-CTAB complexed with CR in the range of 1100 cm^{-1} to 980 cm^{-1} which was due to strong stretches of C-O-C and C-OH groups. Specific peaks between 1924 cm^{-1} to 1886 cm^{-1} for CR and DB are due to C-H bending of aromatic compounds. This is likely due to the aromatic rings found in CR and DB species, thus verifying their adsorption. Conclusively the band peaks from FTIR analysis for AAC and AAC-CTAB suggest the oxidation of surface for acidic functional groups due to acid activation followed surfactant modification using CTAB. Simultaneously, FTIR analysis for AAC-CTAB surface before and after adsorption of CR and DB, revealed the involvement of oxygen and nitrogen containing groups i.e. -NH, C-O-C, C-OH, -C≡N and -C≡C groups. Involvement of such groups was due to combined effect of surface functional groups of AAC and CTAB modified of acid activated carbon surface (Ong et al., 2020; Patra et al., 2019).

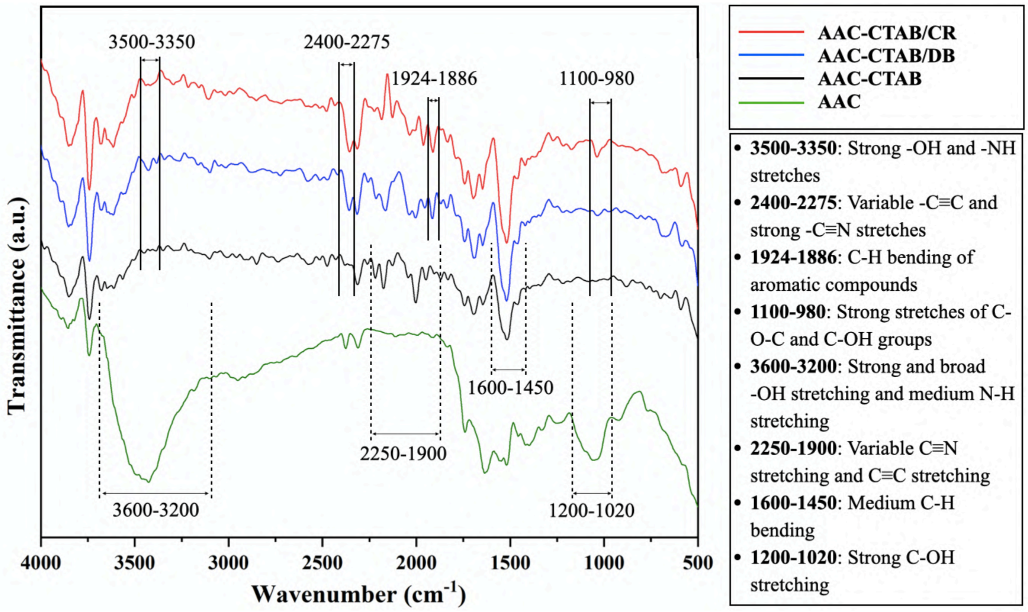

- **3500-3350**: Strong -OH and -NH stretches
- **2400-2275**: Variable -C≡C and strong -C≡N stretches
- **1924-1886**: C-H bending of aromatic compounds
- **1100-980**: Strong stretches of C-O-C and C-OH groups
- **3600-3200**: Strong and broad -OH stretching and medium N-H stretching
- **2250-1900**: Variable C≡N stretching and C≡C stretching
- **1600-1450**: Medium C-H bending
- **1200-1020**: Strong C-OH stretching

Figure 4.8. *FT-IR spectra of AAC and AAC-CTAB before and after adsorption*

4.2.2. Influence of process parameters

The influence of the initial pH of dye solution over the adsorption process involves protonation/de-protonation of the AAC-CTAB surface and speciation of the CR and DB species with varying pH in an aqueous solution. **Figure 4.9.** shows the influence of initial pH of dye solutions (varying from 2.0-10.0) over its adsorption over AAC-CTAB surface with a fixed dosage of adsorbent (0.5 mg/ mL) and fixed initial concentration of adsorbate (50 mg/L). For both CR and DB, AAC-CTAB showed its efficient removal at pH 2.0, which gradually reduced with the increasing pH. This could be because AAC-CTAB acquires a positive charge due to CTAB surfactant modification over an acid-activated surface. Also, at acidic pH (low pH values), carboxylic and hydroxyl groups of the acid-activated carbon surface are heavily protonated to cationic forms (Konicki et al., 2017). Simultaneously, CR and DB are azo anionic dyes and thus contain sulphonic acid groups (R-SO3Na), which dissociate into sulphonate anions ($R\text{-}SO_3^-$) at aqueous solutions. Due to their lower pKa values (less than zero), CR and DB exhibit anionic forms at higher acidic solutions (Guo et al., 2016). Thus, at low pH, the number of protonated and positively charged sites on AAC-CTAB favour the adsorption of negatively charged dye ions via electrostatic force of attraction. However, at acidic pH values, the sulphonate ions can be protonated to the neutral form ($R\text{-}SO_3H$), which is unfavourable to the adsorption process. With the increase in pH, more electronegative charges were formed on the adsorbent's surface, as shown in **Figure 4.5.**, thus rendering its negative surface charge and letting it electrostatically repel the anionic dye molecules. Conclusively, the adsorption behaviour of AAC-CTAB towards CR and DB is influenced by the initial pH of dye solution causing charge-based interactions among them, and pH 2.0 was finally considered as the optimised pH for the rest of the study.

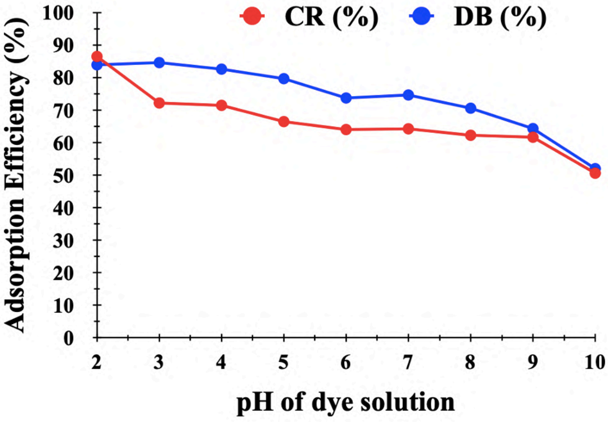

Figure 4.9. *Effect of initial pH of dye solution*

The influence of variable AAC-CTAB dosage on the efficient removal of CR and DB species from simulated dye solutions were carried out with adsorbent dosage ranging from 0.25–1.25 mg/mL (with 20 mL volume of dye solution), at initial pH of 2.0 and initial dye concentration of 50 mg/L for both CR and DB. As illustrated in **Figure 4.10.** the adsorption efficiencies (%) of AAC-CTAB elevated and reached a point of equilibrium with an increase in its dosage for a fixed initial concentration of CR and DB. The driving force for this adsorptive behaviour could be due to the availability of vacant active sites with elevating adsorbent dosages and the concentration of dye species. However, after a certain point due to the fixed concentration of dye molecules, further increase in adsorbent's dosage showed no influence on the adsorption efficiency and thus, the driving force for adsorption resorted to equilibrium.

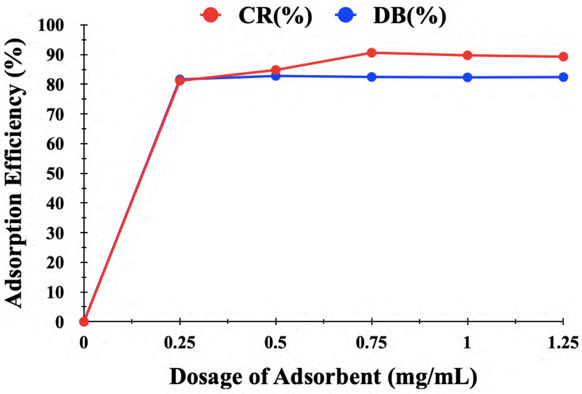

Figure 4.10. *Effect of dosage of AAC-CTAB*

The effect of the initial concentration of dyes (50-250 mg/L) on the optimised dosage of AAC-CTAB (0.25 mg/mL for both CR and DB) and pH (2.0 for both CR and DB) were analysed for an incubation period of 12 h. **Figure 4.11.** shows that adsorption capacity (mg/mL) gradually elevated and adsorption efficiency (%) gradually reduced with the increasing initial CR and DB molecules concentration. Such behaviour of adsorption efficiency (%) and capacity (mg/g) can be attributed to a fixed number of adsorption sites on the AAC-CTAB surface which eventually gets saturated as the initial dye concentration of the dye species elevates. The number of available vacant adsorption sites govern the adsorption efficiency (%) of AAC-CTAB, and as the initial concentration of the dye species elevates, the number of available vacant sites reduces, and so does the adsorption efficiency (%). On the contrary, the extent of filled adsorption sites govern the adsorbent's adsorption capacity (mg/g). Thus, as the initial concentration of dye species increases, the number of filled adsorption sites increases, and so does the adsorption capacity (mg/g) of the AAC-CTAB.

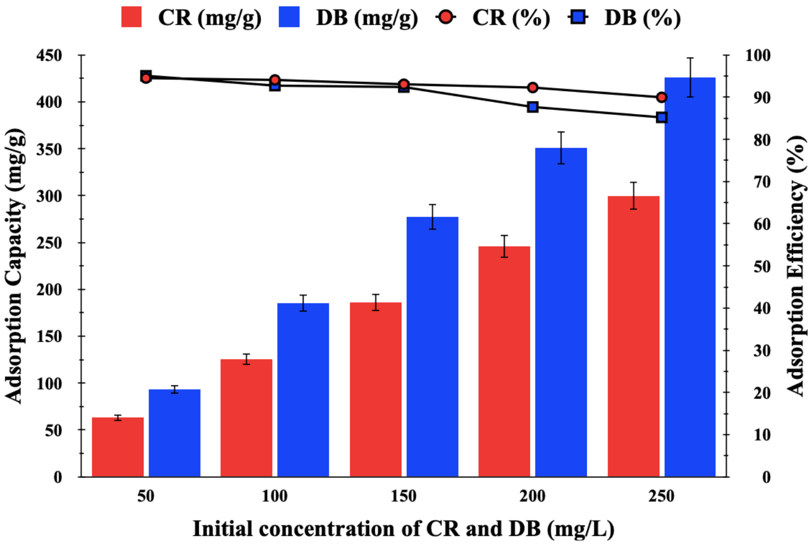

Figure 4.11. *Effect of initial concentrations of dyes influencing adsorption of CR and DB by AAC-CTAB*

4.2.3. Influence of incubation temperature and concerned thermodynamics

The influence of variable incubation temperatures on the adsorption of CR and DB on AAC-CTAB surface was evaluated by varying the incubation temperatures from 293 K to 323 K for variable initial concentrations of dyes (50-250 mg/L) and maintaining the other parameters optimised. With the rise in temperature, the adsorption efficiency of AAC-CTAB for CR and DB elevates up to a certain temperature, after which there was a gradual downfall in the adsorption efficiency. This is possibly due to temperature-dependent active sites formed due to acid activation and pyrolysis.

Another reason could be the disruption of the hydrophobic bonds holding the surfactant molecules. **Table S.4.3.** (Supplementary data) presents the estimated ΔG°, ΔH° and ΔS° values for different temperatures (K) and initial dye concentration (mg/L). Negative ΔG° values for the adsorption of CR and DB by AAC-CTAB affirmed the adsorptive process as spontaneous and thermodynamically favourable. Negative values for ΔH° for both DB and CR affirmed the exothermic adsorptive process. This could be due to the energy involved in the formation of active sites may be less than the energy expelled during sorbate-sorbent interactions, and thus the adsorption phenomenon is likely to be exothermic. Finally, positive ΔS° values for the adsorptive process renders a rise in the degree of dis-orderness and randomness.

4.2.4. Interaction studies

4.2.4.1. Physicochemical properties of adsorbent and adsorption mechanism

Hydrophobic regions over activated carbon surface make it less susceptible and dispersive in aqueous medium and thus limits its uptake capacity of organic molecules from aqueous bodies. Treatment of activated carbon with surfactants enhances the wettability and reduces the surface tension of activated carbon to enhance its performance in the aqueous phase and thus promote its adsorptive capabilities.

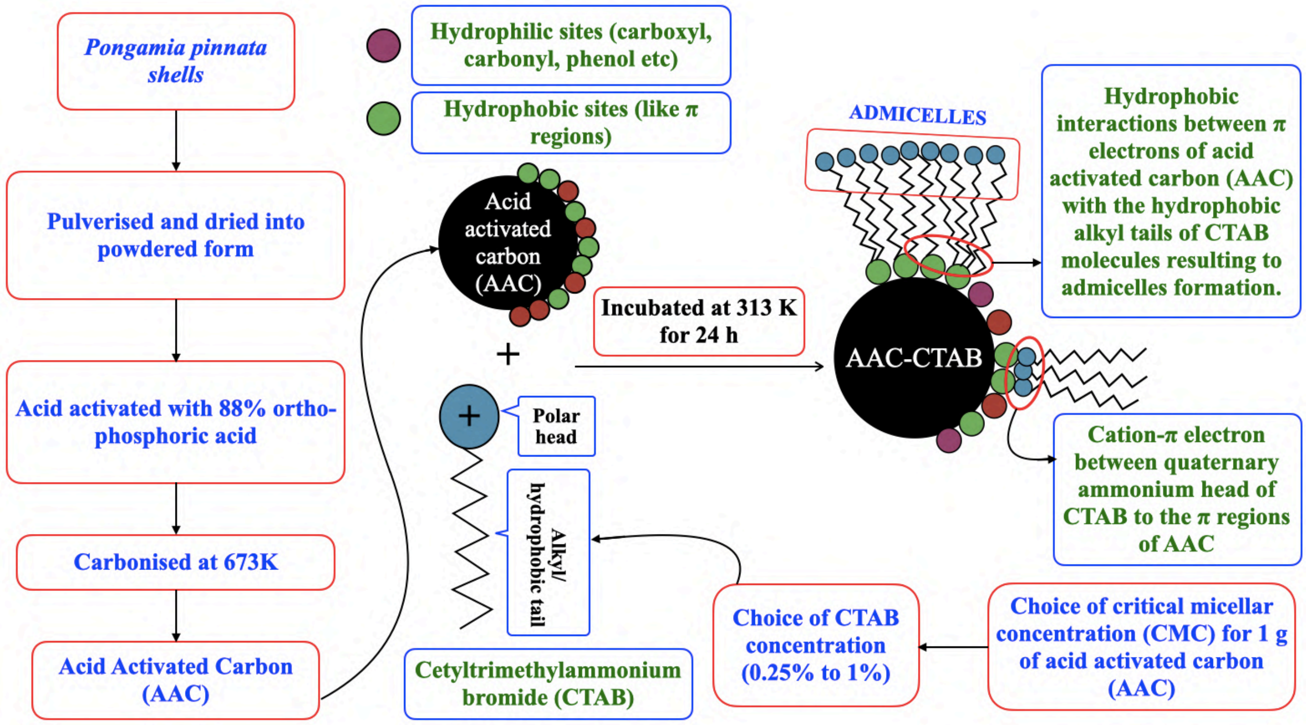

Figure 4.12. *Schematic representation of adsorbent (AAC-CTAB) preparation*

Activated carbon possess π electrons that exhibit favourable hydrophobic interactions with the hydrophobic alkyl tails of CTAB molecules, resulting in the formation of semi-circular admicelles. Inside these admicelles, the hydrophobic tails (alkyl groups) of CTAB species direct inwards and the quaternary ammonium head (polar/cationic groups) direct outwards. Another interaction, viz. cation-π electron interaction, occurs between the quaternary ammonium head group of CTAB to the π regions of activated carbon (Wang et al., 2018). **Figure 4.12.** represents the methodology of CTAB treatment of acid-activated carbon (AAC) and the interactions involved between them. CTAB treatment resorts to elevated water affinity attributing to enhanced sorbate-sorbent interactions, resulting in enhanced adsorption of organic pollutants from aqueous media.

Positively charged cationic heads assist the hydrophilic surface of the activated carbon for adsorbing anionic dye molecules in the aqueous phase. Primarily, the oxidised regions (due to activated carbon surface) or hydrophilic regions (due to polar heads of CTAB) of AAC-CTAB are responsible for the adsorption of CR and DB molecules over AAC-CTAB surface via H-bonding and electrostatic interactions. Hydrophobic interactions due to the hydrophobic tail of CTAB and π-π interactions between the π rings of the dye species and the π regions of the adsorbent are also responsible for dye uptake by AAC-CTAB.

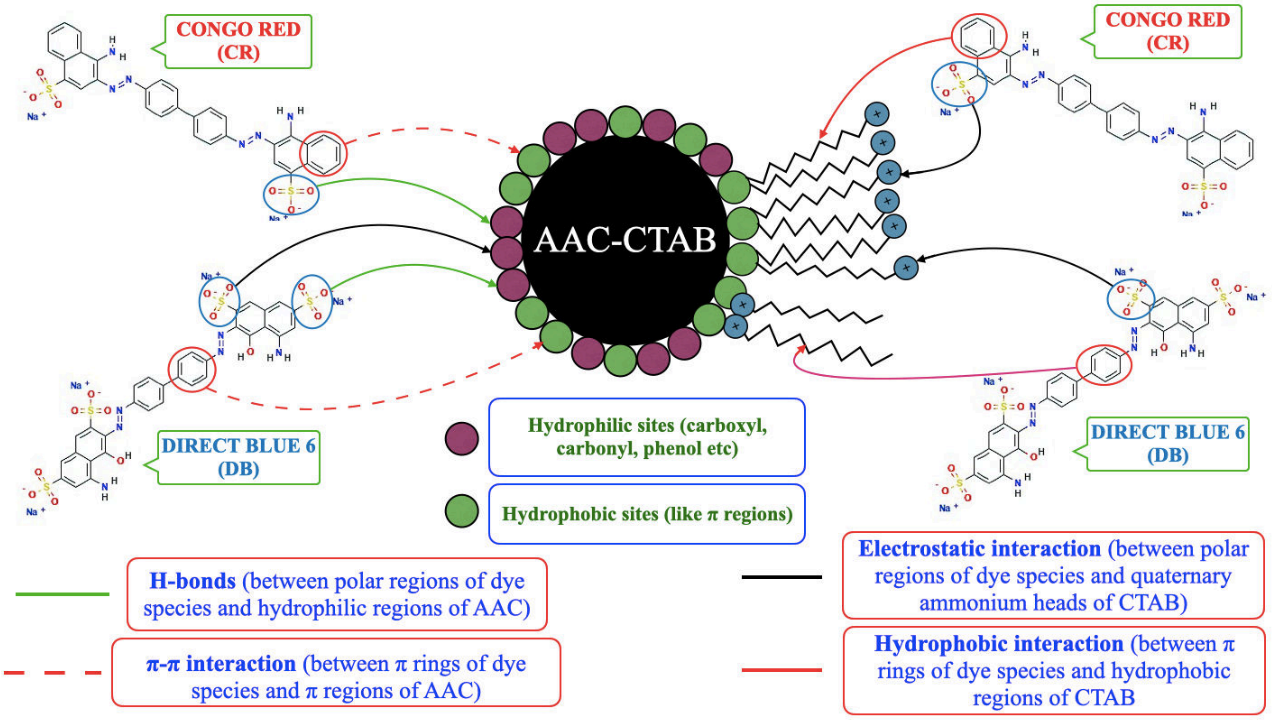

Figure 4.13. Schematic representation of adsorbent (AAC-CTAB)-adsorbate (CR and DB) interactions

Figure 4.13. represents the interactions between AAC-CTAB and anionic azo dyes as discussed. Apart from these, pore-filling and several other adsorption mechanisms also promote the uptake of anionic azo dyes (CR and DB) (Ntakirutimana et al., 2019; Peng et al., 2016).

4.2.4.2. Adsorption isotherm analysis

4.2.4.2.1. Single adsorption system

Sorbate-sorbent isotherm modeling was studied using a single adsorptive system involving CR and DB's adsorption by AAC-CTAB individually. Isothermal constants and regression coefficients from isothermal modelling using equilibrated data obtained from sorbate-sorbent interactions experiment are reported in **Table S.4.1.** (Supplementary data). Langmuir isotherm model reported the best fitting for experimental data for CR and DB adsorption by AAC-CTAB as compared Freundlich, thus supporting the formation of a monolayer of sorbate molecules over the sorbent surface and ruling out the possibility of multilayer formation. The calculated maximum adsorption capacity (Q_L) by the Langmuir model was 555.56 mg/g for CR and 625 mg/g for DR species. The Langmuir equilibrium parameter (K_L) values lie between 0 to 1 (0.049 for CR and 0.057 for DB); thus affirming the favourability of dye adsorption over AAC-CTAB surface. Dubinin-Radushkevich isotherm parameter, mean adsorption energy (E_{DR}) affirm whether the adsorption process is physisorption (E_{DR}<8 kJ/mol) or chemisorption (E_{DR}>16). However, the Dubinin-Radushkevich isotherm model gave the least fit with the experimental data; thus, the values for mean adsorption energy (E_{DR}) cannot be correlated with the adsorption process. Temkin isotherm hypothesises the heat of adsorption (as the function of temperature) decreases linearly as the surface coverage of adsorbate molecules existing in a monolayer increases due to the adsorption process. Temkin isotherm model gave a good fit for both CR and DB adsorption, and thus the heat of adsorption (B) of the dye molecules in the adsorbed monolayer over the adsorbent would decrease linearly with the coverage of CR and DB species. Sips isotherm model (three-parameter isotherm model) also showed good fitting towards CR and DB adsorption on AAC-CTAB surface. Values for Sips model exponent (m) for CR was 1.07 and for DR was 1.10, and both these values are almost near to unity, thus confirming the applicability of Langmuir isotherm model for CR and DB adsorption over AAC-CTAB surface. Non-linear isothermal interaction plots for the sorbate-sorbent interactions are depicted in **Figure 4.14. (A, B)**. The non-linear isothermal plots also verify the applicability of the Langmuir isotherm model with the experimental data over Freundlich and Dubinin-Radushkevich isotherm models.

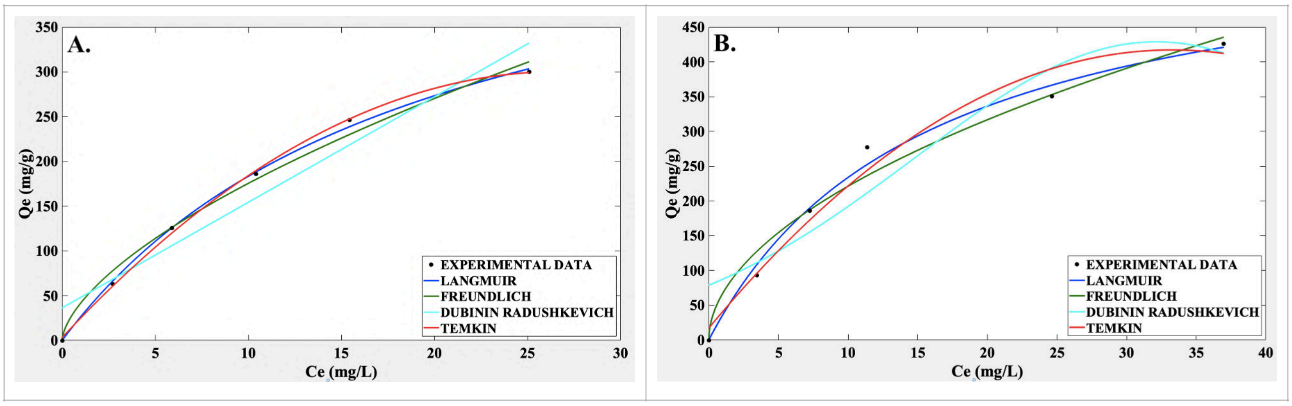

Figure 4.14. Non-linear isotherm model plotting for (A) CR and (B) DB

4.2.4.2.2. Binary adsorption system

The binary adsorption system involved the simultaneous removal of CR and DB species by AAC-CTAB from a binary (CR+DB) mixture under the influence of one another. **Figure 4.15. (A, B)**, represents the relative removal of individual dye species from the single (CR, DB) and binary (CR+DB) adsorptive systems. Adsorption capacities of AAC-CTAB for a dye from single adsorptive systems was more as compared to removal of the same dye species from binary adsorptive (CR+DB) system in all the reported initial concentrations. This could be due to the resistance of mass transfer by one dye species over the uptake of other dye species from the binary adsorptive systems by AAC-CTAB in all the initial concentrations. Overall, DB has more removal affinity towards AAC-CTAB in a single adsorptive system than DB in binary adsorptive systems and CR in both single and binary adsorptive systems, as depicted in **Figure 4.15. (A, B)**. This was due to affinity differences of AAC-CTAB towards CR and DB species, which govern its mass transfer and thus affect individual adsorption capacities.

The competitive adsorption of CR and DB was evaluated using competitive Langmuir adsorption isotherm for a multi-component system. For a multi-component system containing a binary mixture of ‘x’ and ‘y’, competitive Langmuir adsorption isotherm for component ‘x’ can be represented as (Jandera and Komers, 1997; Manjunath and Kumar, 2018):

$$Q_{e,x} = \frac{Q_{CL,x} K_{CL,x} C_{e,x}}{1 + \sum K_{CL,xy} C_{e,xy}} \qquad (4.1.)$$

Here, $Q_{e,xy}$ represents equilibrium adsorption capacity for ‘x’ component from multi-component (binary) system of x+y and $Q_{CL,x}$ represents the maximum adsorption capacity for component ‘x’. $C_{e,x}$ represents the equilibrium concentration of component ‘x’ in the binary mixture (x+y). $K_{CL,x}$

represents competitive Langmuir constant for ‘x’. The denominator represents the summation of products of competitive Langmuir constant ($K_{CL,xy}$) and equilibrium concentration ($C_{e,xy}$) of all the components in the multicomponent mixture. Based on equation 4.1., the individual equilibrium adsorption capacity i.e. $Q_{e,CR}$ and $Q_{e,DB}$ in the binary adsorptive (CR+DB) systems can be represented as follows:

$$\frac{1}{Q_{e,CR}} = \frac{1}{Q_{CL,CR}} + \frac{1}{Q_{CL,CR}K_{CL,CR}}\left[\frac{1 + K_{CL,DB}C_{e,DB}}{C_{e,CR}}\right] \tag{4.2.}$$

$$\frac{1}{Q_{e,DB}} = \frac{1}{Q_{CL,DB}} + \frac{1}{Q_{CL,DB}K_{L,DB}}\left[\frac{1 + K_{CL,CR}C_{e,CR}}{C_{e,DB}}\right] \tag{4.3.}$$

Here, $Q_{CL,CR}$ and $Q_{CL,DB}$ represent the maximum adsorption capacity (mg/g); $C_{e,CR}$ and $C_{e,DB}$ are the equilibrium concentration (mg/L); $Q_{e,CR}$ and $Q_{e,DB}$ represent the adsorption capacity (mg/g) and $K_{CL,CR}$ and $K_{CL,DB}$ represent the competitive Langmuir constants (L/mg) for CR and DB adsorption in the binary (CR+DB) adsorptive systems, respectively by AAC-CTAB.

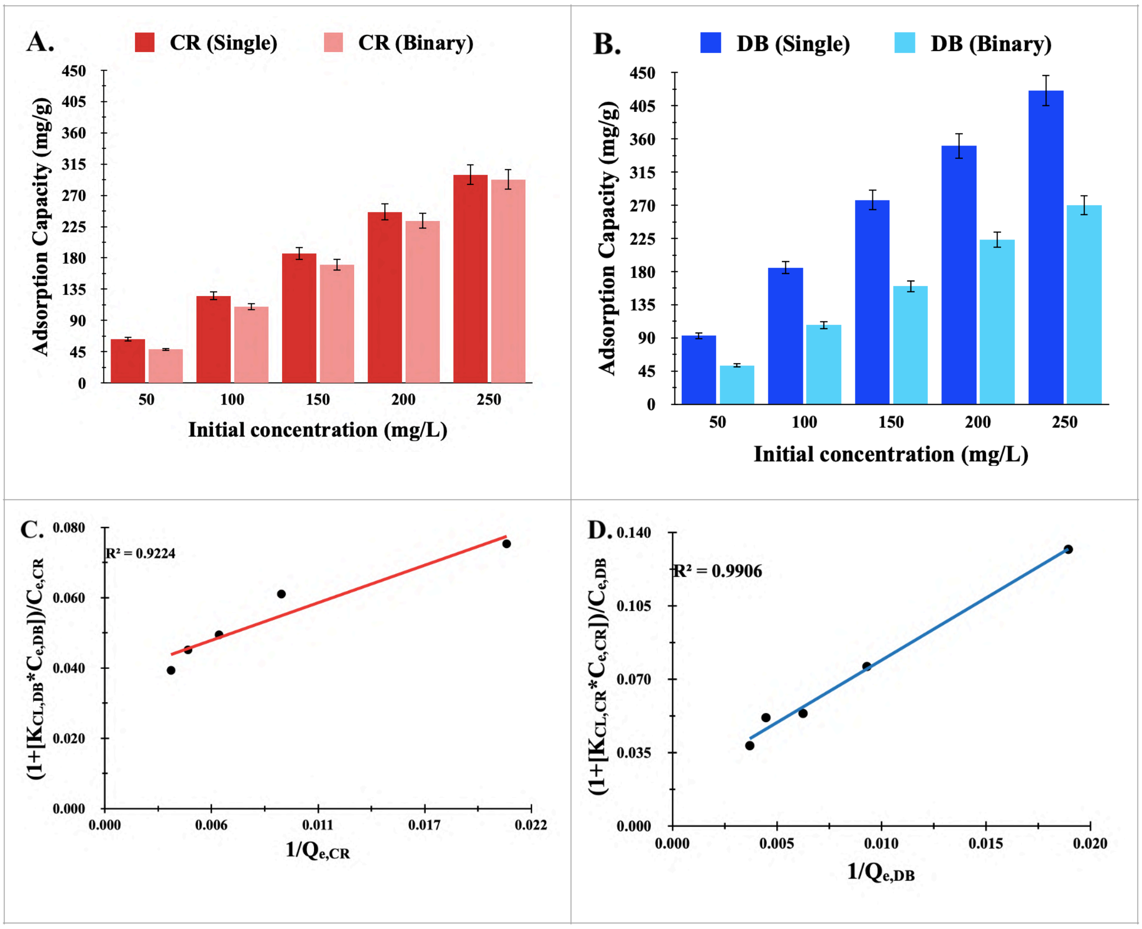

Figure 4.15. *Relative adsorption of dyes in single and binary adsorptive systems for* ***(A)*** *CR and* ***(B)*** *DB; and fitting of Comparative Langmuir Isotherm model for* ***(C)*** *CR and* ***(D)*** *DB*

Competitive Langmuir adsorption isotherm gave a good fit with the experimental data from the binary adsorptive system, as illustrated in **Figure 4.15. (C, D)**. The maximum adsorption capacity (mg/g), i.e. $Q_{CL,CR}$ and $Q_{CL,DB}$ predicted by competitive Langmuir isotherm along with other constants for binary adsorptive systems, were presented in **Table 4.2.** It can be observed that DB species were adsorbed more in comparison with CR adsorption from the binary adsorptive systems. The theoretical explanation for such behaviour could be due to the anionic charge intensity of the dyes in the binary adsorptive systems. DB contains 4 sulphonic acid groups ($R\text{-}SO_3Na$) as compared to 2 sulphonic acid groups in CR. These sulphonic acid groups dissociate to sulphonate anions ($R\text{-}SO_3^-$) in aqueous solutions and thus are responsible for anionic charge in aqueous solutions. Thus, DB has higher anionic charge intensity in aqueous solutions compared to CR. Hence, the cationic AAC-CTAB surface has more affinity towards DB than CR. Positive values for $K_{CL,CR}$ and $K_{CL,DB}$ (competitive Langmuir constants) verify the feasibility of the adsorption process in the binary system.

To understand the influence of one solute over the adsorption of the other solute by AAC-CTAB, the Q_{Binary}/Q_{Single} ratio was calculated. Q_{Binary} and Q_{Single} represent the maximum adsorption capacity of the dyes in binary adsorptive and single adsorptive systems, respectively. Altogether, there could be three possible outcomes that can be anticipated; (a) Q_{Binary}/Q_{Single} equal to 1, i.e. non-interaction of individual components in the binary adsorptive system; (b) Q_{Binary}/Q_{Single} less than 1 i.e. the antagonistic effect on adsorption of the individual component by other in the binary adsorptive system and (c) Q_{Binary}/Q_{Single} more than 1, i.e. the synergistic effect on adsorption of the individual component over the other in the binary adsorptive system (Manjunath and Kumar, 2018).

Table 4.2. *Competitive Langmuir model for individual dye species removal in binary systems (CR+DB)*

BINARY SYSTEMS	Competitive Langmuir maximum adsorption capacity (mg/g)	Competitive Langmuir constants (L/mg)	Q_{Binary}/Q_{Single}	R^2
CR in CR+DB	$Q_{CL,CR}$: **26.88**	$K_{CL,CR}$: **0.027**	**0.048**	**0.92**
DB in CR+DB	$Q_{CL,DB}$: **51.02**	$K_{CL,DB}$: **0.004**	**0.081**	**0.99**

As shown in **Table 4.2.**, the Q_{Binary}/Q_{Single} for CR was 0.048, and DB was 0.081 in the binary adsorptive (CR+DB) system. Since for both CR and DB, Q_{Binary}/Q_{Single} is less than 1; hence both CR and DB has an antagonistic/competitive effect over each other's adsorption on AAC-CTAB surface in binary (CR+DB) adsorptive systems. Similar to the current study, Manjunath et al., 2020 reported similar behaviour for antibiotic adsorption in single- and multi-component adsorptive systems by *Prosopis juliflora* activated carbon; where the adsorption of individual antibiotic species in multi-component adsorptive systems was influenced by the presence of other antibiotic species.

4.2.4.3. Kinetics of adsorption

The sorbate-sorbent interaction kinetics was studied using pseudo-first-order, pseudo-second-order and intra-particle diffusion models. **Table S.4.2.** (Supplementary data) show the regression coefficients (R^2) for different kinetics model for CR and DB adsorption by AAC-CTAB. From the data, it is clear that adsorption of both CR and DB over AAC-CTAB surface follow pseudo-second-order kinetics and thus, theoretically rate-limiting step would involve chemical interaction, i.e. chemisorption. The same can further be verified from the experimental adsorption capacities ($Q_{e\ expt.}$) appear to be almost equal to theoretical adsorption capacity (Q_e) values as predicted by the pseudo-second-order model for both CR and DB. Regression coefficients for pseudo-first-order and intra-particle diffusion were less than pseudo-second-order, thus ruling out its applicability in adsorption of both CR and DB by AAC-CTAB. **Figure 4.16. (A, B)** represents a clear insight into kinetic model fitting for CR and DB adsorption on AAC-CTAB surface. The non-linear kinetics plots also verify the applicability of the pseudo-second-order model with the experimental data over pseudo-first-order and intra-particle diffusion kinetic models.

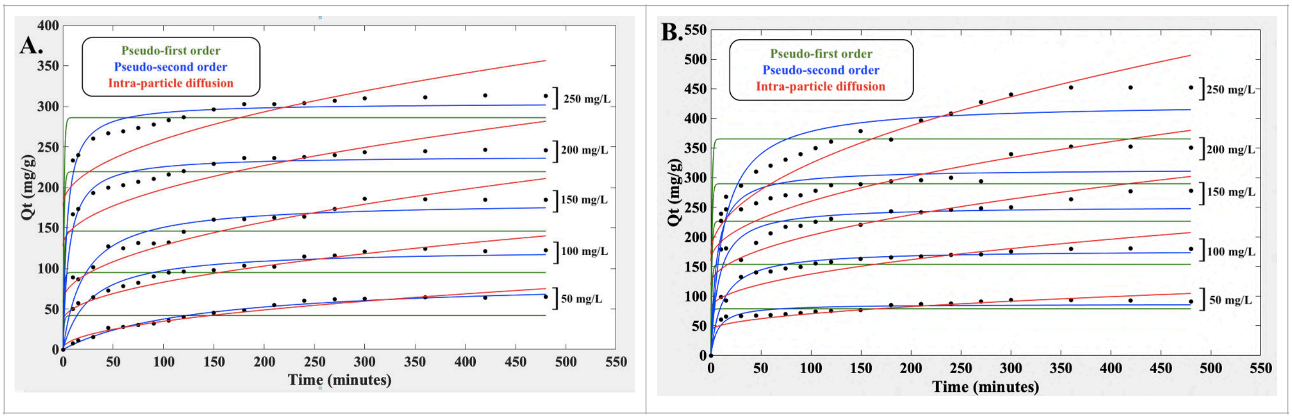

Figure 4.16. *Non-linear kinetics model plotting for **(A)** CR and **(B)** DB*

4.2.5. Effect of Co-existing Anions and Cations on dye adsorption

Figure 4.17. depicts the effect of co-existing cations (Fe^{+3}, Cu^{+2}, Co^{+2} and Zn^{+2}) and anions (SO_4^{-2}, CO_3^{-2}, NO_3^{-1} and Cl^{-1}) over CR and DB adsorption on AAC-CTAB surface. As depicted, the presence of cations and anions has a nominal reduction on CR and DB's adsorption capacities over AAC-CTAB surface compared to ones without the presence of salts. For co-existing cations, the possible reason for such nominal reduction in adsorption capacity may be due to the transition of metal cations into its hydration forms, i.e. majorly $M(OH)_X$ and minor forms of $M(OH)^+$. Simultaneously Tobin et al., 1984, reported the dependency of metal ionic radius to its adsorption on an adsorbent; thus higher the ionic radii, the lower is the size of metal hydrate form, and thus higher is its ion exchange on the adsorbent's surface. The order of ionic radius in picometers (pm) of the 4 considered metal cations are as follows (Dong et al., 2018):

Cu^{+2} (73 pm) < Zn^{+2} (74 pm) < Co^{+2} (74.5 pm) < Fe^{+3} (78.5 pm)

It's important to note that the ionic radii of ferric ion (Fe^{+3}) is based on its coordination form in its salt. Since, ferric chloride salt (anhydrous) was used for the current study, the ionic radii selected for ferric ion (Fe^{+3}) is in the form of 6-coordinate, octahedral shape with high spin and accordingly 78.5 pm was its ionic radii (WebElements Periodic Table).

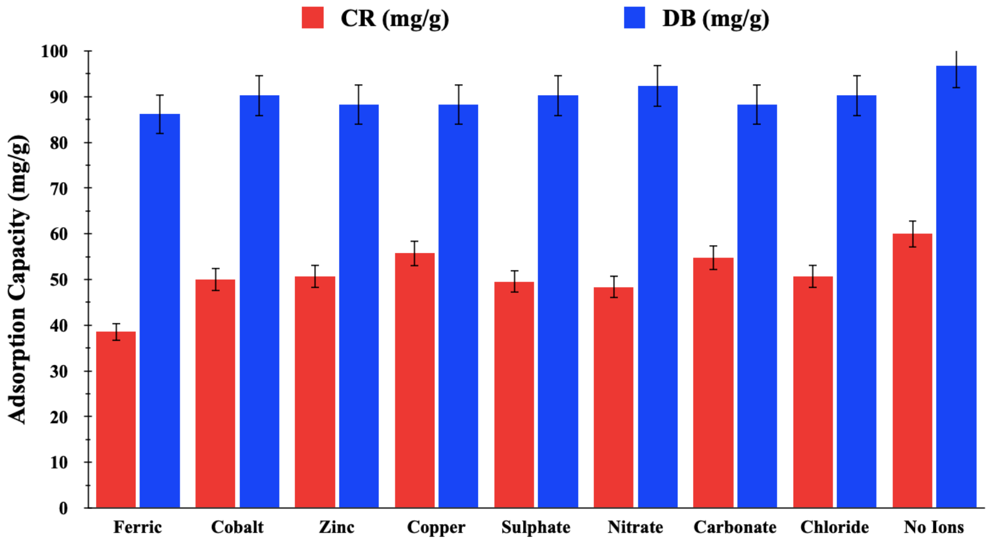

Figure 4.17. *Effect of co-existing cations and anions on the adsorption of CR and DB by ACC-CTAB*

Accordingly, due to its large ionic radii, ferric ions (Fe^{+3}) will have smaller metal hydrate forms as compared to other cationic forms and thus it will undergo more ion exchange over the adsorbent's surface as compared to other cations. Owing to this, ferric ions will compete more with the dye species for adsorption over adsorbent's surface followed by Co^{+2} and Zn^{+2} ion; and least competition form Cu^{+2} ions (due to its smallest ionic radii) (Tobin et al., 1984). Thus, the adsorption capacity of the adsorbent (AAC-CTAB) for dye molecules (CR and DB) in the presence of Fe^{+3} is least followed by other cations. Co-existing anions too resulted in nominal reduction in the adsorption capacity of the dye molecules. This could be possibly due to competitive binding of anionic salts with the anionic forms of dye species for the active sites on the adsorbent's surface (Wang et al., 2014).

4.2.6. Adsorbent desorption and recyclability studies

In order to evaluate the regenerative ability of AAC-CTAB, the adsorbent desorption and recyclability studies were conducted using 0.1 NaOH as the desorbing agent. The desorption and recyclability analysis of the adsorbent (AAC-CTAB) was done at an initial concentration of 100 ppm for both CR and DB while maintaining the other parameters optimised, as discussed already. The choice of NaOH as a desorbing agent could be explained as per the following reasons:

- As discussed earlier, CR and DB are azo anionic dyes and thus contain sulphonic acid groups ($R\text{-}SO_3Na$), which dissociate into sulphonate anions ($R\text{-}SO_3^-$) at aqueous solutions. However, in the presence of excess NaOH, the Na^+ ions tend to neutralise the bound sulphonate groups and thus cause shedding off of the dye molecules from the adsorbent's surface.
- NaOH neutralises the acidic functional groups (carboxylic, phenolic and laconic) of the acid-activated carbon, thus weakening the electrostatic interaction between the activated carbon and dye species (Liu et al., 2016). Neutralising the surface will help in shedding off the bound dye and thus vacating the active sites over the AAC-CTAB surface.

The used adsorbents were incubated with NaOH for 24 h, after which it was thoroughly rinsed with distilled water before being used again. Further treating with distilled water helped to eliminate any remnant dye or alkaline species from the AAC-CTAB surface, thus making the active sites available for the consecutive cycles. **Figure 4.18.** depicts the variation of adsorption efficiency (%) of AAC-CTAB after every desorption-adsorption cycle. After the first cycle, there was some significant drop in the adsorption efficiency by AAC-CTAB surface in adsorbing CR and DB. This was repeated for the subsequent 4 cycles, after which it was irrelevant to regenerate the adsorbed surface of the adsorbent further, basically due to very low adsorption efficiencies (%). With consecutive adsorption-desorption cycles, most of CR and DB species were eluted out with 0.1 N NaOH. After every adsorption-desorption cycle, an inert or non-inert complex of sodium salt (due to washing with 0.1 N NaOH) is likely to form, which is partially removed after rinsing with distilled water.

With consecutive cycles of adsorption and desorption, the size of these complexes gradually increases and at some point, they fail to escape the surface pores; thus, further rinsing isn't that effective. However, in the case of bigger pores, these complexes are washed out, and thus these pores continue to contribute to the adsorption process.

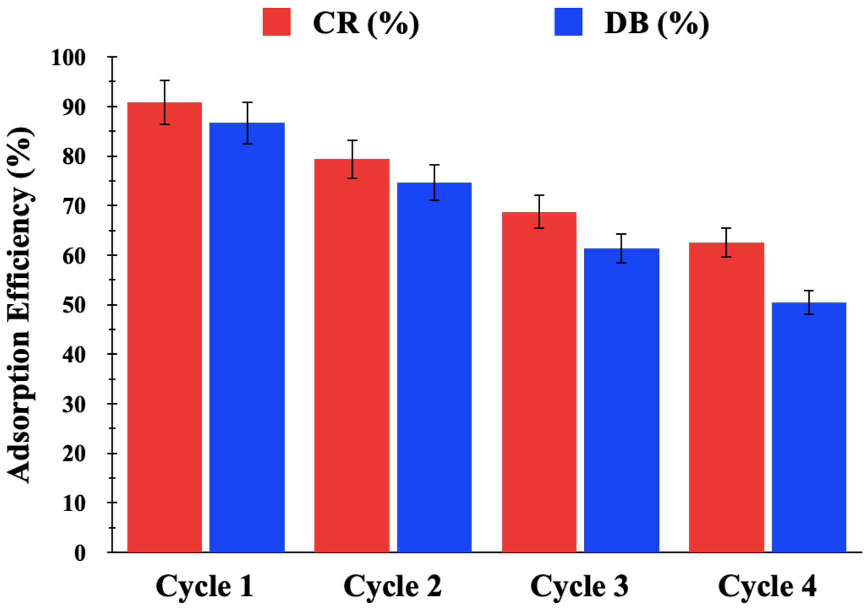

Figure 4.18. *Desorption and recyclability studies of AAC-CTAB in removing CR and DB*

From 1st cycle to 2nd cycle, the adsorption efficiency fell from 90.81% to 79.33% for CR and 86.68% to 74.61% for DB. Simultaneously for 3rd to 4th cycle, the adsorption efficiencies fell from 68.74% to 62.52% for CR and 61.36% and 50.47% for DB, respectively. Conclusively, consecutive adsorption and desorption cycles lead to the deterioration of the adsorbent's surface and thus affect the adsorbent's efficient performance. This was also accompanied by continuous wearing off and morphological disruption of the active sites, which intensified after every consecutive regeneration and adsorption cycle.

4.2.7. Phytotoxicity assays and analysis

The phytotoxicity assay was carried out to assess the adsorbent's effectiveness in eliminating CR and DB species; by analysing the toxic implications of the dye solution (before and after adsorption) over the germination of *Vigna mungo* (black gram) seeds. For this study, before undergoing the adsorption treatment, the dye samples were treated as control samples; dye samples after adsorptive treatment with AAC-CTAB were treated as test samples and distilled water as blank samples. After germinating the seeds for 4 days, the length of the roots from all the samples was measured and reported as depicted in **Figure 4.19.** The mean root length of the *Vigna mungo* (black gram) seeds germinated in distilled water (blank sample plate) was 4.87 cm which gradually reduced for seeds germinated in dye samples before adsorptive treatment (control sample plates). The mean root length was reduced to 1.57 cm for CR, 1.40 cm for DB and 1.93 cm for binary (CR+DB) control samples. Conclusively, it can be reported that both CR and DB dye in single and binary form is toxic for seed germination. However, the seeds germinated with dye samples after adsorptive treatment with AAC-CTAB (test sample plates) showed improved germination with subsequent growth in root length. The mean root length improved to 4.40 cm for CR, 3.37 cm for DB and 3.67 cm for binary (CR+DB). Thus, it can be reported that seeds germinated with dye samples after adsorption showed improved growth in seed root length, thus concluding to effective adsorptive removal of dyes by AAC-CTAB.

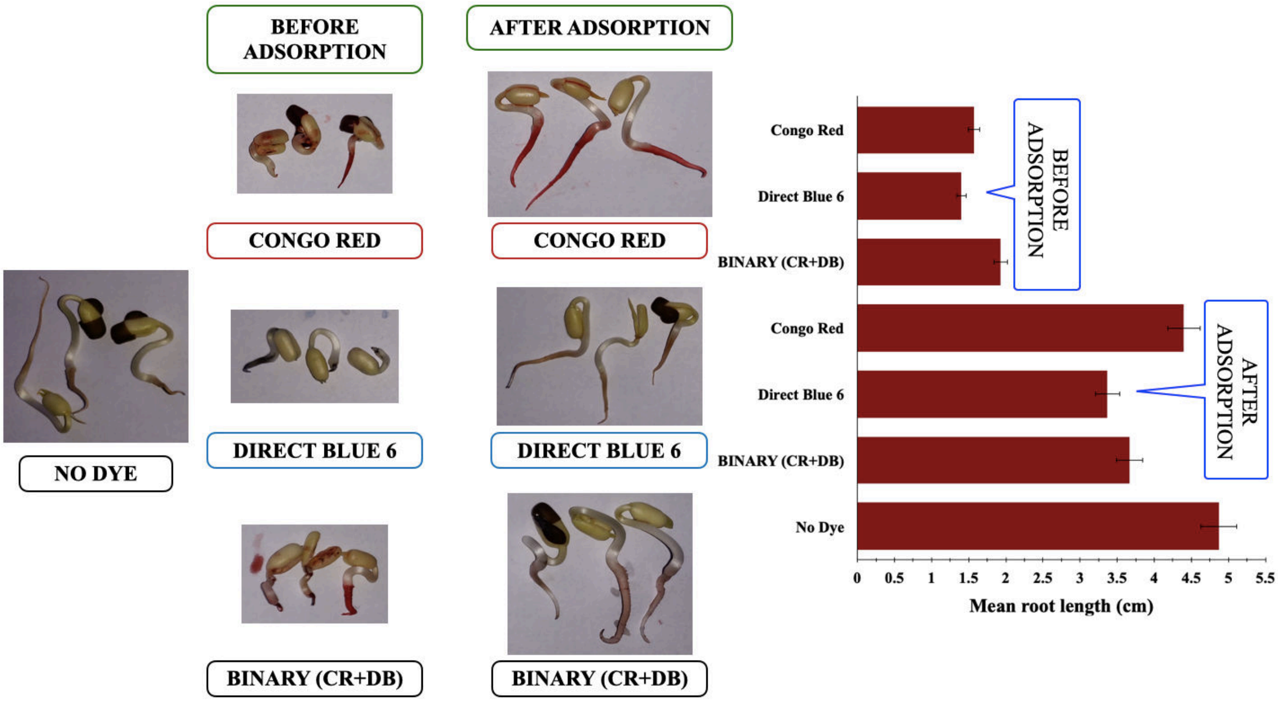

Figure 4.19. *Phytotoxic assessment of AAC-CTAB in removing CR and DB form single and binary adsorptive systems using Vigna mungo (black gram) seeds*

4.2.8. Determination of CTAB leaching

In order to evaluate the possible leaching of CTAB species from the surface of acid-activated carbon, the samples were spectrophotometrically analysed for any CTAB species. After the adsorption experiment, the adsorbents were filtered out from the rest of the dye solution, and then the filtrate, which could contain the CTAB species, was diluted to make it colourless. The dilute filtrate was then subjected to Britton-Robinson buffer (pH 4), followed by dropwise addition of eosin yellow (0.5 μM). The mixture was further diluted and allowed to settle for 5 to 10 mins, after which the absorbance was measured at 547 nm using a UV-Vis spectrophotometer (Infinite 200 PRO, Tecan) (Hussein et al., 2014). A trace amount of CTAB molecules, ranging from 1 mg/L to 10 mg/L, were detected from all the sets of experiments. This could be due to high rpm or constant collision of adsorbent particles during the adsorption experiments that led to disruption of hydrophobic interactions that bound the CTAB species over the activated carbon. However, in the case of desorption and regeneration studies, the amount of CTAB leaching out gradually increased and was in the range of 10-15mg/L to 15-25 mg/L after the third and fourth cycle, respectively. This was due to constant wearing off activated carbon surface due to consecutive desorption and regeneration cycles apart from the reason as explained above.

4.3. Significant findings

Acid activated carbon was surface treated with cationic surfactant CTAB (AAC-CTAB) to efficiently eliminate CR and DB species from single and binary adsorptive systems. Characterisation analysis verified CTAB modification of acid-activated carbon surface in the form of conical CTAB aggregates known as admicelles. Dye removal capacities (mg/g) and efficiencies (%) by AAC-CTAB was influenced by variable parameters such as initial pH of the dye solution, AAC-CTAB dosage, initial dye concentration and sorbent-sorbate incubation temperature. Interaction model studies from a single adsorptive system revealed the fitting of the Langmuir isotherm model and pseudo-second-order kinetics model for both CR and DB adsorption over AAC-CTAB surface under optimised conditions. For binary adsorptive system (CR+DB), both CR and DB had an antagonistic/competitive effect over each other's adsorption. Thermodynamic studies revealed adsorptive removal of CR and DB by AAC-CTAB surface as an exothermic process; spontaneous and thermodynamically favourable with an increased degree of dis-orderedness and randomness. Co-existence of cationic and anionic salts in the adsorptive systems revealed their minimal effect on dye adsorption by AAC-CTAB. Desorption and recyclability studies verified the suitability of AAC-CTAB to be reused for up to 4 cycles after continuous desorption with 0.1 N NaOH, followed by rinsing with distilled water. Phytotoxicity studies revealed the efficacy of AAC-CTAB in eliminating dyes from single and binary systems owing to its effectivity in the germination of model seeds viz. *Vigna mungo* (black gram) seeds. Conclusively, surfactant (CTAB) modified acid activated carbon (AAC-CTAB) can be considered as an economical and efficient alternative to eliminate anionic azo dyes from aqueous solutions.

However, a comparative study with other literature suggests that adsorptive remediation of other anionic azo dyes still needs extensive research, and the current study can be used as a reference for the same. Also, cationic surfactant modification of activated carbon surface successfully enhanced the wettability, reduced the surface tension of the overall adsorbent, and provided extra cationic and hydrophobic regions, which further assisted inefficient removal of the dye species. For future studies, the adsorbent shall be further exploited with other categories of surfactants, chelating agents and functional ligands or a combination for a much-enhanced surface capable of efficiently eliminating other grades of emerging contaminants and pollutants with greater than equivalent efficiencies.

SUPPLEMENTARY DATA FOR CHAPTER 4

Table S.4.1. *Adsorption isotherm model parameters, constants and coefficient of determination (R^2) for removal of CIP and AMX by AAC-CTAB*

ISOTHERMS		**ISOTHERM CONSTANTS**	**CR**	**DB**
Two-parameter isotherm models	**Langmuir**	**Q_L (mg/g)**	555.56	625.00
		K_L (L/mg)	0.049	0.057
		R^2	0.991	0.976
	Freundlich	**K_F (mg/g) (mg/L)$^{-1/n}$**	4.57	5.47
		1/n	0.714	0.619
		R^2	0.984	0.944
	Dubinin-Radushkevich	**Q_{DR} (mg/g)**	238.63	347.10
		K_{DR} (mol2/J2)	2.29	3.41
		E_{DR}	0.66	0.54
		R^2	0.885	0.909
	Temkin	**A_T (L/g)**	0.590	0.619
		B (J/mol)	41.20	54.617
		R^2	0.988	0.990
Three-parameter models	**Sips**	**K_S**	0.05	0.04
		Q_S (mg/g)	500.00	666.67
		m	1.07	1.10
		R^2	0.999	0.994

Table S.4.2. *Kinetic model parameters and coefficient of determination (R^2) for the removal of CR and DB by AAC-CTAB*

		Pseudo-first order			Pseudo-second order			Intra-particle diffusion		
C_i (mg/L)	**$Q_{e\ Exp.}$ (mg/g)**	**K_1 (1/min)**	**Q_e (mg/g)**	**R^2**	**K_2 (g/mg min)**	**Q_e (mg/g)**	**R^2**	**K_{id} (mg/g min$^{0.5}$)**	**C (mg/g)**	**R^2**
					CR					
50	63.017	0.010	47.66	0.20	$1.29\ x10^{-4}$	79.27	0.98	3.38	0.95	0.95
100	125.451	0.007	45.81	0.48	$2.43x10^{-4}$	129.34	0.94	4.79	35.11	0.87
150	186.129	0.010	73.45	0.53	$1.79x10^{-4}$	194.14	0.92	6.92	59.40	0.84
200	246.082	0.008	49.09	0.81	$3.56x10^{-4}$	250.82	0.97	7.03	127.45	0.60
250	299.883	0.009	51.18	0.88	$2.84x10^{-4}$	317.17	0.98	8.16	177.80	0.51
					DB					
50	93.07	0.007	25.01	0.73	$5.47x10^{-4}$	95.75	0.89	2.88	41.66	0.68
100	185.49	0.010	53.79	0.67	$3.46x10^{-4}$	184.64	0.98	5.89	78.40	0.70
150	277.21	0.007	86.48	0.72	$1.74x10^{-4}$	278.35	0.89	8.35	119.09	0.68
200	350.70	0.009	115.16	0.76	$1.29x10^{-4}$	355.82	0.89	10.11	159.32	0.66
250	426.05	0.02	185.80	0.63	$0.86x10^{-4}$	467.68	0.91	15.31	171.26	0.78

Table S.4.3. *Thermodynamics Parameters (ΔG°, ΔH°, and ΔS°) for adsorption of CR and DB by AAC-CTAB*

C_i (mg/L)	**Temp. (K)**	**CR**			**DB**		
		ΔG^o kJ/mol	**ΔH^o kJ/mol**	**ΔS^o J/molK**	**ΔG^o kJ/mol**	**ΔH^o kJ/mol**	**ΔS^o J/molK**
50	**293**	-20.98	-0.28	70.76	-18.61	-0.29	62.12
	303	-21.66			-19.06		
	313	-22.70			-19.69		
	323	-22.97			-20.18		
100	**293**	-22.60	-8.00	101.87	-18.44	-20.57	133.13
	303	-22.15			-21.30		
	313	-22.85			-22.05		
	323	-25.91			-22.27		
150	**293**	-24.00	-2.73	88.16	-18.17	-39.42	196.26
	303	-22.98			-21.34		
	313	-23.92			-23.19		
	323	-26.80			-23.78		
200	**293**	-23.33	-10.36	113.43	-15.93	-57.96	251.52
	303	-23.66			-18.96		
	313	-24.34			-22.34		
	323	-26.99			-22.96		
250	**293**	-24.86	-8.48	54.60	-15.67	-44.41	204.77
	303	-24.68			-18.72		
	313	-25.02			-20.79		
	323	-26.64			-21.55		

CHAPTER 5

Polypyrrole complexation on biomass-derived powdered carbon for adsorptive elimination of emerging pharmaceutical contaminant Sulfamethoxazole

GRAPHICAL ABSTRACT

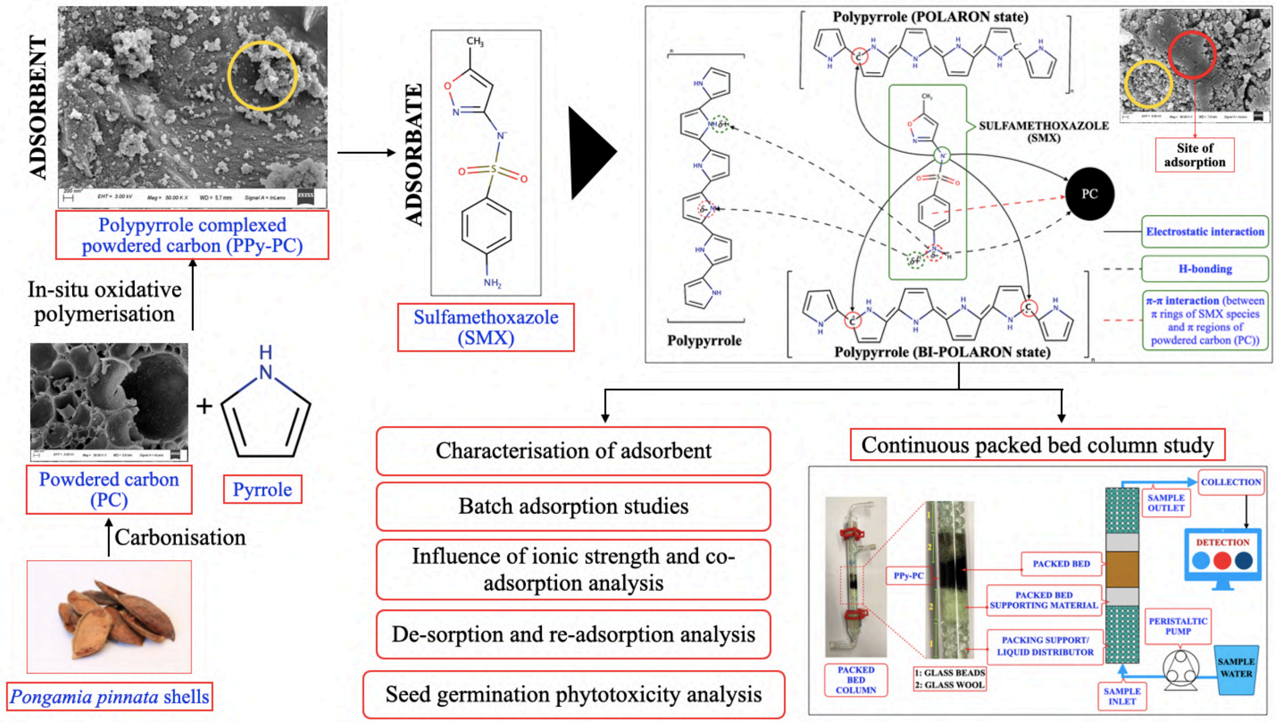

Abstract

Adsorbents rich in Nitrogen-containing functional groups offer positively charged surfaces for efficient adsorptive elimination of anionic antibiotic species from aqueous setups. The current study aims to enrich the surface of biomass-derived powdered carbon with Nitrogen-rich polypyrrole polymer (PPy-PC) via in-situ oxidative polymerisation for adsorptive elimination of emerging antibiotic contaminant Sulfamethoxazole (SMX) from aqueous setups. Morphological alterations due to polypyrrole complexation and post SMX adsorption were studied using atomic force microscopy (AFM), powdered X-ray diffraction (XRD), Fourier-transformed infrared spectroscopy (FTIR), Potential, scanning electron microscopy (SEM), Energy-dispersive X-ray spectroscopy (EDS) and Zeta potential analysis. Efficient adsorptive interactions were reported at pH 6.0, owing to anionic SMX species and cationic polypyrrole forms viz. polaron state (PPy+.) and bi-polaron state (PPy++); apart from other transitional and neutral forms. Both Freundlich and Langmuir isotherm models gave a good fit with the experimental data verifying the possible multilayer adsorption due to stacked pyrrole monomers of polypyrrole and monolayer adsorption by the powdered carbon surface, respectively. Sorbate-sorbent interaction was governed by chemisorption as verified by the pseudo-second-order model and thermodynamically exothermic and spontaneous. Effect of variable ionic strengths of SMX medium and co-existing heavy metals and antibiotics was studied to understand the behaviour of the adsorbent in adsorbing SMX species. De-sorption and re-adsorption analysis verified that the adsorbent could be recycled for multiple cycles. Phytotoxicity assay using *Vigna mungo* seeds verified the adsorbent's efficacy in remediating pharmaceutical waste effluents for its reuse. Continuous column studies verified lower column bed heights (cm), higher inlet feed concentrations (mg/L), and higher initial feed flow rates (mL/min) resorted to quick saturation of the packed bed column.

5.1. Materials and methods

The list of all the reagents and salts and their roles in the present study has been mentioned in **Table A.1.** (Appendix).

5.1.1. Preparation of Polypyrrole complexed powdered carbon

Pulverised *Pongamia pinnata* shells were carbonised at 673 K in a muffle furnace for 2h. The char was thoroughly washed after carbonisation to rinse away any ash content. It was then oven-dried, and the resulting dried carbonaceous material was again pulverised to fine powder form. The powdered carbon matter was then stored in an oven and marked PC.

The prepared carbon (PC) was then complexed with Polypyrrole (PPy) via in-situ oxidative polymerisation using ammonium persulfate (APS) as the oxidant, using a similar protocol reported by Xiang et al., 2021 and Wu et al., 2005, with some modifications for the present study. Carbon dispersion was prepared by mixing 0.5 g of PC with 100 mL distilled water under vigorous stirring conditions at room temperature. This was followed by the addition and overnight mixing of Cetyltrimethylammonium bromide (CTAB) under the same stirring conditions at 313 K. 0.50 mL of pyrrole monomers (aqueous phase) was then added dropwise to the resulting mixture, and it was allowed to mix for 6-12 hours to ensure its uniform mixing. Oxidant solution consisting of 1.7453 g of ammonium persulfate (APS) dissolved in 5M HCl (8.56 mL, 5 M) was prepared separately, and it was then slowly injected into the carbon-pyrrole-CTAB dispersion mixture with a syringe (dropwise) under stirring conditions for 12 h to ensure sufficient polymerisation. After mixing, the obtained composites were filtered and washed with ethanol and distilled water to remove any remnant CTAB species or any other oligomeric component; until the pH of the filtrate was ~7.0 or equivalent to distilled water. The washed composite was then dried in the vacuum oven at 333 K for 12 h, after which it was stored. Powdered carbon complexed (PC) with polypyrrole (PPy) composite in 1:1 (adsorbent: pyrrole) ratio was finally prepared, and it was labelled PPy-PC.

Polypyrrole homopolymers (PPy) were synthesised using a similar preparation process, without the addition of powdered carbon.

5.1.2. Adsorption experiments

All batch experiments were conducted at 150 rpm for 24 hours using a temperature and rpm controlled shaker incubator (ORBITEK-LE, Scigenics Biotech, India). After each batch experiment, the reaction mixture was separated using Whatman filter paper (110 mm, grade 4), and the spent adsorbate medium was assayed for remaining adsorbate (SMX) species at a fixed wavelength of 258 nm via a UV-Visible spectrophotometer (Tecan, Infinite 200 PRO, Switzerland).

5.1.3. Influence of ionic strength and co-adsorption analysis

Pharmaceutical wastewater may contain multiple salt ions affecting its ionic strength, along with several heavy metals and other pharmaceutical wastes, which may affect the adsorptive uptake of specific antibiotic species by the adsorbent. To understand such effects, adsorptive experiments were conducted at variable ionic strengths of SMX solution and in the presence of heavy metals and other antibiotics. Lead (Pb^{+2}), Copper (Cu^{+2}) and Zinc (Zn^{+2}) ions were selected for co-existing heavy metal studies. The choice of heavy metals for the current study was based on previous reports by Kumari and Tripathi, 2019 and Pérez-Alvarez et al., 2018. Two antibiotics viz. Ciprofloxacin (fluoroquinolone) and Amoxicillin (β-lactam) were selected for co-existing antibiotics studies. Such antibiotics were chosen due to their common occurrence in domestic and industrial pharmaceutical wastes, as reported by Githinji et al., 2011 and Mahmood et al., 2019. Effect of co-existing heavy metals and antibiotics was studied with 200 mg/L of SMX mixed to 200 mg/L of heavy metal and antibiotics solutions (separately) in the ratio of 1:1. The concentration of heavy metals for all sets of experiments were assayed using an Inductively Coupled Plasma-Atomic Emission Spectrometer (AES) (PerkinElmer).

For variable ionic strengths, SMX solution was prepared in 5 different molar concentrations of NaCl and KCl solutions viz. 0.01M, 0.05M, 0.1M, 0.5M and 1.0M.

5.1.4. De-sorption and re-adsorption analysis

The recyclability potential of the synthesized adsorbent (PPy-PC) was assessed via consecutive adsorption-desorption cycles. 0.1 NaOH was selected as the desorbing agent for the spent adsorbent after an adsorption cycle. After every adsorption cycle, the spent adsorbent had to undergo a desorption cycle to regenerate its surface for the consecutive cycle. The desorption cycle involves the separation of spent adsorbents from the reaction mixture, followed by its treatment with a fixed volume of 0.1 NaOH for a specified period. It was then washed with distilled water to rinse away any NaOH or adsorbate residues. The washed adsorbent was then oven-dried overnight. The dried desorbed adsorbent was then recycled for the subsequent adsorption cycle, followed by another desorption cycle. Consecutive adsorption and desorption cycles were carried out until the removal efficiency (%) of the adsorbent (PPy-PC) was minimized to ≈50%.

The choice of 0.1N NaOH as the desorbing agent was based on its ionic distribution in aqueous solutions. NaOH could neutralize the ionic forms of pyrrole (PPy) and SMX residue in an aqueous solution, thus preventing their electrostatic interactions. NaOH can also neutralize the oxidized surface functional groups of powdered carbon (PC). This will also result in shedding off of any SMX species adsorbed over the PC surface.

5.1.5. Seed germination phytotoxicity analysis

Phytotoxicity assessment was done to verify the efficacy of PPy-PC in eliminating SMX residues from aqueous setups. It was done by germinating *Vigna mungo* (black gram) seeds in post adsorptive solutions. Following its germination, the root length (in cm) was measured to evaluate the difference in roots germination in pre and post adsorptive solutions. Simultaneously, the root length data were further evaluated to understand the germinated seeds' growth inhibition (%). Seed phytotoxicity assays were carried out following the prescribed guidelines mentioned by USEPA, 1996 (Ecological Effects Test Guidelines, OPPTS 850.4025, Target Area Phytotoxicity), with few additional modifications.

Vigna mungo seeds were first washed with 1% Sodium Hypochlorite (NaClO) solution to rinse away any contaminant sticking to its surface. This was followed by washing with distilled water and overnight drying under normal conditions. A total of 10 dry seeds were then soaked with respective solutions viz. solution that did not undergo any adsorption treatment (control samples), solution post adsorptive treatment (test samples) and distilled water (blank). 3 variable concentrations of SMX solution i.e. 10 mg/L, 50 mg/L and 100 mg/L at pH 7.0; were considered for the experiments. The seeds were germinated in normal conditions for seven days, after which the root lengths were measured and reported.

5.1.6. Continuous-packed bed column studies

Packed bed continuous column studies were performed with simulated SMX solutions in a borosilicate glass column of length 15 cm, column diameter of 15 mm and inlet/outlet diameter of 9 mm. The column dimensions were based on previous studies and reports done for the same purpose. The adsorbent was packed into the glass column and was placed in between a layer of glass beads (<5 mm dia.) and glass cotton as supporting materials, as depicted in **Figure 5.1.**

Variable SMX concentrations of 10 mg/L, 50 mg/L and 100 mg/L were selected for the packed bed column continuous study. The choice of flow rates (mL/min) and adsorbent bed height (cm) values were based on the considered experimental mean value. For lower and upper limits, half and double of mean values were considered, respectively. Thus, variable bed heights of the adsorbent (PPy-PC), i.e. 0.5 cm, 1 cm and 2 cm, was packed in the glass column. Simultaneously, for varying flow rates experiments, 3 flow rates of the effluent solution were considered viz. ≈1.5 ml/min, ≈3.0 ml/min and ≈6.0 ml/min. Uniform flow rates were maintained using a peristaltic pump (Miclins PP 20 ex, India) in an up-flow direction. Samples collected at fixed intervals from the outlet of the column was evaluated for SMX species. Variable parameters governing the packed bed column's efficacy in adsorbing SMX were analysed using various equations as mentioned in **Section A.1.4.** (Appendix).

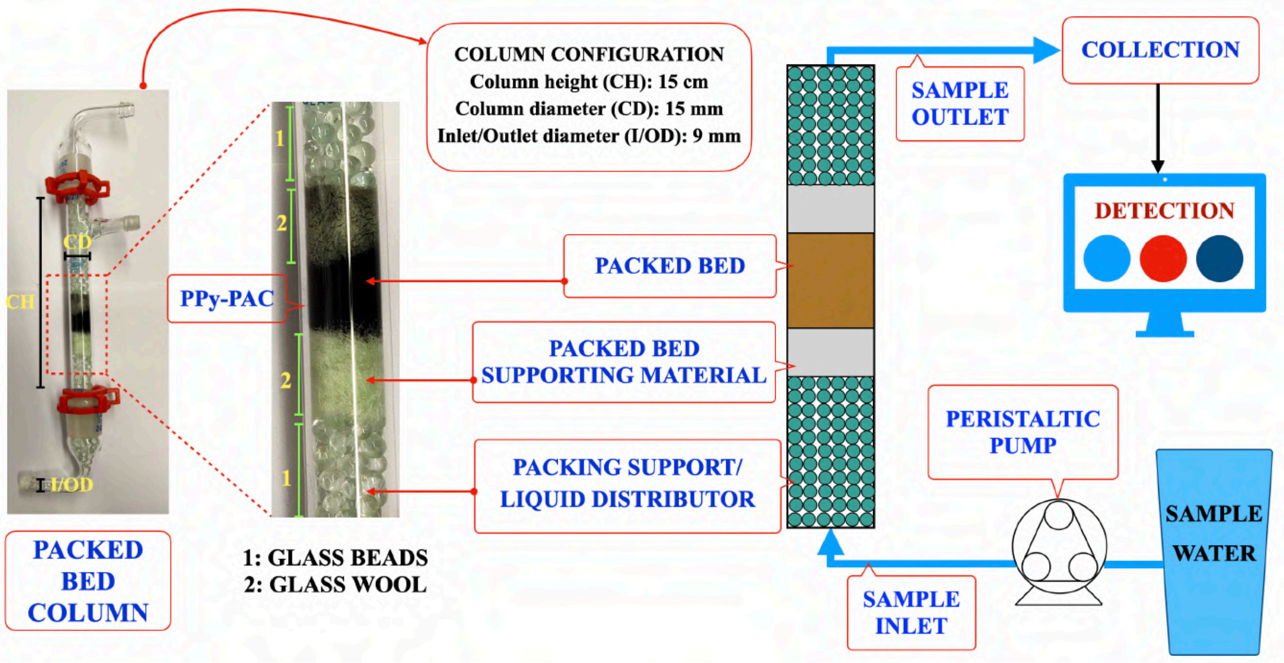

*Figure **5.1**. Schematic representation of packed bed column setup and its working*

5.2. Results and discussion

5.2.1. Characterisation of adsorbent

The list of instruments used for characterisation in the present study with their make and model has been detailed in **Table A.2.** (Appendix).

5.2.1.1. Atomic force microscopy analysis

Atomic force microscopy (AFM) was done to evaluate the morphological alterations before and post polypyrrole (PPy) complexation on powdered carbon (PC) surface, and the same has been depicted in **Figure 5.2. (A, B)**. Due to the erratic distribution of surface peaks, the PC surface shows an uneven surface morphology with a maximum peak height of 4.6 nm (**Figure 5.2. (A)**). However, post complexation with PPy, the surface of PPy-PC shows conical-shaped aggregates protruding upwards from the surface. These conical aggregates could be due to the polymerisation of pyrrole (PPy) groups over the conical-hemispherical aggregates of CTAB on the PC surface.

These aggregates show a maximum peak height of 47 nm, thus verifying surface modifications due to PPy complexation over PC surface, resulting in PPy-PC, as depicted in **Figure 5.2. (B)**.

Such conical aggregates could be due to the involvement of Cetyltrimethylammonium bromide (CTAB) during the in-situ oxidative polymerisation process of PPy. CTAB is responsible for the micellar base where the further polymerisation step occurs. CTAB arranges itself into conical-hemispherical shaped aggregates over the PC surface, as reported comprehensively in our previous study Patra et al., 2020, and also reported by Wang et al., 2018. The polymerisation of pyrrole to polypyrrole over these conical-hemispherical shaped bases could have resulted in the formation of conical-shaped aggregates over PC, as depicted in **Figure 5.2. (B)**.

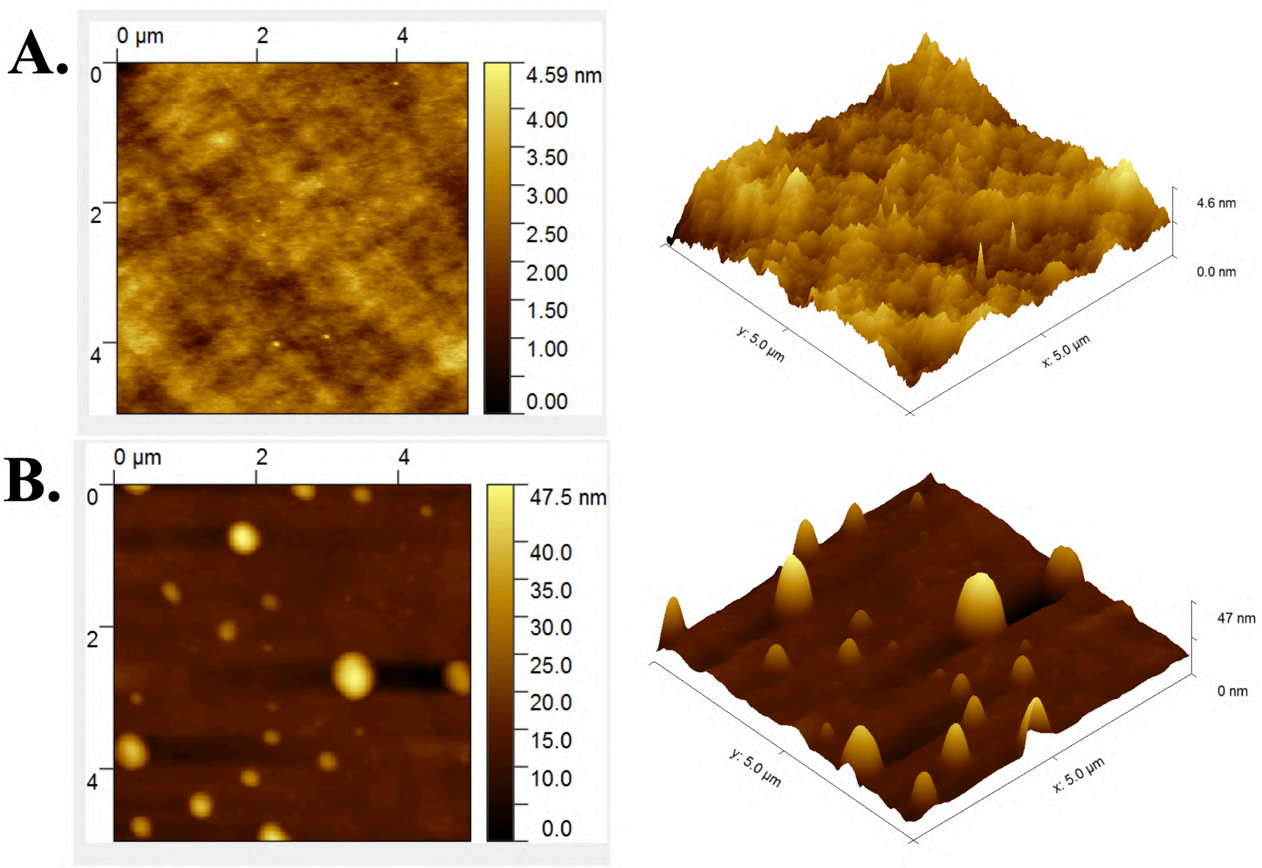

Figure 5.2. *Atomic force microscopy (AFM) image of;* ***(A)****: powdered carbon (PC);* ***(B)****: polypyrrole complexed powdered carbon (PPy-PC)*

5.2.1.2. Powder X-ray diffraction of the adsorbent

Figure 5.3. represents the X-ray diffractograms for powdered carbon (PC) prior and post polypyrrole complexation (PPy-PC). PC shows two broad diffraction peaks at 2θ values of 24° and 43°, corresponding to the diffraction of (002) and (10) planes, respectively. The XRD pattern verified the powdered carbon to be in a semi-crystalline state, which lies in consent with a prior

report on carbonaceous materials, as reported by Prahas et al., 2008. The XRD spectrum of pure polypyrrole shows a broad diffraction peak at 2θ=25.8°, the characteristic of amorphous polypyrrole (PPy). This broadening of the peak can be ascribed to the scattering from PPy fibres at the inter-planar spacing (Fan et al., 2015 and Moarref et al., 2016). However, post PPy complexation over PC, i.e. PPy-PC, showed diffraction peaks similar to powdered carbon before polypyrrole complexation, i.e. at 2θ = 25° and 43°. This verifies that in-situ oxidative polymerisation of pyrrole did not alter the carbon structural sub-structure of the powdered carbon.

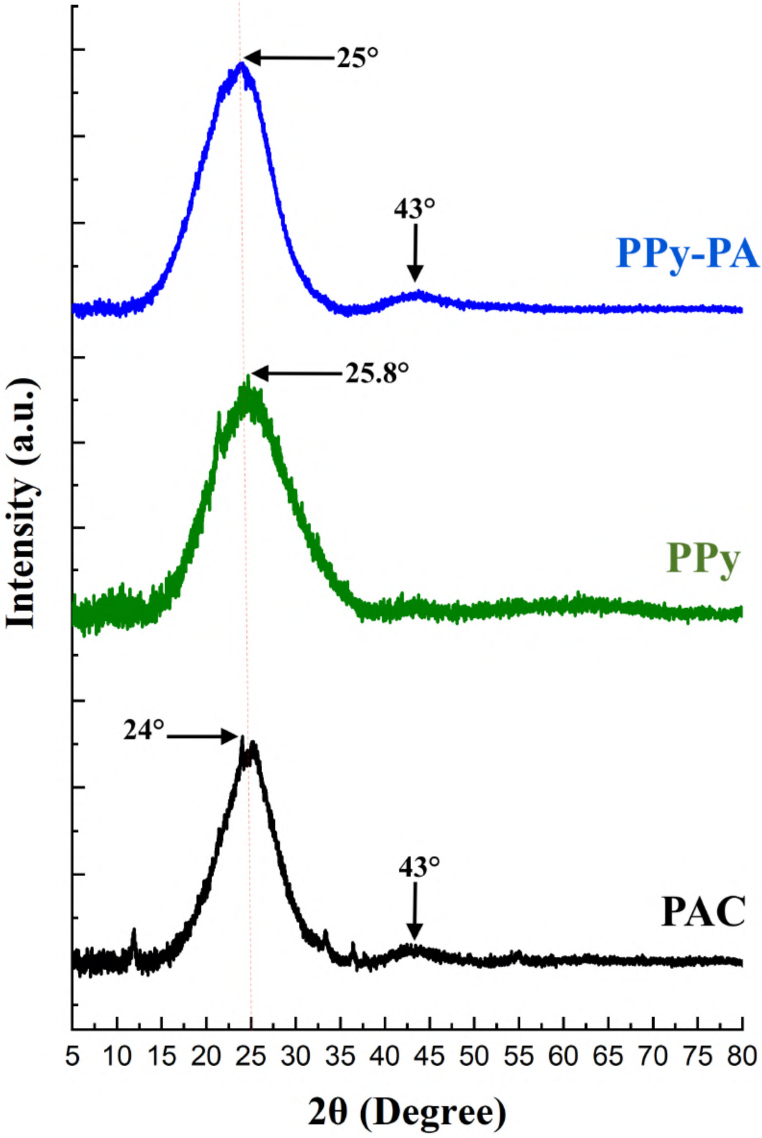

Figure 5.3. *X-ray diffraction patterns for powdered carbon (PC), polypyrrole (PPy) and polypyrrole complexed powdered carbon (PPy-PC)*

5.2.1.3. Surface morphology and elemental analysis

Scanning electron microscopy (SEM) images, as represented in **Figure 5.4. (A, B, C, D)**, depicts major morphological modifications to powdered carbon (PC) surface, prior and post polypyrrole (PPy) complexation. PC surface exhibits the usual honeycomb porous structure with variable pore sizes (macro and micro) and deep cavities. Due to such enhanced porous morphology, carbonaceous materials are preferred as adsorbents for various adsorbate species (**Figure 5.4. (A)**). **Figure 5.4. (B)** represents the traditional fibrous structure of polypyrrole, with individual pyrrole monomers stacked over each other. Simultaneously, **Figure 5.4. (C)** represents the polypyrrole (PPy) complexed carbon surface (PPy-PC). The PPy molecules can be seen complexed over the carbon (PAC) surface, indicating that pyrrole molecules underwent polymerisation to form polypyrrole on the PC surface, resulting in the formation of PPy-PC. Post SMX adsorption, the surface un-uniformity of PPy-PC was affected, as depicted in **Figure 5.4. (D)**. In the figure, PPy molecules can be seen capped with SMX residues, resulting in reduced surface irregularities. This justifies the adsorptive uptake of SMX species by PPy-PC. Conclusively, SEM analysis verifies the polymerisation of pyrrole to polypyrrole and its complexation over the carbon (PC) surface and adsorption of SMX antibiotic species over the PPy-PC surface.

Adsorption of SMX species over PPy-PC surface was further verified by Energy-dispersive X-ray spectroscopy (EDS) analysis (**Figure 5.4. (E, F)**). The presence of prominent sulphur (S) peaks for the EDS spectrum of PPy-PC post SMX adsorption (**Figure 5.4. (F)**) as compared to the spectrum of PPy-PC before adsorption (**Figure 5.4. (E)**) verified the adsorptive deposition of SMX species over the PPy-PC surface.

Conclusively, SEM imaging established the complexation of polypyrrole (PPy) polymers over powdered carbon (PC) surface to form PPy-PC. Both SEM and EDS analysis affirmed the adsorptive uptake of SMX species over the PPy-PC surface.

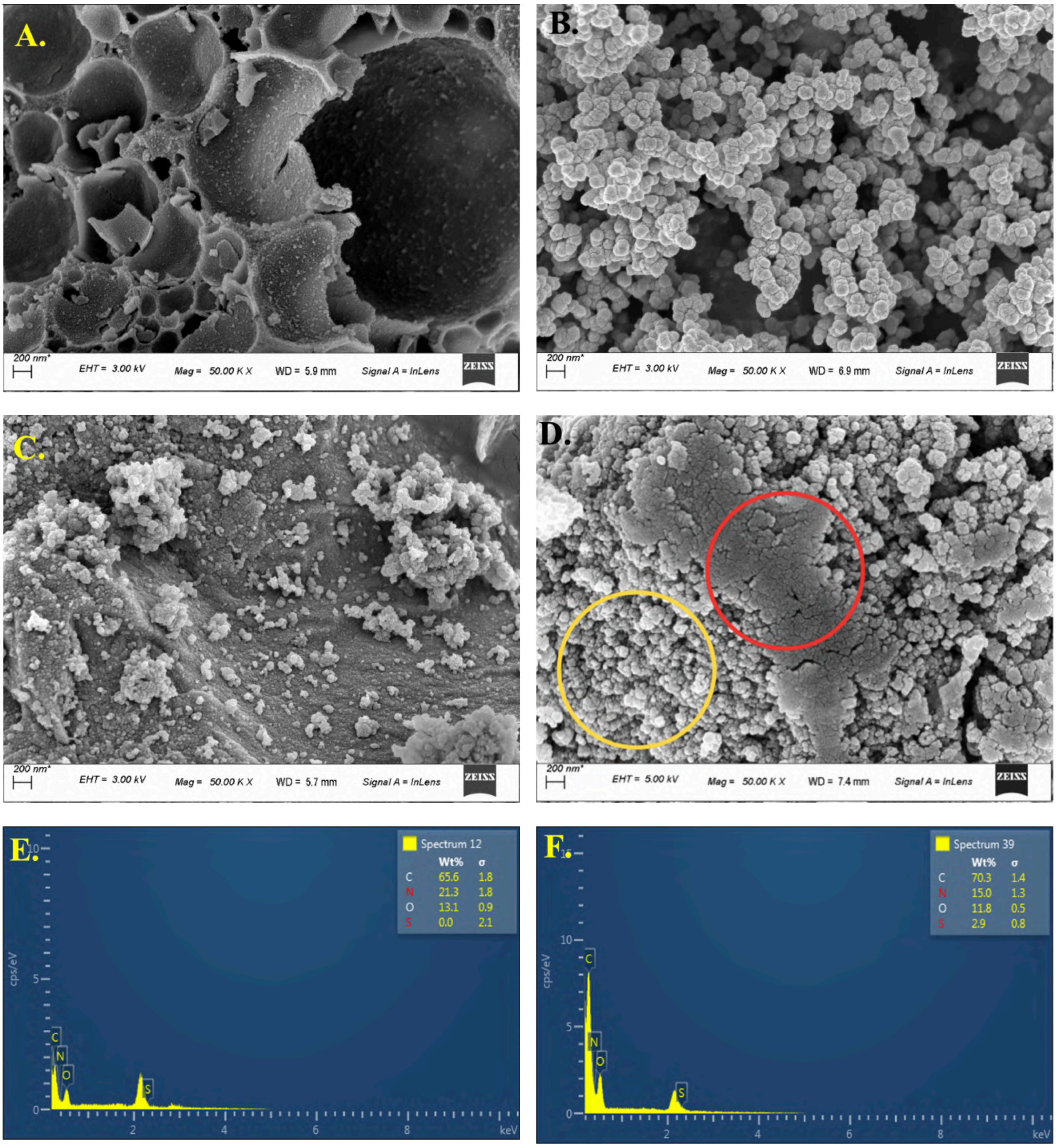

Figure 5.4. *Scanning electron microscopy (SEM) image of* ***(A)****: powdered carbon (PC);* ***(B)****: polypyrrole (PPy);* ***(C)****: polypyrrole complexed powdered carbon (PPy-PC);* ***(D)****: polypyrrole complexed powdered carbon adsorbed with Sulfamethoxazole (PPy-PC/SMX) and Energy-dispersive X-ray spectroscopy (EDS) of* ***(E)****: PPy-PC before SMX adsorption and* ***(F)****: PPy-PC after SMX adsorption*

5.2.1.4. FT-IR spectral analysis

Fourier-transform infrared spectroscopy (FT-IR) analysis was conducted from the spectral wavelength range of 4000 cm^{-1} to 500 cm^{-1} to understand the surface functional groups involved in the complexation and adsorption process; as depicted in **Figure 5.5.** Respective functional groups related to the concerned wavelengths were verified from IR Spectrum Table and Chemistry LibreTexts.

Powdered carbon (PC) showed a significant peak from 3700 cm^{-1} to 2400 cm^{-1}. This peak resulted from strong -OH stretching of carboxylic acid groups and medium N–H stretching of amine and amide groups. Another major peak at 1224 cm^{-1} for PC was due to strong C–OH stretching of alcoholic groups. In addition, peaks between 1650 cm^{-1} and 1450 cm^{-1} were observed due to medium C-H (alkane) bending and strong N-O (nitro) stretching. Carbonaceous materials produced from lignocellulosic precursors will exhibit such spectroscopic peaks. Similar spectroscopic analyses for carbonaceous materials were also carried out by Ali et al., 2020.

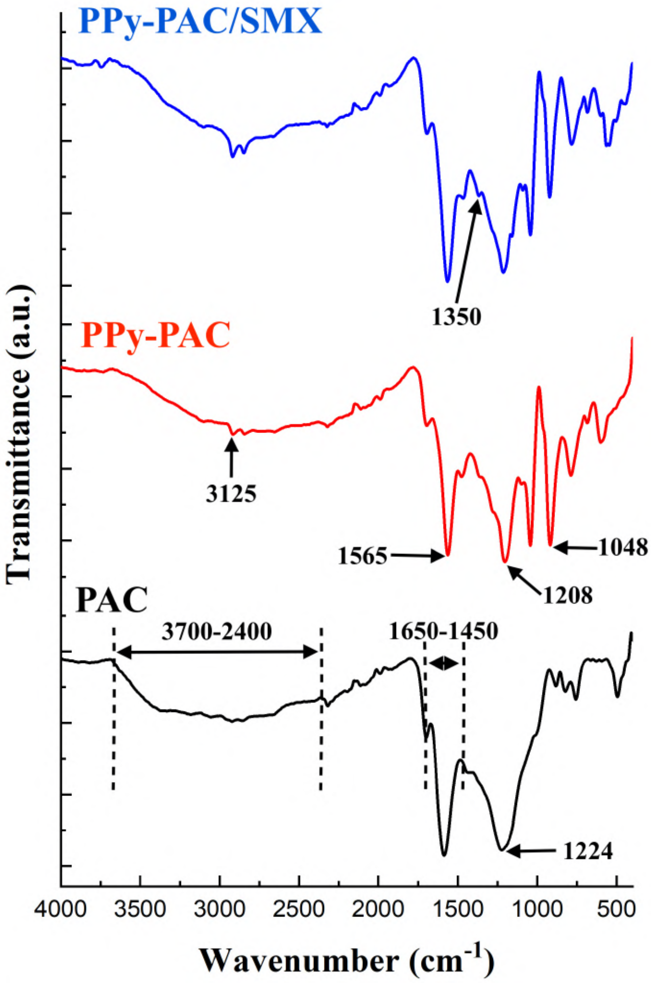

Figure 5.5. *FT-IR spectra of polypyrrole (PPy), polypyrrole complexed powdered carbon (PPy-PC) and polypyrrole complexed powdered carbon adsorbed with Sulfamethoxazole (PPy-PC/SMX)*

Polypyrrole complexed powdered carbon (PPy-PC) showed multiple major peaks at 1565 cm^{-1}, 1208 cm^{-1} and 1048 cm^{-1}, which corresponds to medium C=C (cyclic alkene) stretching, strong C-N (aromatic amine) stretching and C-H plane deformation bonds, respectively. A major peak at

3125 cm^{-1} corresponds to N-H stretching associated with vibrations of the pyrrole ring. Similar peaks specifically for polypyrrole (PPy) species were also reported by Yussuf et al., 2018. This verifies the successful complexation of PPy over powdered carbon (PC) surface. PPy-PC complexed with SMX species showed a distinct minor peak from 1350 cm^{-1} which corresponds to strong S=O (sulfonamide) stretching, thus conforming to the adsorption of SMX species over the PPy-PC surface. Conclusively, the band peaks from FTIR analysis verify the successful complexation of polypyrrole over powdered carbon, followed by successful adsorption of SMX antibiotic species.

5.2.1.5. Zeta potential analysis of adsorbent

The Zeta potential of the adsorbent was measured as a function of pH within the pH range of 2.0–10.0 of the aqueous dispersion medium. PPy-PC showed positive zeta potential values until the iso-electric pH (pH_{IEC}), i.e. 6.65. Beyond pH_{IEC}, PPy-PC showed negative zeta-potential values. This behaviour of PPy-PC at variable pH is depicted in **Figure 5.6. (A)**, was due to the surface functional groups of powdered carbon (PC) and the complexed polypyrrole (PPy) molecules.

High-temperature oxidation provides the adsorbent's surface with negatively charged oxygen functional groups, causing it to attract excess protons (H^+ ions) at lower pH values. Simultaneously, polypyrrole molecules also acquire the two pre-dominant cationic states, i.e. polaron state (PPy+.) and bi-polaron state (PPy++), apart from other transitional and neutral forms (Lei et al., 2014). This results in a positively charged surface creating a potential difference with the dispersive aqueous phase with relatively fewer protons (H^+ ions). This contributes to net positive zeta potential values for the adsorbent at lower pH.

However, gradual elevation in pH resulted in an increased concentration of hydroxide (OH^-) ions. These OH^- ions neutralise the positively charged groups of the adsorbent. This gradually increases the intensity of negative charges on the surface of the adsorbent, rendering the adsorbent with negative zeta potential values.

The influence of the surface charge of the adsorbent (PPy-PC) over its adsorption capabilities has been depicted in **Figure 5.6. (B)**. It was done by linking the adsorption efficiency data at variable pH of SMX medium and the zeta potential values for PPy-PC at variable pH of the dispersion medium. **Figure 5.6. (B)** shows 3 distinct regions with variations in the adsorption efficiencies:

Region 1: This region lies between zeta potential values of +12 mV to +25 mV, corresponding to pH 2.0 to 6.0. This region shows an abrupt increase in the adsorption efficiencies (%), i.e. from almost 34% to 60%. It was due to the developing cationic and anionic charges on the adsorbent (PPy-PC) and the adsorbate (SMX), respectively, causing them to interact electrostatically.

Region 2: This region ranges from -6 mV to +12 mV, corresponding to pH 6.0 to 7.0. The adsorption efficiencies remain almost the same in this region without much variation. It could be due to dominating dispersion forces between the adsorbent (PPy-PC) and the adsorbate (SMX) species, causing the adsorption efficiencies to stand still (Dai, 1994).

Region 3: In this region (where zeta potential values are less than −6 mV), the adsorption efficiency of the adsorbent declines. It was due to dominating repulsive forces between the similar pre-dominant anionic charges of the adsorbate (SMX) and the adsorbent (PPy-PC) species.

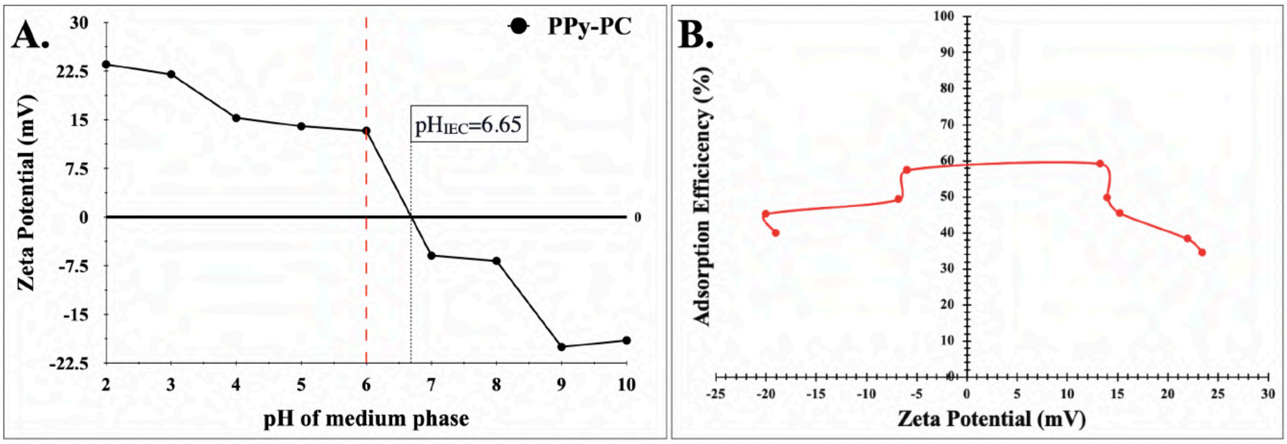

***Figure 5.6. (A)**: Zeta potential analysis of PPy-PC; **(B)**: Influence of zeta potential over the adsorption of SMX species by PPy-PC*

5.2.2. Investigation of sorption parameters

The variable initial pH of the SMX solution caused charge-based interactions between the adsorbate (SMX) and the adsorbent (PPy-PC), as depicted in **Figure 5.7. (A)** SMX was efficiently adsorbed at pH 6.0. Such adsorptive behaviour was due to ionic speciation of SMX species and the protonation/ de-protonation of the adsorbent (PPy-PC) at variable pH. Owing to SMX's pK_a values at 1.6 and 5.7, SMX acquires its anionic form at pH≥5.7 (Boreen et al., 2004). Simultaneously at pH 6.0, polypyrrole (PPy) species will develop two cationic states vis. polaron state (PPy+**.**) and bi-polaron state (PPy++), apart from other transitional and neutral forms (Lei et al., 2014). Hence at pH 6.0, positively charged PPy and negatively charged SMX species will promote strong electrostatic interactions, thus resorting to efficient removal of SMX species. Apart from the electrostatic interactions, partial negatively charged nitrogen atoms and partial positively charged hydrogen atoms in SMX and PPy species interact via H-bonding, thus contributing to the adsorptive interactions. However, at very low pH values vis. pH ≤2.0, SMX is positively charged, and for pH 3.0-5.0, SMX will be in neutral forms. Such conditions do not favour strong adsorptive interactions between SMX species and PPy-PC molecules. Simultaneously at higher pH values, i.e. pH≥7.0, the intensity of polaron and bi-polaron states of PPy are pre-dominantly affected due to competing OH- ions, as explained in zeta potential analysis. This too, inhibits the efficient interaction of PPy and SMX species at higher pH values. Therefore, adsorption of SMX on PPy-PC was influenced by the initial pH of SMX solution, and pH 6.0 was selected as the optimal pH for the rest of the sorbate-sorbent interaction study.

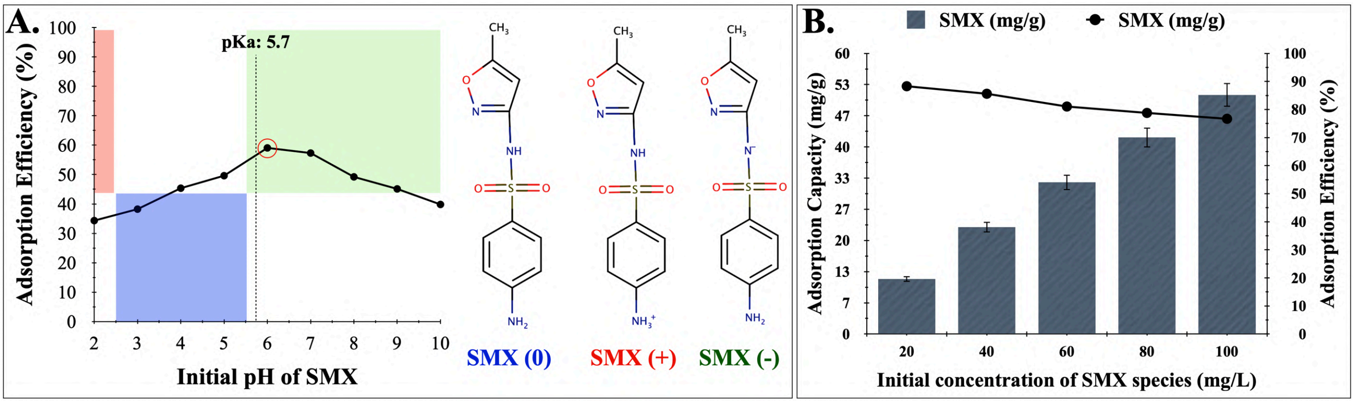

Figure 5.7. ***(A)***: *Influence of initial pH of SMX medium on its adsorption over PPy-PC;* ***(B)***: *Influence of variable initial concentration of SMX medium*

Figure 5.7. (B) depicts the influence of variable initial SMX concentrations (20-100 mg/L) at optimised pH of 6.0 and a fixed dosage of PPy-PC. With the increase in the initial concentration of SMX, the adsorbent's adsorption efficiency (%) and its adsorption capacity (mg/g) showed antagonistic trends. Such behaviour of the adsorbent can be attributed to its fixed intensity of available active sites, which get saturated with the rising initial concentration of SMX species. The adsorption efficiency (%) of an adsorbent is governed by the relative intensity of available active sites. So with the increase in SMX's initial concentration, the relative intensity of the PPy-PC's available active sites is reduced, thus resulting in reduced adsorptive efficiencies.

On the contrary, the adsorbent's adsorption capacity is governed by the intensity of the filled active sites. Thus for a fixed dosage of adsorbent, the rise in initial SMX concentration resulted in increased intensity of the PPy-PC's filled active sites. This resulted in elevated adsorption capacities for the adsorbent (PPy-PC) with the rising initial concentration of the adsorbate (SMX).

5.2.3. Sorbate-sorbent interaction analysis

5.2.3.1. Physiochemical properties of the adsorbent and adsorption mechanism

5.2.3.1.1. Biomass carbonisation and polypyrrole complexation

Powdered carbon (PC) was prepared using *Pongamia pinnata* shell as the lignocellulosic precursor via carbonisation at high temperatures. Carbonisation at high temperatures promotes an oxidised surface with weak acidic functional groups and a porous morphological matrix with rigid pore boundaries (Bhatnagar et al., 2013).

Polypyrrole complexed powdered carbon composite (PPy-PC) was prepared via in-situ oxidative polymerisation using ammonium persulfate (APS) as the oxidant, as mentioned earlier. The first step of the process involved complexing the surface of PC with Cetyltrimethylammonium bromide (CTAB). CTAB/H2O setup forms a micellar setup around the PC surface, with the hydrophobic alkyl tails directing inwards and the polar quaternary ammonium heads directing outwards (Patra et al., 2021). CTAB molecules thus developed self-assembly of surfactant molecules over PAC that serve as the template for the polymerisation process and play an essential role in tailoring the nanostructure of polypyrrole (PPy). Pyrrole, a hydrophobic molecule, will tend to self-locate itself to the interior of the CTAB template. This self-adjustment of the hydrophobic pyrrole molecules to the hydrophobic tails of the surfactant in the micellar setup could be due to and governed by the non-polar to non-polar attraction (like attracts like) (Abdi et al., 2018). Given the fact that pyrrole is hydrophobic in nature, the presence of HCl lets pyrrole form a pseudo-hydrotrope system that helps to stabilise the pyrrole-micellar aggregates via inter-micellar H-bonding. The addition of ammonium persulfate (oxidant) further promotes the polymerisation of pyrrole aggregates to form polypyrrole (PPy) fibres. APS oxidises the pyrrole monomers resulting in anionic pyrrole molecules. These anionic pyrrole molecules then further polymerise, resulting in polypyrrole (PPy) polymer (Wang et al., 2015). It is believed that polymerisation might be initiated at the outer palisade layer of the micellar aggregate; bulk polymerisation may take place in the micellar core. CTAB/HCl system promotes the fibrous structure of polypyrrole (Wu et al., 2005). **Figure 5.8.** represents the schematic representation of the methodology of polypyrrole (PPy) synthesis and complexation over powdered carbon (PC), resulting in PPy-PC.

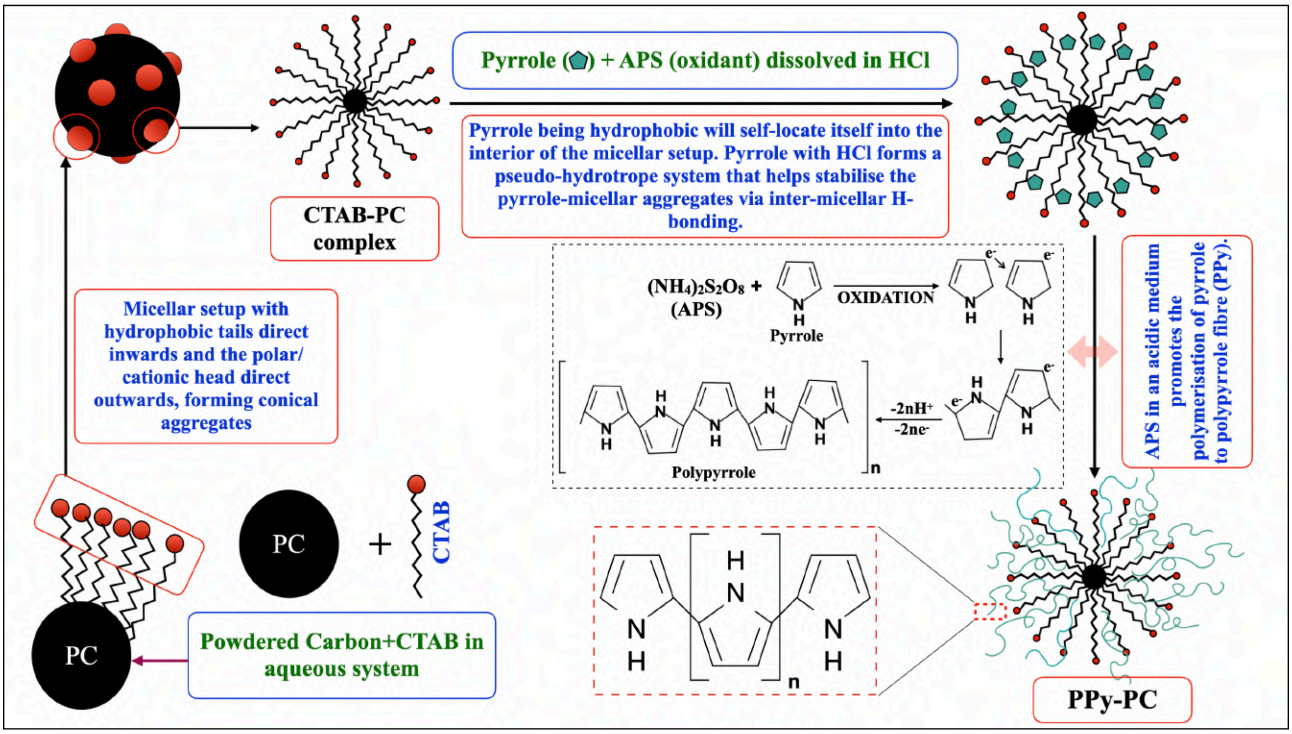

Figure 5.8. Schematic representation of the preparation of polypyrrole complexed powdered carbon (PPy-PC)

5.2.3.1.2. Adsorption mechanism

Polypyrrole possesses two ionic states vis. polaron state (PPy+·) and bi-polaron state (PPy++) in aqueous solutions, apart from other transition and neutral forms at pH 6.0. These two states provide PPy with possible positive charges that promote its electrostatic interaction with the negatively charged SMX species (pH 6.0) (Boreen et al., 2004), as depicted in **Figure 5.9.** Apart from electrostatic interactions, partial negatively charged nitrogen species (δ-), precisely due to the available lone pair of electrons, and partial positively charged hydrogen atoms (δ+) among both SMX and PPy species, contribute to H-bonding between SMX and PPy-PC. **Figure 5.9.** represents all possible adsorptive interactions between PPy-PC and SMX species, as discussed.

Simultaneously, the oxidised and porous surface of powdered carbon also promotes the uptake of SMX species due to electrostatic interactions, H-bonding, π-π interactions and several other adsorption mechanisms (Turk Sekulic et al., 2019).

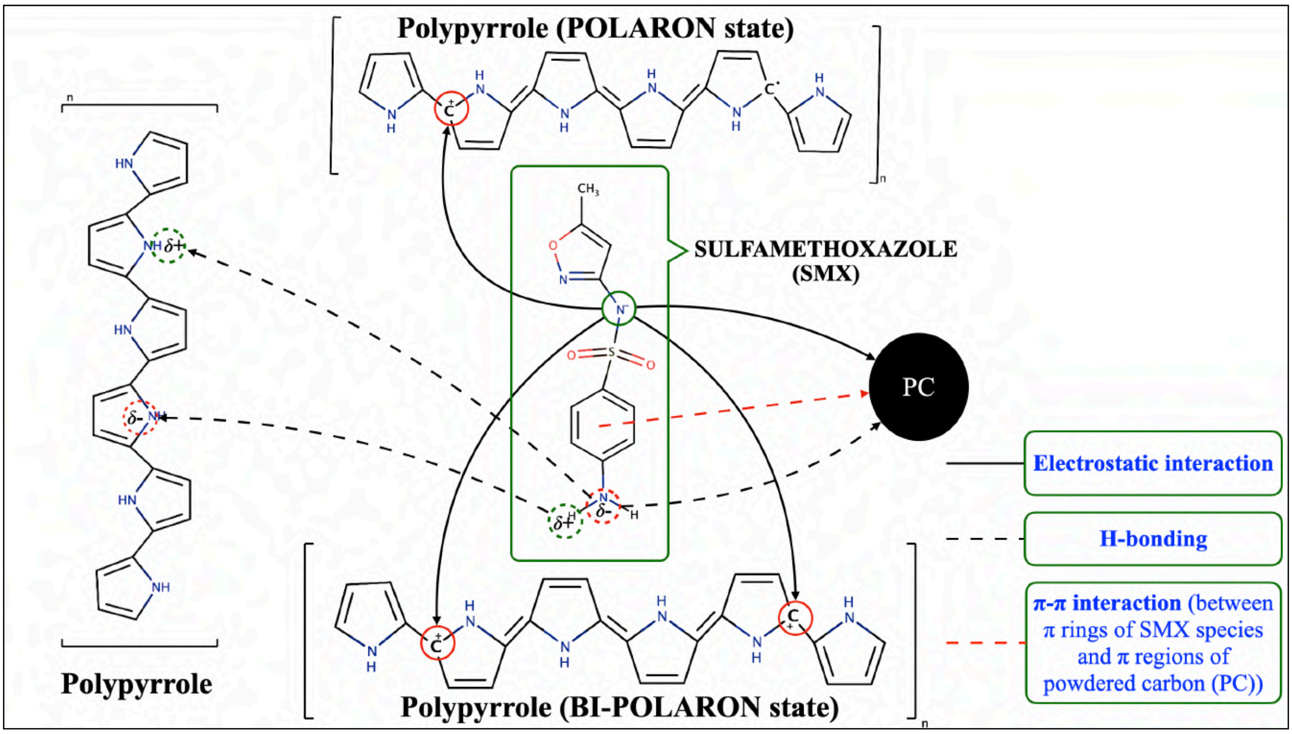

Figure 5.9. Schematic representation of the adsorptive interactions between the polypyrrole complexed powdered carbon (PPy-PC) and Sulfamethoxazole (SMX) molecules as pH 6.0

5.2.3.2. Sorbate-sorbent interaction modeling and thermodynamics analysis

The nature of sorbate-sorbent interactions at any constant temperature was studied using various isotherm models are reported in **Table A.3.** (Appendix). **Table S.5.1.** (Supplementary data) represents the values for the isotherm analysis of the adsorptive interaction. Freundlich isotherm model reported the closest fitting with the equilibrated data obtained from SMX and PPy-PC sorption interaction. Theoretically, Freundlich isotherm model supports the multi-layer adsorption of SMX species over heterogeneous PPy-PC surface. Langmuir isotherm model, which supports sorbate's monolayer adsorption over the adsorbent surface; reported a slightly less close-fitting with the equilibrated data than the Freundlich isotherm. The possible reason for both mono- and multi-layer adsorption by PPy-PC was due to the involvement of both PPy fibres and the carbon surface in the adsorption process. Since pyrrole monomers are stacked one over each other to form PPy polymer fibre; SMX's adsorption to PPy fibres promotes multi-layer adsorption. However, the exposed regions of powdered carbon (PC) will promote monolayer adsorption of SMX species. The calculated Langmuir maximum adsorption capacity ($Q_{L,max}$) for PPy-PC was 80.65 mg/g. Dubinin-Radushkevich isotherm model reported the least fit with the equilibrated experimental data; thus verifying the non-applicability of pore-filling phenomenon towards the adsorptive interaction. Non-linear isothermal plots, as depicted in **Figure 5.10.**, ascertain the applicability of both Freundlich and Langmuir isotherm model with the experimental data.

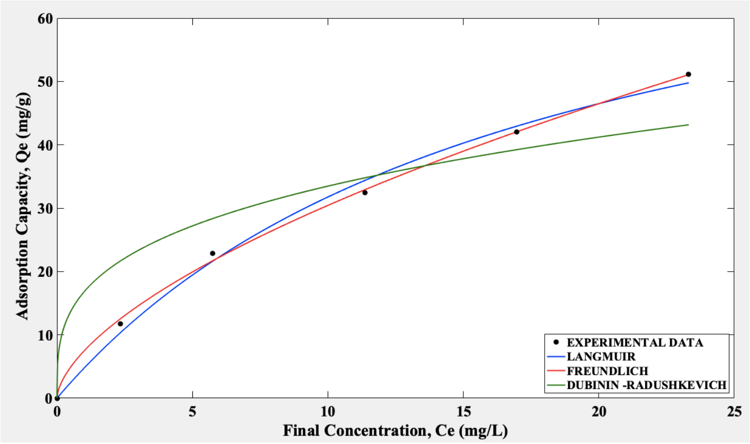

Figure 5.10. *Non-linear isothermal plotting of sorbate-sorbent adsorptive interactions*

Table A.4. (Appendix) represents the kinetic model parameters for the sorbate-sorbent interactions. **Table S.5.2.** (Supplementary data) represents the values for the kinetics of the adsorptive interaction. Coefficient of regression (R^2) values suggest pseudo-second-order kinetics model show the best fit with the experimental data; as compared to the pseudo-first-order and intra-particle diffusion kinetic models. The applicability of the pseudo-second-order kinetics can also be verified from the theoretical adsorption capacity (Q_e) values, as predicted by the model being near equal to the experimental adsorption capacity ($Q_{e\ Exp.}$) values. Theoretically, pseudo-second-order kinetics verifies the involvement of chemisorption, i.e. chemical interactions between SMX and PPy-PC. Non-linear kinetics plots, as depicted in **Figure 5.11.**, ascertain the applicability of the pseudo-second-order kinetics compared to other models.

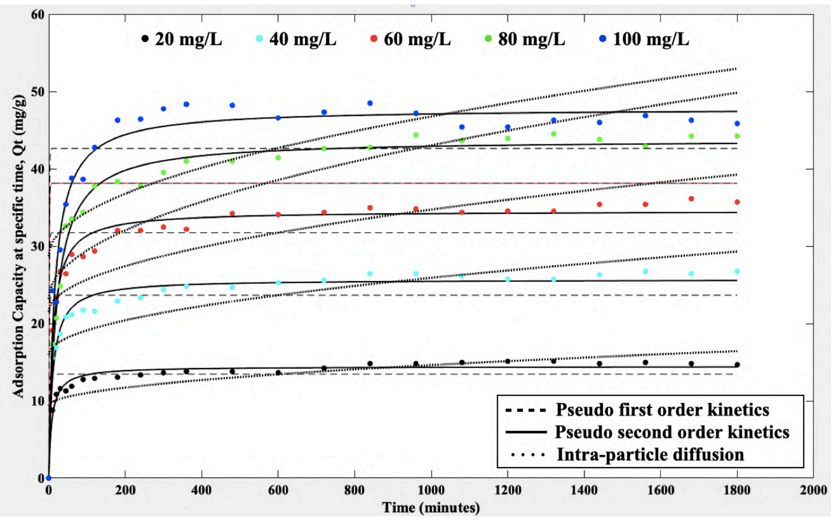

Figure 5.11. *Non-linear kinetics plotting of sorbate-sorbent adsorptive interactions*

Estimated values for thermodynamics variables viz. change in Gibbs free energy (ΔG^o), change in enthalpy (ΔH^O) and change in entropy (ΔS^O) values for different temperatures (K) and variable SMX concentration (mg/L) are reported in **Table S.5.3.** (Supplementary data). Negative values for ΔG^o affirmed spontaneous and thermodynamically favourable adsorptive interactions between SMX and PPy-PC. Simultaneously, positive values for ΔH^o and ΔS^o affirmed endothermic adsorption reaction and rise in degree of dis-orderness, respectively that drove the adsorptive process. Being endothermic in nature, it can be assumed that the energy involved in the adsorbent (PPy-PC) preparation could be more than the energy released during adsorptive interactions.

5.2.4. Influence of variable adsorbate ionic strengths

Figure 5.12. depicts the influence of variable ionic strengths of the sorbent (SMX) medium over its adsorption on PPy-PC. As illustrated, a significant rise in the ionic strengths of Na^+ and K^+ ions (0.01 M to 0.1 M) caused only a nominal reduction in the adsorption capacity of SMX species by PPy-PC. This suggests a weak dependence of the sorbate's (SMX) ionic strength in governing its adsorption on the adsorbent (PPy-PC). This slight decline in the adsorption of SMX species with elevating ionic strengths of SMX medium could be due to multiple reasons.

- One such reason could be salting out of SMX species at higher ionic strengths. This could have led to the limited solubility of the SMX species in the aqueous medium, thus limiting its availability for adsorption over the PPy-PC surface.
- Also, a rise in ionic intensity of cationic charges will result in the electrostatic screening of anionic SMX species and cationic PPy-PC surface, thus hindering the adsorption process (Zhu et al., 2015).

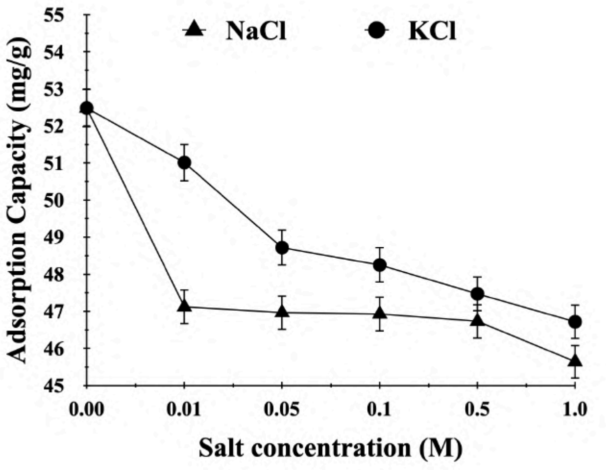

Figure 5.12. *Influence of variable ionic strengths of SMX medium on its adsorption by PPy-PC*

Conclusively, elevating ionic strength of the adsorbate medium have a nominal effect on its adsorption over PPy-PC surface.

5.2.5. Influence of co-existing of heavy metals and antibiotics and their co-adsorption

Figure 5.13. depicts the influence of co-existing and co-adsorption of heavy metals and other antibiotics with their respective EDX spectrums. As illustrated PPy-PC showed very low adsorption efficiencies (%) towards heavy metals as compared to SMX species. This could be due to the low ionic speciation of metal ions at pH 6.0 compared to SMX species. However, the variation in co-adsorbing heavy metals could be associated with their atomic radii. The order of atomic radius for the considered heavy metals in picometer (pm) of the 3 considered heavy metals are as follows (WebElements Periodic Table):

Zn+2 (135 pm) ≈ Cu+2 (135 pm) < Pb+2 (180 pm)

Tobin et al., 1984 reported that metals with greater atomic radii form small-sized metal hydrates ($M(OH)_X$ and $M(OH)^+$), and this promotes higher ion exchange on the adsorbent's surface. Thus due to its large atomic radii, lead ions (Pb^{+2}) will have the smallest metal hydrate form as compared to the other 2 heavy metal cationic forms. Thus, it will undergo more ion exchange over the adsorbent's surface. This effect was verified from the relative EDS spectral peaks of the heavy metals with the Sulphur (S) peaks identifying the adsorbed SMX species. Lead (Pb) showed the highest EDS peak corresponding to a high weight percentage (wt%) followed by Copper (Cu) and Zinc (Zn). Simultaneously 'S' peaks corresponding to SMX species with co-existing heavy metals show a nominal reduction in wt% with respect to the setup with no co-existing heavy metal. The nominal reduction in SMX adsorption due to co-existing heavy metals could be due to the cationic shielding of the anionic charges of the SMX species (at pH 6.0) by the cationic metal hydrate ions. This could have neutralised some of the negatively charged SMX species affecting its electrostatic interactions with the positively charged polaron (PPy+.) and bi-polaron (PPy++) forms of polypyrrole.

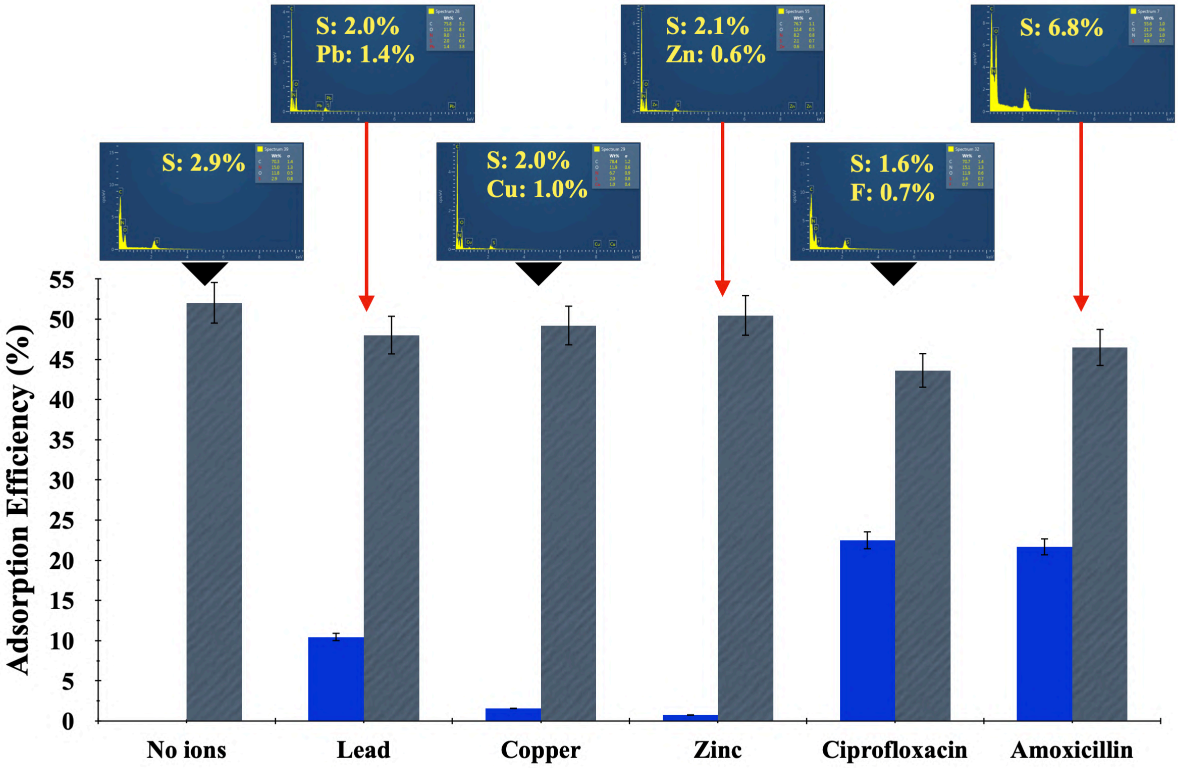

Figure 5.13. *Influence of co-existing heavy metals (Zn^{+2}, Cu^{+2} and Pb^{+2}) and antibiotics (CIP and AMX) on the adsorption of SMX by PPY-PC*

Contrarily co-existing antibiotics viz. Ciprofloxacin (CIP) and Amoxicillin (AMX) showed significant adsorption on the adsorbent's surface (PPy-PC) and also affected the SMX adsorption. At pH 6.0, both CIP and AMX are present in their zwitterionic forms, i.e. having a positive amine group and a negative oxygen functional group. Thus, these negatively charged oxygen groups may have contributed to the competitive electrostatic interactions with the adsorbent, causing their significant co-adsorption. The same can be verified from the EDX spectrum with 'F' peaks identifying the CIP species. Amoxicillin being a Sulfonamide, can be identified with 'S' peaks in EDS spectra. Since SMX also contain 'S' groups, the EDS spectrum for the setup containing both SMX and AMX species showed heightened 'S' peaks compared to the aqueous setup containing only SMX.

5.2.6. De-sorption and re-adsorption analysis

The recyclability potential of PPy-PC was studied by regenerating the adsorbent via desorption using 0.1N NaOH. One cycle of adsorption was followed by desorption for regeneration and then another cycle of adsorption. Ehrlich test verified the leaching of trace levels of PPy species in the desorption solutions. **Figure 5.14.** depicts the variation in adsorption and desorption efficiencies (%) for every adsorption-desorption cycle. As the figure illustrates, the adsorption efficiency of the adsorbent (PPy-PC) gradually declines after every cycle, with 80.82% in the first cycle to 42.52% in the fourth cycle. This was prominently due to morphological disruption and deterioration of the adsorbent's surface due to repeated adsorption-desorption cycles. Another reason could be the possible formation and accumulation of inert or non-inert sodium salt complexes into the adsorbent’s active sites after consecutive adsorption-desorption cycles. Successive adsorption-desorption cycles contribute to enlarging of such complexes. After a specific size limit, they fail to escape the surface pores and shield the active sites, thus rendering them unavailable for the consecutive adsorption cycle. However, post 4th adsorption-desorption cycle, a slight increase in the adsorption efficiency was reported; as depicted in **Figure 5.14.** The possible reason could be the excess disruption or wearing off of the PPy fibres from the adsorbent’s surface due to the constant adsorption-de-sorption cycles. So this should have exposed some of the powdered carbon (PC) surface that may have contributed to the extra adsorption of the SMX species, causing a slight rise in the adsorption efficiency for the 5th adsorption cycle. Following the 5th cycle, the adsorption efficiency followed the gradual decline of 21.28% by the end of the 8th cycle. Beyond this point, further adsorption-desorption cycle was irrelevant.

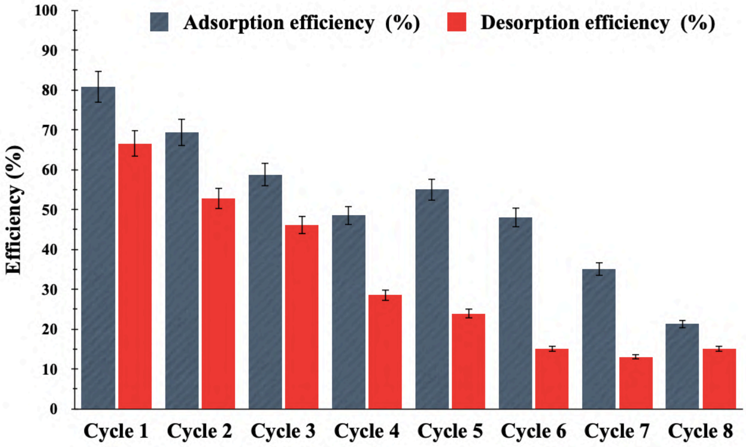

Figure 5.14. Regeneration and reusability analysis of PPy-PC

Figure 5.14. also depicts the gradual reduction in the desorption efficiency with each adsorption-desorption cycle. Desorption efficiency was calculated by considering the amount of SMX adsorbed for each cycle as 100%. This decline can be associated with a gradual reduction in SMX adsorption, further due to the adsorbent’s morphological disruption after every cycle. Also, a small portion of

SMX species contribute to the inert or non-inert sodium salt complexes after each cycle, thus rendering the SMX species unavailable for consecutive desorption cycles.

5.2.7. Seed germination phytotoxicity analysis

Effectivity of adsorbent in eliminating SMX species from aqueous setups was assessed by analysing the toxicity of adsorbate solutions (before and after adsorption) on *Vigna mungo* (black gram) seeds. This involved the analysis of seed root length (in cm) after seed germination and the extent by which the seed growth was limited in untreated SMX solutions, i.e. growth inhibition (%); as depicted in **Figure 5.15.** In distilled water (blank), the *Vigna mungo* seeds germinated with a mean root length of 9.25 cm. The seeds showed reduced root lengths after being germinated in the SMX solution (control samples) with high growth inhibition (%) viz. 7.1 cm (23.24%) for 10 mg/L; 4.7 cm (49.20%) for 50 mg/L and 4.0 cm (56.76%) for 100 mg/L. Seeds germinated in SMX solutions post adsorptive treatment (test samples) showed improved root lengths (cm) with low growth inhibition (%) viz. 9.0 cm (2.7%) for 10 mg/L, 7.7 cm (16.76%) for 50 mg/L and 6.3 cm (31.89%) for 100 mg/L. Conclusively, it can be reported that the *Vigna mungo* seeds showed reduced germination and elevated growth inhibition as the concentration of SMX increased. However, post adsorptive treatment, the seeds showed improved seed root lengths and low growth inhibition. Thus, PPy-PC is efficient enough to eliminate SMX species from aqueous solutions, making it effective for agricultural purposes.

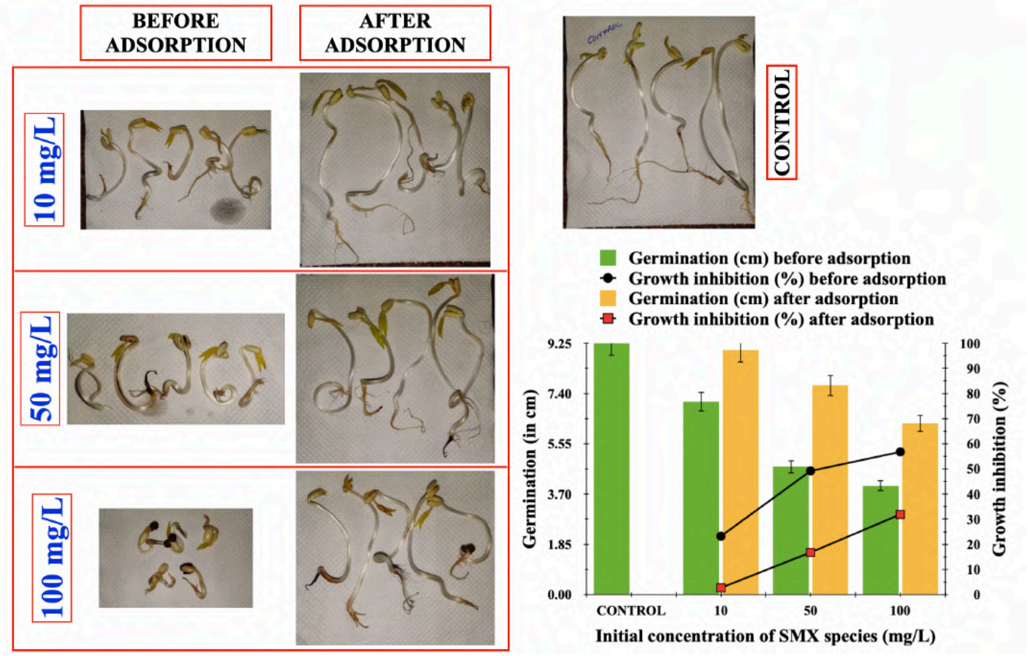

Figure 5.15. Phytotoxic assessment of PPy-PC in eliminating SMX form variable concentrations using Vigna mungo (black gram) seeds

5.2.8. Continuous-packed bed column studies

The effect of variable column bed height (cm), initial feed (SMX) flow rate (mL/min) and the initial feed (SMX) concentration (mg/L) is depicted in **Figure 15.6. (A, B, C)**. All factors that define the variable parameters for the packed bed column has been represented in **Table 5.1.** Effect of variable bed height of PPy-PC viz. 0.5 cm, 1.0 cm and 2.0 cm was evaluated by maintaining a fixed flow rate of ≈3 mL/min at a fixed inlet SMX concentration of 50 mg/L. The total packed bed saturation time (T_{total}) gradually increased with bed height (cm). This resulted in the breakthrough curve to shift right with elevated bed heights, as shown in **Figure 15.6. (A)**. The only possible reason for this would be the rapid saturation of the smaller bed heights compared to larger bed heights. The rise in bed heights showed an increased removal efficiency (Y%) of SMX viz. 35.52% at 0.5 cm, 55.07% at 1.0 cm and 61.87% at 2.0 cm, as larger volume of SMX solution was treated with elevated bed heights. Conclusively, higher SMX removal efficiency was attained at 2.0 cm bed height due to abundant adsorbent binding sites, and more contact time was available at larger bed height for a fixed feed flow rate and initial feed concentration. The equilibrium adsorption capacity ($Q_{e(eqm.)}$) of the packed bed column too followed the same trend, like removal efficiency (Y%) and total packed bed saturation time (T_{total}), as reported in **Table 5.1.**

Table 5.1. *Packed bed column data analysis at variable operating parameters for SMX adsorption by PPy-PC*

Bed Height (cm)	**Flow Rate (mL/min)**	**Initial Conc. (mg/L)**	**T_{total} (min)**	**$M_{total\ (g)}$**	**$Q_{total\ (mg)}$**	**$Q_{e(eqm.)}$ (mg/gm)**	**V_{eff} (mL)**	**Y (%)**
1	3	10	2760	82.8	49.98	90.86	8280	60.36
1	3	50	1800	270	148.68	270.34	5400	55.07
1	3	100	1380	414	170.57	310.12	4140	41.20
1	1.5	50	3240	243	143.67	261.22	4860	59.12
1	6	50	1260	378	159.19	289.44	7560	42.11
0.5	3	50	900	135	47.95	174.35	2700	35.52
2	3	50	3060	459	283.97	258.16	9180	61.87

Effect of variable flow rates of SMX effluent viz. ≈1.5 mL/min, ≈3.0 mL/min and ≈6.0 mL/min was evaluated on a fixed packed bed (PPy-PC) height of 1.0 cm and at a fixed initial SMX concentration of 50 mg/L. The total packed bed saturation time (T_{total}) gradually reduced with the increase in SMX flow rates (mL/min) i.e. 3240 min at ≈1.5 mL/min, 1800 min at ≈3.0 mL/min and 1260 min at ≈6.0 mL/min. This resulted the breakthrough curves to shift left with elevated flow rates, as shown in **Figure 15.6. (B)**. This was because higher flow rates resorts to inadequate residence time for the SMX species in the packed bed column; resulting to limited diffusivity of SMX species over PPy-PC bed. The increase in SMX flow rates resulted to reduced SMX removal efficiencies, viz. 59.12% at 1.5 mL/min, 55.07% at ≈3.0 mL/min and ≈42.11% at ≈6.0 mL/min. This was because higher contact time of the SMX species was allowed with the specific section of the column bed at lower flow rate as compared to higher flow rate. Thus, this resorted to more adsorption of SMX species at lower flow rates as compared to higher flow rates.

Effect of variable inlet SMX concentration viz. 10 mg/L, 50 mg/L and 100 mg/L cm was evaluated by maintaining a fixed flow rate at ≈3 mL/min, on a fixed bed height of 1.0 cm. T_{total} gradually reduced with the increase in inlet SMX concentration (mg/L), which resulted in the breakthrough curves shifting left, as shown in **Figure 15.6. (C)**. This was due to increased SMX concentration that resulted in quick saturation of the packed bed at fixed bed height and a constant feed flow rate. The increase in initial SMX concentration caused a reduction in the SMX removal efficiencies (Y%) of the fixed column bed, viz. 60.36% for 10 mg/L, 55.07% for 50 mg/L and 41.20% for 100 mg/L. This could be due to the dependency of removal efficiency (%) towards the intensity of available active sites over the adsorbent with respect to time. So for the same volume of SMX solution passing through a fixed column bed at any given time, the intensity of available active sites will be least for the column bed with the highest initial feed concentration, rendering the column bed with the least removal efficiency. On the contrary, since the adsorption capacity of the fixed packed bed is associated with the intensity of filled active sites, it increases with the rise in the inlet SMX concentration at a fix flow rate. The equilibrium adsorption capacity of the packed bed column ($Q_{e(eqm.)}$) for variable SMX inlet concentration at fixed bed height and flow rate were 90.86 mg/g for 10 mg/L, 270.34 mg/g for 50 mg/L and 310.12 mg/g for 100 mg/L.

Conclusively, as the results suggest, lower column bed heights (cm), higher inlet SMX concentrations (mg/L), and higher initial feed flow rates (mL/min) could saturate the adsorbent bed more quickly.

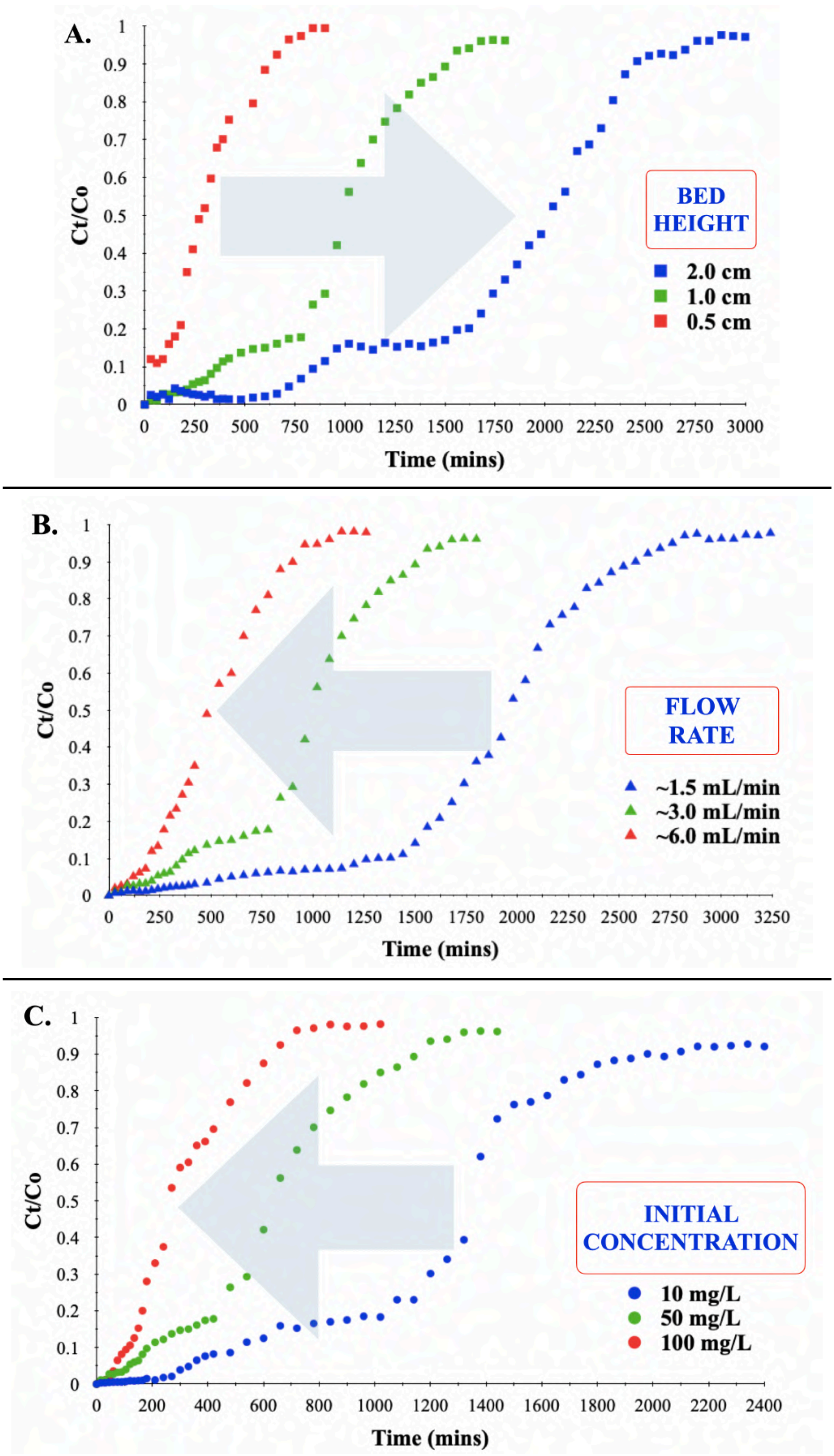

Figure 5.16. *(**A**): Influence of variable bed height; (**B**): Influence of variable inlet flow rate and; (**C**) Influence of variable SMX initial concentration on packed bed column*

5.3. Significant findings

Biomass-derived powdered carbon (PC) was complexed with polypyrrole (PPy) via in-situ oxidative polymerisation to enhance its N-content for enhanced adsorptive elimination of Sulfamethoxazole (SUX) species from its aqueous setups. Morphological and physiochemical characterisation verified the complexation of PPy fibres on the PC surface. Adsorptive interactions between the adsorbent (PPy-PC) and the adsorbate (SMX) was significantly influenced by electrostatic interactions and hydrogen bonding between anionic SMX species and polaron state (PPy+.), bi-polaron states (PPy++) and neutral states of polypyrrole at the optimised pH 6.0; apart from other adsorptive interactions. Isotherm modelling concluded both monolayer and multilayer adsorption as verified by Langmuir and Freundlich isotherm models, respectively; basically due to participation of exposed PC surface and stacked pyrrole monomers of the PPy fibre. Pseudo-second order kinetics verified chemisorption mode of sorbate-sorbent interaction. Adsorptive interactions were defined as endothermic and thermodynamically favourable. Variable ionic strengths and coexisting heavy metals and other antibiotics affected the adsorption capabilities of PPy-PC. Recyclability studies verified the adsorbent's reusability for multiple cycles, and phytotoxicity analysis verified the adsorbent's efficacy in remediating pharmaceutical waste effluents for agricultural or other reuse. Packed bed column studies verified lower column bed heights (cm), higher inlet feed concentrations (mg/L), and higher initial feed flow rates (mL/min) saturated the adsorbent bed more quickly. Maximum removal efficiency of 61.87% was achieved for continuous column packed bed with a bed height of 2.0 cm, SMX flow rate of ≈3 mL/min and initial inlet SMX concentration of 50 mg/L. Overall, this work presented a detailed concept and significant interpretation of polypyrrole complexation over carbonaceous material to synthesise a Nitrogen-rich adsorbent for the adsorptive eliminating of emerging pharmaceutical contaminant Sulfamethoxazole. It also presents a basic idea of the adsorbent's recyclability, its performance at variable ionic strengths and coexisting pollutants, and its performance in continuous packed bed column.

SUPPLEMENTARY DATA FOR CHAPTER 5

Table S.5.1. *Adsorption isotherm model analysis for removal of SMX by PPy-PC*

ISOTHERMS		**ISOTHERM CONSTANTS**	**SMX**
TWO PARAMETERS ISOTHERMS	**Langmuir**	**Q_L (mg/g)**	80.65
		K_L (L/mg)	0.067
		R^2	0.97
	Freundlich	**K_F (mg/g) (mg/L)$^{-1/n}$**	2.35
		1/n	0.63
		R^2	0.99
	Dubinin-Radushkevich	**Q_{DR} (mg/g)**	39.66
		K_{DR} (mol^2/J^2)	1.59
		E_{DR}	0.79
		R^2	0.86

Table S.5.2. *Kinetic model analysis for the removal of SMX by PPy-PC*

C_i (mg/L)	**$Q_{e\ Exp.}$ (mg/g)**	**Pseudo-first order**			**Pseudo-second order**			**Intra-particle diffusion**		
		K_1 (1/min)	**Q_e (mg/g)**	**R^2**	**K_2 (g/mg min)**	**Q_e (mg/g)**	**R^2**	**K_{id} (mg/g min$^{0.5}$)**	**C (mg/g)**	**R^2**
20	11.77	1.2x10^{-3}	3.03	0.74	3.4 x10^{-3}	15.02	0.96	0.17	9.34	0.48
40	22.83	1.1 x10^{-3}	5.45	0.70	1.8 x10^{-3}	26.69	0.96	0.31	15.96	0.53
60	32.42	1.3 x10^{-3}	6.96	0.69	1.3 x10^{-3}	35.77	0.97	0.42	21.48	0.51
80	42.02	6.0 x10^{-4}	13.02	0.60	9.0 x10^{-4}	44.58	0.98	0.63	23.14	0.51
100	51.12	2.0 x10^{-4}	13.03	0.58	6.0 x10^{-3}	46.45	0.97	0.57	28.68	0.43

Table S.5.3. *Thermodynamics Parameters (ΔG°, ΔH°, and ΔS°) for adsorption of SMX by PPy-PC*

C_i (mg/L)	**Temp. (K)**	**ΔG^o (kJ/mol)**	**ΔH^o (kJ/ mol)**	**ΔS^o (J/molK)**
20	**303**	-21.26	18.72	8.82
	313	-22.38		
	323	-21.08		
	333	-21.74		
40	**303**	-20.99	15.17	18.50
	313	-21.57		
	323	-20.69		
	333	-21.53		
60	**303**	-20.09	6.56	43.38
	313	-20.66		
	323	-20.36		
	333	-21.11		
80	**303**	-20.06	11.46	25.73
	313	-19.64		
	323	-19.97		
	333	-19.49		
100	**303**	-18.66	9.45	29.85
	313	-19.09		
	323	-18.99		
	333	-19.43		

CHAPTER 6

Fabrication of Chitosan to porous Chitosan for adsorptive elimination of synthetic anionic dyes from single and multi-adsorptive systems

The work embodied in this chapter is published in:

CHANDI PATRA, E. Suganya, Senthilkumar Sivaprakasam, G. Krishnamoorthy, Selvaraju Narayanasamy; 2021, “A detailed insight on fabricated porous chitosan in eliminating synthetic anionic dyes from single and multi-adsorptive systems with related studies”; ***CHEMOSPHERE***, 281, 130706 **(ELSEVIER, IF: 7.086)**

GRAPHICAL ABSTRACT

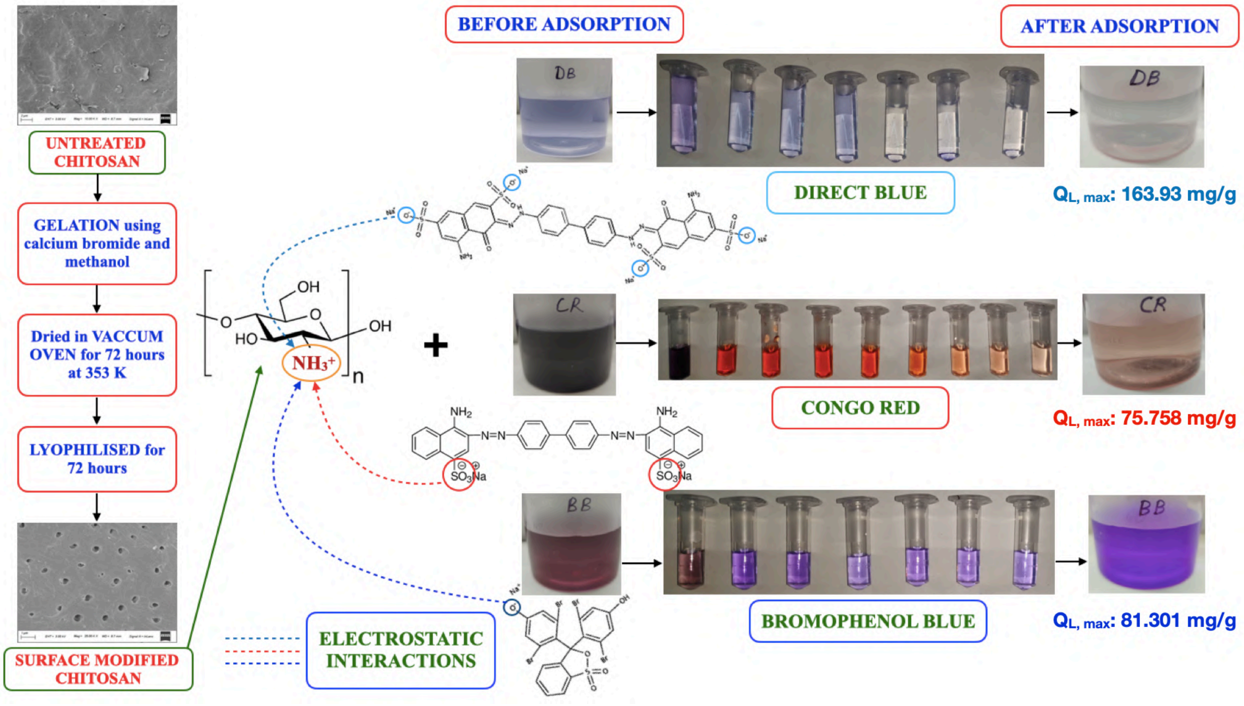

Abstract

Chitosan was fabricated via gelation method using $CaBr_2 \cdot xH_2O$/methanol solution. It was studied as a potential adsorbent (MCh) in adsorbing anionic synthetic dyes like Bromophenol blue (BB), Direct blue 6 (DB) and Congo red (CR) from single (one dye species at a time) and multi (having two dyes; binary and all three dyes; tertiary) adsorptive systems. Physico-chemical modifications of MCh surface prior and post-modification and dye adsorption were evaluated using scanning electron microscopy, Energy-dispersive X-ray spectroscopy, powder X-ray diffraction analysis, surface area analysis and Fourier-transformed infrared spectroscopy. Influential parameters influencing the adsorption process viz. initial pH of dye solution, MCh dosage, adsorption temperature and initial concentration of dye species were optimised. Adsorptive studies involving single adsorptive setups verified the formation of sorbate's (dye species) monolayer over the sorbent's (MCh) surface via chemisorption, as established by Langmuir isotherm and pseudo-second-order kinetics model analysis. Theoretical maximum adsorption capacities of MCh for BB, DB and CR were found to be 81.301 mg/g, 163.934 mg/g and 75.758 mg/g, respectively. Meanwhile, for all multi-adsorptive systems, competitive Langmuir isotherm model verified the antagonistic behaviour of an individual dye over other dye adsorption over MCh surface in their respective adsorptive systems. Thermodynamics of the sorbate-sorbent interaction was exothermic, spontaneous, with an elevated degree of disorderedness, concluding the interaction as thermodynamically favourable. Co-existing metal cations and anionic salts had minimal effect on MCh's adsorption efficiency. Phytotoxicity assay via germination of *Vigna mungo* seeds verified the efficacy of the adsorbent in eliminating the dye species from single and multi-adsorptive systems.

6.1. Materials and methods

The list of all the reagents and salts and their roles for the present study has been mentioned in **Table A.1.** (Appendix).

6.1.1. Formation and characterisation of adsorbent

Fabricated porous chitosan was prepared by gelation method using a mixture of $CaBr_2{\cdot}xH_2O$ and methanol (CH_3OH) solution, followed by prolonged heating under vacuum conditions as described by Kadokawa et al., 2015 and Cao et al., 2018. 180 mg of commercial chitosan was added to 3.85 mol/L solution of Calcium Bromide using methanol as solvent and was allowed to mix for 48 h in a shaker incubator (ORBITEK-LE) at 303K. Mixture of chitosan and $CaBr_2{\cdot}xH_2O$/methanol solution caused the conversion of chitosan from dried flake form to gel form. This process is known as gelation, resulting in the formation of chitosan gel, which was further dried at 353K under vacuum conditions using a vacuum oven (Daihan Labtech). Vacuum oven caused quick removal of methanolic media under reduced pressure and high temperature, resulting in porous chitosan. The dried material was then washed thoroughly with water until all the Calcium Bromide (CaBr2·xH2O) and the remaining organic salts were completely washed away. The final washed product was then lyophilised at 193 K at -20 Pa using lyophiliser (Labconco) to obtain dry fabricated porous chitosan (MCh). **Figure 6.1.** illustrates the preparation scheme resulting in the synthesis of fabricated chitosan (MCh).

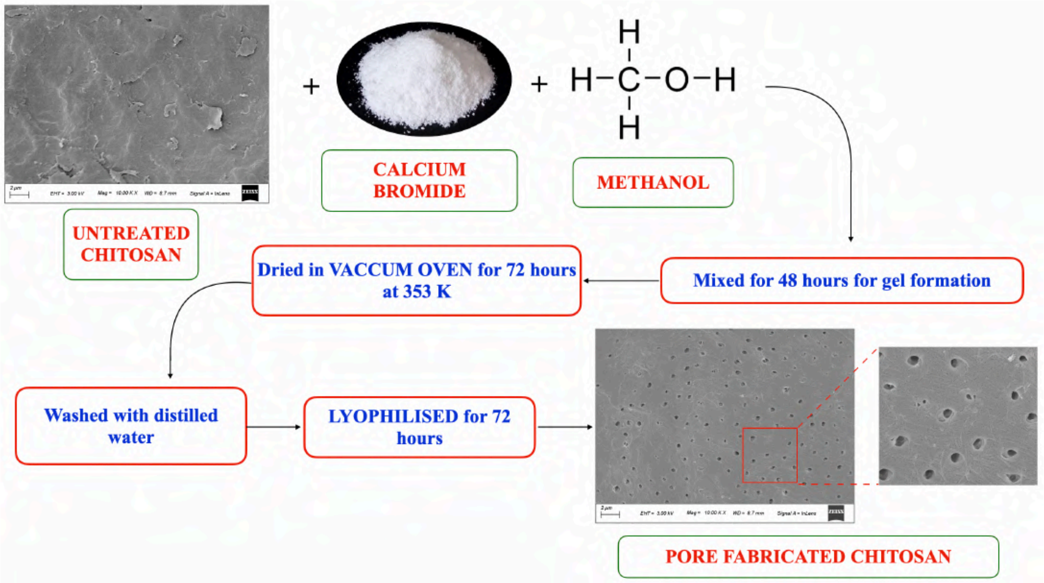

Figure 6.1. *Schematic representation of the preparation process of pore fabricated chitosan (MCh)*

To ensure complete removal of Calcium Bromide from the dried gel, the filtrate water after each wash was spectrophotometrically tested for calcium ions using a technique described by Li et al., 1999. **Figure 6.2.** depicts the relative removal efficiencies of anionic azo dyes (CR, DB and BB) using commercial chitosan and fabricated chitosan (MCh). It's evident that porosity led fabricated chitosan (MCh) showed enhanced dye adsorption efficiencies as compared to commercial chitosan. The prepared adsorbent was characterised for its morphological modifications, surface porosity, surface elemental analysis etc., using instrumentations detailed in **Table A.2.** (Appendix).

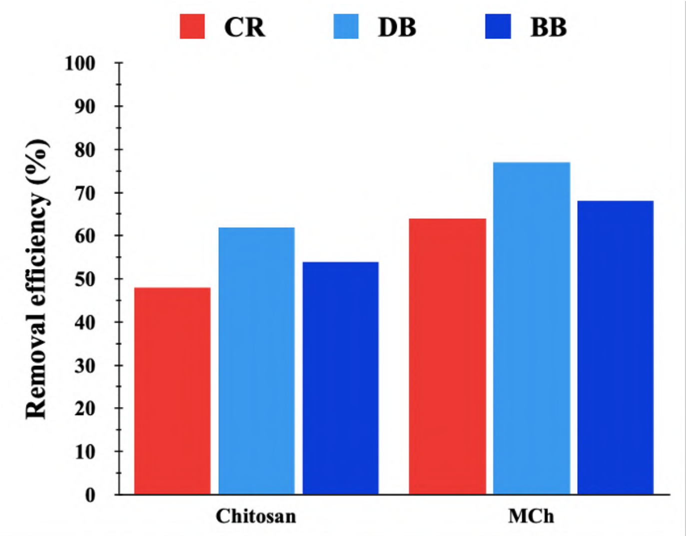

Figure 6.2. *Comparative removal efficiencies of Congo red (CR), Direct blue 6 (DB) and Bromophenol blue (BB) using commercial chitosan and pore fabricated chitosan*

6.1.2. Adsorption experiments and analysis

Effect of influential variable parameters, like initial pH of anionic synthetic dye solution (CR, DB and BB) ranging from 2.0-10.0, initial dye concentration (20–100 mg/L), adsorbent's (MCh) dosage (0.25–1.75 mg/mL) and sorbate-sorbent interaction temperatures (293–313 K) were studied via batch experiments. All interaction experiments were carried out in a thermo-regulated shaker (ORBITEK-LE) at specific rpm for a duration of 12 h. Following the incubation process, the spent adsorbent (MCh) was filtered out, and the spent dye solution was then analysed for any remnant dye species using UV-Vis spectrophotometer (Infinite 200 PRO (Tecan)) at wavelength 595 nm for BB, 585 nm for DB and 500 nm for CR.

6.1.3. Single and multi-adsorptive system analysis

Sorbate-sorbent interactions in single adsorptive systems were analysed using two and three-parameter isotherms models (**Table A.3.** (Appendix)). Kinetics of the same was analysed using pseudo-first-order, pseudo-second-order and intra-particle diffusion models (**Table A.4.** (Appendix)). Thermodynamics analysis of the adsorptive removal of the dye molecules by the adsorbent was evaluated at variable temperatures ranging from 293 K to 318 K. Theoretical explanations to the thermodynamics parameters have been detailed in **Section A.1.3.** (Appendix).

Binary adsorptive systems (having 2 dye species at a time) viz. CR+BB, CR+DB and DB+BB dye setups, were studied with working concentrations of 20+20, 40+40, 60+60, 80+80 and 100+100 mg/L. For multiple adsorptive systems involving all the dyes at one system i.e. CR+DB+BB; sorbate-sorbent interactions were evaluated at working concentrations of 20+20+20, 40+40+40, 60+60+60, 80+80+80 and 100+100+100 mg/L. All binary and tertiary adsorptive systems were studied at pH similar to that of distilled water. Competitive Langmuir isotherm model was studied to evaluate the antagonistic or synergistic implications of the co-existing dye species on the adsorptive removal of an individual dye species in a particular binary and tertiary adsorptive system.

6.1.4. Impact of co-existing metal cations and anions

Impact of co-existing metal cations and anionic salts on the adsorptive efficiency of anionic azo dyes on MCh surface was investigated via batch adsorption experiments with cationic metal salts of Nickel (Ni^{+2}), Cobalt (Co^{+2}), Lead (Pb^{+2}), Copper (Cu^{+2}) and Chromium (Cr^{+6}); and anionic salts of Nitrate (NO_3^{-2}), Phosphate (PO_4^{-3}), Sulphate (SO_4^{-2}), Carbonate (CO_3^{-2}) and Chloride (Cl^{-1}). The choice of metal cations and anions were based on various literatures claiming the presence of common salts present in dye wastewater effluents as reported by Yaseen and Scholz, 2019; Nahar et al., 2018 and Siddiqui et al., 2018. The impact of co-existing metal cations and anionic salts were analysed with the adsorption studies of CR, DB and BB dye solutions blended with the same concentrations of metal cations and anionic salt solutions in the ratio of 1:1.

6.1.5. Seed phytotoxicity assay and analysis

Vigna mungo (black gram) seed germination studies were done for phytotoxic evaluation of the adsorbent's (MCh) efficacy in adsorptive removal of BB, DB and CR dye species from single and multi (binary and tertiary) adsorptive setups. *Vigna mungo* seeds were selected for this analysis because of their easy availability, does not need any specific germination conditions and short germination period.

Seed phytotoxicity assay studies were done per the protocols laid by USEPA, 1996 (Dutta et al., 2018; Prasad and Rao,2013; Naraginti and Yong, 2019) with slight modifications. *Vigna* *mungo* seeds were thoroughly washed and rinsed with 1% Sodium Hypochlorite (NaClO), followed by brief drying at room temperature. The washed and dried seeds were then germinated on Petri plates with dye solutions (labelled as sample plates); adsorbent treated solutions (labelled as test plates), and de-ionised water (labelled as blank). The initial concentration of 100 mg/L of BB, DB and CR dye species were considered for single adsorptive systems. For multi adsorptive setups, 100+100 mg/L for binary and 100+100+100 mg/L for tertiary adsorptive systems were taken with a fixed dosage of MCh. *Vigna mungo* seeds were germinated at normal room temperature; under low light conditions (<1.00 lux) for 7 days (a week). After the germination period, average seed root lengths were measured, and further evaluation was done.

6.2. Results and discussion

6.2.1. Characterisation of the adsorbent

6.2.1.1. Adsorbent's morphological and surface elemental analysis

Scanning electron microscopy (SEM) images verified distinct morphological modifications after chitosan fabrication, resulting in fabricated porous chitosan (MCh). **Figure 6.3.** illustrates the SEM analysis for the MCh surface prior to and after fabrication. MCh surface shows a unique surface morphology with distinct and uniform pore density with visible pores. SEM analysis for chitosan surface prior and after fabrication goes parallelly with the surface area and porosity (BET) data as depicted in **Table 6.1.** Enhanced specific surface area and porosity (BET) values for MCh post-fabrication verify the development of pores over the chitosan.

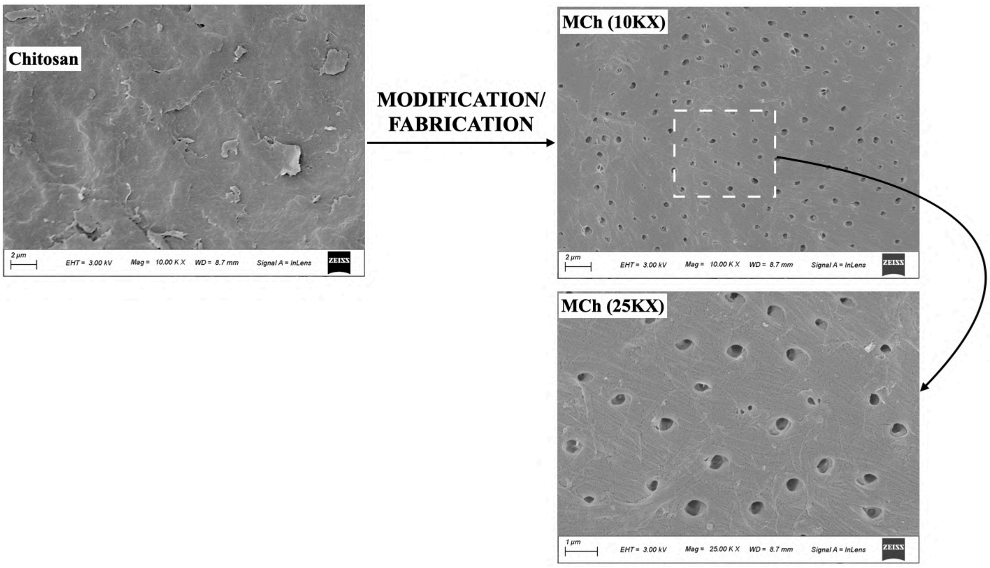

Figure 6.3. *Scanning electron microscopy (SEM) image of Chitosan surface before fabrication (at 10,000X magnification) and MCh surface after fabrication/modification at 10,000X and 25,000X times magnified*

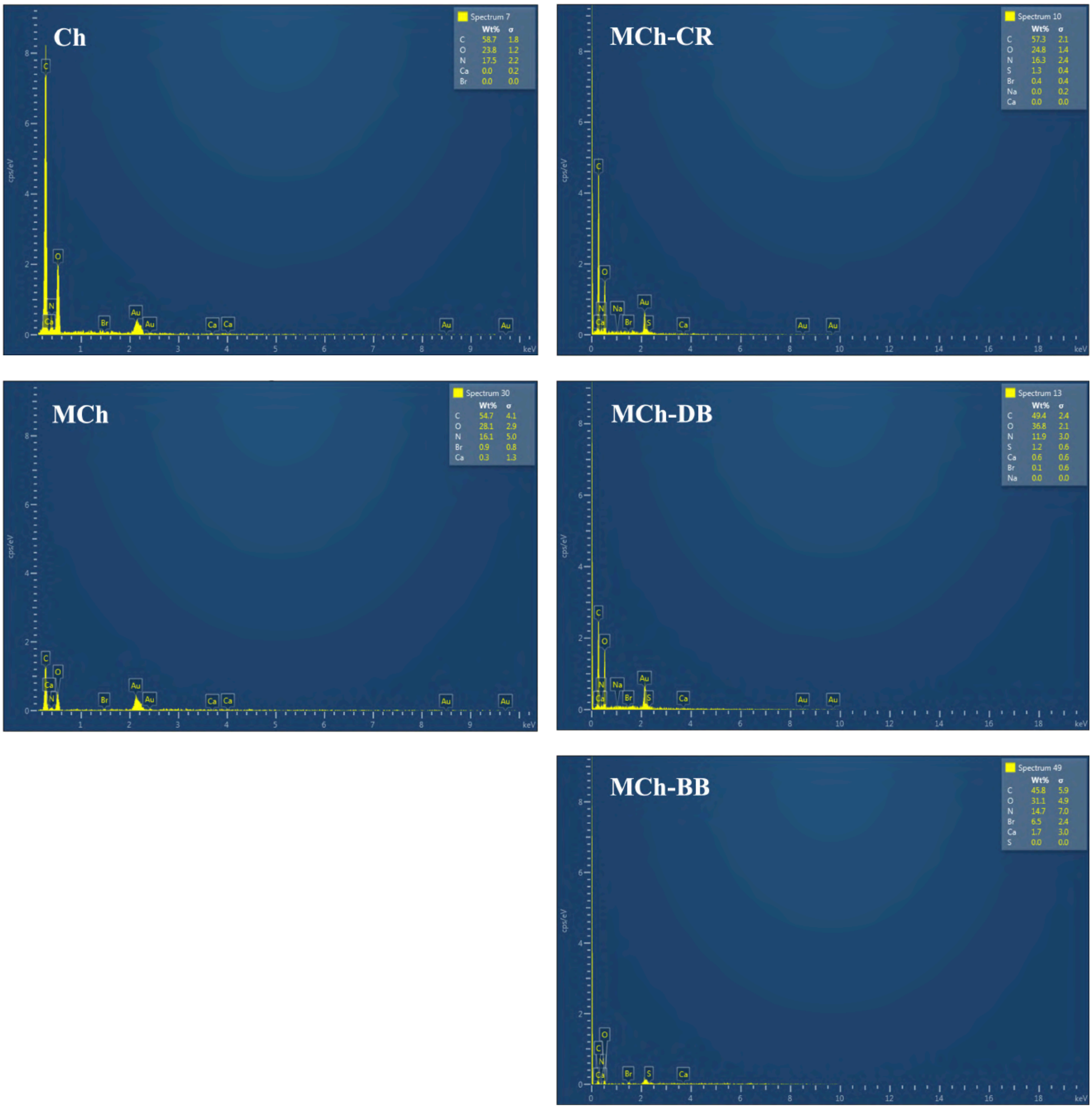

Figure 6.4. *EDS spectra of adsorbents surface before (as Ch) and after fabrication/modification (as MCh) and after adsorption of CR, DB and BB dye species by MCh surface*

Qualitative elemental changes of the MCh surface to verify the adsorption of BB, DB and CR dye species in a single adsorptive system was analysed by EDS analysis. Minor Bromine (Br) peaks were observed on the MCh surface. This could be due to the remnants of calcium bromide (CaBr2.xH2O) used for the gelation process that resulted in fabricated porous chitosan (MCh). Thus these minor Br peaks verify the fabrication of chitosan surface to form MCh. Further, the presence of Sulphur (S) peaks for CR and DB dye species adsorbed MCh samples verified the adsorptive uptake of CR and DB dye species over the MCh surface, as shown in **Figure 6.4.** (MCh-CR, MCh-

DB). Sulphur (S) peaks were due to the Sulfonate groups present in CR and DB species. Simultaneously, for BB adsorbed MCh samples, prominent Bromine (Br) peaks verified BB adsorption over the MCh surface, as represented in **Figure 6.4.** (MCh-BB). These Bromine (Br) peaks were due to the Bromine groups bonded to the aromatic rings of the dye molecule. Conclusively, SEM images verify the fabrication of porous chitosan surface (MCh), resulting in enhanced porosity compared to untreated chitosan and simultaneously, EDS spectrums verified the adsorptive removal of the synthetic anionic dyes over the MCh surface.

6.2.1.2. Powder X-ray diffraction analysis of adsorbent

Figure 6.5. represents the X-ray diffractograms for chitosan prior fabrication and chitosan post-fabrication (MCh). As depicted in the figure, both chitosan and MCh shows two major peaks at 2θ values of 10.22° and 20.20°, corresponding to planes 020 and 110, respectively. Such peaks correspond to a high degree of crystalline lattice for chitosan and MCh (Hai and Sugimoto, 2018). **Figure 6.5.** also depicts the absence of peaks corresponding for $CaBr_2.xH_2O$/methanol (28–38°), thus suggesting the absence of any organic/inorganic impurities due to fabrication (Kadokawa et al., 2015). Similar peaks for both chitosan and MCh suggest no modification to the lattice of the chitosan sub-structure due to fabrication. Conclusively, $CaBr_2.xH_2O$/methanol fabrication resulted to porous chitosan and not any alteration into its structural sub-structure.

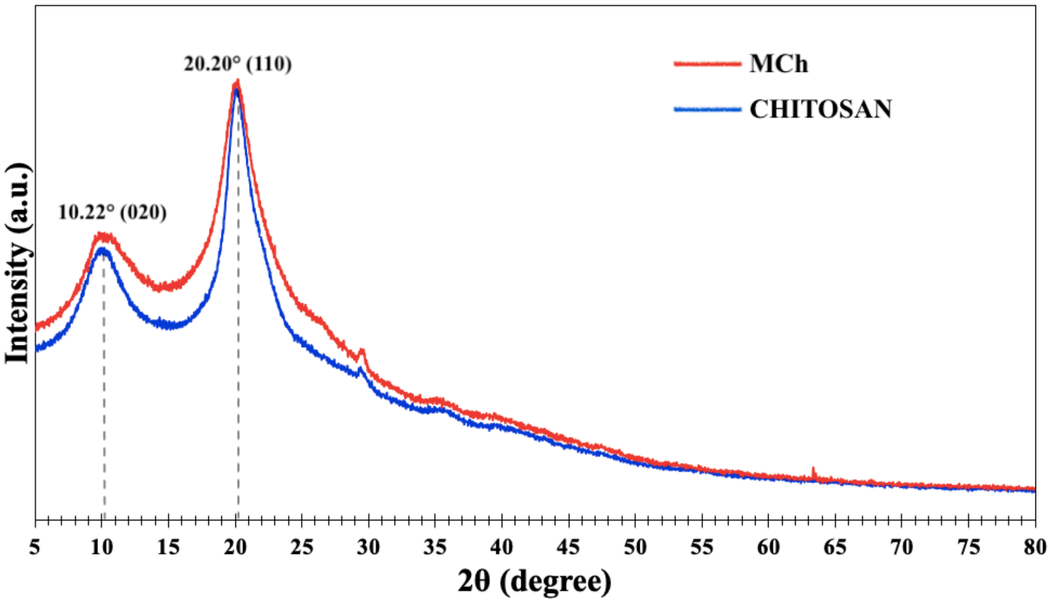

Figure 6.5. *X-ray diffraction patterns for chitosan before and after fabrication (MCh)*

6.2.1.3. Surface area and porosity analysis (BET analysis)

Surface area and porosity analysis (BET analysis) of the MCh surface, prior and after fabrication, was evaluated using total pore analysis/Brunauer-Emmett-Teller (BET). BET analysis verified enhanced values for surface parameters like total pore volume (cm^3/g), specific surface area (m^2/g) and pore diameter (nm) for MCh surface post modification as reported in **Table 6.1.**

Table 6.1. *Surface area/BET analysis of adsorbent prior modification (Ch) and post modification (MCh)*

Porosity parameters	Ch	MCh
Total pore volume (cm^3/g)	0.002	0.304
Average Pore Diameter (nm)	3.150	97.428
Specific Surface Area (m^2/g)	5.030	53.90

Figure 6.6. depicts the adsorption-desorption isothermal curves for untreated chitosan and fabricated chitosan (MCh). The adsorption-desorption isothermal curves verified type IV nitrogen adsorption-desorption isotherms, resorting to meso- and micro-porous sub-structure (Hu and Hsieh, 2017).

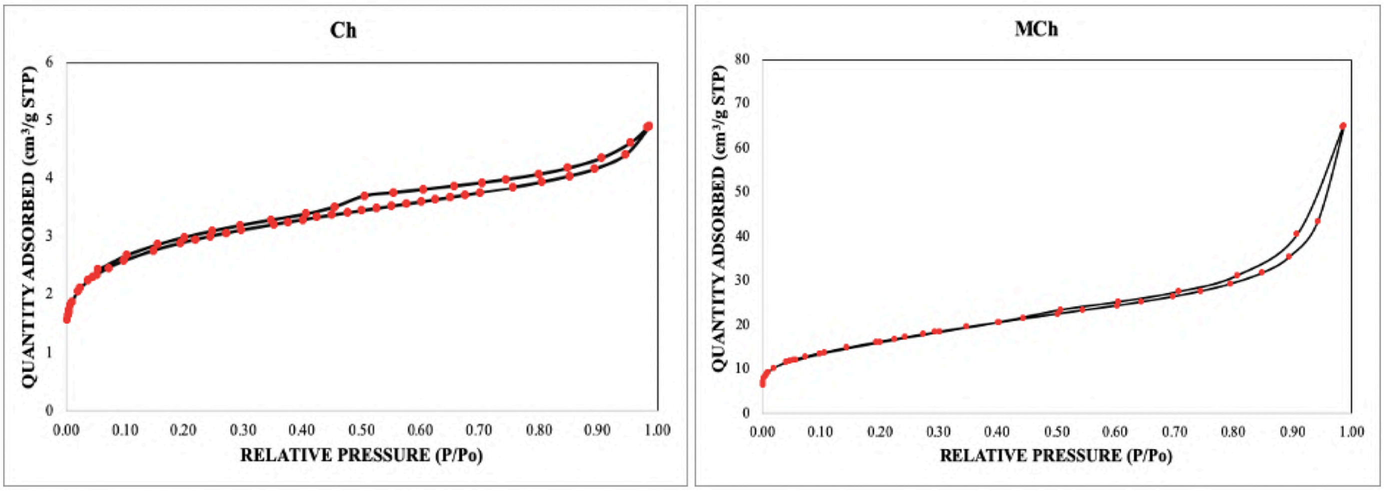

Figure 6.6. *Adsorption-desorption isothermal curves for raw chitosan (Ch) surface and fabricated chitosan (MCh)*

6.2.1.4. FTIR spectral analysis

Surface functional groups modification of fabricated chitosan (MCh) active sites that were involved in the adsorptive removal of the studied anionic synthetic dye species were evaluated using FTIR within the spectral range from 4000 cm^{-1} to 500 cm^{-1} as depicted in **Figure 6.7.** Chitosan before and after fabrication (MCh) shows strong C=C bending (due to alkene) between 995 cm^{-1} to 985 cm^{-1}; strong C-H bending between 900 cm^{-1} to 700 cm^{-1}; medium C-N stretches between 1250 cm^{-1} to 1020 cm^{-1} and medium sharp OH stretching between 3700 cm^{-1} to 3584 cm^{-1}. These are characteristic peaks for chitosan, verifying the integrity of chitosan post-fabrication (MCh). Medium N-H (amine) bending between 1650 cm^{-1} to 1580 cm^{-1} verify the involvement of functional groups of chitosan in eliminating the dye species. Equivalent peak modifications were recorded within the range of 1342 cm^{-1} to 1266 cm^{-1}, possibly due to strong aromatic -CN stretches. These aromatic stretches could be due to the aromatic rings of adsorbed BB, DB and CR dye species over the MCh surface. Finally, minor peak modifications were recorded for MCh adsorbed with CR and DB dye species in the range of 1372 cm^{-1} to 1335 cm^{-1}, possibly due to stretches of sulphonate (-S=O) groups of CR and DB dye species. Conclusively these modifications in the band peaks during FTIR studies for MCh surface, prior and later sorptive removal of CR, DB and BB species, revealed the involvement of amine groups in binding the anionic dye species (Vishnu Priyan et al., 2021; Ong et al., 2020).

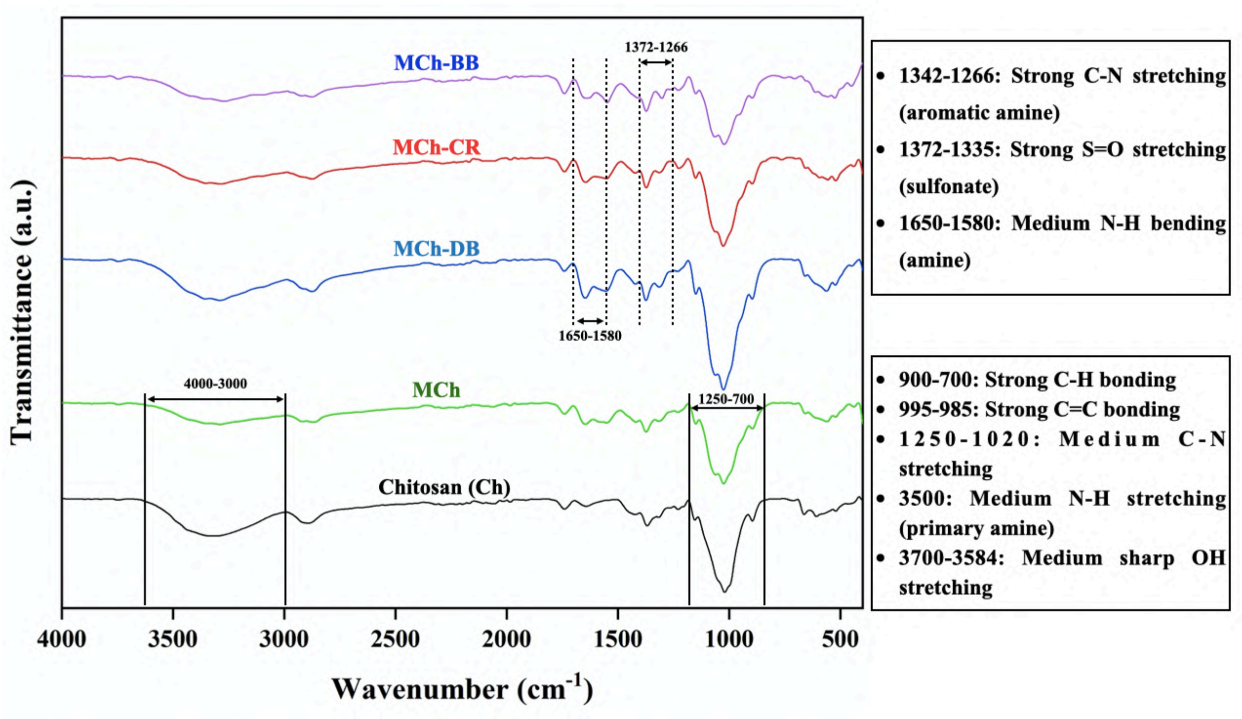

Figure 6.7. *FT-IR spectra of Chitosan (Ch) and fabricated/modified Chitosan (MCh) before and after adsorption*

6.2.2. Effect of variable process parameters

Variable initial pH of the dye solutions involved protonation and de-protonation of the amino and hydroxyl functional groups of the fabricated chitosan (MCh) and the dye species' ionic speciation. **Figure 6.8.** depicts the effect of initial pH of anionic synthetic dye solutions in the range from 3.0-8.0, over its adsorption over fixed dosage of MCh and fixed concentration of dye species. For both DB and BB, MCh showed efficient removal at pH 4.0, and for CR, MCh showed efficient removal at 6.0, which gradually declined with elevating pH. The possible reason for this could be due to the protonation of amino and hydroxyl functional groups at low pH values, resulting in cationic forms of MCh. Also, at low initial pH, chitosan tends to lose its crystallinity, and lower crystallinity could reflect an elevated availability of the amino groups for protonation, thus enhancing the accessibility of the adsorption sites (Kloster et al., 2020).

Simultaneously, Direct blue 6 (DB) and Congo red (CR), being azo anionic in nature, have sulphonate groups (R-SO_3Na), which tends to dissociate into anionic sulphonate (R-SO_3^-) groups in the aqueous phase. These azo-anionic dyes exhibit lowered pK_a values (less than zero), due to which it tends to possess anionic charges at lowered pH values (Guo et al., 2016). Bromophenol blue (BB) possess 2 hydroxyl groups ($pK_a = 4.0$). Most BB dye species exist in the molecular form under lowered pH values (i.e. pH <4.0). At elevated pH values (i.e. pH >4.0), these hydroxyl groups tend to dissociate to release free protons and render them to anionic forms (Mohammadzadeh et al., 2016). At lowered pH values, the amount of protonated active sites on MCh promotes the sorption of oppositely charged anionic dyes via electrostatic forces. With the elevation in pH values, the adsorbent's surface attains more electronegativity, thus rendering the adsorbent's surface negative charges and thus electrostatically repelling the anionic dye species. Conclusively, the adsorption capabilities of MCh towards the CR, DB and BB dye species was prominently determined by the initial pH of the synthetic dye solution resorting to mutual charged-based interactions.

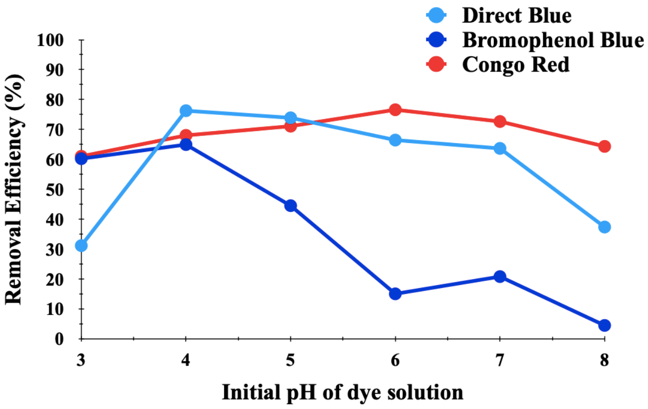

Figure 6.8. *Influence of initial pH of dye solution*

The effect of variable adsorbent's (MCh) dosage over the effective adsorptive uptake of CR, DB and BB dye species from the aqueous solutions was analysed with MCh dosages varying from 0.25–1.75 mg/mL, in 20 mL dye solution, at optimised pH as mentioned above for all the dye solutions; for an incubation period of 12 h. The adsorption efficiencies (%) elevated until it attained equilibrium with a further rise in MCh dosage, as depicted in **Figure 6.9.** The possible explanation for such behaviour was the driving force owing to accessibility of available binding sites with elevated MCh dosages for a fixed concentration of dye species. Gradually, beyond a certain limit, a further rise in dosage values had a null effect on the adsorption efficiency (%) of the adsorbent (MCh), and hence, the driving force for the adsorptive uptake of dyes ceased to equilibrium.

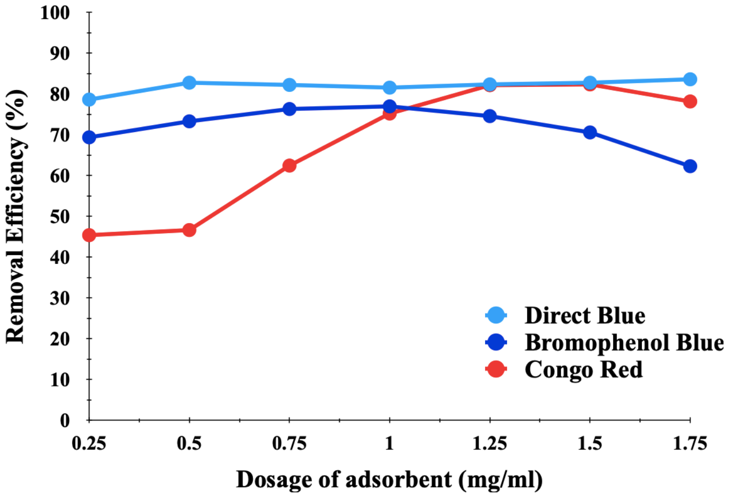

Figure 6.9. *Influence of variable dosage of adsorbent (MCh)*

Influence of variable initial concentrations of dye species (10-100 mg/L) under the influence of optimised pH (4.0 for DB and BB; 6.0 for CR), temperature (293 K for BB, 298 K for DB and 313 K for CR) and MCh dosage (1.0 mg/mL for BB, 0.5 mg/mL for DB and 1.25 mg/mL for CR) were evaluated for a period of 12 hours. **Figure 6.10.** represents that adsorption efficiency (%) gradually declined, and the adsorption capacity (mg/mL) gradually increased with elevating initial concentrations of CR, DB and BB dye species. This behaviour could be associated with a fixed proportion of available binding sites on the MCh surface, which gradually gets saturated with elevated dye concentrations. These available adsorption sites attribute to the adsorbent's effective adsorption efficiency (%), and as the initial dye concentration elevates, the extent of available vacant sites on the adsorbent surface declines, and so does its adsorption efficiency (%). Simultaneously, the degree of occupied adsorptive sites attributed to the adsorbent's driving force towards its adsorption capacity (mg/g). Hence, with the increase in initial dye concentration, the extent of occupied adsorptive sites increases, which elevates adsorption capacities (mg/g) of the adsorbent (MCh).

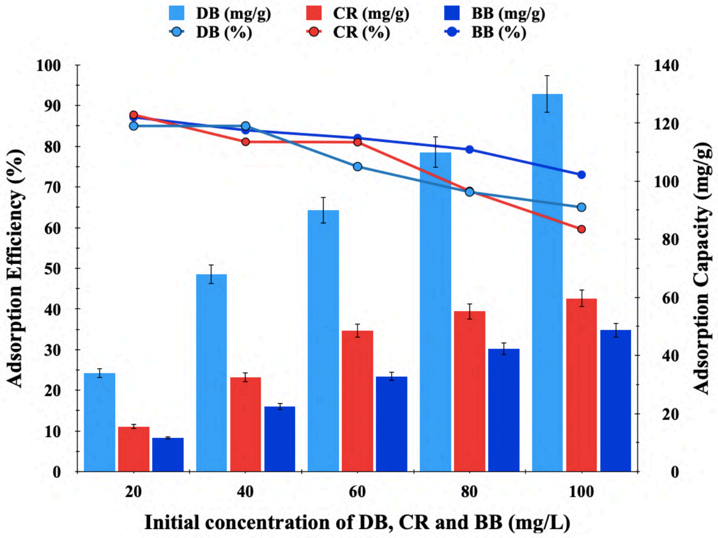

Figure 6.10. *Effect of variable initial concentrations of dyes influencing adsorption of CR, DB and BB by MCh*

6.2.3. Effect of interaction temperature and related thermodynamic analysis

Effect of variable sorbate-sorbent interaction temperatures on the sorption of BB, DB and CR dye species on MCh surface was analysed via changing the interaction temperatures from 293 K to 318 K. With elevated temperatures, the adsorption capabilities of the MCh surface towards BB, DB and CR dye species elevates up to a desired temperature, following which there was a decline in the adsorption capacities, as depicted in **Figure 6.11.** This could be due to the existence of temperature reliant binding sites.

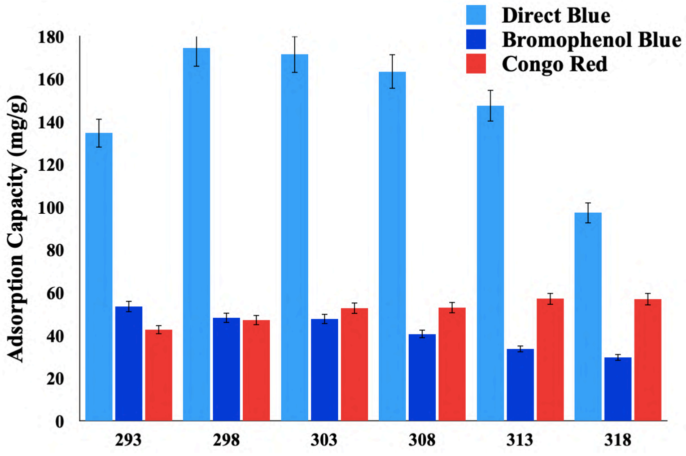

Figure 6.11. *Influence of variable incubation temperatures on the adsorption of dye species over MCh surface*

Table S.6.3. (Supplementary data) represents the estimated values for ΔG°, ΔH° and ΔS° for variable initial concentrations of the dye species (mg/L) and variable sorbate-sorbent interaction temperatures (K). Negative values for ΔG° affirmed that the adsorptive process of the dye species by the adsorbent (MCh) was thermodynamically favourable and spontaneous. Negative ΔH° values affirmed that the adsorptive process is exothermic. This could be due to the energy released during the sorbate-sorbent interactions, resulting in exothermic adsorptive interactions as verified by negative ΔH° values. Finally, positive ΔS° values verified elevated dis-orderness and randomness among the sorbate species, promoting adsorption over the MCh surface.

6.2.4. Interaction studies

6.2.4.1. Adsorption Mechanism

Chitosan has a high amount of amino and hydroxyl functional groups, making it a potent adsorbent for eliminating anionic pollutants from aqueous solutions. In acidic aqueous solutions, these amino groups are much more easily protonated, causing them to adsorb the anionic dyes strongly via strong electrostatic binding. However, as mentioned earlier, low porosity limits the efficiency of chitosan as a potent adsorbent. Fabrication of chitosan to MCh leads to enhanced surface porosity as verified in SEM images (**Figure 6.3.**) and BET pore analysis (**Table 6.1.**). Elevated porosity resorts to the increased surface area, and thus more amino-functional groups are exposed for protonation. This assists in enhanced adsorption of the studied anionic synthetic dyes (BB, DB and CR), as discussed in this article. Other interactions that promoted the adsorptive uptake of BB, DB and CR dye species involved H-bonding, pore-filling mechanism, or the simultaneous occurrence of several other adsorption mechanisms.

6.2.4.2. Isotherm model analysis

6.2.4.2.1. Single adsorptive system

Isotherm modeling of sorbate-sorbent interactions was evaluated via single adsorptive systems, which involved the sorptive elimination of BB, DB and CR dye species by MCh surface, independently at optimised conditions as discussed above. **Table S.6.1.** (Supplementary data) represents the isothermal constants and coefficients of regression values of isothermal modelling utilising the equilibrated experimental data attained from the adsorption experiments from single adsorptive systems. Langmuir isotherm modelling gave a good fit with the equilibrated experimental data obtained for BB, DB and CR dye adsorption by the MCh surface as compared to the Freundlich isotherm model, thus verifying monolayer formation of sorbate dye species on the MCh surface and thus nullifying any prospects of sorbate multilayer formation. As evaluated, Langmuir theoretical maximum adsorption capacities (Q_L) were 81.301 mg/g for CR, 163.934 mg/g for DB, and 75.758 mg/g for BB dye species. Langmuir equilibrium parameter (K_L) lies between 0 to 1 (0.070 for BB, 0.092 for DB and 0.078 for CR), thus favouring favourable dye adsorption over the MCh surface. Frumkin isotherm also showed a good fit for the adsorption process and positive values for the interaction parameter (α), verified attractive forces among the adsorbate (dye) species. The attractive forces could be due to the ionic charges on the dye species in the aqueous solution. Temkin isotherm too gave a good fit verifying the heat-related to dye adsorption in the sorbate monolayer declined gradually with the adsorption of the dye species, thus limiting multilayer formation. Three-parameter isotherm model viz. Sips isotherm model too showed a better fit for the CR, DB and BB dye adsorption over MCh surface. Sips exponent (m) values for BB was 0.97, DB was 1.56, and CR was 1.85. Since all these values for Sips exponent were almost equal to one, verified the feasibility of the Langmuir isotherm for evaluating BB, DB and CR dye adsorption over MCh surface. Curve fitting plots depicting the interaction of the dye species with the MCh surface has been depicted in **Figure 6.12.** These plots also verified good fitting of the Langmuir isotherm model to the equilibrated experimental data over other isotherm models.

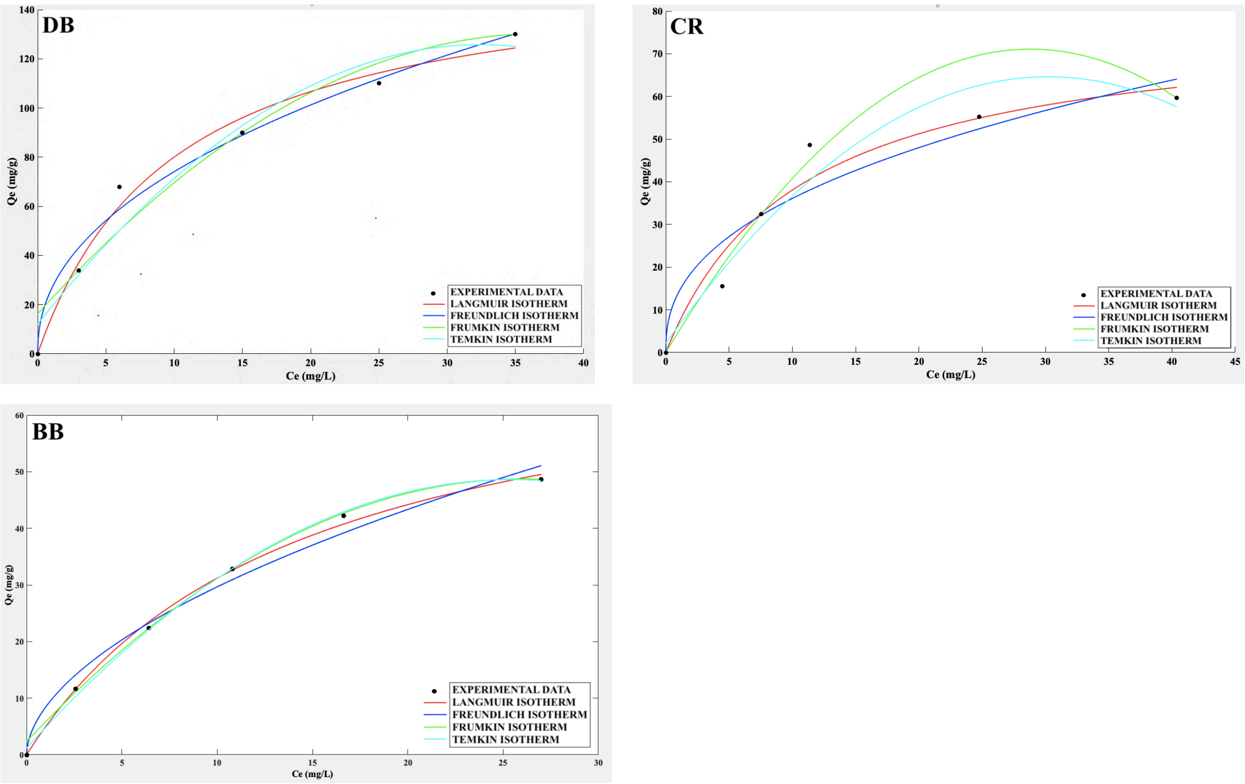

Figure 6.12. *Non-linear isotherm modelling plots for Direct blue (DB), Congo red (CR) and Bromophenol blue (BB)*

6.2.4.2.2. Multi-adsorptive system

6.2.4.2.2.1. Binary adsorptive system

Binary adsorptive systems refer to adsorptive setups having two dyes in the same system, viz. CR+BB, CR+DB and DB+BB and this study involved the influence of a specific dye over the sorption of its counterpart and vice versa, along with affinity analysis of the adsorbent for a specific dye in an individual system. Adsorption capacities (mg/g) of MCh for a specific dye in a single adsorptive system were found high compared to the capacities in the binary and multi-adsorptive systems, as reported in **Table S.6.1.** (Supplementary data) and **Table 6.2.**, respectively. This could be due to mass transfer resistance by a specific dye molecule over the adsorptive elimination of the other dye molecules from the multi- (binary and tertiary) adsorptive setups.

Such competitive sorption of specific dye species in the multi- (binary and tertiary) adsorptive systems was verified utilising the competitive Langmuir adsorption isotherm model. For a multi-adsorbate setup consisting of ‘x’ and ‘y’ elements, competitive Langmuir adsorption isotherm model for element ‘x’ with respect to element ‘y’ can be depicted as follows (Manjunath and Kumar, 2018; Jandera and Komers, 1997):

$$Q_{e,a} = \frac{Q_{CL,a}K_{CL,a}C_{e,a}}{1 + \sum K_{CL,ab}C_{e,ab}} \tag{6.1}$$

Here, $Q_{e,xy}$ and $Q_{CL,x}$ represents adsorption capacity at equilibrium and competitive Langmuir maximum adsorption capacity for element ‘a’, respectively. $K_{CL,x}$ represents the competitive Langmuir coefficient for element ‘x’. $C_{e,x}$ represents the initial concentration of component ‘x’ at equilibria in ‘x+y’ composition. Individual competitive Langmuir adsorption capacities i.e. $Q_{e,BB}$ $Q_{e,DB}$ and $Q_{e,CR}$ in the binary adsorptive (DB+BB, DB+CR and CR+BB) systems were derived from equation 6.1 and are depicted as follows:

$$\frac{1}{Q_{e,CR}} = \frac{1}{Q_{CL,CR}} + \frac{1}{Q_{CL,CR}K_{CL,CR}}[\frac{1 + K_{CL,DB}C_{e,DB}}{C_{e,CR}}] \tag{6.2}$$

$$\frac{1}{Q_{e,DB}} = \frac{1}{Q_{CL,DB}} + \frac{1}{Q_{CL,DB}K_{CL,DB}}[\frac{1 + K_{CL,CR}C_{e,CR}}{C_{e,DB}}] \tag{6.3}$$

$$\frac{1}{Q_{e,CR}} = \frac{1}{Q_{CL,CR}} + \frac{1}{Q_{CL,CR}K_{CL,CR}}[\frac{1 + K_{CL,BB}C_{e,BB}}{C_{e,CR}}] \tag{6.4}$$

$$\frac{1}{Q_{e,BB}} = \frac{1}{Q_{CL,BB}} + \frac{1}{Q_{CL,BB}K_{CL,BB}}[\frac{1 + K_{CL,CR}C_{e,CR}}{C_{e,BB}}] \tag{6.5}$$

$$\frac{1}{Q_{e,DB}} = \frac{1}{Q_{CL,DB}} + \frac{1}{Q_{CL,DB}K_{CL,DB}}[\frac{1 + K_{CL,BB}C_{e,BB}}{C_{e,DB}}] \tag{6.6}$$

$$\frac{1}{Q_{e,BB}} = \frac{1}{Q_{CL,BB}} + \frac{1}{Q_{CL,BB}K_{CL,BB}}[\frac{1 + K_{CL,DB}C_{e,DB}}{C_{e,BB}}] \tag{6.7}$$

Here, $Q_{CL,BB}$, $Q_{CL,DB}$ and $Q_{CL,CR}$ represents the theoretical maximum adsorption capacity (mg/g); $C_{e,BB}$, $C_{e,DB}$ and $C_{e,CR}$ are the final equilibrated concentrations (mg/L); $Q_{e,BB}$, $Q_{e,DB}$ and $Q_{e,CR}$ represents the adsorption capacities (mg/g) and $K_{CL,BB}$, $K_{CL,DB}$ and $K_{CL,CR}$ represents the competitive Langmuir constants (L/mg) for the respective dyes. Equations 6.2 and 6.3 represents CR+DB, equations 6.4 and 6.5 represents CR+BB and equations 6.6 and 6.7 represents DB+BB, binary adsorptive systems. Competitive Langmuir adsorption isotherm showed near perfect fitting towards the equilibrated experimental data as obtained from the binary adsorptive setups and the same has been depicted in **Figure 6.13.**

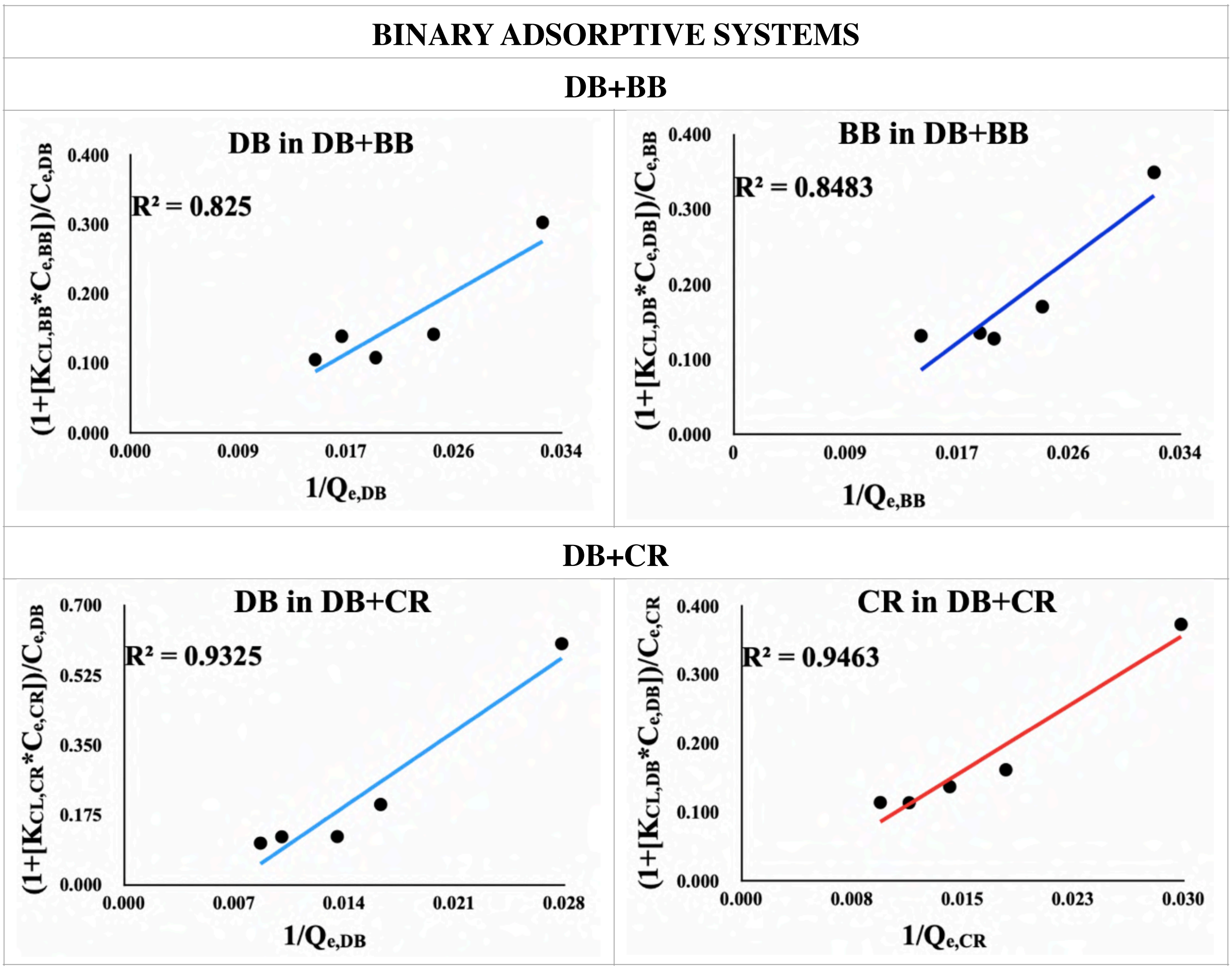

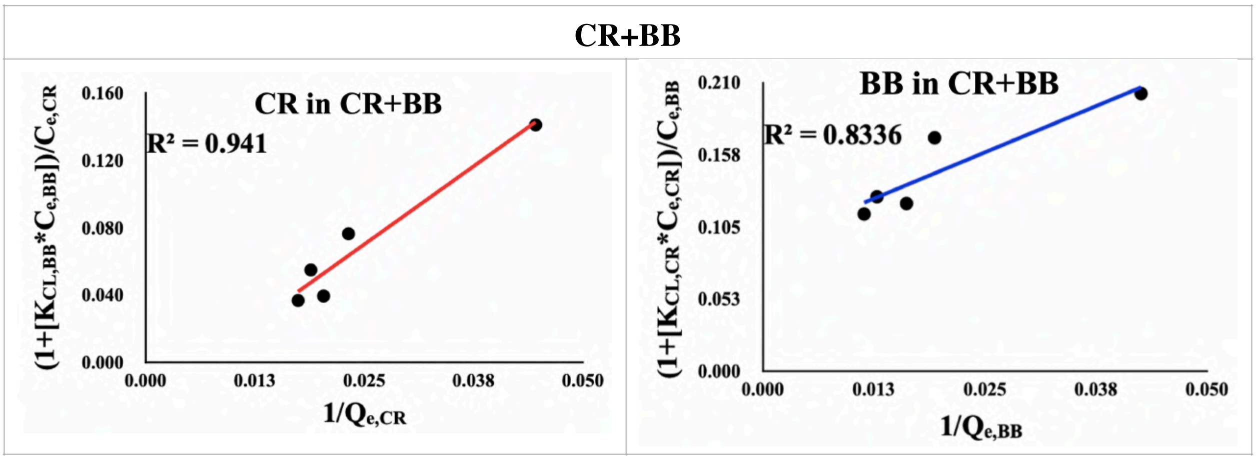

Figure 6.13. *Fitting of Comparative Langmuir Isotherm model for binary adsorptive systems (DB+BB, DB+CR and CR+BB)*

Table 6.2. depicts the values for competitive Langmuir maximum adsorption capacities (mg/g) i.e. $Q_{CL,BB}$, $Q_{CL,DB}$ and $Q_{CL,CR}$, along with associated constants for the binary adsorptive systems. Higher values of adsorption capacity for one dye over another dye in a binary adsorptive system could possibly be due to variation in affinity by MCh surface for a specific dye with respect to another; in an individual binary adsorptive system. Positive values for competitive Langmuir constants viz. $K_{CL,CR}$, $K_{CL,DB}$ and $K_{CL,BB}$ verified the easiness of the adsorptive removal of dye species in the binary adsorptive system.

Further, to evaluate the influence of a specific adsorbate over the adsorptive removal efficiency of the counter dye species in an adsorptive setup, by the adsorbent (MCh), Q_{Binary}/Q_{Single} and $Q_{Tertiary}/Q_{Single}$ ratio was evaluated. Q_{Single}, Q_{Binary} and $Q_{Tertiary}$ refer to the theoretical maximum adsorption capacity values of the adsorbent in single, binary and tertiary adsorptive setups, respectively. 3 possibilities that can be anticipated from the ratio values (Patra et al., 2020):

A. Values equal to unity, resorts to non-interaction among individual adsorbate species;

B. Values more than unity, represents the synergistic adsorption of specific adsorbate species due to other adsorbate species;

C. Values less than unity represents the antagonistic adsorption of specific adsorbate species due to other adsorbate species, in the multi-adsorptive system.

Table 6.2. represents the Q_{Binary}/Q_{Single} values for BB, DB and CR dye species in binary adsorptive (DB+BB, CR+DB and CR+BB) systems. Since for all BB, DB and CR dyes species, the Q_{Binary}/Q_{Single} values are less than 1 thus verifying to a conclusion that all 3 dye species competed antagonistically with each other individually in their respective setups, for adsorption over MCh

surface. Such antagonistic behaviour in binary adsorptive systems could be due to the fact that both anionic dyes in an individual adsorptive system compete with each other to bind to the protonated MCh surface. The results also verified the affinity of the MCh surface for a specific dye in a binary adsorptive system. Higher values for maximum adsorption capacity for a specific dye in a binary adsorptive setup, can be inferred to higher affinity of the adsorbent's surface towards that specific dye species.

Table 6.2. *Competitive Langmuir model for individual dye species removal in multi component (binary and tertiary) adsorptive systems*

BINARY ADSORPTIVE SYSTEMS

ADSORPTIVE MODELS	Competitive Langmuir maximum adsorption capacity (mg/g)	Competitive Langmuir constants (L/mg)	Q_{Binary}/Q_{Single}	R^2
CR in CR+DB	$Q_{CL,CR}$: 25.974	$K_{CL,CR}$: 0.003	0.320	0.946
DB in CR+DB	$Q_{CL,DB}$: 5.534	$K_{CL,DB}$: 0.007	0.034	0.933
CR in CR+BB	$Q_{CL,CR}$: 44.444	$K_{CL,CR}$: 0.006	0.548	0.941
BB in CR+BB	$Q_{CL,BB}$: 10.881	$K_{CL,BB}$: 0.034	0.144	0.834
DB in BB+DB	$Q_{CL,DB}$: 15.576	$K_{CL,DB}$: 0.006	0.095	0.825
BB in BB+DB	$Q_{CL,BB}$: 9.911	$K_{CL,BB}$: 0.008	0.131	0.848

TERTIARY ADSORPTIVE SYSTEMS

ADSORPTIVEMODELS	Competitive Langmuir maximum adsorption capacity (mg/g)	Competitive Langmuir constants (L/mg)	$Q_{Tertiary}/Q_{Single}$	R^2
CR in CR+DB+BB	$Q_{CL,CR}$: 39.216	$K_{CL,CR}$: 0.002	0.482	0.929
DB in CR+DB+BB	$Q_{CL,DB}$: 12.240	$K_{CL,DB}$: 0.010	0.075	0.869
BB in CR+DB+BB	$Q_{CL,BB}$: 7.294	$K_{CL,BB}$: 0.008	0.096	0.885

6.2.4.2.2.2. Tertiary adsorption system

In order to evaluate the influence of multiple dyes in adsorptive removal of individual dye by adsorbent MCh i.e. CR in DB+CR+BB, DB in DB+CR+BB and BB in DB+CR+BB, competitive Langmuir adsorption isotherm for multi-component (binary and tertiary) system was studied for systems having all the 3 dyes in one system viz. DB+CR+BB. Equation 6.1 can thus be modified to evaluate equations for the tertiary adsorptive systems and they are as follows:

$$\frac{1}{Q_{e,CR}} = \frac{1}{Q_{CL,CR}} + \frac{1}{Q_{CL,CR}K_{CL,CR}}[\frac{1 + K_{CL,DB}C_{e,DB} + K_{CL,BB}C_{e,BB}}{C_{e,CR}}] \tag{6.8}$$

$$\frac{1}{Q_{e,DB}} = \frac{1}{Q_{CL,DB}} + \frac{1}{Q_{CL,DB}K_{CL,DB}}[\frac{1 + K_{CL,CR}C_{e,CR} + K_{CL,BB}C_{e,BB}}{C_{e,DB}}] \tag{6.9}$$

$$\frac{1}{Q_{e,BB}} = \frac{1}{Q_{CL,BB}} + \frac{1}{Q_{CL,BB}K_{CL,BB}}[\frac{1 + K_{CL,CR}C_{e,CR} + K_{CL,DB}C_{e,DB}}{C_{e,BB}}] \tag{6.10}$$

The denotations used for equations 6.8, 6.9 and 6.10 are same as that for explained for equations representing binary adsorptive systems. As represented in **Table 6.2.**, the $Q_{Tertiary}/Q_{Single}$ for BB was 0.096, DB was 0.075 and CR was 0.482 in tertiary (DB+CR+BB) adsorptive setup. Values for $Q_{Tertiary}/Q_{Single}$ is less than 1 for all the individual dye species in an specific tertiary adsorptive system, thus verifying antagonistic effect by other dyes in the adsorption effect on an individual dye over MCh surface in tertiary adsorptive systems. It can also be reported that CR has highest adsorptive removal as compared to DB and BB, with BB having the least removal capacity in the tertiary adsorptive system. This could possibly be due to the affinity of MCh surface towards the individual dye species in the tertiary adsorptive mixture, which resulted in variable adsorption capacities. Competitive Langmuir adsorption isotherm showed near perfect fitting towards the equilibrated experimental data as obtained from the tertiary adsorptive setups and the same has been depicted in **Figure 6.14.**

TERTIARY ADSORPTIVE SYSTEM (DB+CR+BB)	
DB in DB+CR+BB	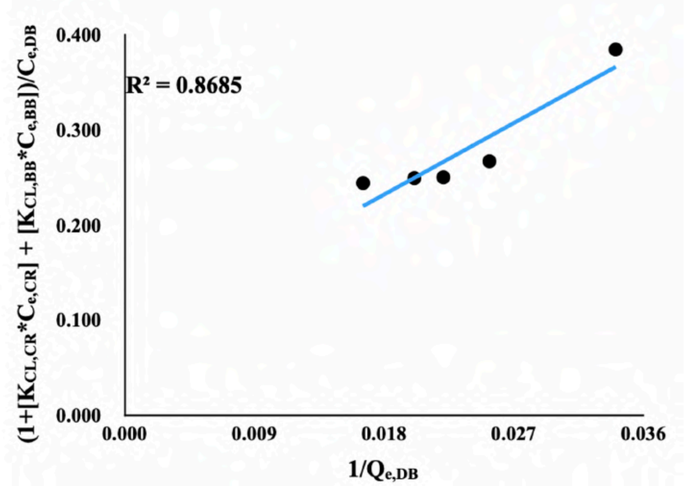
CR in DB+CR+BB	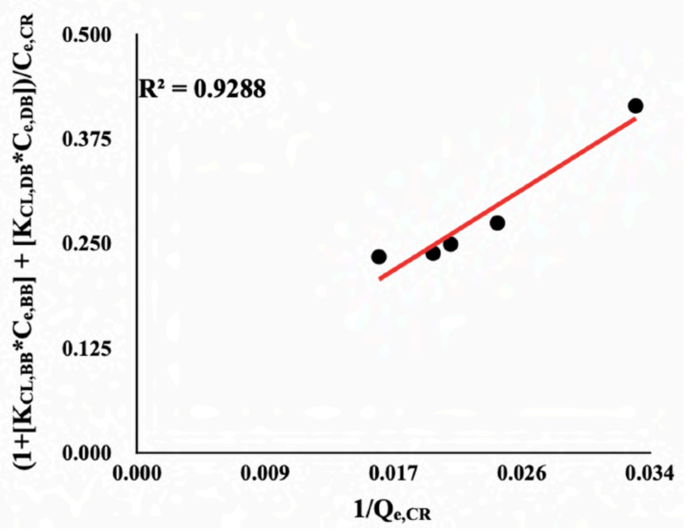
BB in DB+CR+BB	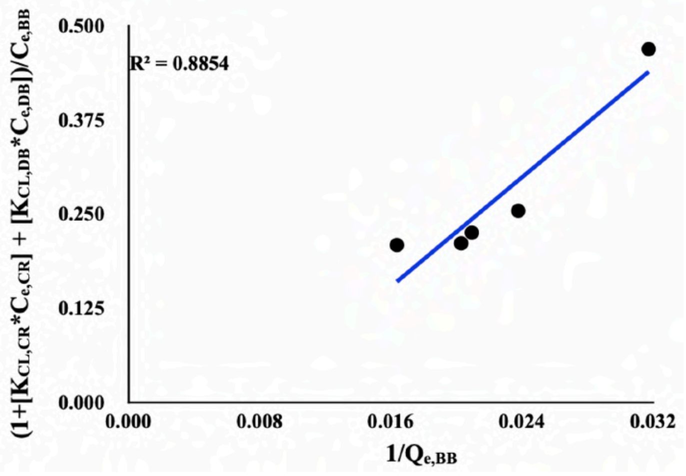

Figure 6.14. *Fitting of Comparative Langmuir Isotherm model for tertiary adsorptive system (DB+CR+BB)*

6.2.4.3. Adsorption kinetics

Kinetics models like pseudo-first-order, pseudo-second-order and intra-particle diffusion models were studied to evaluate the kinetics of the sorbate-sorbent interactions. **Table S.6.2.**

(Supplementary data) represents the fitting coefficients (R^2) for the studied kinetic models for the adsorption of BB, DB and CR dye species by the adsorbent MCh. The data thus obtained verified good fitting of pseudo-second-order kinetics compared to pseudo-first-order and intra-particle diffusion, thus verifying the applicability of chemisorption as the rate-limiting step between the sorbate (dye species) and the sorbent (MCh). The fitting was further verified with the near similarity of the theoretical adsorption capacity (Q_e) values as anticipated by pseudo-second-order kinetics with the experimental adsorption capacity ($Q_{e\ exp.}$) values. **Figure 6.15.** represents non-linear curve fitting for the studied kinetic models, and as depicted, it verifies the pseudo-second-order model being in close proximity fitting with the experimental data with respect to other models.

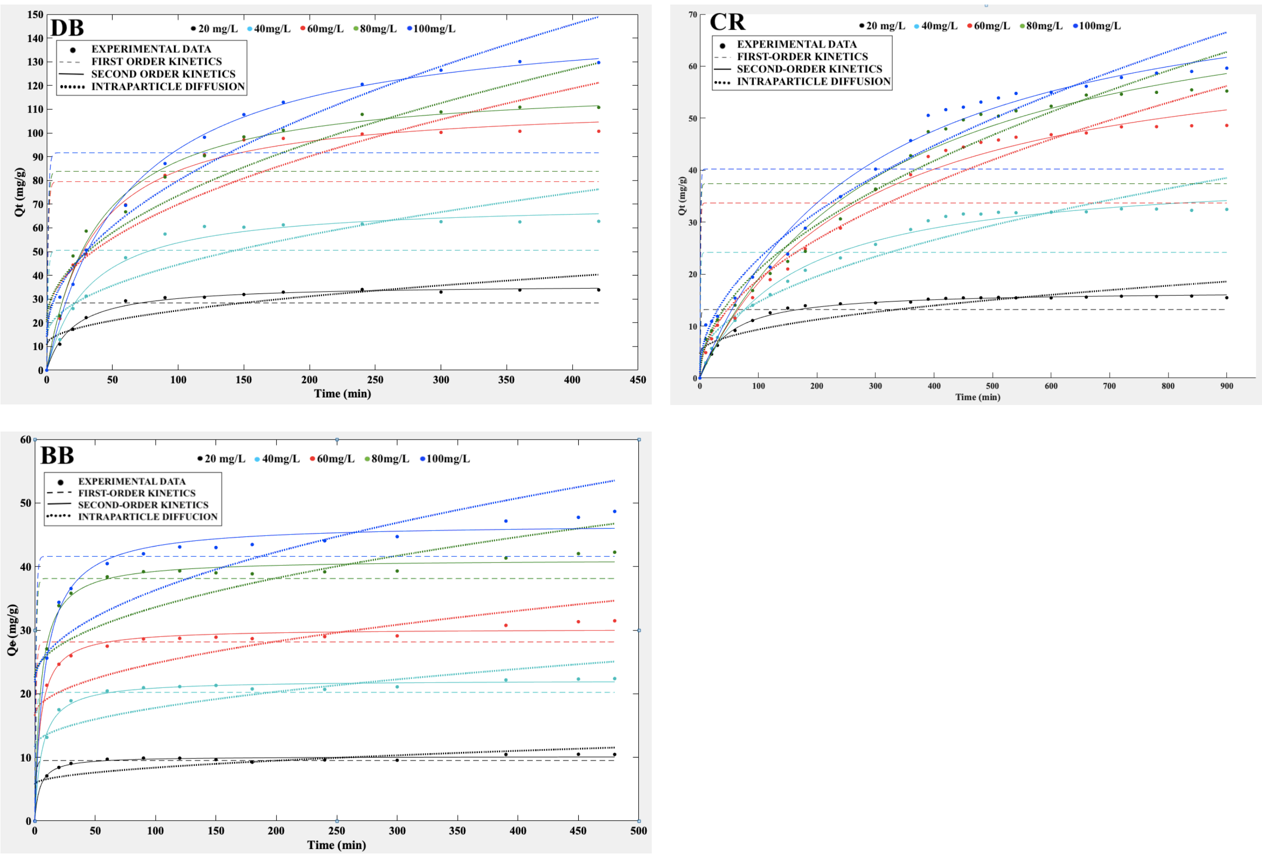

Figure 6.15. *Non-linear kinetics modelling plots for Direct blue (DB), Congo red (CR) and Bromophenol blue (BB)*

6.2.5. Influence of Co-existing metal cations and anionic salts

Co-existing metal cations (Ni^{+2}, Co^{+2}, Pb^{+2}, Cu^{+2} and Cr^{+6}) and anionic salts (NO_3^{-2}, SO_4^{-2}, CO_3^{-2}, PO_4^{-3} and Cl^{-1}) affected the efficient adsorption of the dye species over adsorbent's (MCh) surface, and the same has been depicted in **Figure 6.16.** Co-existing metal cations, showed a nominal reduction in the adsorption efficiencies as compared to the setup with no ions. It can be speculated that this decline in the adsorption efficiencies could be due to conversion of the metal ions into its specific hydration forms in aqueous solution, specifically into $M(OH)_X$ and $M(OH)^+$ forms. Also, as reported by Tobin et al., 1984, metal ionic radii in aqueous solutions influence its adsorption i.e. greater the ionic radii of the metal cation, lower will be the span of its metal hydrate form and hence greater will be its uptake via ion-exchange over the adsorbent's (MCh) surface. Size distribution of the cationic metals in terms of their ionic radii in angstrom (Å) are as follows: (Quintelas et al., 2009; Dong et al., 2018):

Cr^{+6} (0.44 Å) < Ni^{+2} (0.69 Å) < Cu^{+2} (0.73 Å) < Co^{+2} (0.745 Å) < Pb^{+2} (1.20 Å)

Accordingly, metal ions with greater ionic radii (like Pb^{+2}, Co^{+2}) will tend to have relatively smaller metal hydrate forms in aqueous solutions and thus these metal ions will show more uptake via ion exchange on the adsorbent's (MCh) surface with respect to metal cations with lower ionic radii (like Cr^{+6}, Ni^{+2}). Owing to such properties, metal ions with higher ionic radii (like Pb^{+2}, Co^{+2}) will resort to compete more with the anionic dye species (BB, DB and CR) for getting adsorbed over the adsorbent's surface followed by metal ions with least ionic radii like Cr^{+6}, Ni^{+2} etc. as depicted in **Figure 6.16.**

Co-existing anionic salts also showed minimal effect on the adsorption efficiencies (%) of the dye species as compared to dye set up with no coexisting ions. This could also be due to the competitive adsorption of the negatively charged salts with respect to the negatively charged anionic dye species, over MCh (Wang et al., 2014).

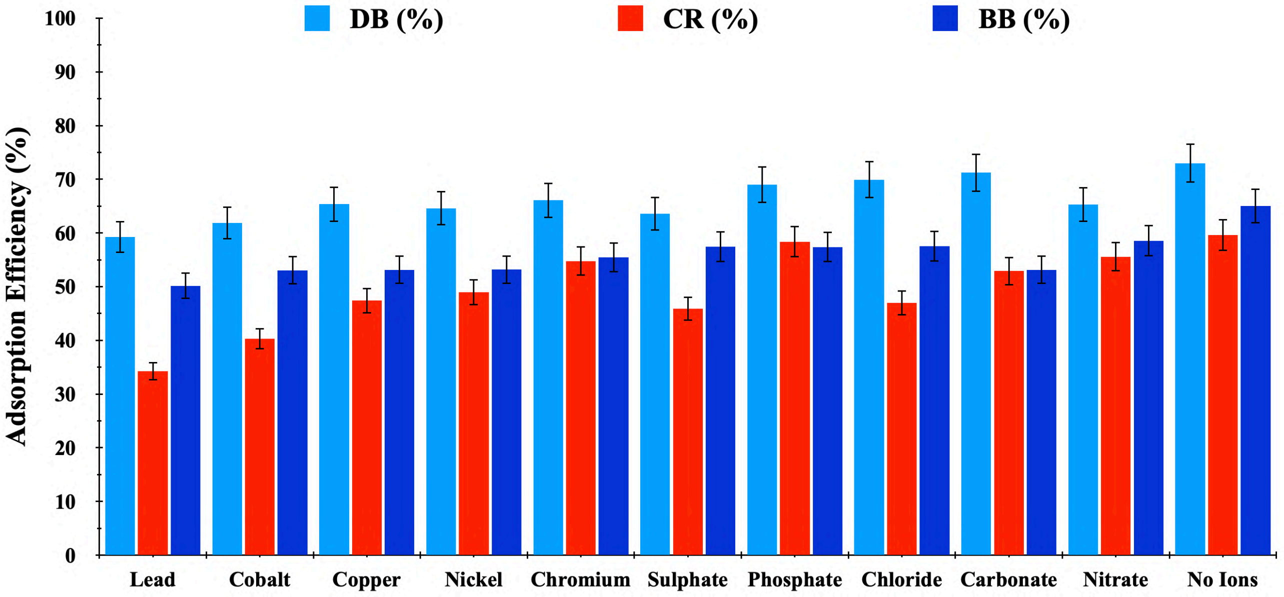

Figure 6.16. *Effect of co-existing metal cations and anionic salts on the adsorption of DB, CR and BB dye species by MCh surface*

6.2.6. Phytotoxicity assays and evaluation

Phytotoxicity assays were done to test the adsorbent's effectivity in remediating CR, DB and BB dye species from aqueous solutions. This was done by evaluating the toxicity effects of the dye solution (before and after the adsorbent's treatment) on the germinative growth of the *Vigna mungo* (black gram) seeds. For this, 10 *Vigna mungo* seeds were germinated in 100 mg/L of dye solutions before adsorbent treatment (control samples); dye solutions after adsorbent treatment, i.e. after adsorption process (test samples) and in distilled water (blank). The seeds were germinated for seven days (1 week) in an artificially created low light setup (with intensity <1.00 lx) at normal room temperature. After seven days, the root lengths were measured and reported, as illustrated in **Figure 6.17.** As shown in **Figure 6.17.**, the root length of the germinated seeds in distilled water (blank) showed the maximum root length with an average root length of 23.20 cm. This average root length in distilled water was considered full growth root length (100% root length).

Relatively, the average root lengths of the seed samples germinated in single adsorptive systems (before adsorbent treatment) were found to be 11.25 cm (48.50%), 13.75 cm (59.27%) and 7.88 cm (33.97%) for DB, CR and BB dye species, respectively. Average root lengths for the same adsorptive systems post adsorbent treatment (after adsorption) were found to be 14.30 cm (61.64%) for DB, 19 cm (81.90%) for CR and 18.2 cm (78.45%) for BB.

Average root lengths for seeds germinated in binary adsorptive systems (before adsorbent treatment) were found to be 9 cm (38.79%), 10 cm (43.10%) and 11.33 cm (48.84%) for DB+BB, DB+CR and BB+CR binary adsorptive systems, respectively. After adsorbent treatment (i.e. after adsorption), root lengths for germinated seeds showed an elevated root length, viz. 20.66 cm (89.05%) for DB+BB, 18.66 cm (80.43%) for DB+CR and 19.33 cm (83.32%) for BB+CR.

Finally, for the tertiary adsorptive system (DB+BB+CR), the average root length of seeds germinated in dye mixture without adsorbent treatment was 11.56 cm (49.83%) and seeds germinated in dye mixture after adsorbent treatment and was found to be 13.25 cm (57.11%).

Relatively, the average root length for seeds germinated in single and multi (binary and tertiary) adsorptive systems post adsorption was high with respect to seeds germinated in adsorptive systems before the adsorbent treatment. The possible reason for elevated and improved average root lengths for seeds germinated in dye solutions post adsorbent treatment (after adsorption) could be due to lowered dye toxicity attributed to the reduced concentration of dyes due to adsorption.

Conclusively, it can be reported that fabricated porous chitosan (MCh) can potentially adsorb dye species from single and multi-adsorptive systems, which resorted to improved seed root lengths, thus concluding to efficient adsorption of dye species by MCh.

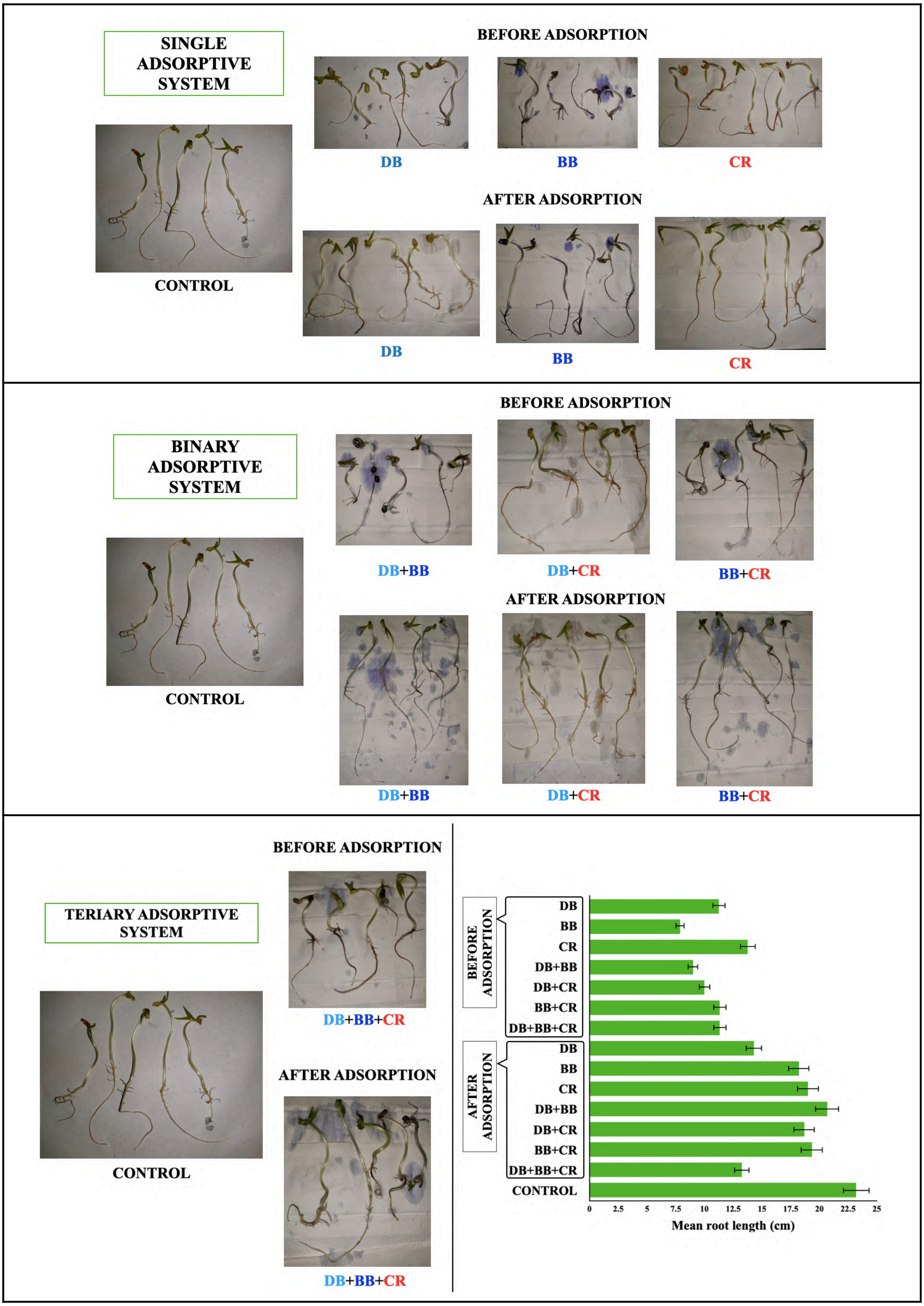

Figure 6.17. Phytotoxic assessment of MCh surface in removing DB, CR and BB form single and multi (binary and tertiary) adsorptive systems using Vigna mungo (black gram) seeds

6.3. Significant findings

Chitosan was fabricated to porous chitosan (MCh) via gelation method using $CaBr_2.xH_2O$/methanol solution to eliminate anionic synthetic dyes viz. BB, DB and CR from single and multi (binary and tertiary) adsorptive systems. Characterisation of MCh surface verified enhanced pore density and porosity. Variable process parameters like the initial pH of the anionic dye solution, sorbate-sorbent interaction temperature, initial dye concentration and adsorbent's dosage influenced the optimal adsorptive uptake of the dye species by the sorbent (MCh). Adsorptive studies involving single adsorptive setups verified the formation of dye species monolayer over the sorbent's (MCh) surface via chemisorption, as established by Langmuir isotherm and pseudo-second-order kinetics model analysis. Multi-adsorptive systems viz. binary and tertiary adsorptive systems analysis verified the antagonistic effect of individual dye over its counterpart dye species in their respective systems. This was possibly due to variable affinities of the MCh surface towards a specific anionic dye species. Thermodynamic analysis of the sorbate-sorbent interaction was verified as exothermic, spontaneous, with an elevated degree of disorderedness, thus concluding the interaction as thermodynamically favourable. Co-existing metal cations and anionic salts revealed a nominal reduction in the adsorbent's efficiency in adsorbing the dye species. A phytotoxic assay using *Vigna mungo* (black gram) seeds verified the potential of the adsorbent (MCh) in adsorptive uptake of dyes from single and multi-adsorptive systems resorting to successful germination of the *Vigna mungo* seeds. Overall, fabricated porous chitosan (MCh) can be concluded as an efficient and effective adsorbent to eliminate anionic synthetic dye species from dye wastewater. It can further be investigated to eliminate pollutants of different grades and other possible modifications to enhance its uptake capacity.

SUPPLEMENTARY DATA FOR CHAPTER 6

Table S.6.1. *Adsorption isotherm model parameters, constants and coefficient of determination (R^2) for removal of CR, DB and BB dye species by MCh*

ISOTHERMS		ISOTHERM CONSTANTS	CR	DB	BB
Two-parameter isotherm models	**Langmuir**	**Q_L (mg/g)**	81.301	163.934	75.758
		K_L (L/mg)	0.078	0.092	0.070
		R^2	0.928	0.982	0.993
	Freundlich	**K_F (mg/g) (mg/L)$^{-1/n}$**	2.608	3.876	2.298
		1/n	0.558	0.502	0.629
		R^2	0.802	0.942	0.982
	Frumkin	**K_{FK}**	$1.32\text{x}10^{-5}$	$0.11\text{x}10^{-5}$	$0.001\text{x}10^{-5}$
		α	6.601	8.199	11.238
		R^2	0.881	0.968	0.935
	Temkin	**A_T (L/g)**	0.680	0.909	0.720
		B (J/mol)	130.195	69.373	154.095
		R^2	0.897	0.982	0.986
Three-parameter models	**Sips**	**K_S**	0.019	0.070	0.069
		Q_S (mg/g)	69.444	121.951	78.740
		m	1.85	1.56	0.97
		R^2	0.990	0.991	0.998

Table S.6.2. *Kinetic model parameters and coefficient of determination (R^2) for the removal of CR, DB and BB by MCh*

C_i (mg/l)	Q_e Exp. (mg/g)	Pseudo-First Order			Pseudo-Second Order			Intra-Particle Diffusion		
		K_1 (1/min)	Q_e (mg/g)	R^2	K_2 (1/min)	Q_e (mg/g)	R^2	K_{id} (mg/g min$^{1/2}$)	C (mg/g)	R^2
CR										
20	15.55	0.004	7.18	34.30	1.669	16.42	99.60	0.46	4.72	78.08
40	32.44	0.005	27.38	20.51	0.232	37.49	98.94	1.19	2.69	92.95
60	48.60	0.006	55.79	16.83	0.094	59.52	98.28	1.86	0.33	95.43
80	55.22	0.006	79.27	21.98	0.075	68.07	98.45	2.10	0.15	92.84
100	59.62	0.005	67.43	17.67	0.080	79.86	97.81	2.18	1.11	96.67
DB										
20	34.00	0.009	14.41	78.08	2.039	35.03	98.64	1.45	10.71	89.80
40	68.00	0.013	32.88	82.19	0.678	66.88	99.47	3.03	14.25	90.82
60	90.00	0.015	70.10	82.40	0.369	108.06	99.78	4.88	21.04	92.67
80	110.00	0.015	108.06	82.19	0.265	119.42	99.68	5.33	20.30	94.61
100	130.00	0.040	147.94	77.42	0.152	143.61	99.79	6.58	14.12	97.24
BB										
20	11.62	0.009	3.34	98.09	0.012	10.45	99.73	0.26	5.74	75.23
40	22.39	0.008	6.38	96.98	0.006	22.40	99.86	0.61	11.66	77.22
60	32.81	0.009	11.89	98.03	0.001	31.38	99.84	0.83	16.55	76.91
80	42.25	0.007	12.08	97.79	0.003	42.08	99.88	1.10	22.57	76.30
100	48.67	0.007	19.93	95.58	0.002	48.53	99.81	1.45	21.83	81.46

Table S.6.3. *Thermodynamics Parameters (ΔG°, ΔH°, and ΔS°) for adsorption of CR, DB and BB by MCh*

C_i (mg/L)	**Temp. (K)**	**CR**			**DB**			**BB**		
		ΔG^o kJ/mol	**ΔH^o kJ/mol**	**ΔS^o J/molK**	**ΔG^o kJ/mol**	**ΔH^o kJ/mol**	**ΔS^o J/molK**	**ΔG^o kJ/mol**	**ΔH^o kJ/mol**	**ΔS^o J/molK**
20	**293**	-18.40	-31.05	39.48	-19.00	-48.84	98.20	-17.31	-49.81	107.23
	298	-20.68			-20.86			-19.18		
	303	-21.27			-21.57			-19.88		
	308	-19.71			-22.08			-20.39		
	313	-20.08			-20.28			-18.59		
40	**293**	-19.92	-19.88	3.72	-20.37	-53.45	107.44	-18.65	-55.55	120.32
	298	-21.87			-22.03			-20.31		
	303	-22.16			-22.93			-21.21		
	308	-22.56			-23.44			-21.72		
	313	-21.59			-23.25			-21.47		
60	**293**	-17.53	-2.19	76.58	-19.53	-40.16	59.76	-17.78	-40.22	65.69
	298	-20.52			-21.67			-19.92		
	303	-21.78			-22.80			-21.05		
	308	-21.87			-23.55			-21.80		
	313	-21.86			-23.67			-21.92		
80	**293**	-24.66	-38.61	191.51	-19.82	-20.97	6.61	-18.04	-20.22	3.35
	298	-21.98			-21.74			-19.97		
	303	-20.02			-23.17			-21.40		
	308	-19.18			-23.91			-22.14		
	313	-17.70			-24.28			-22.51		
100	**293**	-18.52	-34.90	179.15	-16.67	-11.85	114.32	-14.87	-11.67	107.95
	298	-21.18			-18.19			-16.38		
	303	-22.66			-19.81			-18.01		
	308	-23.09			-21.90			-20.10		
	313	-22.96			-22.47			-20.66		

CHAPTER 7

Overall summary and singnificance of thesis work

7.1. Overall summary

The current thesis emphasised the development and fabrication of adsorbents to eliminate pollutants of varying grades under simulated conditions efficiently. Such modifications were implied for the adsorbents to overcome their shortcomings and thus efficiently develop their surface to eliminate pollutants from aqueous setups.

Chapter 1 emphasises the background study of the pollutants and the irreversible damages they cause to the ecosystem and its living beings and how we as humans are responsible for it and are getting affected by it altogether. The three classes of pollutants considered for the current research work were heavy metals (Chromium), dyes (Congo red, Direct blue and Bromophenol blue) and antibiotics (Sulfamethoxazole). A detailed list of conventional methods for wastewater treatment and their demerits has been listed, along with the significance of adsorption as an efficient alternative for eliminating pollutants. This chapter also highlights the studied adsorbents, their demerits and the modifications implied to overcome their shortcomings.

Chapter 2 emphasises the synthesis of acid activated carbon from a shelled biomass viz. *Pongamia pinnata* shells. The free and easy availability of the shelled biomass amalgamated the prepared carbon with the property of economic scalability and eco-friendliness. The shelled biomass was crushed and dried, followed by its acid activation (treatment) with different acids, followed by carbonisation at high temperatures. The raw powdered biomass and prepared acid activated carbon adsorbents were studied to eliminate Cr(VI), a heavy metal pollutant, from simulated aqueous setups. This was associated with optimising the process parameters that promote the efficient elimination of Cr(VI) from aqueous setups. A comparative study was carried out to conclude that acid activation caused the biomass to achieve an oxidised porous carbon surface that promoted the efficient elimination of Cr(VI) species under optimised conditions.

Chapter 3 emphasises the synthesis of acid activated carbon from another shelled biomass viz. *Sterculia villosa Roxb*. shells. The prepared carbon was chelated with Ethylenediaminetetraacetic acid (EDTA) to enhance its surface uptake capacity towards Cr(VI). A comparative analysis verified that chelated acid activated carbon had better adsorption capacity towards Cr(VI) than non-chelated acid activated carbon. However, chelated acid-activated carbon showed reduced adsorptive capabilities at higher temperatures, thus verifying low bond stability between EDTA and acid-activated carbon at higher temperatures.

Chapter 4 details the fabrication of the prepared acid activated carbon with cationic surfactant Cetyltrimethylammonium bromide (CTAB) for enhancing the wettability of the carbon surface. For this chapter, the target pollutants were azo anionic dyes viz. Congo red and Direct blue. The CTAB molecules tend to cover the hydrophobic regions on the carbon surface, thus allowing more contact between the adsorbent and the dye adsorbate molecules, apparently enhancing the adsorption capabilities of the prepared adsorbent.

Chapter 5 emphasises polypyrrole complexation of the biomass-derived powdered carbon adsorbent to enhance its Nitrogen-containing functional groups. This shall let the carbon adsorbent acquire a positively charged surface for efficient adsorptive elimination of an emerging antibiotic pollutant viz Sulfamethoxazole from aqueous setups. Polypyrrole was complexed via in-situ oxidative polymerisation using ammonium persulfate (APS) as the oxidant. Efficient adsorptive interactions were reported at pH 6.0, owing to anionic Sulfamethoxazole species and cationic polypyrrole forms viz. polaron state (PPy+.) and bi-polaron state (PPy++); apart from other transitional and neutral forms. This chapter also highlighted the adsorbent's performance in eliminating an adsorbate via packed bed columns. Continuous column studies verified lower column bed heights (cm), higher inlet feed concentrations (mg/L), and higher initial feed flow rates (mL/min) resorted to quick saturation of the packed bed column.

In Chapter 6, Chitosan was fabricated to porous Chitosan via gelation method using $CaBr_2.xH_2O$/ methanol solution. It was studied as a potential adsorbent in adsorbing anionic synthetic dyes like Bromophenol blue, Direct blue and Congo red from single (one dye species at a time) and multi (having two dyes, i.e. binary and all three dyes, i.e. tertiary) adsorptive systems. Competitive Langmuir modelling studies verified the antagonistic effect of one dye over the adsorption of other dyes for all the dye species in all binary and tertiary adsorptive systems.

7.2. Significance of thesis work

Since the industrial revolution era, humans have been poised by the revolutionary benefits of technological advancements and the associated economic and ease of living benefits. However, this comes at the cost of various detrimental effects on the environment and the associated ecosystems. The population boom also has a fair share of the ecological crisis the present generation is doomed to face. Water, the chief component of an ecosystem, is the worst affected resource, and current efforts seem very little to avoid the drastic effects of water pollution. Most countries still rely on ages-old conventional water remediation techniques to provide clean potable drinking water to their citizens. For example, the carbon filters of the household water purifiers are limited to heavy metal remediation and elimination of any foul taste or smell from the drinking water. However, the load of different grades of pollutants is gradually increasing. It is time such household water purifiers be equipped with carbon filters that could target a variety of pollutants with efficiency. The current thesis has tried to imply some of the modifications that adsorbents could be implied with to minimise some of its limitations and make them capable of targetting various pollutants of different grades. Many pollutants like microplastics and various other organic pollutants like antibiotics, fertilisers etc., have already been categorised as emerging contaminants (ECs) as they could potentially end up in drinking water in the coming times. The current thesis could lay the base for future researchers to develop more potential adsorbents or surface modifications/functionalisation of existing adsorbents to counter such emerging contaminants.

Also, with generations, the quantitative load of pollutants in the drinking water is gradually rising. This is causing the water purifier manufacturers to include more state of the art technologies in their purifiers to minimise the load. One such technology is the inclusion of capacitive deionisation (CDI) units to water purifiers to counter ionic pollutants that could bypass the RO filters or UF units. One of the key components to such CDI units are the carbon electrodes. This study could allow future researchers to efficiently modify such carbon electrodes to eliminate emerging contaminants.

The following schematic representation summarises the significance of the current thesis work.

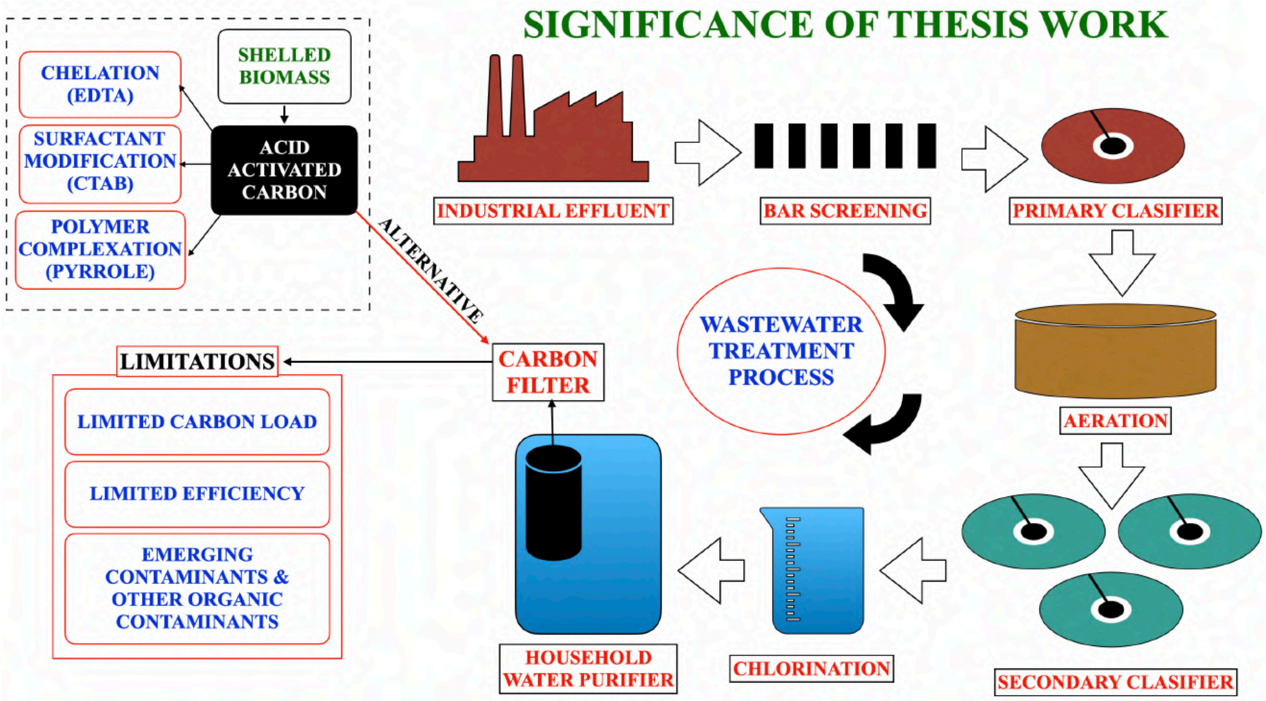

7.3. Overall conclusion

Biomass-derived adsorbents have the potential to eliminate various pollutants like heavy metals, dyes, and antibiotics. The current study concludes that biomass-derived adsorbents associated with their surface modification/functionalisation could be a good alternative in the current water remediation technologies or could be a part of any existing or future technology. For every modification, a rise in the adsorptive potential of the adsorbents was observed for all reported adsorbents towards specific pollutants.

Surface modification or functionalisation or fabrication provided the adsorbents with an enhanced adsorptive surface and uplifted other associated properties like their reusability (for carbonaceous adsorbents); their adsorptive efficacy in concentrated or dilute systems, and their performance in aqueous systems with co-existing pollutants or ionic salts.

For future studies, researchers could venture into more alternative biomass-derived adsorbents to eliminate a varying grade of present-day pollutants and other emerging contaminants or modify/ fabricate the current adsorbents with more efficient modifiers or functional groups to further enhance their uptake capacities.

BIBLIOGRAPHY

- Abdi, M.M., Azli, N.F.W.M., Lim, H.N., Tahir, P.M., Karimi, G., Hoong, Y.B., Khorram, M., 2018. Polypyrrole/tannin biobased nanocomposite with enhanced electrochemical and physical properties. RSC Adv. 8, 2978–2985.
- Ahmetović, E., Ibrić, N., Kravanja, Z., Grossmann, I.E., 2015. Water and energy integration: A comprehensive literature review of non-isothermal water network synthesis. Computers & Chemical Engineering 82, 144–171.
- Ali, R., Aslam, Z., Shawabkeh, R.A., Asghar, A., Hussein, I.A., 2020. BET, FTIR, and RAMAN characterizations of activated carbon from waste oil fly ash. Turk J Chem 44, 279–295.
- Alorabi, A.Q., Shamshi Hassan, M., Azizi, M., 2020. Fe3O4-CuO-activated carbon composite as an efficient adsorbent for bromophenol blue dye removal from aqueous solutions. Arabian Journal of Chemistry 13, 8080–8091.
- Ameen, S., Shaheer Akhtar, M., Shik Shin, H., 2017. Speedy photocatalytic degradation of bromophenol dye over ZnO nanoflowers. Materials Letters 209, 150–154.
- Aneyo, I.A., Doherty, F.V., Adebesin, O.A., Hammed, M.O., 2016. Biodegradation of Pollutants in Waste Water from Pharmaceutical, Textile and Local Dye Effluent in Lagos, Nigeria. Journal of Health and Pollution 6, 34–42.
- Anitha, T., P., SenthilKumar, P., SatishKumar, K., 2016. Synthesis of nano-sized chitosan blended polyvinyl alcohol for the removal of Eosin Yellow dye from aqueous solution. Journal of Water Process Engineering 13, 127–136.
- Assadi, Y., Farajzadeh, M.A., Bidari, A., 2012. 2.10 - Dispersive Liquid–Liquid Microextraction, in: Pawliszyn, J. (Ed.), Comprehensive Sampling and Sample Preparation. Academic Press, Oxford, pp. 181–212.
- Bendjeffal, H., Djebli, A., Mamine, H., Metidji, T., Dahak, M., Rebbani, N., Bouhedja, Y., 2018. Effect of the chelating agents on bio-sorption of hexavalent chromium using Agave sisalana fibers. Chinese Journal of Chemical Engineering 26, 984–992.
- Benes, B., Spěvácková, V., Smíd, J., Cejchanová, M., Cerná, M., Subrt, P., Marecek, J., 2000. The concentration levels of Cd, Pb, Hg, Cu, Zn and Se in blood of the population in the Czech Republic. Cent Eur J Public Health 8, 117–119.
- Benkhaya, S., M' rabet, S., El Harfi, A., 2020. A review on classifications, recent synthesis and applications of textile dyes. Inorganic Chemistry Communications 115, 107891.
- Bharagava, R.N., Mishra, S., 2018. Hexavalent chromium reduction potential of Cellulosimicrobium sp. isolated from common effluent treatment plant of tannery industries. Ecotoxicology and Environmental Safety 147, 102–109.

- Bharagava, R.N., Saxena, G., Mulla, S.I., Patel, D.K., 2018. Characterization and Identification of Recalcitrant Organic Pollutants (ROPs) in Tannery Wastewater and Its Phytotoxicity Evaluation for Environmental Safety. Arch Environ Contam Toxicol 75, 259–272.
- Bhatnagar, A., Hogland, W., Marques, M., Sillanpää, M., 2013. An overview of the modification methods of activated carbon for its water treatment applications. Chemical Engineering Journal 219, 499–511.
- Bhaumik, M., Agarwal, S., Gupta, V.K., Maity, A., 2016. Enhanced removal of Cr(VI) from aqueous solutions using polypyrrole wrapped oxidized MWCNTs nanocomposites adsorbent. Journal of Colloid and Interface Science 470, 257–267.
- Binkley, J., Simpson, J.A., 2003. 35 - Heavy metals in wastewater treatment processes, in: Mara, D., Horan, N. (Eds.), Handbook of Water and Wastewater Microbiology. Academic Press, London, pp. 597–610.
- Blin, J.L., Gigot, L., Léonard, A., Su, B.L., 2002. Mesoporous zirconium oxides : an investigation of physico-chemical synthesis parameters, in: Sayari, A., Jaroniec, M. (Eds.), Studies in Surface Science and Catalysis, Nanoporous Materials III. Elsevier, pp. 257–264.
- Boeckel, T.P.V., Brower, C., Gilbert, M., Grenfell, B.T., Levin, S.A., Robinson, T.P., Teillant, A., Laxminarayan, R., 2015. Global trends in antimicrobial use in food animals. PNAS 112, 5649–5654.
- Bonsignore, M., Salvagio Manta, D., Mirto, S., Quinci, E.M., Ape, F., Montalto, V., Gristina, M., Traina, A., Sprovieri, M., 2018. Bioaccumulation of heavy metals in fish, crustaceans, molluscs and echinoderms from the Tuscany coast. Ecotoxicology and Environmental Safety 162, 554–562.
- Boreen, A.L., Arnold, W.A., McNeill, K., 2004. Photochemical Fate of Sulfa Drugs in the Aquatic Environment: Sulfa Drugs Containing Five-Membered Heterocyclic Groups. Environ. Sci. Technol. 38, 3933–3940.
- Briffa, J., Sinagra, E., Blundell, R., 2020. Heavy metal pollution in the environment and their toxicological effects on humans. Heliyon 6, e04691.
- Cao, Y.-L., Pan, Z.-H., Shi, Q.-X., Yu, J.-Y., 2018. Modification of chitin with high adsorption capacity for methylene blue removal. International Journal of Biological Macromolecules 114, 392–399.
- Carvalho, I.T., Santos, L., 2016. Antibiotics in the aquatic environments: A review of the European scenario. Environment International 94, 736–757.

- Chelating Agents, 2012. , in: LiverTox: Clinical and Research Information on Drug-Induced Liver Injury. National Institute of Diabetes and Digestive and Kidney Diseases, Bethesda (MD).
- Chen, B.-Y., Chang, J.-S., 2007. Assessment upon species evolution of mixed consortia for azo dye decolorization. Journal of the Chinese Institute of Chemical Engineers 38, 259–266.
- Chen, H., Wang, R.-F., Cerniglia, C.E., 2004. Molecular cloning, overexpression, purification, and characterization of an aerobic FMN-dependent azoreductase from Enterococcus faecalis. Protein Expression and Purification 34, 302–310.
- Chowdhary, P., Yadav, A., Kaithwas, G., Bharagava, R.N., 2017. Distillery Wastewater: A Major Source of Environmental Pollution and Its Biological Treatment for Environmental Safety, in: Singh, R., Kumar, S. (Eds.), Green Technologies and Environmental Sustainability. Springer International Publishing, Cham, pp. 409–435.
- Cortés-Arriagada, D., Toro-Labbé, A., 2016. Aluminum and iron doped graphene for adsorption of methylated arsenic pollutants. Applied Surface Science 386, 84–95.
- Costa, M., 2003. Potential hazards of hexavalent chromate in our drinking water. Toxicology and Applied Pharmacology 188, 1–5.
- Crini, G., Lichtfouse, E., 2019. Advantages and disadvantages of techniques used for wastewater treatment. Environ Chem Lett 17, 145–155.
- Dąbrowski, A., 2001. Adsorption — from theory to practice. Advances in Colloid and Interface Science 93, 135–224.
- Dai, M., 1994. The Effect of Zeta Potential of Activated Carbon on the Adsorption of Dyes from Aqueous Solution: I. The Adsorption of Cationic Dyes: Methyl Green and Methyl Violet. Journal of Colloid and Interface Science 164, 223–228.
- Dane, H., Şişman, T., 2020. A morpho-histopathological study in the digestive tract of three fish species influenced with heavy metal pollution. Chemosphere 242, 125212.
- De Gisi, S., Lofrano, G., Grassi, M., Notarnicola, M., 2016. Characteristics and adsorption capacities of low-cost sorbents for wastewater treatment: A review. Sustainable Materials and Technologies 9, 10–40.
- de la Cruz, E.F., Zheng, Y., Torres, E., Li, W., Song, W., Burugapalli, K., 2012. Zeta Potential of Modified Multi-walled Carbon Nanotubes in Presence of poly (vinyl alcohol) Hydrogel.
- Deng, S., Bai, R., 2004. Removal of trivalent and hexavalent chromium with aminated polyacrylonitrile fibers: performance and mechanisms. Water Research 38, 2424–2432.
- Deng, Y., Zhao, R., 2015. Advanced Oxidation Processes (AOPs) in Wastewater Treatment. Curr Pollution Rep 1, 167–176.

- Di Bonito, M., 2008. CHAPTER ELEVEN - SEWAGE SLUDGE IN EUROPE AND IN THE UK: ENVIRONMENTAL IMPACT AND IMPROVED STANDARDS FOR RECYCLING AND RECOVERY TO LAND, in: De vivo, B., Belkin, H.E., Lima, A. (Eds.), Environmental Geochemistry. Elsevier, Amsterdam, pp. 251–286.
- Dong, L., Liang, J., Li, Y., Hunang, S., Wei, Y., Bai, X., Jin, Z., Zhang, M., Qu, J., 2018. Effect of coexisting ions on Cr(VI) adsorption onto surfactant modified Auricularia auricula spent substrate in aqueous solution. Ecotoxicology and Environmental Safety 166, 390–400.
- Duffus, by J.H., 2001. “Heavy Metals”–A Meaningless Term. Chemistry International -- Newsmagazine for IUPAC 23, 163–167.
- Dutta, P., Karmakar, A., Majumdar, S., Roy, S., 2018. Klebsiella pneumoniae (HR1) assisted alleviation of Cd(II) toxicity in Vigna mungo: a case study of biosorption of heavy metal by an endophytic bacterium coupled with plant growth promotion. Euro-Mediterr J Environ Integr 3, 27.
- Ecological Effects Test Guidelines, OPPTS 850.4025, Target Area Phytotoxicity | NEPIS | US EPA [WWW Document], n.d. URL https://nepis.epa.gov/Exe/ZyPURL.cgi?Dockey=P100XGVV.txt (accessed 2.4.22).
- Elmaleh, S., Jabbouri, A., 1991. Flocculation energy requirement. Water Research 25, 939–943.
- Enniya, I., Rghioui, L., Jourani, A., 2018. Adsorption of hexavalent chromium in aqueous solution on activated carbon prepared from apple peels. Sustainable Chemistry and Pharmacy 7, 9–16.
- Fan, X., Yang, Z., He, N., 2015. Hierarchical nanostructured polypyrrole/graphene composites as supercapacitor electrode. RSC Adv. 5, 15096–15102.
- Fatima, M., Farooq, R., Lindström, R.W., Saeed, M., 2017. A review on biocatalytic decomposition of azo dyes and electrons recovery. Journal of Molecular Liquids 246, 275–281.
- Feng, J.-B., Li, Y., Zhang, Y., Xu, Y., Cheng, X.-W., 2022. Adsorptive removal of indomethacin and diclofenac from water by polypyrrole doped-GO/COF-300 nanocomposites. Chemical Engineering Journal 429, 132499.
- Flora, S.J.S., Pachauri, V., 2010. Chelation in Metal Intoxication. Int J Environ Res Public Health 7, 2745–2788.
- Gautam, P.K., Gautam, R.K., Banerjee, S., Chattopadhyaya, M.C. and Pandey, J.D., 2016. Heavy metals in the environment: fate, transport, toxicity and remediation technologies. Nova Sci Publishers, 60, 101-130.

- Gerçel, Ö., Gerçel, H.F., 2007. Adsorption of lead(II) ions from aqueous solutions by activated carbon prepared from biomass plant material of Euphorbia rigida. Chemical Engineering Journal 132, 289–297.
- Githinji, L.J.M., Musey, M.K., Ankumah, R.O., 2011. Evaluation of the Fate of Ciprofloxacin and Amoxicillin in Domestic Wastewater. Water Air Soil Pollut 219, 191–201.
- Guo, Y., Deng, J., Zhu, J., Zhou, Chao, Zhou, Caiyun, Zhou, X., Bai, R., 2016. Removal of anionic azo dye from water with activated graphene oxide: kinetic, equilibrium and thermodynamic modeling. RSC Advances 6, 39762–39773.
- Gupt, C.B., Bordoloi, S., Sekharan, S., Sarmah, A.K., 2020. Adsorption characteristics of Barmer bentonite for hazardous waste containment application. Journal of Hazardous Materials 396, 122594.
- Gupta, P.K., Ranjan, S., Kumar, D., 2018. Groundwater Pollution by Emerging Industrial Pollutants and Its Remediation Techniques, in: Recent Advances in Environmental Management. CRC Press.
- Gupta, V.K., Agarwal, S., Saleh, T.A., 2011. Chromium removal by combining the magnetic properties of iron oxide with adsorption properties of carbon nanotubes. Water Research 45, 2207–2212.
- Gupta, V.K., Gupta, B., Rastogi, A., Agarwal, S., Nayak, A., 2011. A comparative investigation on adsorption performances of mesoporous activated carbon prepared from waste rubber tire and activated carbon for a hazardous azo dye—Acid Blue 113. Journal of Hazardous Materials 186, 891–901.
- Hai, T.A.P., Sugimoto, R., 2018. Fluorescence control of chitin and chitosan fabricated via surface functionalization using direct oxidative polymerization. RSC Advances 8, 7005–7013.
- Han, W., Wang, H., Xia, K., Chen, S., Yan, P., Deng, T., Zhu, W., 2020. Superior nitrogen-doped activated carbon materials for water cleaning and energy storing prepared from renewable leather wastes. Environment International 142, 105846.
- Harrabi, M., Varela Della Giustina, S., Aloulou, F., Rodriguez-Mozaz, S., Barceló, D., Elleuch, B., 2018. Analysis of multiclass antibiotic residues in urban wastewater in Tunisia. Environmental Nanotechnology, Monitoring & Management 10, 163–170.
- Hashimoto, T., Ohori, M., Kashima, T., Yamamoto, H., Tachibana, M., 2013. Chemical cystitis due to crystal violet dye: a case report. Journal of Medical Case Reports 7, 145.

- Hassan, M.F., Sabri, M.A., Fazal, H., Hafeez, A., Shezad, N., Hussain, M., 2020. Recent trends in activated carbon fibers production from various precursors and applications—A comparative review. Journal of Analytical and Applied Pyrolysis 145, 104715.
- He, Z.L., Yang, X.E., Stoffella, P.J., 2005. Trace elements in agroecosystems and impacts on the environment. Journal of Trace Elements in Medicine and Biology 19, 125–140.
- Henriksson, P.J.G., Rico, A., Troell, M., Klinger, D.H., Buschmann, A.H., Saksida, S., Chadag, M.V., Zhang, W., 2018. Unpacking factors influencing antimicrobial use in global aquaculture and their implication for management: a review from a systems perspective. Sustain Sci 13, 1105–1120.
- Herawati, N., S. Suzuki, N., Hayashi, K., Rivai, I.F., 2000. Cadmium, Copper, and Zinc Levels in Rice and Soil of Japan, Indonesia, and China by Soil Type. Bulletin of Environmental Contamination and Toxicology 64, 33–39.
- Hong, S., Deng, S., Yao, X., Wang, B., Wang, Y., Huang, J., Yu, G., 2016. Bromate removal from water by polypyrrole tailored activated carbon. Journal of Colloid and Interface Science 467, 10–16.
- Hu, S., Hsieh, Y.-L., 2017. Lignin derived activated carbon particulates as an electric supercapacitor: carbonization and activation on porous structures and microstructures. RSC Advances 7, 30459–30468.
- Hussein, L.A.A., Fares, N.V., El-Kosasy, A.M., 2014. Spectrophotometric, Spectrofluorimetric, and Potentiometric Assays of Cetyltrimethylammonium Bromide in Industrial Wastewater Samples. Journal of AOAC INTERNATIONAL 97, 1175–1182.
- IR Spectrum Table [WWW Document], n.d. URL https://www.sigmaaldrich.com/IN/en/technical-documents/technical-article/analytical-chemistry/photometry-and-reflectometry/ir-spectrum-table (accessed 2.4.22).
- Jandera, P., Komers, D., 1997. Fitting competitive adsorption isotherms to the experimental distribution data in reversed-phase systems. Journal of Chromatography A, 20th International Symposium on High Performance Liquid Phase Separation and Related Techniques 762, 3–13.
- Jawad, A.H., Razuan, R., Appaturi, J.N., Wilson, L.D., 2019. Adsorption and mechanism study for methylene blue dye removal with carbonized watermelon (Citrullus lanatus) rind prepared via one-step liquid phase H2SO4 activation. Surfaces and Interfaces 16, 76–84.
- Jubeen, F., Liaqat, A., Sultan, M., Zafar Iqbal, S., Sajid, I., Sher, F., 2019. Green synthesis and biological evaluation of novel 5-fluorouracil derivatives as potent anticancer agents. Saudi Pharmaceutical Journal 27, 1164–1173.

- Kabra, A.N., Khandare, R.V., Kurade, M.B., Govindwar, S.P., 2011a. Phytoremediation of a sulphonated azo dye Green HE4B by Glandularia pulchella (Sweet) Tronc. (Moss Verbena). Environ Sci Pollut Res 18, 1360–1373.
- Kabra, A.N., Khandare, R.V., Waghmode, T.R., Govindwar, S.P., 2011b. Differential fate of metabolism of a sulfonated azo dye Remazol Orange 3R by plants Aster amellus Linn., Glandularia pulchella (Sweet) Tronc. and their consortium. Journal of Hazardous Materials 190, 424–431.
- Kadokawa, J., Endo, R., Tanaka, K., Ohta, K., Yamamoto, K., 2015. Fabrication of porous chitin with continuous substructure by regeneration from gel with CaBr2·2H2O/methanol. International Journal of Biological Macromolecules 78, 313–317.
- Kagalkar, A.N., Jagtap, U.B., Jadhav, J.P., Govindwar, S.P., Bapat, V.A., 2010. Studies on phytoremediation potentiality of Typhonium flagelliforme for the degradation of Brilliant Blue R. Planta 232, 271–285.
- Karagöz, S., Tay, T., Ucar, S., Erdem, M., 2008. Activated carbons from waste biomass by sulfuric acid activation and their use on methylene blue adsorption. Bioresource Technology 99, 6214–6222.
- Khan, R., Bhawana, P., Fulekar, M.H., 2013. Microbial decolorization and degradation of synthetic dyes: a review. Rev Environ Sci Biotechnol 12, 75–97.
- Khezami, L., Capart, R., 2005. Removal of chromium(VI) from aqueous solution by activated carbons: Kinetic and equilibrium studies. Journal of Hazardous Materials 123, 223–231.
- Kinuthia, G.K., Ngure, V., Beti, D., Lugalia, R., Wangila, A., Kamau, L., 2020. Levels of heavy metals in wastewater and soil samples from open drainage channels in Nairobi, Kenya: community health implication. Sci Rep 10, 8434.
- Kloster, G.A., Valiente, M., Marcovich, N.E., Mosiewicki, M.A., 2020. Adsorption of arsenic onto films based on chitosan and chitosan/nano-iron oxide. International Journal of Biological Macromolecules 165, 1286–1295.
- Konicki, W., Aleksandrzak, M., Moszyński, D., Mijowska, E., 2017. Adsorption of anionic azo-dyes from aqueous solutions onto graphene oxide: Equilibrium, kinetic and thermodynamic studies. Journal of Colloid and Interface Science 496, 188–200.
- Kraemer, S.A., Ramachandran, A., Perron, G.G., 2019. Antibiotic Pollution in the Environment: From Microbial Ecology to Public Policy. Microorganisms 7, 180.
- Kumar, K.Y., Raj, T.N.V., Archana, S., Prasad, S.B.B., Olivera, S., Muralidhara, H.B., 2016. SnO2 nanoparticles as effective adsorbents for the removal of cadmium and lead from aqueous

solution: Adsorption mechanism and kinetic studies. Journal of Water Process Engineering 13, 44–52.

- Kumar, M., Jaiswal, S., Sodhi, K.K., Shree, P., Singh, D.K., Agrawal, P.K., Shukla, P., 2019. Antibiotics bioremediation: Perspectives on its ecotoxicity and resistance. Environment International 124, 448–461.
- Kumari, V., Tripathi, A.K., 2019. Characterization of pharmaceuticals industrial effluent using GC–MS and FT-IR analyses and defining its toxicity. Appl Water Sci 9, 185.
- Kundu, S., Chowdhury, I.H., Naskar, M.K., 2018. Nitrogen-Doped Nanoporous Carbon Nanospheroids for Selective Dye Adsorption and Pb(II) Ion Removal from Waste Water. ACS Omega 3, 9888–9898.
- Lei, Y., Sheng, N., Hyono, A., Ueda, M., Ohtsuka, T., 2014. Influence of pH on the synthesis and properties of polypyrrole on copper from phytic acid solution for corrosion protection. Progress in Organic Coatings 77, 774–784.
- Li, R., Zhang, Y., Deng, H., Zhang, Z., Wang, J.J., Shaheen, S.M., Xiao, R., Rinklebe, J., Xi, B., He, X., Du, J., 2020. Removing tetracycline and Hg(II) with ball-milled magnetic nanobiochar and its potential on polluted irrigation water reclamation. Journal of Hazardous Materials 384, 121095.
- Li, S., Lu, X., Xue, Y., Lei, J., Zheng, T., Wang, C., 2012. Fabrication of Polypyrrole/Graphene Oxide Composite Nanosheets and Their Applications for Cr(VI) Removal in Aqueous Solution. PLOS ONE 7, e43328.
- Li, Z., Zhu, Z., Chen, Y., Hsu, C.-G., Jiaomai Pan, 1999. Spectrophotometric determination of lead in biological samples with dibromo-p-methyl-methylsulfonazo. Talanta 48, 511–516.
- Liu, Huaqing, Hu, Z., Liu, Hai, Xie, H., Lu, S., Wang, Q., Zhang, J., 2016. Adsorption of amoxicillin by Mn-impregnated activated carbons: performance and mechanisms. RSC Advances 6, 11454–11460.
- Liu, J., Guo, D., Zhou, Y., Wu, Z., Li, W., Zhao, F., Zheng, X., 2011. Identification of ancient textiles from Yingpan, Xinjiang, by multiple analytical techniques. Journal of Archaeological Science 38, 1763–1770.
- Mackenzie L. Davis, P.D., 2020. Water and Wastewater Engineering: Design Principles and Practice, Second Edition. McGraw-Hill Education.
- Mahmood, A.R., Al-Haideri, H.H., Hassan, F.M., 2019. Detection of Antibiotics in Drinking Water Treatment Plants in Baghdad City, Iraq. Advances in Public Health 2019, e7851354.

- Malakootian, M., Nasiri, A., Mahdizadeh, H., 2018. Preparation of CoFe2O4/activated carbon@chitosan as a new magnetic nanobiocomposite for adsorption of ciprofloxacin in aqueous solutions. Water Science and Technology 78, 2158–2170.
- Manganese [WWW Document], n.d. URL https://wqa.org/learn-about-water/water-q-a/manganese (accessed 2.3.22).
- Mangla, D., Annu, Sharma, A., Ikram, S., 2022. Critical review on adsorptive removal of antibiotics: Present situation, challenges and future perspective. Journal of Hazardous Materials 425, 127946.
- Mani, S., Bharagava, R.N., 2016. Exposure to Crystal Violet, Its Toxic, Genotoxic and Carcinogenic Effects on Environment and Its Degradation and Detoxification for Environmental Safety, in: de Voogt, W.P. (Ed.), Reviews of Environmental Contamination and Toxicology Volume 237, Reviews of Environmental Contamination and Toxicology. Springer International Publishing, Cham, pp. 71–104.
- Manjunath, S.V., Kumar, M., 2018. Evaluation of single-component and multi-component adsorption of metronidazole, phosphate and nitrate on activated carbon from Prosopıs julıflora. Chemical Engineering Journal 346, 525–534.
- Manjunath, S.V., Singh Baghel, R., Kumar, M., 2020. Antagonistic and synergistic analysis of antibiotic adsorption on Prosopis juliflora activated carbon in multicomponent systems. Chemical Engineering Journal 381, 122713.
- Mehmood, M.A., Qadri, H., Bhat, R.A., Rashid, A., Ganie, S.A., Dar, G.H., Shafiq-ur-Rehman, 2019. Heavy metal contamination in two commercial fish species of a trans-Himalayan freshwater ecosystem. Environ Monit Assess 191, 104.
- Mishra, S., Bharagava, R.N., 2016. Toxic and genotoxic effects of hexavalent chromium in environment and its bioremediation strategies. Journal of Environmental Science and Health, Part C 34, 1–32.
- Moarref, P., Pishvaei, M., Soleimani-Gorgani, A., Najafi, F., 2016. Synthesis of polypyrrole/indium tin oxide nanocomposites via miniemulsion polymerization. Designed Monomers and Polymers 19, 138–144.
- Mohammadzadeh, A., Ramezani, M., Ghaedi, A.M., 2016. Synthesis and characterization of Fe2O3–ZnO–ZnFe2O4/carbon nanocomposite and its application to removal of bromophenol blue dye using ultrasonic assisted method: Optimization by response surface methodology and genetic algorithm. Journal of the Taiwan Institute of Chemical Engineers 59, 275–284.

- Nabarlatz, D., de Celis, J., Bonelli, P., Cukierman, A.L., 2012. Batch and dynamic sorption of Ni(II) ions by activated carbon based on a native lignocellulosic precursor. Journal of Environmental Management 97, 109–115.
- Nahar, K., Chowdhury, Md.A.K., Chowdhury, Md.A.H., Rahman, A., Mohiuddin, K.M., 2018. Heavy metals in handloom-dyeing effluents and their biosorption by agricultural byproducts. Environ Sci Pollut Res 25, 7954–7967.
- Najafpoor, A.A., Nemati Sani, O., Alidadi, H., Yazdani, M., Navaei Fezabady, A.A., Taghavi, M., 2019. Optimization of ciprofloxacin adsorption from synthetic wastewaters using γ-Al2O3 nanoparticles: An experimental design based on response surface methodology. Colloid and Interface Science Communications 33, 100212.
- Nakagawa, Y., Molina-Sabio, M., Rodríguez-Reinoso, F., 2007. Modification of the porous structure along the preparation of activated carbon monoliths with H3PO4 and ZnCl2. Microporous and Mesoporous Materials 103, 29–34.
- Nakama, Y., 2017. Chapter 15 - Surfactants, in: Sakamoto, K., Lochhead, R.Y., Maibach, H.I., Yamashita, Y. (Eds.), Cosmetic Science and Technology. Elsevier, Amsterdam, pp. 231–244.
- Naraginti, S., Yong, Y.-C., 2019. Enhanced detoxification of p-bromophenol by novel Zr/Ag-TiO2@rGO ternary composite: Degradation kinetics and phytotoxicity evolution studies. Ecotoxicology and Environmental Safety 170, 355–362.
- Naseem, R., Tahir, S.S., 2001. Removal of Pb(II) from aqueous/acidic solutions by using bentonite as an adsorbent. Water Research 35, 3982–3986.
- Nidheesh, P.V., Singh, T.S.A., 2017. Arsenic removal by electrocoagulation process: Recent trends and removal mechanism. Chemosphere 181, 418–432.
- Nodehi, R., Shayesteh, H., Kelishami, A.R., 2020. Enhanced adsorption of congo red using cationic surfactant functionalized zeolite particles. Microchemical Journal 153, 104281.
- Novotný, Č., Dias, N., Kapanen, A., Malachová, K., Vándrovcová, M., Itävaara, M., Lima, N., 2006. Comparative use of bacterial, algal and protozoan tests to study toxicity of azo- and anthraquinone dyes. Chemosphere 63, 1436–1442.
- Ntakirutimana, S., Tan, W., Wang, Y., 2019. Enhanced surface activity of activated carbon by surfactants synergism. RSC Advances 9, 26519–26531.
- Ødegaard, H., 1995. Optimization of flocculation/flotation in chemical wastewater treatment. Water Science and Technology, Flotation Processes in Water and Sludge Treatment 31, 73–82.

- Ong, H.C., Chen, W.-H., Singh, Y., Gan, Y.Y., Chen, C.-Y., Show, P.L., 2020. A state-of-the-art review on thermochemical conversion of biomass for biofuel production: A TG-FTIR approach. Energy Conversion and Management 209, 112634.
- Pandey, A., Singh, P., Iyengar, L., 2007. Bacterial decolorization and degradation of azo dyes. International Biodeterioration & Biodegradation 59, 73–84.
- Parshetti, G.K., Kalme, S.D., Gomare, S.S., Govindwar, S.P., 2007. Biodegradation of Reactive blue-25 by Aspergillus ochraceus NCIM-1146. Bioresource Technology 98, 3638–3642.
- Pathania, D. (Ed.), 2016. Heavy metals: sources, toxicity and remediation techniques, Materials science and technologies. Nova Publishers, New York.
- Patra, C., Gupta, R., Bedadeep, D., Narayanasamy, S., 2020. Surface treated acid-activated carbon for adsorption of anionic azo dyes from single and binary adsorptive systems: A detail insight. Environmental Pollution 266, 115102.
- Patra, C., Medisetti, R.M.N., Pakshirajan, K., Narayanasamy, S., 2019. Assessment of raw, acid-modified and chelated biomass for sequestration of hexavalent chromium from aqueous solution using Sterculia villosa Roxb. shells. Environ Sci Pollut Res 26, 23625–23637.
- Patra, C., Shahnaz, T., Subbiah, S., Narayanasamy, S., 2020. Comparative assessment of raw and acid-activated preparations of novel Pongamia pinnata shells for adsorption of hexavalent chromium from simulated wastewater. Environ Sci Pollut Res 27, 14836–14851.
- Patra, C., Suganya, E., Sivaprakasam, S., Krishnamoorthy, G., Narayanasamy, S., 2021. A detailed insight on fabricated porous chitosan in eliminating synthetic anionic dyes from single and multi-adsorptive systems with related studies. Chemosphere 281, 130706.
- Pattanaik, L., Padhi, S.K., Hariprasad, P., Naik, S.N., 2020. Life cycle cost analysis of natural indigo dye production from Indigofera tinctoria L. plant biomass: a case study of India. Clean Techn Environ Policy 22, 1639–1654.
- Paulino, A.T., Minasse, F.A.S., Guilherme, M.R., Reis, A.V., Muniz, E.C., Nozaki, J., 2006. Novel adsorbent based on silkworm chrysalides for removal of heavy metals from wastewaters. Journal of Colloid and Interface Science 301, 479–487.
- Peng, B., Chen, L., Que, C., Yang, K., Deng, F., Deng, X., Shi, G., Xu, G., Wu, M., 2016. Adsorption of Antibiotics on Graphene and Biochar in Aqueous Solutions Induced by π-π Interactions. Sci Rep 6, 31920.
- Pérez-Alvarez, I., Islas-Flores, H., Gómez-Oliván, L.M., Barceló, D., López De Alda, M., Pérez Solsona, S., Sánchez-Aceves, L., SanJuan-Reyes, N., Galar-Martínez, M., 2018. Determination of

metals and pharmaceutical compounds released in hospital wastewater from Toluca, Mexico, and evaluation of their toxic impact. Environmental Pollution 240, 330–341.

- Piña, B., Bayona, J.M., Christou, A., Fatta-Kassinos, D., Guillon, E., Lambropoulou, D., Michael, C., Polesel, F., Sayen, S., 2020. On the contribution of reclaimed wastewater irrigation to the potential exposure of humans to antibiotics, antibiotic resistant bacteria and antibiotic resistance genes – NEREUS COST Action ES1403 position paper. Journal of Environmental Chemical Engineering 8, 102131.
- Prahas, D., Kartika, Y., Indraswati, N., Ismadji, S., 2008. Activated carbon from jackfruit peel waste by H3PO4 chemical activation: Pore structure and surface chemistry characterization. Chemical Engineering Journal 140, 32–42.
- Prasad, A.S.A., Rao, K.V.B., 2013. Aerobic biodegradation of Azo dye by Bacillus cohnii MTCC 3616; an obligately alkaliphilic bacterium and toxicity evaluation of metabolites by different bioassay systems. Appl Microbiol Biotechnol 97, 7469–7481.
- Prasannamedha, G., Kumar, P.S., 2020. A review on contamination and removal of sulfamethoxazole from aqueous solution using cleaner techniques: Present and future perspective. Journal of Cleaner Production 250, 119553.
- Primary, Secondary, and Tertiary Wastewater Treatment: How Do They Work?, 2017. . Innovative Solutions for Wastewater Treatment | Organica Water Inc. URL https://www.organicawater.com/primary-secondary-tertiary-wastewater-treatment-work/ (accessed 2.3.22).
- PubChem1, n.d. C.I. Direct Blue 6 [WWW Document]. URL https://pubchem.ncbi.nlm.nih.gov/compound/17449 (accessed 2.3.22).
- PubChem2, n.d. Congo red [WWW Document]. URL https://pubchem.ncbi.nlm.nih.gov/compound/11313 (accessed 2.3.22).
- PubChem3, n.d. Bromophenol blue [WWW Document]. URL https://pubchem.ncbi.nlm.nih.gov/compound/8272 (accessed 2.3.22).
- PubChem4, n.d. Sulfamethoxazole [WWW Document]. URL https://pubchem.ncbi.nlm.nih.gov/compound/5329 (accessed 2.3.22).
- Quintelas, C., Rocha, Z., Silva, B., Fonseca, B., Figueiredo, H., Tavares, T., 2009. Removal of Cd(II), Cr(VI), Fe(III) and Ni(II) from aqueous solutions by an E. coli biofilm supported on kaolin. Chemical Engineering Journal 149, 319–324.
- Qurrat-ul-Ain, Khurshid, S., Gul, Z., Khatoon, J., Raza Shah, M., Hamid, I., Tawab Khan, I.A., Aslam, F., 2020. Anionic azo dyes removal from water using amine-functionalized cobalt–iron

oxide nanoparticles: a comparative time-dependent study and structural optimization towards the removal mechanism. RSC Advances 10, 1021–1041.

- Rakhunde, R., Deshpande, L., Juneja, H.D., 2012. Chemical Speciation of Chromium in Water: A Review. Critical Reviews in Environmental Science and Technology 42, 776–810.
- Ramos, S.N. do C., Xavier, A.L.P., Teodoro, F.S., Gil, L.F., Gurgel, L.V.A., 2016. Removal of cobalt(II), copper(II), and nickel(II) ions from aqueous solutions using phthalate-functionalized sugarcane bagasse: Mono- and multicomponent adsorption in batch mode. Industrial Crops and Products 79, 116–130.
- Rangabhashiyam, S., Selvaraju, N., 2015. Evaluation of the biosorption potential of a novel Caryota urens inflorescence waste biomass for the removal of hexavalent chromium from aqueous solutions. Journal of the Taiwan Institute of Chemical Engineers 47, 59–70.
- Ravi, Pandey, L.M., 2019. Enhanced adsorption capacity of designed bentonite and alginate beads for the effective removal of methylene blue. Applied Clay Science 169, 102–111.
- Rouhani Shirvan, A., Shakeri, M., Bashari, A., 2019. 5 - Recent advances in application of chitosan and its derivatives in functional finishing of textiles, in: Shahid-ul-Islam, Butola, B.S. (Eds.), The Impact and Prospects of Green Chemistry for Textile Technology, The Textile Institute Book Series. Woodhead Publishing, pp. 107–133.
- Rudi, N.N., Muhamad, M.S., Te Chuan, L., Alipal, J., Omar, S., Hamidon, N., Abdul Hamid, N.H., Mohamed Sunar, N., Ali, R., Harun, H., 2020. Evolution of adsorption process for manganese removal in water via agricultural waste adsorbents. Heliyon 6, e05049.
- Saleem, J., Shahid, U.B., Hijab, M., Mackey, H., McKay, G., 2019. Production and applications of activated carbons as adsorbents from olive stones. Biomass Conv. Bioref. 9, 775–802.
- Saleh, T.A., Naeemullah, Tuzen, M., Sarı, A., 2017. Polyethylenimine modified activated carbon as novel magnetic adsorbent for the removal of uranium from aqueous solution. Chemical Engineering Research and Design 117, 218–227.
- Samsami, S., Mohamadizaniani, M., Sarrafzadeh, M.-H., Rene, E.R., Firoozbahr, M., 2020. Recent advances in the treatment of dye-containing wastewater from textile industries: Overview and perspectives. Process Safety and Environmental Protection 143, 138–163.
- Saranya, N., Ajmani, A., Sivasubramanian, V., Selvaraju, N., 2018. Hexavalent Chromium removal from simulated and real effluents using Artocarpus heterophyllus peel biosorbent - Batch and continuous studies. Journal of Molecular Liquids 265, 779–790.
- Saratale, R.G., Gandhi, S.S., Purankar, M.V., Kurade, M.B., Govindwar, S.P., Oh, S.E., Saratale, G.D., 2013. Decolorization and detoxification of sulfonated azo dye C.I. Remazol Red and textile

effluent by isolated Lysinibacillus sp. RGS. Journal of Bioscience and Bioengineering 115, 658–667.

- Sathishkumar, K., AlSalhi, M.S., Sanganyado, E., Devanesan, S., Arulprakash, A., Rajasekar, A., 2019. Sequential electrochemical oxidation and bio-treatment of the azo dye congo red and textile effluent. Journal of Photochemistry and Photobiology B: Biology 200, 111655.
- Saxena, G., Bharagava, R.N., 2017. Organic and Inorganic Pollutants in Industrial Wastes: Ecotoxicological Effects, Health Hazards, and Bioremediation Approaches, in: Environmental Pollutants and Their Bioremediation Approaches. CRC Press.
- Saxena, G., Chandra, R., Bharagava, R.N., 2017. Environmental Pollution, Toxicity Profile and Treatment Approaches for Tannery Wastewater and Its Chemical Pollutants, in: de Voogt, P. (Ed.), Reviews of Environmental Contamination and Toxicology Volume 240, Reviews of Environmental Contamination and Toxicology. Springer International Publishing, Cham, pp. 31–69.
- Schmidt, S.-A., Gukelberger, E., Hermann, M., Fiedler, F., Großmann, B., Hoinkis, J., Ghosh, A., Chatterjee, D., Bundschuh, J., 2016. Pilot study on arsenic removal from groundwater using a small-scale reverse osmosis system—Towards sustainable drinking water production. Journal of Hazardous Materials 318, 671–678.
- Shahnaz, T., S., M.M.F., V.c., P., Narayanasamy, S., 2020. Surface modification of nanocellulose using polypyrrole for the adsorptive removal of Congo red dye and chromium in binary mixture. International Journal of Biological Macromolecules 151, 322–332.
- Sher, F., Hanif, K., Iqbal, S.Z., Imran, M., 2020. Implications of advanced wastewater treatment: Electrocoagulation and electroflocculation of effluent discharged from a wastewater treatment plant. Journal of Water Process Engineering 33, 101101.
- Siddiqui, S.I., Fatima, B., Tara, N., Rathi, G., Chaudhry, S.A., 2019. 15 - Recent advances in remediation of synthetic dyes from wastewaters using sustainable and low-cost adsorbents, in: Shahid-ul-Islam, Butola, B.S. (Eds.), The Impact and Prospects of Green Chemistry for Textile Technology, The Textile Institute Book Series. Woodhead Publishing, pp. 471–507.
- Singh, R.L., Singh, P.K., Singh, R.P., 2015. Enzymatic decolorization and degradation of azo dyes – A review. International Biodeterioration & Biodegradation 104, 21–31.
- Song, X., Liu, H., Cheng, L., Qu, Y., 2010. Surface modification of coconut-based activated carbon by liquid-phase oxidation and its effects on lead ion adsorption. Desalination 255, 78–83.

- Sonwani, R.K., Swain, G., Giri, B.S., Singh, R.S., Rai, B.N., 2020. Biodegradation of Congo red dye in a moving bed biofilm reactor: Performance evaluation and kinetic modeling. Bioresource Technology 302, 122811.
- Srinivasan, A., Viraraghavan, T., 2010. Decolorization of dye wastewaters by biosorbents: A review. Journal of Environmental Management 91, 1915–1929.
- Stolz, A., 2001. Basic and applied aspects in the microbial degradation of azo dyes. Appl Microbiol Biotechnol 56, 69–80.
- Sun, Y., Yue, Q., Gao, B., Gao, Y., Li, Q., Wang, Y., 2013. Adsorption of hexavalent chromium on Arundo donax Linn activated carbon amine-crosslinked copolymer. Chemical Engineering Journal 217, 240–247.
- Sun, Y., Yue, Q., Mao, Y., Gao, B., Gao, Y., Huang, L., 2014. Enhanced adsorption of chromium onto activated carbon by microwave-assisted H3PO4 mixed with Fe/Al/Mn activation. Journal of Hazardous Materials 265, 191–200.
- Tang, Y., Shao, Y., Chen, N., Yao, K.-F., 2015. Rapid decomposition of Direct Blue 6 in neutral solution by Fe–B amorphous alloys. RSC Advances 5, 6215–6221.
- Tang, Z., Peng, S., Hu, S., Hong, S., 2017. Enhanced removal of bisphenol-AF by activated carbon-alginate beads with cetyltrimethyl ammonium bromide. Journal of Colloid and Interface Science 495, 191–199.
- Tchounwou, P.B., Yedjou, C.G., Patlolla, A.K., Sutton, D.J., 2012. Heavy Metal Toxicity and the Environment, in: Luch, A. (Ed.), Molecular, Clinical and Environmental Toxicology: Volume 3: Environmental Toxicology, Experientia Supplementum. Springer, Basel, pp. 133–164.
- Tobin, J.M., Cooper, D.G., Neufeld, R.J., 1984. Uptake of Metal Ions by Rhizopus arrhizus Biomass. Appl Environ Microbiol 47, 821–824.
- Toles, C.A., Marshall, W.E., Johns, M.M., 1999. Surface functional groups on acid-activated nutshell carbons. Carbon 37, 1207–1214.
- Tonucci, M.C., Gurgel, L.V.A., Aquino, S.F. de, 2015. Activated carbons from agricultural byproducts (pine tree and coconut shell), coal, and carbon nanotubes as adsorbents for removal of sulfamethoxazole from spiked aqueous solutions: Kinetic and thermodynamic studies. Industrial Crops and Products 74, 111–121.
- Tulcan, R.X.S., Ouyang, W., Lin, C., He, M., Wang, B., 2021. Vanadium pollution and health risks in marine ecosystems: Anthropogenic sources over natural contributions. Water Research 207, 117838.

- Turk Sekulic, M., Boskovic, N., Milanovic, M., Grujic Letic, N., Gligoric, E., Pap, S., 2019. An insight into the adsorption of three emerging pharmaceutical contaminants on multifunctional carbonous adsorbent: Mechanisms, modelling and metal coadsorption. Journal of Molecular Liquids 284, 372–382.
- US EPA, O., 2013. Ground Water and Drinking Water [WWW Document]. URL https://www.epa.gov/ground-water-and-drinking-water (accessed 2.3.22).
- US EPA, O., 2015. Chromium in Drinking Water [WWW Document]. URL https://www.epa.gov/sdwa/chromium-drinking-water (accessed 2.3.22).
- Van, T.T.H., Yidana, Z., Smooker, P.M., Coloe, P.J., 2020. Antibiotic use in food animals worldwide, with a focus on Africa: Pluses and minuses. Journal of Global Antimicrobial Resistance 20, 170–177.
- Vishnu Priyan, V., Shahnaz, T., Suganya, E., Sivaprakasam, S., Narayanasamy, S., 2021. Ecotoxicological assessment of micropollutant Diclofenac biosorption on magnetic sawdust: Phyto, Microbial and Fish toxicity studies. Journal of Hazardous Materials 403, 123532.
- Waghmode, T.R., Kurade, M.B., Sapkal, R.T., Bhosale, C.H., Jeon, B.-H., Govindwar, S.P., 2019. Sequential photocatalysis and biological treatment for the enhanced degradation of the persistent azo dye methyl red. Journal of Hazardous Materials 371, 115–122.
- Walker, C.H., Sibly, R.M., Sibly, R.M., Peakall, D.B., 2005. Principles of Ecotoxicology, 0 ed. CRC Press.
- Wang, A., Zhao, W., Yu, W., 2015. Effect of acid/base on the third-order optical nonlinearity of polypyrrole. Journal of Molecular Structure 1099, 291–296.
- Wang, L.-C., Ni, X., Cao, Y.-H., Cao, G., 2018. Adsorption behavior of bisphenol A on CTAB-modified graphite. Applied Surface Science 428, 165–170.
- Wang, W., Zhou, J., Achari, G., Yu, J., Cai, W., 2014. Cr(VI) removal from aqueous solutions by hydrothermal synthetic layered double hydroxides: Adsorption performance, coexisting anions and regeneration studies. Colloids and Surfaces A: Physicochemical and Engineering Aspects 457, 33–40.
- WebElements Periodic Table » Iron » radii of atoms and ions [WWW Document], n.d. URL https://www.webelements.com/iron/atom_sizes.html (accessed 2.4.22).
- WebElements Periodic Table » Periodicity » Atomic radii (Clementi) » Periodic table gallery [WWW Document], n.d. URL https://www.webelements.com/periodicity/atomic_radius/ (accessed 2.4.22).

- White, B., Banerjee, S., O'Brien, S., Turro, N.J., Herman, I.P., 2007. Zeta-Potential Measurements of Surfactant-Wrapped Individual Single-Walled Carbon Nanotubes. J. Phys. Chem. C 111, 13684–13690.
- Wu, A., Kolla, H., Manohar, S.K., 2005. Chemical Synthesis of Highly Conducting Polypyrrole Nanofiber Film. Macromolecules 38, 7873–7875.
- Xi, Y., Luo, Y., Luo, J., Luo, X., 2015. Removal of Cadmium(II) from Wastewater Using Novel Cadmium Ion-Imprinted Polymers. J. Chem. Eng. Data 60, 3253–3261.
- Xiang, L., Niu, C.-G., Tang, N., Lv, X.-X., Guo, H., Li, Z.-W., Liu, H.-Y., Lin, L.-S., Yang, Y.-Y., Liang, C., 2021. Polypyrrole coated molybdenum disulfide composites as adsorbent for enhanced removal of Cr(VI) in aqueous solutions by adsorption combined with reduction. Chemical Engineering Journal 408, 127281.
- Xie, R., Wang, H., Chen, Y., Jiang, W., 2013. Walnut shell-based activated carbon with excellent copper (II) adsorption and lower chromium (VI) removal prepared by acid–base modification. Environmental Progress & Sustainable Energy 32, 688–696.
- Yadav, A., Chowdhary, P., Kaithwas, G., Bharagava, R.N., 2017. Toxic Metals in the Environment: Threats on Ecosystem and Bioremediation Approaches, in: Handbook of Metal-Microbe Interactions and Bioremediation. CRC Press.
- Yaseen, D.A., Scholz, M., 2019. Textile dye wastewater characteristics and constituents of synthetic effluents: a critical review. Int. J. Environ. Sci. Technol. 16, 1193–1226.
- Yenkie, K.M., 2019. Integrating the three E's in wastewater treatment: efficient design, economic viability, and environmental sustainability. Current Opinion in Chemical Engineering, Energy, Environment & Sustainability: Sustainability Modeling Reaction engineering and catalysis: Green Reaction Engineering 26, 131–138.
- Yussuf, A., Al-Saleh, M., Al-Enezi, S., Abraham, G., 2018. Synthesis and Characterization of Conductive Polypyrrole: The Influence of the Oxidants and Monomer on the Electrical, Thermal, and Morphological Properties. International Journal of Polymer Science 2018, 1–8.
- Zamora-Ledezma, C., Negrete-Bolagay, D., Figueroa, F., Zamora-Ledezma, E., Ni, M., Alexis, F., Guerrero, V.H., 2021. Heavy metal water pollution: A fresh look about hazards, novel and conventional remediation methods. Environmental Technology & Innovation 22, 101504.
- Zaynab, M., Al-Yahyai, R., Ameen, A., Sharif, Y., Ali, L., Fatima, M., Khan, K.A., Li, S., 2022. Health and environmental effects of heavy metals. Journal of King Saud University - Science 34, 101653.

- Zhang, F., Yediler, A., Liang, X., Kettrup, A., 2004. Effects of dye additives on the ozonation process and oxidation by-products: a comparative study using hydrolyzed C.I. Reactive Red 120. Dyes and Pigments 60, 1–7.
- Zhang, L., Lv, T., Zhang, Y., Stein, O.R., Arias, C.A., Brix, H., Carvalho, P.N., 2017. Effects of constructed wetland design on ibuprofen removal – A mesocosm scale study. Science of The Total Environment 609, 38–45.
- Zhu, X., Tsang, D.C.W., Chen, F., Li, S., Yang, X., 2015. Ciprofloxacin adsorption on graphene and granular activated carbon: kinetics, isotherms, and effects of solution chemistry. Environmental Technology 36, 3094–3102.

APPENDIX

Table A.1. *Detail list of chemicals, reagents and salts*

Serial no.	Chemicals/Reagents/Salts	Purpose
1	Sulphuric acid (98%)	Preparation of adsorbent (chemical activation)
2	Ortho-phosphoric acid (88%)	Preparation of adsorbent (chemical activation)
3	Phosphoric acid (85%)	Preparation of adsorbent (chemical activation)
4	Ethylenediaminetetra acetic acid (EDTA)	Chelating agent for acid activated carbon
5	Sodium bicarbonate ($NaHCO_3$)	For washing prepared carbon
6	Chitosan flakes	Raw material for fabrication
7	Calcium Bromide ($CaBr_2.xH_2O$)	Preparation of adsorbent (Gelation of chitosan)
8	Methanol	Preparation of adsorbent (Gelation of chitosan)
9	Pyrrole	Preparation of adsorbent
10	Acetone	Preparation of adsorbent
11	Cetyltrimethylammonium bromide (CTAB)	Preparation of adsorbent
12	Ammonium persulfate (APS)	Preparation of adsorbent
13	Congo Red (CR)	Adsorbate
14	Direct Blue 6 (DB)	Adsorbate
15	Bromophenol Blue (BB)	Adsorbate
16	Potassium dichromate ($K_2Cr_2O_7$)	Adsorbate
17	Sulfamethoxazole (SMX)	Adsorbate
18	Diphenyl carbazide (DPC)	For detecting Cr(VI)
19	Potassium Dichromate ($K_2Cr_2O_7$)	Source of chromium (Cr^{+6}) ions
20	Lead Nitrate ($Pb(NO_3)_2$)	Source of lead (Pb^{+2}) ions

21	Iron(III) Chloride ($FeCl_3$)	Source of ferric (Fe^{+3}) ions
22	Cobalt (II) Chloride ($CoCl_2$)	Source of cobalt (Co^{+2}) ions
23	Nickel Sulphate ($NiSO_4$)	Source of Nickel (Ni^{+2}) ions
24	Zinc Chloride ($ZnCl_2$)	Source of zinc (Zn^{+2}) ions
25	Copper(II) Chloride ($CuCl_2$)	Source of copper (Cu^{+2}) ions
26	Sodium Sulphate (Na_2SO_4)	Source of sulphate (SO_4^{-2}) ions
27	Sodium Nitrate ($NaNO_3$)	Source of nitrate (NO_3^{-2}) ions
28	Sodium Carbonate (Na_2CO_3)	Source of carbonate (CO_3^{-2}) ions
29	Sodium Chloride (NaCl)	Source of chloride (Cl^{-1}) ions
30	Sodium Phosphate (Na_3PO_4)	Source of phosphate (PO_4^{-3}) ions
31	0.1 N Sodium Hydroxide (NaOH)	Desorbing agent
32	1% Sodium Hypochlorite (NaClO)	Rinsing *Vigna mungo* seeds
33	0.1 M Sodium Hydroxide (NaOH)	For adjusting pH
34	0.1 M Hydrochloric acid (HCl)	For adjusting pH
35	Ciprofloxacin	For co-existing antibiotic analysis
36	Amoxicillin	For co-existing antibiotic analysis
37	p-dimethylaminobenzaldehyde (p-DAB)	For Ehrlich test
38	1% Sodium Hypochlorite (NaClO)	Rinsing *Vigna mungo* seeds
39	0.1 N Sodium Hydroxide (NaOH)	Desorbing agent

***Table A.2.** Detail list of instrumentation used for characterisation of the adsorbent*

Serial no.	Instrumentation	Make and model	Purpose
1	Scanning electron microscopy (SEM)	Zeiss, GeminiSEM, Germany	For surface morphology analysis
2	Energy-dispersive X-ray spectroscopy (EDS)	Zeiss, SigmaSEM, Germany	For surface elemental analysis
3	Atomic force microscopy (AFM)	Cypher, Oxford, United Kingdom	For surface morphology analysis
4	Powder X-ray diffraction (XRD)	Rigaku, Micromax-007HF, Japan	Analysing substructural modifications caused due to modification
5	Total pore analysis or Brunauer-Emmett-Teller (BET) analysis	Quantachrome-Autosorb-IQ MP, USA	For total pore/porosity analysis of the adsorbent
6	Zeta potential analysis	Delsa nano C, Beckman Coulter, Switzerland	For analysing surface charge of the adsorbent
7	Fourier-transform infrared spectroscopy (FT-IR)	Spectrum two, PerkinElmer, Singapore	For analysing surface functional groups involved in adsorption or modification

A.1. Theoretical background

Adsorption capacities (Q_t) and the percentage removal (%) of adsorbate by the adsorbents (NPP, PPP and SPP) were all calculated using the following equations:

$$Q_t = \left(\frac{C_i - C_e}{M}\right)V \tag{A.1}$$

$$\%\text{Removal} = \left(\frac{C_i - C_e}{C_i}\right)100 \tag{A.2}$$

Here, 'Q_t' is the adsorption capacity (mg/g) at time t; 'C_e' and 'C_i' are the concentration of adsorbate at equilibrium and initial phase, respectively; 'M' is the mass of adsorbent (g); and 'V' represents the adsorbate volume in litres (L) (Rezakazemi and Zhang, 2018).

A.1.1. Isotherm model studies

Two-parameter isotherm models were studied to analyze the sorbate-sorbent interactions from single adsorptive systems. The evaluated models are as follows:

Table A.3*. Detailed theory of Two and three-parameter adsorption models*

Isotherm	**Equation**	**Notations**	**Inference**
Two-parameter isotherm model			
Langmuir (Langmuir, 1918)	$Q_e = \frac{Q_L K_L C_e}{1 + K_L C_e}$	• C_e:Concentration of adsorbate at equilibrium after adsorption (mg/L) • C_i: Initial adsorbate concentration (mg/L) • Q_e: Adsorption capacity of adsorbent at equilibrium (mg/g) • Q_L: Langmuir maximum adsorption capacity (mg/g) • K_L: Langmuir constant (L/mg)	• Hypothesizes monolayer formation of adsorbate over the homogenous sites of adsorbent's surface with assumptions of no steric hindrance among the adsorbent and sorbate molecules. • K_L values between 0 and 1 suggest favorable Langmuir adsorption. • $K_L > 1$, $K_L = 1$ and $K_L = 0$ suggest unfavorable, linear and irreversible Langmuir adsorption respectively.
Freundlich (Freundlich and Heller, 1939)	$Q_e = K_F C_e^{1/n}$	• K_F: Freundlich adsorption constant (mg/g) $(mg/L)^{-1/n}$ • 1/n: Freundlich heterogeneity factor	Hypothesizes multilayer formation of adsorbate species over the heterogeneous sites of adsorbent's surface with non-uniform distribution of sorption heat.
Dubinin-Radushkevich (Dubinin, 1965)	$Q_e = Q_{DR} \exp^{-K_{DR}\varepsilon^2}$ $\varepsilon = RT \ln\left(1 + \frac{1}{C_e}\right)$ $E_{DR} = \frac{1}{\sqrt{2K_{DR}}}$	• Q_{DR}: Dubinin-Radushkevich maximum adsorption capacity (mg/g) • K_{DR}: Mean free energy of adsorption (mol^2/J^2) • ε: Polyani potential • R: Universal gas constant (8.314 J/mol/K) • T: Temperature (K)	• Predicts the apparent energy of sorbate-sorbent interaction. • If values of mean bio-sorption energy i.e. E_{DR}<8 kJ/mol, then adsorption process is physisorption, whereas E_{DR}>16 kJ/mol implies chemisorption.
Frumkin (Patra et al., 2019)	$\frac{\theta}{1-\theta} e^{-2\alpha_{FK}\theta} = K_{FK} C_e$	• K_{FK} represents the Frumkin constant. • θ is fractional coverage of sorption sites (1-Ce/Co). • α_{FK} represents the interaction parameter for sorbate-sorbent interaction. Value of α_{FK} depends on interaction among the adsorbate species. $\alpha_{FK} > 0$ and $\alpha_{FK} < 0$ values indicate attraction and repulsion among adsorbed species, respectively	Frumkin isotherm model defines sorption phenomenon over homogenous surface of the sorbent. It is based on possible interactions among the adsorbate molecules within the formed monolayer.

Temkin (Rangabhashiya et al., 2014)	$Q_e = \frac{RT}{B}\ln(A_T C_e)$ $B = \frac{RT}{b_T}$	• A_T: Temkin isotherm constant (L/g) • B: Temkin adsorption heat constant (J/mol)	Assumes the adsorption heat (as the function of temperature) of sorbate molecules existing in a monolayer due to adsorption, decreases linearly and not logarithmically as the surface coverage increases.
Three-parameter isotherm model			
Redlich-Peterson (Redlich and Peterson, 1959)	$Q_e = \frac{Q_{RP} K_{RP} C_e}{1 + K_{RP} C_e^g}$	• Q_{RP}: R-P maximum adsorption capacity (mg/g) • K_{RP} and g are Redlich-Peterson constants Values of g vary from 0 to 1. For g = 1, Redlich-Peterson model equation is reduced to the Langmuir isotherm model	R-P isotherm combines the features of both the Langmuir and Freundlich isotherm models and amends the inaccuracies of both the two-parameter isotherms.
Sips (Sips, 1948)	$Q_e = \frac{Q_s K_S C_e^m}{1 + K_s C_e^m}$	• Q_s: Sips maximum adsorption capacity (mg/g) • K_s: Sips adsorption constant (L/mg) • m: Sips model exponent	• Blends the features of Langmuir and Freundlich isotherm models. • At low sorbate concentrations it transforms to the Freundlich form; whereas at higher sorbate concentrations it reduces to Langmuir isotherm. • Mathematically, Sips model reduces to the Langmuir model, when m=1.

A.1.2. Kinetic model studies

To evaluate the correlation of adsorption capacity of adsorbents with time, kinetic models were used to evaluate the equilibrated data.

Table A.4. *Detailed theory of Kinetic models*

KINETICS MODEL	EQUATION	NOTATIONS	INFERENCE
Pseudo-First order (Lagergren, 1898)	$\frac{dQ_t}{dt} = K_1(Q_e - Q_t)$	• Q_e: Extent of sorbate adsorbed at equilibrium (mg/g) • Q_t: Extent of sorbate adsorbed at specific time (mg/g) • t: Time (min) • K_1: Pseudo-First order rate constant (1/min)	• Describes the initial phase of the adsorption when the rate of adsorption directly depends on the intensity of available active sites. • Rate-limiting step in pseudo-first order is diffusion and independent of sorbate-sorbent concentrations (physisorption)
Pseudo-Second order (Ho and McKay, 1999)	$\frac{dQt}{dt} = K_2(Q_e - Q_t)^2$	• K_2: Pseudo-Second order rate constant (1/ min)	• Rate of adsorption is directly proportional to the squared difference between the adsorbate uptake at time "t" and at equilibrium. • Rate-limiting step in pseudo-second order is surface adsorption and involves chemical interaction (chemisorption).
Intra-Particle Diffusion (Weber and Morris, 1962)	$Q_t = K_{id}t^{1/2} + C$	• K_{id}: Intra-Particle Diffusion rate constant (mg/g/min$^{1/2}$)	This model defines 3 different phases of adsorption over porous adsorbents • external mass transfer on the porous sorbent surface; • intra-particle diffusion; • adsorption within the pore.

A.1.3. Thermodynamics parameter studies

Thermal analysis of sorbate-sorbent interactions were done to determine the energy distribution, involved heat exchange and spontaneity of the sorbate-sorbent interaction. Change in Gibb's free energy (ΔG^{o}; kJ/mol), change in enthalpy (ΔH^{o}; kJ/mol) and change in entropy (ΔS^{o}; kJ/mol/K) were studied for the same (Milonjic, 2007):

$$\Delta G^{\circ} = -RTln\left(\rho k_a\right) \tag{A.3}$$

$$\ln\left(\rho k_a\right) = \frac{(-\Delta H^{\circ})}{RT} + \frac{(\Delta S^{\circ})}{R} \tag{A.4}$$

Where, 'ρ' (g/l) is the density of investigated solution and 'k_a' (l/g) represents the distribution co-efficient (Rodrigues et al., 2018). Since aqueous solution was used for all the investigations, thus value of ρ was taken as 1000 g/l. k_a can be represented as (Aljeboree et al., 2017):

$$k_a = \frac{Q_e}{C_e} \times \frac{v_1}{v_2} \tag{A.5}$$

Here, v_1 represents coefficient of activity of the adsorbed solute and v_2 represents coefficient of activity of solute in solution at equilibrium. However, ratio of v_1 and v_2 can be assumed to be equal to one in case of dilute solutions. Thus, the equation can be represented as (Rangabhashiyam and Selvaraju, 2015):

$$k_a = C_e \overset{\lim}{\rightarrow} 0 \frac{Q_e}{C_e} \tag{A.6}$$

A.1.4 Packed bed column parameters

Variable parameters governing the efficacy of the packed bed column was analysed using various equations (Saranya et al., 2018; Rangabhashiyam et al., 2016). The maximum column capacity, Q_{total} (mg) for a given inlet concentration and flow rate is equal to the area under the plot of the adsorbed adsorbate concentration, C_{ads} (mg/L), versus 't' (min) and is calculated as follows:

$$Q_{total} = \frac{FA}{1000} = \frac{F}{1000}\int_{t=0}^{t=T_{total}} C_{ads}dt \qquad (A.7)$$

Here, $C_{ads} = C_0\text{-}Ce$ (mg/L), C_0 (mg/L), and C_e (mg/L) are the initial and equilibrium adsorbate concentrations, respectively, 't' total represent the total flow time (min), F is the flow rate (mL/min), and A is the area under the breakthrough curve (cm^2). The equilibrium adsorption capacity ($Q_{e(eqm.)}$), the amount of adsorbate ions adsorbed (mg) per unit weight of adsorbent (mg/g) in the column can be determined using the following equation:

$$Q_{e(eqm)} = \frac{Q_{total}}{W} \qquad (A.8)$$

Here, 'W' is the total dry weight of the adsorbent used in the column (g). The total amount of adsorbate ions sent to the column (M_{total}) can be calculated from the following equation:

$$M_{total} = \frac{C_0FT_{total}}{1000} \qquad (A.9)$$

The percentage removal of adsorbate (Y(%)) with respect to flow volume can be calculated from the ratio of column capacity (Q_{total}) to the amount of adsorbate ions sent to the column (M_{total}). The expression is represented as follows:

$$Y(\%) = \frac{Q_{total}}{M_{total}} \times 100 \qquad (A.10)$$

The total volume of the effluent, V_{eff} (mL), can be calculated using the following equation:

$$V_{eff} = FT_{total} \qquad (A.11)$$

Bibliography

- Aljeboree, A.M., Alshirifi, A.N., Alkaim, A.F., 2017. Kinetics and equilibrium study for the adsorption of textile dyes on coconut shell activated carbon. Arabian Journal of Chemistry 10, S3381–S3393.

- Dubinin, M.M., 1965. Modern state of the theory of volume filling of micropore adsorbents during adsorption of gases and steams on carbon adsorbents. Zhurnal Fizicheskoi Khimii, 39(19), 1305-1317.

- Freundlich, Herbert., Heller, Wilfried., 1939. The Adsorption of *cis* - and *trans* -Azobenzene. Journal of the American Chemical Society 61, 2228–2230.

- Han, R., Wang, Y., Han, P., Shi, J., Yang, J., Lu, Y., 2006. Removal of methylene blue from aqueous solution by chaff in batch mode. Journal of Hazardous Materials 137, 550–557.

- Ho, Y.S., McKay, G., 1999. Pseudo-second order model for sorption processes. Process Biochemistry 34, 451–465.

- Lagergren, S., 1898. About the Theory of so-called Adsorption of Soluble Substances, Kungliga Svenska Vetenskapsakademiens Handlingar 24, 1-39.

- Langmuir, I., 1918. THE ADSORPTION OF GASES ON PLANE SURFACES OF GLASS, MICA AND PLATINUM. J. Journal of the American Chemical Society 40, 1361–1403.

- Milonjic, S., 2007. A consideration of the correct calculation of thermodynamic parameters of adsorption. Journal of the Serbian Chemical Society 72, 1363–1367.

- Patra, C., Medisetti, R.M.N., Pakshirajan, K., Narayanasamy, S., 2019. Assessment of raw, acid-modified and chelated biomass for sequestration of hexavalent chromium from aqueous solution using Sterculia villosa Roxb. shells. Environ Sci Pollut Res 26, 23625–23637.

- Rangabhashiyam, S., Anu, N., Giri Nandagopal, M.S., Selvaraju, N., 2014. Relevance of isotherm models in biosorption of pollutants by agricultural byproducts. Journal of Environmental Chemical Engineering 2, 398–414.

- Rangabhashiyam, S., Nandagopal, M.S.G., Nakkeeran, E., Selvaraju, N., 2016. Adsorption of hexavalent chromium from synthetic and electroplating effluent on chemically modified Swietenia mahagoni shell in a packed bed column. Environ Monit Assess 188, 411.

- Rangabhashiyam, S., Selvaraju, N., 2015. Evaluation of the biosorption potential of a novel Caryota urens inflorescence waste biomass for the removal of hexavalent chromium from aqueous solutions. Journal of the Taiwan Institute of Chemical Engineers 47, 59–70.

- Redlich O, Peterson DL (1959) A useful adsorption isotherm. J Phys Chem 63:1024–1024.

- Rezakazemi, M., Zhang, Z., 2018. 2.29 Desulfurization Materials, in: Dincer, I. (Ed.), Comprehensive Energy Systems. Elsevier, Oxford, pp. 944–979.

- Rodrigues, D.A.S., Moura, J.M., Dotto, G.L., Cadaval, T.R.S., Pinto, L.A.A., 2018. Preparation, Characterization and Dye Adsorption/Reuse of Chitosan-Vanadate Films. J Polym Environ 26, 2917–2924.

- Saranya, N., Ajmani, A., Sivasubramanian, V., Selvaraju, N., 2018. Hexavalent Chromium removal from simulated and real effluents using Artocarpus heterophyllus peel biosorbent - Batch and continuous studies. Journal of Molecular Liquids 265, 779–790.

- Sips, R., 1948. On the Structure of a Catalyst Surface. The Journal of Chemical Physics 16, 490–495.

- Weber W.J., Morris J.C., 1962. Advances in water pollution research: removal of biologically resistant pollutant from wastewater by adsorption, in Proceedings of the International Conference on Water Pollution Symposium, Pergamon Press, Oxford, UK 2, 231–266.

LIST OF PUBLICATIONS

A. Publications from PhD thesis

1. **Patra, C.**, Suganya, E., Sivaprakasam, S., Krishnamoorthy, G., Selvaraju, N., **2021**. A detailed insight on fabricated porous chitosan in eliminating synthetic anionic dyes from single and multi-adsorptive systems with related studies. ***Chemosphere***, 281, 130706. https://doi.org/10.1016/j.chemosphere.2021.130706 *(IF: 7.086)*

2. **Patra, C.**, Gupta, R., Bedadeep, D., Selvaraju, N., **2020**. Surface treated acid-activated carbon for adsorption of anionic azo dyes from single and binary adsorptive systems: A detail insight. ***Environmental Pollution***, 266, 115102. https://doi.org/10.1016/j.envpol.2020.115102 *(IF: 8.071)*

3. **Patra, C.**, Shahnaz, T., Subbiah, S., Selvaraju, N., **2020**. Comparative assessment of raw and acid-activated preparations of novel Pongamia pinnata shells for adsorption of hexavalent chromium from simulated wastewater. ***Environmental Science and Pollution Research***, 27, 14836–14851. https://doi.org/10.1007/s11356-020-07979-y *(IF: 4.223)*

4. **Patra, C.**, Medisetti, R.M.N., Pakshirajan, K., Selvaraju, N., **2019**. Assessment of raw, acid-modified and chelated biomass for sequestration of hexavalent chromium from aqueous solution using Sterculia villosa Roxb. shells. ***Environmental Science and Pollution Research***, 26, 23625–23637. https://doi.org/10.1007/s11356-019-05582-4 *(IF: 4.223)*

5. **Chandi Patra**, Selvaraju Narayanasamy. "Polypyrrole complexation on biomass-derived powdered carbon for adsorptive elimination of emerging pharmaceutical contaminant Sulfamethoxazole: A comprehensive insight" *(UNDER REVIEW)*

B. Publications from Collaborative work

1. Kumar, A., **Patra, C.**, Kumar, S., Selvaraju, N., **2022**. Effect of magnetization on the adsorptive removal of an emerging contaminant ciprofloxacin by magnetic acid activated carbon. ***Environmental Research***, 206, 112604. https://doi.org/10.1016/j.envres.2021.112604 *(IF: 6.498)*

2. Chandrasekaran, A., **Patra, C.**, Selvaraju, N., Subbiah, S., **2020**. Adsorptive removal of Ciprofloxacin and Amoxicillin from single and binary aqueous systems using acid-activated carbon from Prosopis juliflora. ***Environmental Research***, 188, 109825. https://doi.org/10.1016/j.envres.2020.109825 *(IF: 6.498)*

3. Kumar, S., **Patra, C.**, Selvaraju, N., Rajaraman, P.V., **2020**. Performance of acid-activated water caltrop (Trapa natans) shell in fixed bed column for hexavalent chromium removal from simulated wastewater. ***Environmental Science and Pollution Research***, 27, 28042–28052. https://doi.org/10.1007/s11356-020-09155-8 *(IF: 4.223)*

4. Ajmani, A., **Patra, C.**, Subbiah, S., Selvaraju, N., **2020**. Packed bed column studies of hexavalent chromium adsorption by zinc chloride activated carbon synthesized from Phanera vahlii fruit biomass. ***Journal of Environmental Chemical Engineering***, 8, 103825. https://doi.org/10.1016/j.jece.2020.103825 *(IF: 5.909)*

5. Shahnaz, T., **Patra, C.**, Sharma, V., Selvaraju, N., **2020**. A comparative study of raw, acid-modified and EDTA-complexed Acacia auriculiformis biomass for the removal of hexavalent chromium. ***Chemistry and Ecology***, 36, 360–381. https://doi.org/10.1080/02757540.2020.1723560 *(IF: 2.244)*

6. Karthik, V., Saravanan, K., **Patra, C.**, Ushadevi, B., Vairam, S., Selvaraju, N., **2019**. Biosorption of Acid Yellow 12 from simulated wastewater by non-viable T. harzianum: kinetics, isotherm and thermodynamic studies. ***International Journal of Environmental Science and Technology***, 16, 6895–6906. https://doi.org/10.1007/s13762-018-2073-4 *(IF: 2.860)*

7. Suganya, E., Saranya, N., **Patra, C.**, Varghese, L.A., Selvaraju, N., **2019**. Biosorption potential of Gliricidia sepium leaf powder to sequester hexavalent chromium from synthetic aqueous

solution. ***Journal of Environmental Chemical Engineering***, 7, 103112. https://doi.org/10.1016/j.jece.2019.103112 *(IF: 5.909)*

8. Nakkeeran, E., **Patra, C.**, Shahnaz, T., Rangabhashiyam, S., Selvaraju, N., **2018**. Continuous biosorption assessment for the removal of hexavalent chromium from aqueous solutions using Strychnos nux vomica fruit shell. ***Bioresource Technology Reports***, 3, 256–260. https://doi.org/10.1016/j.biteb.2018.09.001

C. Conference Proceedings

1. **CHANDI PATRA**, Selvaraju Narayanasamy, **2022**. 'Understanding the adsorptive elimination of Sulfamethoxazole by polypyrrole complexed carbon from aqueous setups under simulated conditions'. **Research & Industrial Conclave 2022 (RIC, 2022)**, Indian Institute of Technology Guwahati, Assam, India. 21-23, January, 2022. **(SECOND BEST POSTER PRESENTATION AWARD)**

2. **CHANDI PATRA**, Ajit Kumar, Selvaraju Narayanasamy, **2021**. 'Polypyrrole doped acid activated carbon for efficient removal of emerging antibiotic contaminant from simulated wastewater setups'. **International Conference on Biotechnology For Resource Efficiency, Energy, Environment, Chemicals and Health (BRE3CH-2021)**, CSIR-Indian Institute of Petroleum and the Biotech Research Society, India, at Dehradun, India. 01-04, December, 2021. **(BEST RAPID PRESENTATION & POSTER AWARD)**

3. **CHANDI PATRA**, Ajit Kumar, Selvaraju Narayanasamy, **2019**. 'Surface porosity modified biopolymer for enhanced sequestration of dye from simulated water'. **REFLUX 2019**, Department of Chemical Engineering, Indian Institute of Technology Guwahati, Assam, India. 28-29, September, 2019.